

Deposition, Mixing and Storage Timescales at the Benthic Boundary Layer

Louise Brown

Submitted for the degree of Doctor of Philosophy at the
University of Glasgow, following research carried out at
the Scottish Universities Research and Reactor Centre.

September 2001

ProQuest Number: 13818890

All rights reserved

INFORMATION TO ALL USERS

The quality of this reproduction is dependent upon the quality of the copy submitted.

In the unlikely event that the author did not send a complete manuscript and there are missing pages, these will be noted. Also, if material had to be removed, a note will indicate the deletion.



ProQuest 13818890

Published by ProQuest LLC (2018). Copyright of the Dissertation is held by the Author.

All rights reserved.

This work is protected against unauthorized copying under Title 17, United States Code
Microform Edition © ProQuest LLC.

ProQuest LLC.
789 East Eisenhower Parkway
P.O. Box 1346
Ann Arbor, MI 48106 – 1346

GLASGOW
UNIVERSITY
LIBRARY:

12402
COPY 1

Abstract

With an area of approximately $3.6 \times 10^8 \text{ km}^2$, the oceans constitute a reservoir of central importance in global biogeochemical cycles and represent a major sink for anthropogenic contaminants. The fluxes of biological, geological and anthropogenic materials to deep ocean sediments and their subsequent burial are key processes in the removal of particulate matter from the zone of bioavailability. However, within the benthic boundary layer, a host of physical, biological and chemical processes modify the material arriving at the sea floor and influence its rate of removal from the biosphere. The NERC Benthic Boundary (BENBO) study, of which this project is a component, was initiated in order to examine these fluxes to the sea floor and their fate in the benthic zone. Radionuclides are an important tool in quantitatively determining a number of key benthic boundary processes; specifically sediment accumulation and the biological mixing processes acting on sediments after deposition. Analyses of natural and man-made radionuclides incorporated in the sediment were used to examine these processes on 10^3 -year (^{14}C), 10^2 -year ($^{210}\text{Pb}_{\text{excess}}$) and decadal (^{241}Am , ^{137}Cs , ^{238}Pu , $^{239,240}\text{Pu}$) timescales at the three Benthic Boundary Layer Experiment (BENBO) sites in the North East Atlantic Ocean. Radiometric dating of bulk carbonate was used to determine both the Holocene sediment accumulation history and depth of sediment homogenisation by biological mixing on the 10^3 -year timescale. At two of the sites, BENBO B and BENBO C, sediment accumulated at a constant rate over the Holocene, at 4.3 cm ky^{-1} and 6.5 cm ky^{-1} respectively. At the third site, BENBO A, the irregular radiocarbon-depth profile is considered to be generated by erosion and redeposition of sediments in the mid-Holocene. The two sites demonstrating constant sediment accumulation both show surface mixed layers which are deeper than is

typical of open ocean sites. Fluxes of $^{210}\text{Pb}_{\text{excess}}$ to the sediments follow the general pattern of increasing flux with increasing water column depth, and comparison with North-East Atlantic water column ^{226}Ra data indicates that the BENBO sites are not regions of enhanced radionuclide scavenging. The mean $^{238}\text{Pu}:$ $^{239,240}\text{Pu}$ activity ratios determined at sites B and C are 0.032 and 0.039 indicates atmospheric weapons testing fallout is the dominant source of man-made radionuclides to these sites. The $^{210}\text{Pb}_{\text{excess}}$ and man-made radionuclide profiles were also used to determine the prevailing short term ($<10^2$ y) mixing mechanism. The profile at site A indicated mixing dominated by biodiffusive processes, and a biodiffusion coefficient of 0.088 cm ky^{-1} was calculated. The profile at site B was also initially interpreted as biodiffusive mixing. The rate determined by $^{210}\text{Pb}_{\text{excess}}$ at this site was 0.045 cm ky^{-1} , with no significant variation between the mixing coefficients calculated for natural ($^{210}\text{Pb}_{\text{excess}}$) and man-made ($^{239,240}\text{Pu}$) radionuclides. At site C, subsurface peaks in $^{210}\text{Pb}_{\text{excess}}$ specific activity indicated bioturbation by advective rather than biodiffusive processes. Replicate sub cores from sites B and C were also analysed for $^{210}\text{Pb}_{\text{excess}}$, ^{241}Am and ^{137}Cs , and indicated strong variability in bioturbation over a small ($<1 \text{ m}^2$) spatial scale. Measurement of the $^{210}\text{Pb}_{\text{excess}}$ activity of sipunculid burrow material confirmed that bioturbation by large, infaunal organisms is responsible for generating the subsurface peaks in radionuclide activity found in sub cores B(vi), C(ii) and C(iv). Size selective mixing was examined by ^{14}C dating of hand picked planktonic foraminifera samples. The extent and direction of the foraminiferal sample age offset, relative to bulk carbonate are shown to be a function of both sampling method and the ecology of the site.

Acknowledgements

I would like to express my gratitude to everyone who was involved in this project, and without whom it wouldn't have been completed. At SURRC, my supervisors Gus MacKenzie and Gordon Cook for their help and advice, Caroline Donnelly and Alison Stewart for help with gamma and alpha spectrometry, and Bob Anderson and Phil Naysmith for teaching me how to run vacuum lines with the minimum amount of chaos.

The contribution of ideas and ancillary data from the BENBO community were invaluable, particularly the considerable input of Dr. John Thomson and Sharon Nixon at SOC. Dr. D. Hughes at DML provided the faecal pellet samples, Prof. I.N. McCave, University of Cambridge supplied the grain size data in Table 4.1, Emily Good, University of Edinburgh permitted the use of her organic carbon flux data, and Dr. S. Wakefield at Cardiff provided the additional BOFS samples.

Thanks to Steve for proof reading and general usefulness during the final stages of writing up. Best wishes for the future to my fellow students, Colin, Elaine, Kay and Pauline, who made the whole thing bearable along the way, and thanks to my parents for coping admirably for another four years with a daughter who refuses to go out and get a proper job.

This project was financially supported by Natural Environment Research Council grant no. GST/1762 and tied studentship GT24/97/1/BENB.

All work presented in the thesis 'Deposition, Mixing and Storage Timescales at the Benthic Boundary Layer' was completed and interpreted by the candidate. Where other sources have been consulted this is duly acknowledged in the text. No part of this thesis has been submitted for any other degree at any other academic institution. Some aspects of the work presented herein have been published previously in the following papers:

Brown, L., Cook, G.T., MacKenzie, A.B., Thomson, J., Nixon, S. 1999 Radionuclide tracers of contaminant fate in the NE Atlantic. *Environmental Geochemistry and Health* **21**:323-329

Brown, L., Cook, G.T., MacKenzie, A.B., Naysmith, P., Anderson, R., Thomson, J., Nixon, S. 2000 ^{14}C characterisation of differential mixing between foraminifera and bulk carbonate in NE Atlantic sediments. *Nuclear Instruments and Methods in Physics Research B* **172**: 490-494

Thomson, J., Brown, L., Nixon, S., Cook, G.T., MacKenzie, A.B. 2000 Bioturbation and Holocene sediment accumulation fluxes in the north-east Atlantic Ocean (Benthic Boundary Layer experiment sites). *Marine Geology* **169**: 21-39

Thomson, J., Nixon, S., Croudace, I.W., Pederson, T.F., Brown, L., Cook, G.T., MacKenzie, A.B. 2001 Redox-sensitive element uptake in north-east Atlantic Ocean sediments (Benthic Boundary Layer experiment sites). *Earth and Planetary Science Letters* **184**: 535-547

Contents

Chapter 1 - Introduction	1
1.1 The Benthic Boundary Layer	1
1.1.1 Introduction to the benthic boundary layer	1
1.1.2 Importance of the benthic boundary layer	3
1.1.3 Benthic boundary layer processes	5
1.2 Project Rationale	10
1.3 Location of Study	13
1.4 Scientific Approach	19
1.4.1 Radiocarbon dating	19
1.4.1.1 <i>Introduction to radiocarbon dating</i>	19
1.4.1.2 <i>Dating of marine sediments</i>	24
1.4.1.3 <i>Dating of planktonic foraminifera</i>	28
1.4.2 $^{210}\text{Pb}_{\text{excess}}$	31
1.4.2.1 <i>Production and behaviour in the marine environment</i>	31
1.4.2.2 <i>Sediment $^{210}\text{Pb}_{\text{excess}}$ inventories</i>	34
1.4.2.3 <i>$^{210}\text{Pb}_{\text{excess}}$ and bioturbation</i>	36
1.4.3 Man-made Radionuclides	41
1.4.3.1 <i>Production of man-made radionuclides</i>	41
1.4.3.2 <i>Geochemistry of radionuclides used in this study</i>	44
1.4.3.3 <i>Bioturbation of man-made radionuclides</i>	47
1.4.3.4 <i>Radionuclide activity ratios</i>	49
Chapter 2 - Methods and Materials	52
2.1 Sample Collection and Storage	52
2.2 Radiocarbon Analysis	52
2.2.1 Methods of detection of ^{14}C	52
2.2.1.1 <i>Radiometric methods</i>	53
2.2.1.2 <i>Atom-counting methods</i>	61
2.2.2 ^{14}C analysis by liquid scintillation counting - method	63
2.2.2.1 <i>Sample preparation</i>	63

3.3 Man-made radionuclides	128
3.3.1 ²⁴¹ Am and ¹³⁷ Cs	128
3.3.2 ²³⁸ Pu and ^{239,240} Pu	134
3.4 Burrow sediments	136
Chapter 4 - Discussion	139
4.1 Sedimentary Processes and Fluxes to Sediment	139
4.1.1 Sedimentation - BENBO B and C	138
4.1.2 Sedimentation - BENBO A	146
4.1.3 ²¹⁰ Pb _{excess} and sediment fluxes	151
4.1.4 Man-made radionuclides - fluxes and source inputs	155
4.2 Bioturbation	162
4.2.1 Biodiffusive mixing - cores A(i) and B(i)	162
4.2.2 Non-local (advective) mixing - cores B(vi), C(ii) and C(iv)	164
4.2.3 Temporal and spatial variations in bioturbation	165
4.2.4 Variation in bioturbation models from man-made and NDS radionuclides	173
4.2.5 Size-selective mixing	175
4.2.5.1 <i>Causes of bulk carbonate-foram age offsets</i>	175
4.2.5.2 <i>Pretreated samples</i>	179
4.2.5.3 <i>Reasons for differences in age offsets between sites</i>	181
Chapter 5 - Conclusions	188
Appendix - Tables of Results	194
Cited References	213

List of Figures

1.1 Processes occurring at the benthic boundary layer	2
1.2 Location of BENBO sampling sites	14
1.3 North East Atlantic bottom current circulation	16
1.4 Phytoplankton productivity in the North Atlantic	18
1.5 Erlenkeuser model of radiocarbon in sediments	27
1.6 Radiocarbon age offsets between different sediment fractions	30
1.7 The natural radioactive decay series	32
1.8 $^{210}\text{Pb}_{\text{excess}}$ inventories in Atlantic sediments relative to supply	35
2.1 Schematic diagram of a liquid scintillation counter	54
2.2 Schematic diagram of an accelerator mass spectrometer	62
2.3 Vacuum system for synthesis of CO_2 in LSC method	64
2.4 Vacuum system for synthesis of ethyne in LSC method	66
2.5 Vacuum system for synthesis of benzene in LSC method	68
2.6 Vacuum system for synthesis of CO_2 in AMS method	77
2.7 Vacuum system for synthesis of graphite in AMS method	79
2.8 Schematic diagram of semiconductor detector for gamma spectrometry	88
2.9 Comparison of $^{210}\text{Pb}_{\text{excess}}$ results for core A(i) from two gamma spectrometers	96
2.10 Schematic diagram of semiconductor detector for alpha spectrometry	103
2.11 Potential NDS radionuclide interferences in ^{238}Pu and $^{239,240}\text{Pu}$ alpha spectra	105
3.1 Erlenkeuser box models for BENBO sites B and C radiocarbon data	111
3.2 BENBO site A radiocarbon and CaCO_3 profiles	112
3.3 BENBO site A - size fractionated sediment radiocarbon data	115
3.4 BENBO site B - size fractionated sediment radiocarbon data	116
3.5 BENBO site C - size fractionated sediment radiocarbon data	117
3.6 BOFS sites 11881 and 11886 radiocarbon profiles	120
3.7 BENBO site A, sub core (i) ^{226}Ra , $^{210}\text{Pb}_{\text{total}}$ and $^{210}\text{Pb}_{\text{excess}}$ profiles	123
3.8 BENBO site B, sub core (i) ^{226}Ra , $^{210}\text{Pb}_{\text{total}}$ and $^{210}\text{Pb}_{\text{excess}}$ profiles	124
3.9 BENBO site C, sub core (ii) ^{226}Ra , $^{210}\text{Pb}_{\text{total}}$ and $^{210}\text{Pb}_{\text{excess}}$ profiles	125
3.10 Comparison of replicate $^{210}\text{Pb}_{\text{excess}}$ profiles at BENBO sites B and C	126
3.11 BENBO site A, sub core (i) ^{137}Cs and ^{241}Am profiles	129
3.12 BENBO site B, sub core (i) ^{137}Cs and ^{241}Am profiles	130

3.13 BENBO site C, sub core (ii) ^{137}Cs and ^{241}Am profiles	131
3.14 BENBO site B, sub core (vi) ^{137}Cs and ^{241}Am profiles	132
3.15 BENBO site C, sub core (iv) ^{137}Cs and ^{241}Am profiles	133
3.16 BENBO site B, sub core (i) ^{238}Pu and $^{239,240}\text{Pu}$ profiles	135
3.17 Radiocarbon age of faecal pellets (site C) compared to ambient sediment	138
4.1 BENBO sites B and C - CaCO_3 profiles	140
4.2 BENBO sites A and B $\text{SML-C}_{\text{org}}$ relationship: comparison with published data	145
4.3 BENBO site A core logs, sub cores (i) and (iii)	147
4.4 BENBO site A - CaCO_3 vs Ti content and deconvoluted radiocarbon ages	150
4.5 Comparison of BENBO $^{210}\text{Pb}_{\text{excess}}$ inventory-water depth with BOFS data	152
4.6 ^{210}Pb water column removal fluxes and atmospheric input	154
4.7 Comparison of BENBO A (i) and B(i) DB values with two empirical models	163
4.8 Organisms and biological structures observed in BENBO box cores	166
4.9 Core logs for sub cores B(i), B(iv), C(ii) and C(vi)	167
4.10 Potential mechanism at site B creating negative T_0 value	170
4.11 BENBO site B profile modelled without advective bioturbation	171
4.12 Sediment age distribution and sampling strategy effects on apparent age	183

List of Tables

1.1 Redox reactions in marine sediments	7
1.2 Applications of radionuclides in marine studies	12
1.3 Man-made radionuclide sources and activities	51
2.1 Comparison of radiocarbon ages derived from LSC and AMS analysis	81
2.2 Characteristics of radionuclides analysed by gamma spectrometry	91
2.3 Gamma spectrometry detection efficiencies	93
2.4 Comparison of gamma spectrometry samples analysed at SOC and SURRC	95
2.5 Gamma spectrometry detector backgrounds	99
2.6 Characteristics of Pu radionuclides	101
3.1 BENBO sites B and C - Erlenkeuser box model parameters	113
3.2 Modelling of BOFS radiocarbon data - comparison with Thomson <i>et al.</i> 1995	118
3.3 Inventories and fluxes of $^{210}\text{Pb}_{\text{excess}}$ in BENBO cores	127
3.4 $^{210}\text{Pb}_{\text{excess}}$ and ^{14}C from material associated with subsurface burrows	137
4.1 Particle size and composition distribution of BENBO sediments	142
4.2 Organic carbon fluxes and SML depth at BENBO sites A and B	144
4.3 Inventories and fluxes of man-made radionuclides in BENBO sub cores	159
A1 BENBO site A bulk radiocarbon ages	194
A2 BENBO site B bulk radiocarbon ages	195
A3 BENBO site C bulk radiocarbon ages	196
A4 BENBO site A planktonic foram and $<63\ \mu\text{m}$ sediment radiocarbon ages	197
A5 BENBO site B planktonic foram and $<63\ \mu\text{m}$ sediment radiocarbon ages	198
A6 BENBO site C planktonic foram and $<63\ \mu\text{m}$ sediment radiocarbon ages	199
A7 BOFS planktonic foram and $<63\ \mu\text{m}$ sediment radiocarbon ages	200
A8 BENBO site A sub core (i) ^{210}Pb , ^{226}Ra , $^{210}\text{Pb}_{\text{excess}}$, ^{137}Cs and ^{241}Am specific activities	201
A9 BENBO site B sub core (i) ^{210}Pb , ^{226}Ra , $^{210}\text{Pb}_{\text{excess}}$, ^{137}Cs and ^{241}Am specific activities	203

A10 BENBO site C sub core (ii) ^{210}Pb , ^{226}Ra , $^{210}\text{Pb}_{\text{excess}}$, ^{137}Cs and ^{241}Am specific activities	205
A11 BENBO site B sub core (vi) ^{210}Pb , ^{226}Ra , $^{210}\text{Pb}_{\text{excess}}$, ^{137}Cs and ^{241}Am specific activities	207
A12 BENBO site A sub core (iv) ^{210}Pb , ^{226}Ra , $^{210}\text{Pb}_{\text{excess}}$, ^{137}Cs and ^{241}Am specific activities	209
A13 BENBO site B, sub core (i) and C sub core (ii) ^{238}Pu and $^{239,240}\text{Pu}$ specific activities	211

Glossary of Key Abbreviated Terms

AABW	Antarctic Bottom Water
AMS	Accelerator Mass Spectrometry
BBL	Benthic Boundary Layer
BENBO	Benthic Boundary Layer Experiment study (NERC thematic programme)
BOFS	Biogeochemical Ocean Flux Study (NERC thematic programme)
D_B	Biodiffusion coefficient
HPGe	High purity Germanium semiconductor detector
LSC	Liquid Scintillation Counter
NADW	North Atlantic Deep Water
NSDW	Norwegian Sea Deep Water
PMT	Photomultiplier tube
$^{210}\text{Pb}_{\text{excess}}$	Total ^{210}Pb in sediment minus the component of ^{210}Pb produced in situ by decay of ^{238}U -series radionuclides
SML	Surface mixed layer

Chapter 1 - Introduction

1.1. The Benthic Boundary Layer

1.1.1 Introduction to the benthic boundary layer

The benthic boundary layer (BBL) is the term used to describe the region between the ocean floor and the overlying water column, where a number of interacting physical, biological and chemical processes facilitate the transfer of energy and dissolved and particulate material between marine sediments and overlying ocean water (Fig.1.1).

Quantification of these processes and the energy and material fluxes which they govern is of major importance in environmental studies, particularly with regard to biogeochemical cycling, anthropogenic contaminant removal and the quality of preservation of marine sedimentary records of past environmental change.

The benthic boundary layer includes all zones where exchange of particulate and dissolved components between sediment and overlying water occurs. In this context, the BBL is considered to include the suspended sediment above, and the biologically mixed sediment below the actual physical boundary. Water column temperature and salinity measurements show the existence of a homogeneous mixed layer, varying between a few metres and over 100 metres height above the water-sediment interface and separated from the overlying water column by strong thermo- and pycnoclines, which constrain the upper boundary of the BBL. This also coincides with a sharp drop in light transmittance, signalling a change in suspended sediment load. Boundary layer mixing is caused by the turbulence created as bottom water currents are slowed down by interaction with the sea

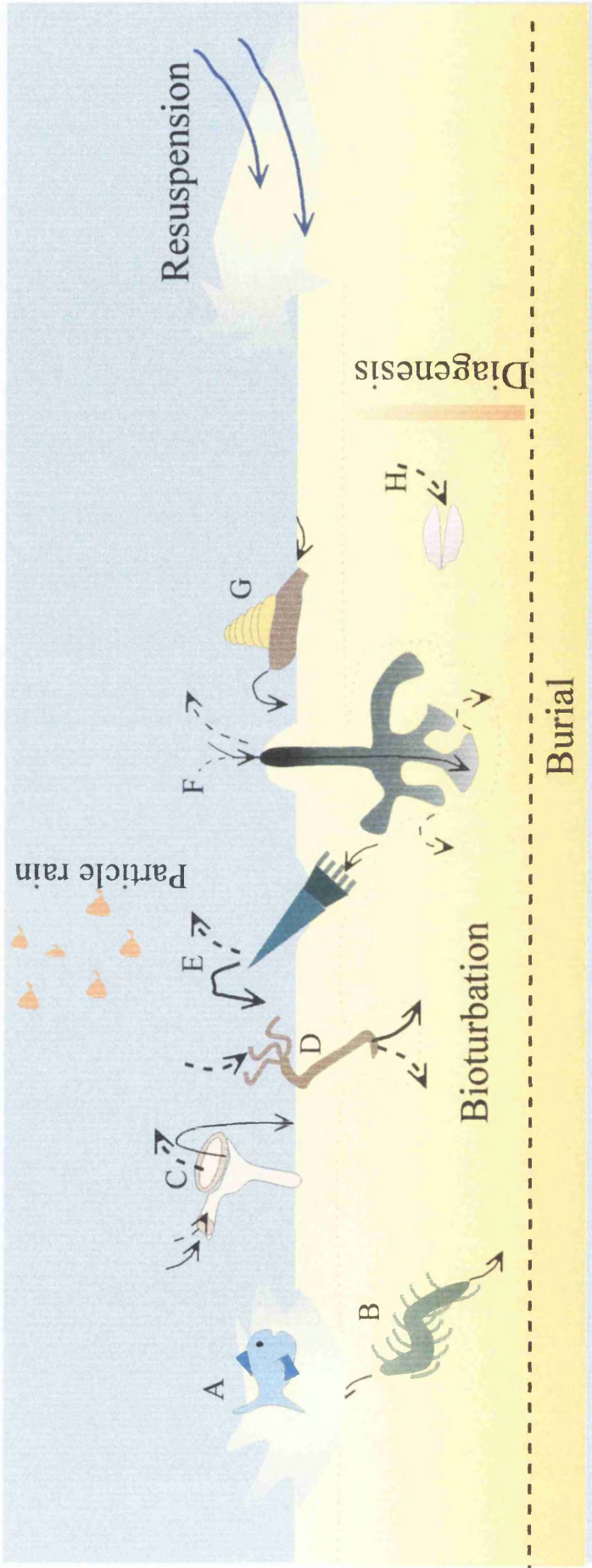
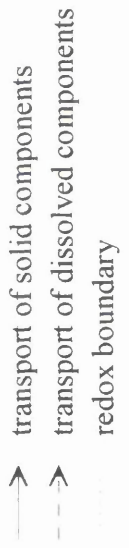


Fig. 1.1: A schematic diagram showing some benthic boundary layer processes, which affect the fluxes and fate of material arriving there. A key to the bioturbation processes is given below.

- A - surface dweller disturbing sediment surface
- B - infaunal burrower disturbing sediment
- C - epifaunal suspension feeder: suspended solids - solid
- D - infaunal suspension feeder: porewater circulation
- E - infaunal deposit feeder (head down): particulate transport up
- F - infaunal deposit feeder (head up): particulate transport down
- G - epifaunal deposit feeder: horizontal particulate transport
- H - bivalve: concentrating dissolved ions into hard parts



floor. This variable horizontal structure of the BBL is important in enabling exchange of water and suspended constituents between the BBL and overlying water (Richards 1990). The lower BBL boundary is determined by the depth of biological mixing. The base of the BBL is defined as the depth to which the sediment is homogenised by biological mixing by infaunal and epifaunal organisms, a zone known as the surface mixed layer (SML). The depth of the SML in the open ocean is generally accepted to be in the region of 10 cm (Boudreau 1994).

1.1.2 Importance of the benthic boundary layer

Palaeoenvironmental records

A wide range of sedimentological, palaeontological and geochemical techniques have been used to interpret past changes in climate, ocean circulation and nutrient content recorded in ocean sediments (e.g. Emiliani 1955; Sanyal *et al.* 1995; Boyle 1988; Broecker *et al.* 1984; McCave *et al.* 1995). The resolution of these records is highly dependent on the relative rates of sediment burial and bioturbation, the latter having the effect of decreasing the magnitude of a signal whilst smearing it across a longer timescale. For example, Anderson (2001) estimated that the apparent amplitude of a 4000 y-long climatic fluctuation recorded in sediment records would be reduced to 50% of its real value under conditions of moderate biological mixing and sedimentation of 10 cm ky⁻¹. The quality of the records may also be diminished by chemical processes such as dissolution or reprecipitation of minerals, or current transportation of material to or from a site, distorting the record found at the site. Thus, if a correct reconstruction of palaeoceanographic or climatic events is to be obtained, the BBL processes affecting the

preservation of records must be accounted for (Bard *et al.* 1987; Schiffelbein 1984; Broecker *et al.* 1999).

Biogeochemical cycling

Over geological timescales, ocean sediments constitute a major sink, with an area of 3.6×10^8 km², for particulate or particle-bound materials, and the rates of removal or biological or chemical modification of this material in the BBL has an important influence in determining the availability of major and trace nutrients. The resuspension of material from the sediment by bottom water currents creates a layer rich in suspended particulate matter (SPM) where organic decomposition, dissolution and the scavenging of particle-reactive elements may occur at much faster rates than in the overlying water column or underlying sediments (Rutgers van der Loeff and Boudreau 1997).

Fate of Anthropogenic Contaminants

The deep ocean and its sediments are the ultimate sink for contaminants produced by human activity, either by direct introduction into the marine environment or by biogeochemical cycling and transport from coastal, terrestrial and atmospheric sources. Only when contaminants are buried in sea floor sediments are they no longer available for biological uptake or exchange between reservoirs. Benthic boundary processes, such as resuspension, sediment accumulation and bioturbation control the rate of transport of such contaminants out of the biogeochemically active zones and immobilise them in sediments, and are therefore important in modelling toxicological and environmental impacts of human activity.

Resource exploitation

The North Atlantic Frontier - the area of deep sea off the western coast of Scotland and Ireland - is one example of a region under increasing pressure for exploitation of hydrocarbon and fisheries resources. The limited knowledge of deep sea BBL processes and biological communities means that at present it is impossible to quantify meaningfully the impact of such activities on the deep sea environment.

1.1.3 Benthic Boundary Layer Processes

Sedimentation

Typical sediment accumulation rates in the deep sea are of the order of a few centimetres every thousand years (e.g. Balsam and McCoy 1987). Variation in sedimentation rate is a function of the pelagic input from the overlying water column and the bottom current activity either limiting or enhancing the deposition of the finer sediment fractions, or the supply of material from terrestrial sources by currents, ice-rafting or aeolian input. Where sedimentation is enhanced by bottom currents, topographic features such as sand waves and sediment drifts (e.g. Howe 1996) may be formed. Due to the relative constancy of depth of the open ocean SML, the residence time of sedimentary components within this zone will be primarily dependent on sedimentation rate. Furthermore, resuspension of deposited material by bottom water currents will prolong the bioavailability of particulate and particle reactive components in the marine system.

Remineralisation and biogeochemical cycling

The input of organic matter from the surface ocean is a major force in driving BBL biogeochemical reactions. Organic detritus from the pelagic ocean sinks to the sea floor as

large, rapidly sinking (100-200 m d⁻¹; McCave 1995) aggregates. The repeated break-up and degradation of these particles as they sink through the water column means that the composition and organic content of phytodetritus on reaching the sea floor is significantly different from that leaving the pelagic zone (Ransom 1998). Over most of the open ocean floor, only about 1% of overlying primary productivity reaches the sediment (Brown *et al.* 1989). However, as organic matter acts as a strong reducing agent, that small fraction which does enter the sediment is sufficient to drive the primary early diagenetic reactions in marine sediment. Oxidising species of decreasing redox potential are sequentially used up by the degradation of organic matter, and consequently, the amount of organic matter reaching the sediments will affect the distribution of redox-sensitive species. Table 1.1 shows the order of utilization of electron acceptors in early diagenesis of organic matter in oceanic sediments (Froelich *et al.* 1979).

In addition to the direct effect on sediment chemistry, the rain of organic matter to the sea floor is the primary food source for the benthic biological community. Bacteria are also thought to utilise the dissolved organic carbon (DOC) pool, transported from the surface ocean to the BBL (Gage 1991). Reaction rates are often accelerated by microbial catalysis by several orders of magnitude than would be expected if ion transport was by purely diffusive means. Bioturbation and bioirrigation also recycle electron acceptors from the surface sediment or porewaters to depth, thus enhancing the amount of degradation of organic matter. The rates and mechanisms of biological activity are therefore important in the cycling of redox sensitive elements and nutrients. For example, where primary production in the overlying water column, and the subsequent input of organic matter to

Table 1.1: Oxidation reactions of sedimentary organic matter, given in order of decreasing free energy of reaction (Froelich *et al.* 1979). The reactions are balanced to oxidise a unit of ‘average’ organic matter, of the form $(\text{CH}_2\text{O})_{106}(\text{NH}_3)_{16}(\text{H}_3\text{PO}_4)$, containing C, N and P in the ratios observed in sinking oceanic biogenic debris (Redfield 1958). Free energies of reaction (ΔG°) are reported as kJ per Redfield molecule-mole.

* The free energy expected from MnO_2 reduction depends on the mineral phase of MnO_2 .

Reaction	ΔG°
$(\text{CH}_2\text{O})_{106}(\text{NH}_3)_{16}(\text{H}_3\text{PO}_4) + 138 \text{O}_2 \rightarrow 106 \text{CO}_2 + 16 \text{HNO}_3 + \text{H}_3\text{PO}_4 + 122 \text{H}_2\text{O}$	-56367
$(\text{CH}_2\text{O})_{106}(\text{NH}_3)_{16}(\text{H}_3\text{PO}_4) + 236 \text{MnO}_2 + 472\text{H}^+ \rightarrow 236 \text{Mn}^{2+} + 106 \text{CO}_2 + 8 \text{N}_2 + \text{H}_3\text{PO}_4 + 366 \text{H}_2\text{O}$	-54600, -53893, -51596*
$(\text{CH}_2\text{O})_{106}(\text{NH}_3)_{16}(\text{H}_3\text{PO}_4) + 94.4 \text{HNO}_3 \rightarrow 106 \text{CO}_2 + 55.2 \text{N}_2 + \text{H}_3\text{PO}_4 + 177.2 \text{H}_2\text{O}$	-53540
$(\text{CH}_2\text{O})_{106}(\text{NH}_3)_{16}(\text{H}_3\text{PO}_4) + 84.8 \text{HNO}_3 \rightarrow 106 \text{CO}_2 + 42.4 \text{N}_2 + 16 \text{NH}_3 + \text{H}_3\text{PO}_4 + 148.4 \text{H}_2\text{O}$	-48593
$(\text{CH}_2\text{O})_{106}(\text{NH}_3)_{16}(\text{H}_3\text{PO}_4) + 212 \text{Fe}_2\text{O}_3 \rightarrow 424 \text{Fe}^+ + 106 \text{CO}_2 + 16 \text{NH}_3 + \text{H}_3\text{PO}_4 + 530 \text{H}_2\text{O}$	-24915
$(\text{CH}_2\text{O})_{106}(\text{NH}_3)_{16}(\text{H}_3\text{PO}_4) + 424 \text{FeOOH} + 848\text{H}^+ \rightarrow 424 \text{Fe}^+ + 106 \text{CO}_2 + 16 \text{NH}_3 + \text{H}_3\text{PO}_4 + 742 \text{H}_2\text{O}$	-23501
$(\text{CH}_2\text{O})_{106}(\text{NH}_3)_{16}(\text{H}_3\text{PO}_4) + 53 \text{SO}_4^{2-} \rightarrow 106 \text{CO}_2 + 16 \text{NH}_3 + 53 \text{S}^{2-} + \text{H}_3\text{PO}_4 + 106 \text{H}_2\text{O}$	-6715
$(\text{CH}_2\text{O})_{106}(\text{NH}_3)_{16}(\text{H}_3\text{PO}_4) \rightarrow 53 \text{CO}_2 + 53 \text{CH}_4 + 16 \text{NH}_3 + \text{H}_3\text{PO}_4$ (<i>methanogenesis</i>)	-6185

the BBL, is seasonal, there is a benthic community response and increase in organic turnover (Gooday 1988).

Bioturbation

Biological activity in the BBL modifies material arriving at the sediment surface so that the sediment passing out of the SML into the inactive buried 'historical zone' is altered chemically and physically from the freshly delivered material. When bottom water flow is weak, physical mixing and transport of the sediment is dominated the deposit feeding meio- and megafauna living in the sediment column (Yingst and Aller 1982). Sediment disturbance by benthic organisms alters the porosity of the SML, increasing sediment erodibility, or conversely, sediment cohesiveness may be enhanced by biogenic mucus secretion or compaction of sediment in faecal pellet production. Other activities, such as construction of biogenic pits or mounds on the sediment surface, alter sea bed roughness and bottom current flow. Sediment geochemical profiles are also altered by bioturbation of sediments and the formation of biogenic structures. In unbioturbated sediments, movement of sedimentary components may be modelled as a one dimensional vertical process, in burrowed sediment solute concentration gradients may be altered by biogenic transport of particles, remineralisation of particles by the burrow inhabitant, and irrigation of the burrow by overlying water (Aller 1982; Aller 1984). The resulting changes in sediment and porewater distribution alter the sediment profiles of redox sensitive elements and the extent of oxidation of organic matter, thereby influencing the burial rates and fluxes out of the BBL.

The effect of biological mixing in the SML is often represented as generating a zone of homogeneously mixed sediment (Boudreau 1986a). The mean deep sea SML depth is 9.8 ± 4.5 cm (Boudreau 1994), irrespective of water depth or sedimentation rate. This constancy of SML depth has been explained as a consequence of feedback between food quality, sediment depth and bioturbation rate (Boudreau 1998), or by the increased energy expenditure required to burrow to depth, negating the value of any food resource found there (Jumars *et al.* 1990). However, it has been noted that in the mesotrophic eastern Atlantic, SML depths are greater than the oligotrophic western Atlantic (DeMaster and Cochran 1982; Buffoni *et al.* 1992), which is generally accepted to be a response to the increased input of organic matter. On examining a series of cores from below 2500 m water depth in the North East Atlantic, Trauth *et al.* (1997) found that SML depth increased by 2 cm for every $1 \text{ g C m}^{-2} \text{ y}^{-1}$ increase in organic carbon flux to the sediments. This increased depth is considered to be mainly a function of increased abundance of deeper-burrowing macrofauna, but meiofauna may also be found to influence bioturbation to greater depths in the sediment as they have been shown to concentrate at oxic microsites generated by the burrowing of the larger organisms (Soetaert *et al.* 1994).

Optimal foraging theory predicts that organisms will evolve feeding strategies to maximise the energy difference between that required for food collection and calorific return (Hughes 1980). In certain cases, the model presented above of instantaneous, random mixing may not be appropriate. In environments, with varying organic matter input, current speeds or sediment type, the strategies chosen will affect sediment mixing in the benthic boundary layer. For example, Nowell (1984) records that whilst Ampharetidae polychaete worms living in high energy intertidal zones rely on currents to supply

sufficient food and to remove faecal pellets, Ampharetidae in the less energetic deep ocean create pits to focus food, and ensure faeces are deposited some distance from these pits. In areas subject to seasonal inputs of organic matter, macrofaunal burrowers, such as siphunculid and echurid worms, have been reported to cache food by means of deep burial of faecal pellet and subsequent coprophagy. The size of these pellets means they are less easily broken down by smaller organisms, and are protected from bacterial attack by an organic coating (Jumars *et al.* 1990). This type of feeding represents an advective, directional transfer of sediment from the surface to depth (e.g. Smith *et al.* 1986), in contrast to homogeneous mixing of sediment resulting from random activity of smaller benthic infauna. Some deep burrowing organisms are also thought to ‘mine’ organic rich sediments buried by turbidity currents (Jumars and Wheatcroft 1989). The preferential ingestion of particles on the basis of size, density, and shape in order to maximise food quality intake has been recorded in a wide range of species in laboratory studies (Bock and Miller 1999; Wheatcroft 1992; Self and Jumars 1988; Wheatcroft and Jumars 1987). In addition to size-selective ingestion, McCave (1988) proposed that infaunal organisms actively and preferentially push larger particles upwards relative to fine material when travelling through the sediment. The implications of these different mechanisms on sediment properties and the mixing of specific sedimentary components are discussed fully in section 1.4.2.3.

1.2 Project Rationale

In order to assess quantitatively the importance of BBL processes on biogeochemical cycling and contaminant fate, it is necessary to find a means of determining rates of the key biological and physical processes taking place in the benthic zone. Radionuclides are

one of the most useful geochemical tools available for determining rates of many processes in the marine environment (Table 1.2). Many radionuclides are easily and accurately detected in comparison to other tracers, and, by utilising tracers with different half lives, a range of processes operating over different timescales may be studied. They may be used both directly as tracers of environmental processes, or as analogue tracers for elements with similar environmental behaviour to the radionuclide tracer, but which are less easily analysed. In addition, artificial radionuclides may be used to assess the fate of anthropogenic contaminants and to determine transport mechanisms on the basis of the known quantities of specific radionuclides released into the environment.

The UK Natural Environment Research Council-funded North East Atlantic Benthic Boundary (BENBO) Study was a three-year multidisciplinary project designed to examine contemporary BBL processes and thus better quantify the impact of anthropogenic activity on this poorly-understood environment. The specific objectives of BENBO were:

1. To determine the quantitative impact of the BBL on the deep ocean fate of biological and geochemical constituents.
2. To determine the relative importance of the depositional setting of the BBL versus *in situ* diagenetic cycling in driving the sign and magnitude of the flux of biochemical components and energy flow.
3. To determine how physical, biological and geochemical factors influence the role of the BBL in determining the residence times and fates of anthropogenic inputs to the North East Atlantic continental margins and abyssal plains.

Radionuclide	Half-life	Applications	Examples
<i>NDS radionuclides</i>			
$^{230}\text{Th}_{\text{excess}}$	75 200 y	Sedimentary fluxes	Kadko 1980; Thomson <i>et al.</i> 1993
$^{234}\text{Th}_{\text{excess}}$	24 d	Bioturbation (10^0 y timescale) Particle fate	Aller & DeMaster 1984 Santschi <i>et al.</i> 1980
$^{228}\text{Th}_{\text{excess}}$	1.9 y	Bioturbation (10^1 y timescale) Particle fate	Santschi <i>et al.</i> 1980 Legeleux <i>et al.</i> 1994
$^{210}\text{Pb}/^{210}\text{Pb}_{\text{excess}}$	22.3 y	Sediment dating Bioturbation modelling Organic carbon fluxes	Benninger 1978 Nozaki <i>et al.</i> 1977 Fisher 1988
^{210}Po	138 d	Sedimentary organic C flux	Cochran 1983
^{226}Ra	1602 y	Ocean circulation	Chung & Craig 1973
<i>Cosmogenic</i>			
^{32}Si	c. 170 y	Bioturbation (10^3 y timescale) Sediment dating	DeMaster <i>et al.</i> 1982 Somayajulu <i>et al.</i> 1987
^{14}C	5370 y	Sedimentary processes Ocean ventilation Ocean circulation	Erlenkeuser 1980 Broecker <i>et al.</i> 1988 Broecker <i>et al.</i> 1985
^{10}Be	1.5×10^6 y	Palaeoenvironmental reconstruction	Somayajulu <i>et al.</i> 1983
<i>Man-made Radionuclides</i>			
mainly conservative, e.g. ^{137}Cs , ^{90}Sr , ^{99}Tc	present since 1945	Ocean circulation Tracer of dissolved contaminant fate	McKinley <i>et al.</i> 1981 Aarkog <i>et al.</i> 1999
particle-reactive, e.g. ^{241}Am , $^{239,240}\text{Pu}$	present since 1945	Bioturbation Tracer of particle-bound contaminant fate	Buffoni <i>et al.</i> 1992 Fowler <i>et al.</i> 2000

Table 1.2: A selection of radionuclides and their applications in marine science

4. To determine how the BBL biota and diagenetic reactions modify biological and geochemical inputs to the BBL before their eventual incorporation into the permanent palaeoceanographic record.

The aim of this project is to provide quantitative information on a range of BBL processes using natural and artificial radionuclides, aspects of which are of key importance to the BENBO community as a whole. The specific objectives are as follows:

1. To utilise ^{14}C to model accumulation rates and sedimentary processes over the Holocene timescale.
2. To utilise ^{14}C , $^{210}\text{Pb}_{\text{excess}}$ and the artificial radionuclides ^{137}Cs , ^{241}Am , ^{238}Pu and $^{239,240}\text{Pu}$ to examine bioturbation over different timescales.
3. To compare ^{14}C ages of fine and coarse sediment fractions in order to examine size selective mixing processes.
4. To utilise radionuclide inventories to determine fluxes and source terms of sedimentary material to the sea floor.

1.3 Location of Study

As an integral sub-project of the UK NERC Benthic Boundary Study (BENBO), this project is based on the three BENBO sampling sites identified in the initial survey cruise (CD111) in August, 1997 (Fig.1.2). Each site is a gently sloping apron approximately 8 x 8 km in area, located in the Rockall Trough off the European continental shelf. The study locations were chosen specifically to represent the widest possible range of benthic

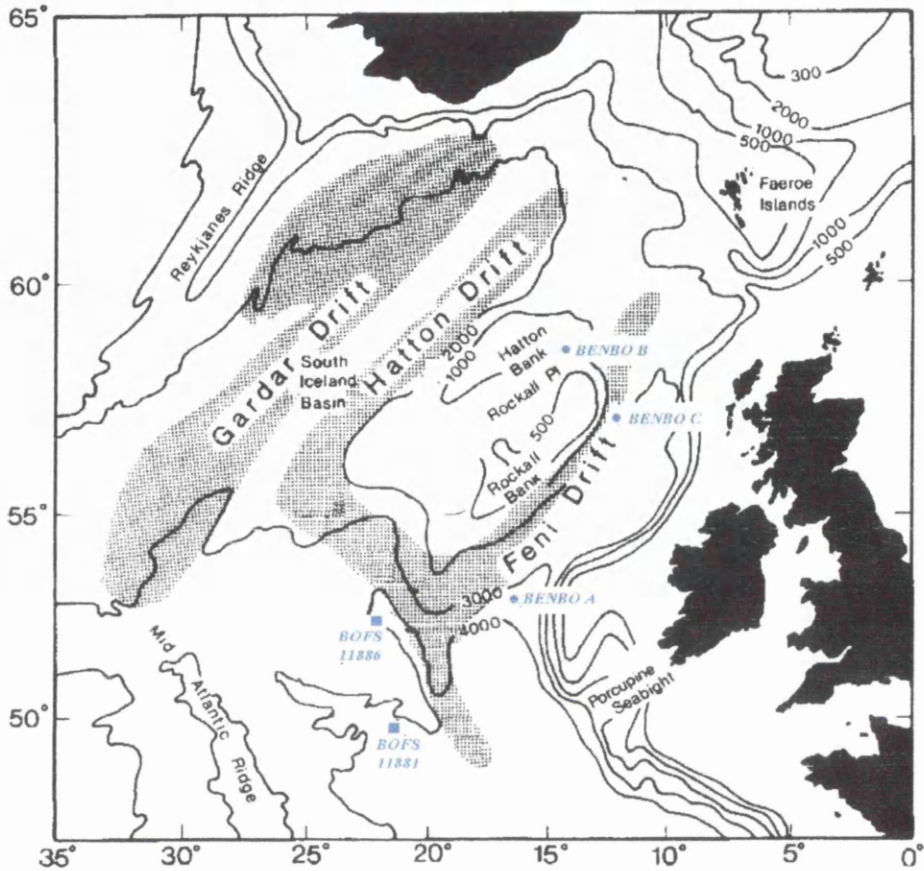


Fig. 1.2: Bathymetric map highlighting the locations of the BENBO sampling sites A, B and C in relation to the major sea bed topographical features. The Biogeochemical Ocean Flux Study (BOFS) stations 11881 and 11886, which are referred to later in this study, are also shown. The stippled areas represent sediment drift features, created by current-influenced focussing of sediment accumulation. Map modified from the bathymetric map of Thomson *et al.* (1993).

boundary conditions, with each site experiencing contrasting water depth, bottom current regimes, sedimentation and overlying primary productivity.

Site A (52° 55.1' N, 16° 54.8' W) is a deep water (3570 m) site, located at the mouth of the Rockall Trough just as it reaches the Porcupine Abyssal Plain. It was anticipated that this site would experience low current strengths and material fluxes. Site B (57° 25.6' N, 15° 41.1' W) is situated on the western side of the Rockall Bank, at a relatively shallow water depth of 1100 m. This site was expected to experience low current energies and high sediment fluxes. Site C (57° 06.0' N, 12° 31.0' W) lies on the western flank of Feni Drift, a large sediment drift feature, at a water depth of 1925 m in what was anticipated to be a high energy environment.

The BENBO study area, west of the continental shelf off Scotland and Ireland, has an important role to play in the northwards transfer of heat from equator to pole. Under the contemporary regime, warm, saline North Atlantic Drift surface waters flow northwards between Iceland and Scotland from the western equatorial Atlantic, then cool and sink at high latitudes, returning southwards as the cold, dense North Atlantic Deep Water (NADW). NADW is sourced primarily from water overflowing the Greenland-Scotland Ridge, but also from dense waters from the Labrador and Mediterranean seas. Its southward transport is constrained by the bathymetry of the Rockall Trough, which, in combination with the Coriolis force, creates the system of bottom currents shown in Fig.1.3. The Rockall Slope current, flowing northwards along the continental slope to depths of up to 1500 m, limits cross-slope exchange velocities between shelf and open ocean waters to 2 cm s^{-1} (Huthnance 1986). A difference of 0.2% in salinity exists between

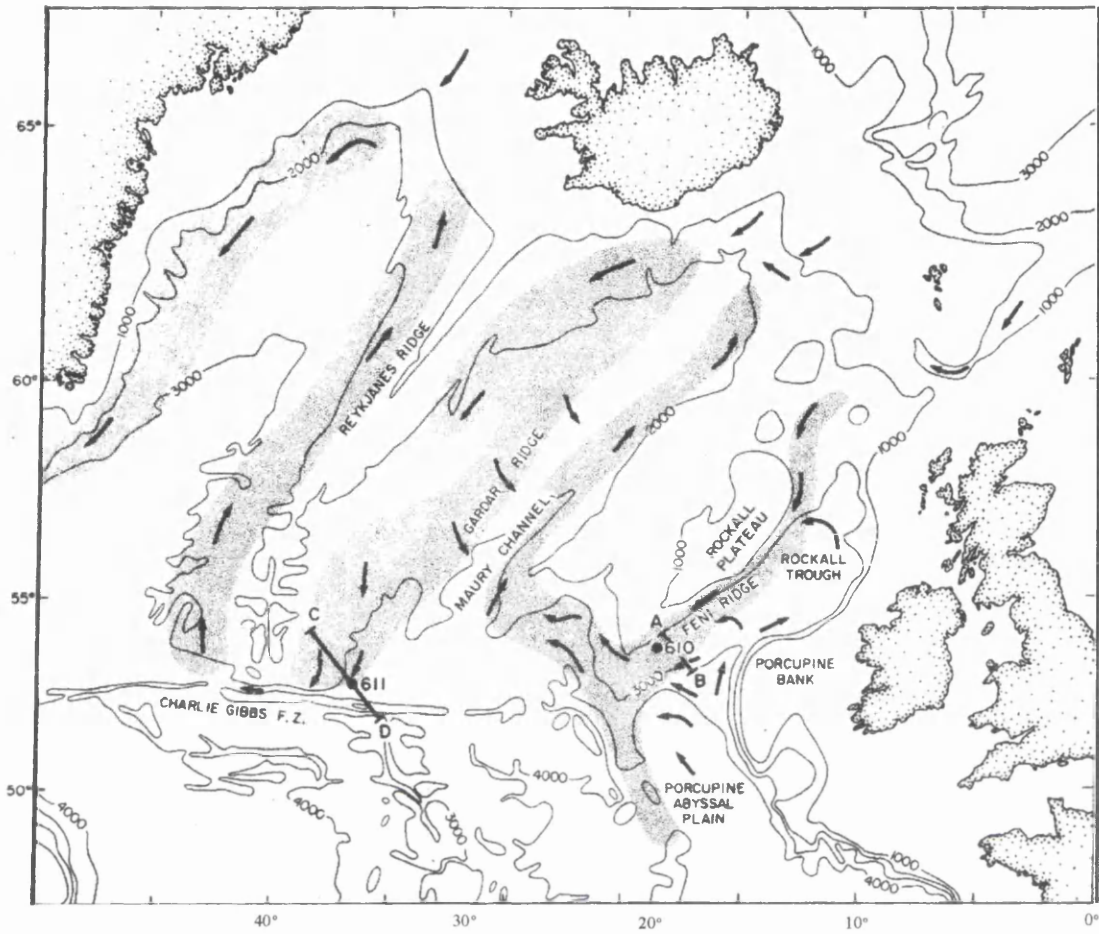


Fig. 1.3: Bathymetric map of the North-East Atlantic, showing the location of major sediment drifts (stippled areas) and general bottom water circulation (arrows). From Kidd and Hill 1986.

water in the Rockall Channel and shelf water, much larger than expected if the two water bodies were well mixed (Ellet and Martin 1973).

Large, rapidly accumulating sediment drifts are characteristic of the North East Atlantic. They cover a total area of $94 \times 10^4 \text{ km}^2$, and have a combined mass of $691 \times 10^{18} \text{ g}$ (Wold 1994). The largest drifts are located where southward-travelling bottom currents flowing against the western bank of a topographic high, are forced back northwards by the Coriolis Force. Where sedimentation is the result of dominantly pelagic processes, the sedimentation rate in the North East Atlantic is of the order of $2 - 4 \text{ cm ky}^{-1}$ (Balsam and McCoy 1987). However, areas of rapid sedimentation, upwards of 10 cm ky^{-1} , are known to occur on the Rockall Plateau (Broecker *et al.* 1988a; Duplessey *et al.* 1986). The sediments are typically dominated by carbonate ooze, formed from the tests of CaCO_3 -shelled planktonic organisms, such as coccolithophores and foraminifera, which inhabit the overlying water column. In terms of biological productivity, the North East Atlantic is an area of mesotrophic surficial productivity; i.e. $50\text{-}100 \text{ g C m}^{-2} \text{ y}^{-1}$ (Fig.1.4). The area is subject to annual springtime productivity blooms (Rice 1994), to which the benthic fauna are known to respond by increasing carbon turnover (Gooday 1988).

The present regime of circulation and sedimentation was established at the end of the last glaciation in the North East Atlantic. Prior to this, geochemical (e.g. Boyle and Keigwin 1987) and sedimentological (McCave *et al.* 1995) evidence reveals much less intense thermohaline circulation than at present. Deep water formation occurred at lower latitudes, possibly in the Rockall Trough itself, and the region was subjected to stronger bottom current activities than at present (Dowling and McCave 1993). Sediment

accumulation rates were typically higher than in the Holocene due to an enhanced flux of terrestrial material to the oceans. Decreased vertical mixing in the glacial North East Atlantic is thought to have resulted in a fall in primary production due to a reduction in exchange between nutrient-poor surface waters and nutrient-rich bottom waters. Until recently, climatic conditions in the Holocene were considered to be comparatively warm and stable since the resumption of the present-day thermohaline circulation regime; however, evidence is mounting for climatic variations on 10^3 or 10^2 year timescales. Bond *et al.* (1997) found evidence for a 1.5 ky^{-1} cyclicity in Holocene cooling, indicated by a movement southwards of ice-rafted terrestrial material. Kroon *et al.* (2000) also found century-scale cooling events as indicated by particle flux changes in a high-resolution core from the Barra Fan.

1.4 Scientific Approach

1.4.1 Radiocarbon Dating

1.4.1.1 Introduction to Radiocarbon Dating

Carbon exists as three naturally occurring isotopes ^{12}C , ^{13}C and ^{14}C , at a natural abundance ratio of $10^{12}:10^{10}:1$, corresponding to a total global inventory of ^{14}C of 63 kg. ^{12}C and ^{13}C are stable isotopes, whilst ^{14}C is radioactive. ^{14}C is a cosmogenic radionuclide, produced in the upper troposphere and lower stratosphere by the interaction of thermal neutrons with ^{14}N , at a rate of approximately $2.5 \text{ cm}^{-2} \text{ s}^{-1}$, and rapidly oxidised to $^{14}\text{CO}_2$. ^{14}C decays by emission of soft beta particles ($E_{\text{max}} = 156 \text{ keV}$) to stable ^{14}N , and has a radioactive half life of 5730 y.

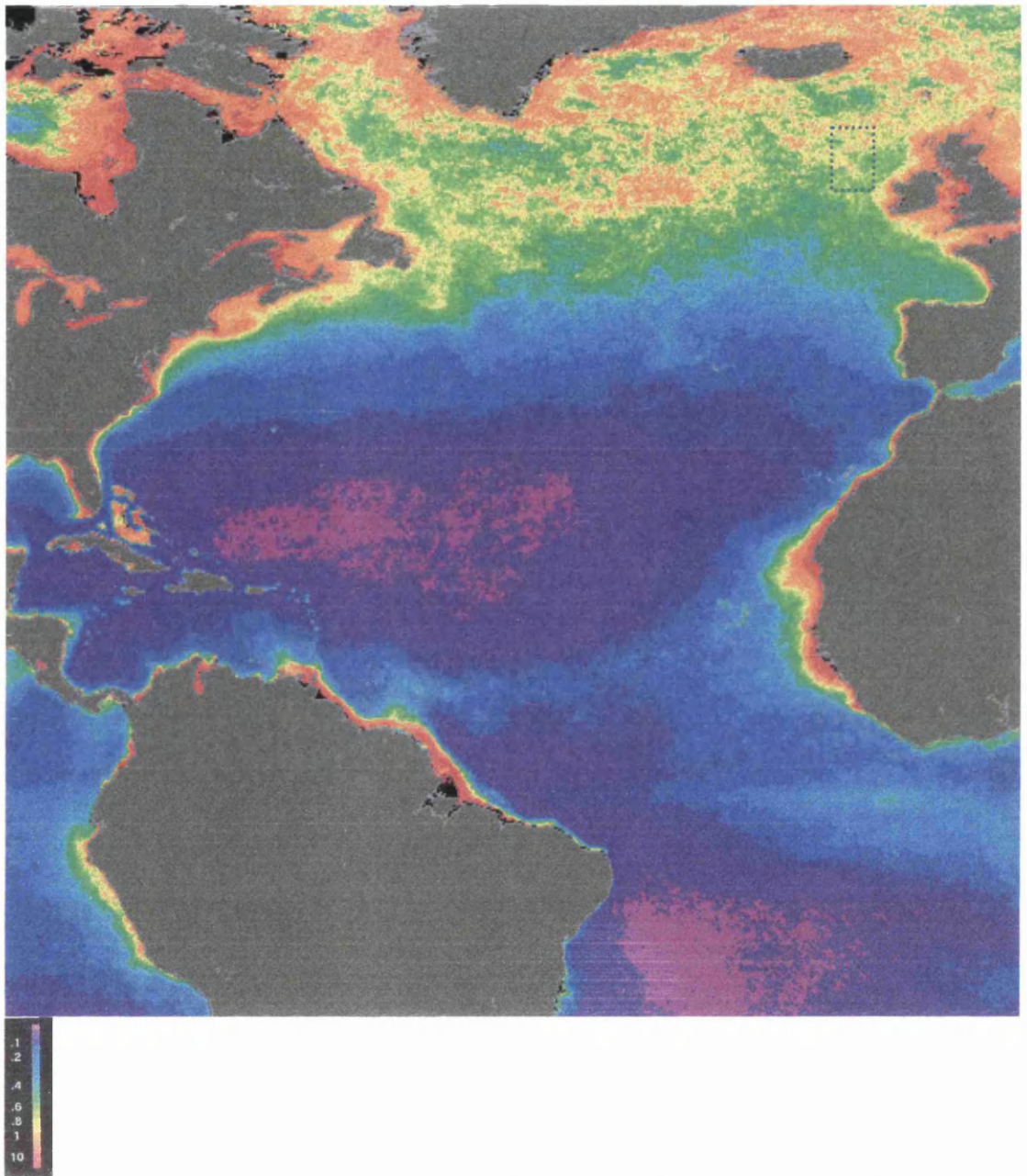


Fig. 1.4: Map of phytoplankton productivity in the North Atlantic, indicated by water column phytoplankton pigment concentrations (in mg m^{-3}). The image above is a composite of all SeaWiFS data collected between November 1978 and June 1986, presented on the SeaWiFS website (<http://seawifs.gsfc.nasa.org>). The box highlights the approximate sampling area for this study.

After formation in the atmosphere, ^{14}C may be incorporated into the terrestrial global carbon cycle via atmospheric mixing and photosynthesis by land plants. In the aquatic environment, diffusion into lake and ocean surface waters is followed by photosynthesis by phytoplankton or inorganic uptake for carbonate shell or skeleton formation. ^{14}C is thus assimilated into all living organisms.

The concept of using ^{14}C as a dating tool for materials of biological origin was first identified in the 1940s (e.g. Libby *et al.* 1949, and references therein). Libby recognised that if the ^{14}C content of an organism was in equilibrium with environmental concentrations at the time of its death, the known rate of decay could be used to determine the time elapsed since ^{14}C uptake ceased. According to first-order kinetics:

$$t = \frac{1}{\lambda} \cdot \ln\left(\frac{A_0}{A_t}\right) \quad (1.1)$$

where t is the time elapsed since death of the organism, λ is the ^{14}C decay constant ($\ln 2 / ^{14}\text{C}$ half life), A_0 is the equilibrium living activity of ^{14}C , and A_t is the ^{14}C activity measured after time, t . The upper age limit of material which can be dated in this way is restricted by the half life of ^{14}C , the size of the sample available and the analytical background of the measurement technique employed. Contemporary ^{14}C analytical techniques enable radiocarbon ages to be determined for samples up to about 60 000 y (Schleicher 1998).

There are a number of assumptions inherent in the method, which, over time, have been shown to be incorrect, although in most cases a correction may be applied. The main difficulties are as follows:

Known half life of ^{14}C

The first radiocarbon analyses used a radiocarbon half life of 5568 y to calculate ages. By the time the half life was revised to 5730 y (Godwin 1962), the number of radiocarbon measurements in published literature was such that it was decided that altering the half life used in calculations would create confusion in the interpretation and comparison of data. For the purposes of comparing radiocarbon ages, it is critical that consistency is maintained. Stuiver and Polach (1977) recommended that where the measured age itself was the most important aspect, e.g. in sediment dating, ages should be reported as ‘conventional’ radiocarbon ages, using the Libby half life. For geochemical or reservoir studies, or dendrochronological calibrations, they recommend that age corrections based on the physical half life should be applied.

Known initial ^{14}C activity

A known value for initial ^{14}C activity - A_0 - is required to calculate a radiocarbon age. However, comparison of radiocarbon ages with independent chronologies demonstrates that atmospheric and surface ocean water ^{14}C activities have varied over time. One reason for this is that the rate of production of ^{14}C in the atmosphere has not been constant over time. Helimagnetic (e.g. Stuiver and Quay 1981) and geomagnetic (e.g. Mazaud 1991) activity both inversely affect the cosmic ray flux to the atmosphere, thus influencing the ^{14}C production rate. Cyclical variations in the production of ^{14}C have been identified, the most important of these having frequencies of 11 y, 88 y, 210 y 512 y (Stuiver and Braziunas 1993) and 2000 y (Dergachev and Chistyakov 1995). Further affecting A_0 values over time is the exchange of ^{14}C between reservoirs. Brown *et al.* (1993) demonstrated large changes in surface water ^{14}C measured in corals, corresponding to the

amount of upwelling induced by the El Niño-Southern Oscillation circulation pattern. On longer timescales, changes in the rate of thermohaline circulation in the North Atlantic is also reflected in the quantity of ^{14}C advected into the deep ocean, thus affecting the relative amounts of atmospheric and surface water CO_2 in glacial and interglacial periods (Mangerud *et al.* 1976; Bard *et al.* 1994; Hunt *et al.* 1995). To counter these production variations, calibration curves for radiocarbon chronologies are constructed by comparing radiocarbon ages with independent chronologies, such as annually banded tree ring (Becker 1993) or coral records (Bard 1993) or varved sediments (Wohlfarth *et al.* 1995).

Transfer between reservoirs

Another assumption in the radiocarbon dating method is that carbon transfer between reservoirs must be rapid on the timescale of the process being studied. However, calibration of radiocarbon dating by dendrochronology has revealed an apparent age difference of 27.2 ± 4.7 y between the hemispheres (McCormac *et al.* 1998). CO_2 exchange between surface water and the atmosphere in the southern hemisphere is greater because of the larger ocean surface area, but prevailing wind patterns mean that atmospheric exchange between the hemispheres is limited, and thus the atmosphere in the southern hemisphere is depleted in ^{14}C . In other environments, such as lakes, there may be a contribution to the carbon pool from 'old' carbon derived from carbonate rocks (e.g. Lin *et al.* 1996). In the oceans, the apparent A_0 age of surface ocean-derived carbonate ranges between approximately 1200 and 300 y, dependent on latitude and ocean upwelling, and the rate of exchange of atmospheric CO_2 with dissolved HCO_3^- (Bard 1988). As a result, when constructing chronologies or dating objects, the apparent age, or reservoir age, must be subtracted from the measured value. However, as noted above, the changes in high

latitude North Atlantic ocean circulation between warm and cool climate periods alters the distribution of radiocarbon between surface and deep waters. Current North East Atlantic reservoir ages are typically given as about 400 y (Bard 1988), whilst those observed at the Younger-Dryas cold stage during the last deglaciation are of the order of 700-800 y (Austin *et al.* 1995; Bondevik *et al.* 1999). Thus, application of a constant reservoir age through time may not be appropriate.

In addition to these assumptions, the carbon isotope balance has been perturbed by anthropogenic activity in the last century. The first is the introduction of ^{14}C -free carbon into the atmosphere by burning of fossil fuel from the late 19th onwards. By 1955, relative concentrations of ^{14}C to ^{12}C ($\Delta^{14}\text{C}$) in the atmosphere had decreased by an average of -25 ‰ from pre-industrial values (Broecker *et al.* 1960). The second perturbation was the introduction to the atmosphere of ^{14}C produced by atmospheric nuclear weapons testing. A total bomb-produced ^{14}C inventory of 2.89×10^{28} atoms was calculated for the ocean (Broecker *et al.* 1985). Measurements of bomb radiocarbon in the surface ocean made in the 1970s showed that distribution of activity was highly latitude-dependent, taking the form of a bimodal peak with the highest $\Delta^{14}\text{C}$ values of 150-200‰ at around 30 °N and 30 °S. (Nydal *et al.* 1984; Broecker *et al.* 1985). Whilst these perturbations mean sample ages cannot be calculated using the present-day A_0 activity of ^{14}C , the problem is remedied by relating all ages to the activity of pre-Suess effect 1890s wood, back-corrected for decay to 1950.

A necessary condition for radiocarbon dating is that the only process affecting the ^{14}C content of the sample is radioactive decay; that is, there is no post-depositional exchange

of carbon between the sample and its environment. However, many commonly dated materials are susceptible to carbon exchange with the environment. In the marine environment, for example, aragonitic corals are more prone to recrystallisation than the kinetically more stable calcite; a process which may allow for incorporation of non-sample environmental carbon. Burr (1992) found that over 40% of the outer surface of a coral had to be removed before the measured radiocarbon age corresponded to that from $^{230}\text{Th}/^{238}\text{U}$ dating. SEM photographs of foraminifera (Schleicher *et al.* 1998) appeared to show encrustation by secondary carbonates. This potential problem is often remedied by analysing only the least-exchangeable fraction (e.g. collagen in bone), or by pretreating the sample so that the contaminated outer layer is removed (Gupta and Polach 1985).

1.4.1.2 *Dating of Marine Sediments*

Radiocarbon analysis of deep sea sediment is commonly carried out on the inorganic carbonate fraction, which is typically dominated by the CaCO_3 tests of planktonic marine microorganisms, mainly coccolithophores and foraminifera. These organisms accrete carbonate shells from dissolved inorganic carbon in the surface ocean, and after the organism's death, the shells sink rapidly to the sea floor. Carbonate ooze, composed of 70% or more of these tests, covers large areas of the open ocean, including the North Atlantic.

Radiocarbon dating of marine carbonate is commonly used for one of two purposes. The first is in determining a direct chronology for palaeoceanographic records, such as $\delta^{18}\text{O}$ or foraminiferal species changes, so that the timing and rates of environmental change may be determined (e.g. Berger *et al.* 1985; Duplessey *et al.* 1986; Thomson and Weaver

1994). The second is the use of radiocarbon age-depth profiles to derive information on long term (10^3 y) sediment accumulation histories (e.g. Thomson *et al.* 1993) and bioturbation profiles (e.g. Peng and Broecker 1979).

Where sediment has been accumulating at a steady rate for several thousand years, ^{14}C age-depth profiles can be modelled using a simple box model (Erlenkeuser 1980; Officer 1982). These models enable assessment of the effects of sedimentary and biological processes on the stratigraphic column. Fig.1.5 shows an ideal ^{14}C profile from a steady state site, with some of the parameters which may be determined from the data. Some of the more important parameters, as given by Erlenkeuser (1980), include:

1. *Sediment accumulation rate* (s) is derived from the gradient of the age-depth profile below the SML:

$$s = \frac{dx}{dt} \quad (1.2)$$

where t is ^{14}C age and x is depth, for any depth below the SML. Irregularities in the age-depth profile indicate changes in sediment accumulation rates or other disturbances of sedimentation.

2. *Surface age* (T_{SF}) is the radiocarbon age at which the line of constant accumulation intercepts the surface sediment. It is extrapolated from the accumulation rate using:

$$T_{SF} = t_1 - \left[x_1 \cdot \left(\frac{t_2 - t_1}{x_2 - x_1} \right) \right] \quad (1.3)$$

where t_1 and t_2 are the radiocarbon ages of the sediment at depths x_1 and x_2 respectively.

3. *SML thickness* (X) gives the long term depth of bioturbation, and is derived from the surface age T_{SF} , the measured mixed layer age, T_{ML} , and a ^{14}C age, t , at depth x below the mixed layer, so that:

$$X = x \cdot \left[\frac{T_{ML} - T_{SF}}{t - T_{SF}} \right] \quad (1.4)$$

4. The *age of freshly deposited material* (T_0) is determined by taking into account the residence time of material in the mixed layer, i.e. X/s , which is responsible for creating the averaged SML age T_{ML} . T_0 is given by:

$$T_0 = T_{ML} - \ln \left[1 - \lambda \cdot (T_{ML} - T_{SF}) \right] / \lambda_L \quad (1.5)$$

where λ is the physical decay constant of ^{14}C and λ_L is the Libby decay constant. If the sedimentary carbonate is indeed derived from the overlying surface waters, T_0 should be zero, once the reservoir effect for that surface ocean is accounted for. Input of sediment redistributed by bottom currents, or loss of core top material in recovery may account for T_0 values greater than the reservoir effect (e.g. Berger and Johnson 1978).

The resolution of sedimentary records is blurred by biological mixing of the surface mixed layer (SML). In its simplest form, the extent of mixing of sediment of different ages is determined by the rate of sediment accumulation and the depth to which it is bioturbated; i.e. X/s will give a measure of the average time any particle resides in the SML (Berger and Heath 1968; Erlenkeuser 1980). This may therefore be used to estimate the precision of radiocarbon age records in bioturbated sediments; an important factor when considering rates of environmental change determined from sedimentary records. However, more complex models have also been developed to take into account processes such as species abundance changes in foraminifera or dissolution of calcite. The former set of models

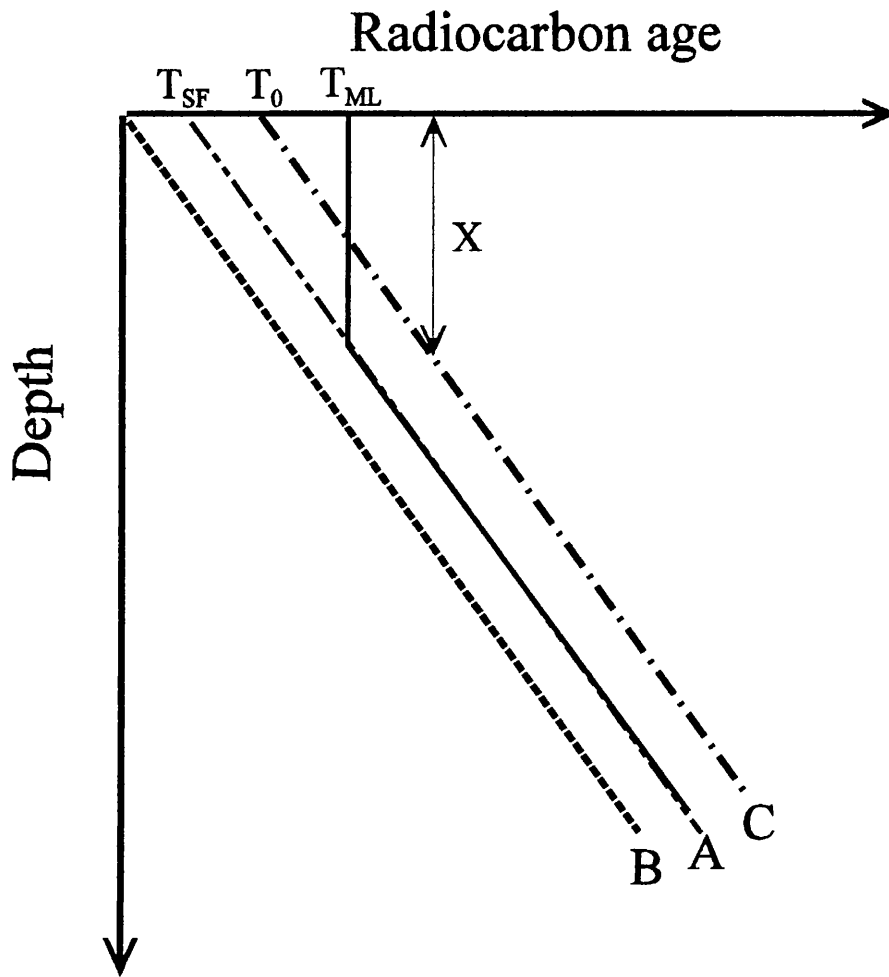


Fig. 1.5: Geometrical relationships between the parameters modelled by Erlenkeuser (1980). T_{SF} is the extrapolated age of the surface sediment; T_0 is the age of the material freshly arriving at the sediment surface; T_{ML} is the measured ^{14}C age of the mixed layer sediment; X is the depth of the surface mixed layer. Line A is the measured sediment ^{14}C profile, line B is the depositional profile (i.e. time elapsed since arrival of a particle at the sediment surface) and line C is the age profile with the influence of bioturbation removed.

(Schiffelbein 1984; Bard *et al.* 1987; Manighetti *et al.* 1993) introduce a correction for mixing of forams across a horizon where the relative abundance of a species has changes with time, e.g. due to a change in surface water temperatures. Under constant abundance, bioturbation of forams results in an averaging of the sample age, depending on the depth of the SML and the sediment accumulation rate. However, where species abundance changes, mixing will introduce a large number of specimens from the high-abundance zone into the low abundance zone, and these will have a disproportionate influence of the age of that horizon. The dissolution models (Peng and Broecker 1984) account for the effect of dissolution of some of the forams arriving at the surface sediment, at sites where the bottom water is undersaturated with respect to calcite. The amount of dissolution depends partly on the length of time spent in the mixed layer, therefore the oldest specimens in a horizon are more likely to have dissolved, and the age of the horizon would be biased towards the younger specimens.

1.4.1.3 *Dating of planktonic foraminifera*

Whilst much useful information may be gathered from bulk carbonate profiles, the input of current redistributed fine carbonate limits the ability to determine accurate chronologies for sedimentary records (e.g. Berger *et al.* 1985; Broecker *et al.* 1988). For example, for the well-studied period at the start of the Holocene, addition of 5 % old (¹⁴C-free carbon) to a 10 000 year old sample would increase the apparent age of the sediment horizon by 400 y (Gupta and Polach 1985). In order to generate more precise radiocarbon chronologies for environmental change, researchers began to date specific sedimentary components, which they considered would best represent the age of the record being studied. By this means, more tightly constrained and higher resolution chronological

records may be obtained than is possible by analysis of the multi-component bulk carbonate.

In light of this, the preferred method in many sedimentary studies (e.g. Duplessey *et al.* 1986; Manighetti *et al.* 1995; Jansen and Veum 1990) has been AMS dating of large (usually >150 μm) planktonic foraminifera (forams). The large planktonic forams are less prone to current redistribution than fine sediment, and since they are known to form their carbonate in the surface ocean, their initial ^{14}C content should be dependent only on the ^{14}C content of this source (corrected for fractionation by stable isotope analysis). Dating only planktonic foram material should therefore more tightly constrain the radiocarbon chronology within a core. Furthermore, foram radiocarbon ages can be unequivocally applied to other palaeoceanographic data derived from forams.

Whilst the models described above account for a number of processes which may affect the radiocarbon chronology of a site, all assume that the same rates and mechanisms of bioturbation apply to all sediment components in the SML. However, radiocarbon dating of different components of deep sea sediment has yielded age offsets between the size fractions, which vary in both direction and magnitude (Fig.1.6). The cause of these age offsets is not fully understood, although they have been variously interpreted as a consequence of processes such as current redistribution of fine carbonate, changing species abundance, preferential dissolution, or biological reworking of the SML (Andree *et al.* 1984; Jones *et al.* 1989; Paull *et al.* 1991). One study directly addressing the problem of size fraction age offsets is that of Thomson *et al.* (1995) at the Biogeochemical Ocean Flux Study (BOFS) sites, also in the North East Atlantic. In this study, both bulk carbonate

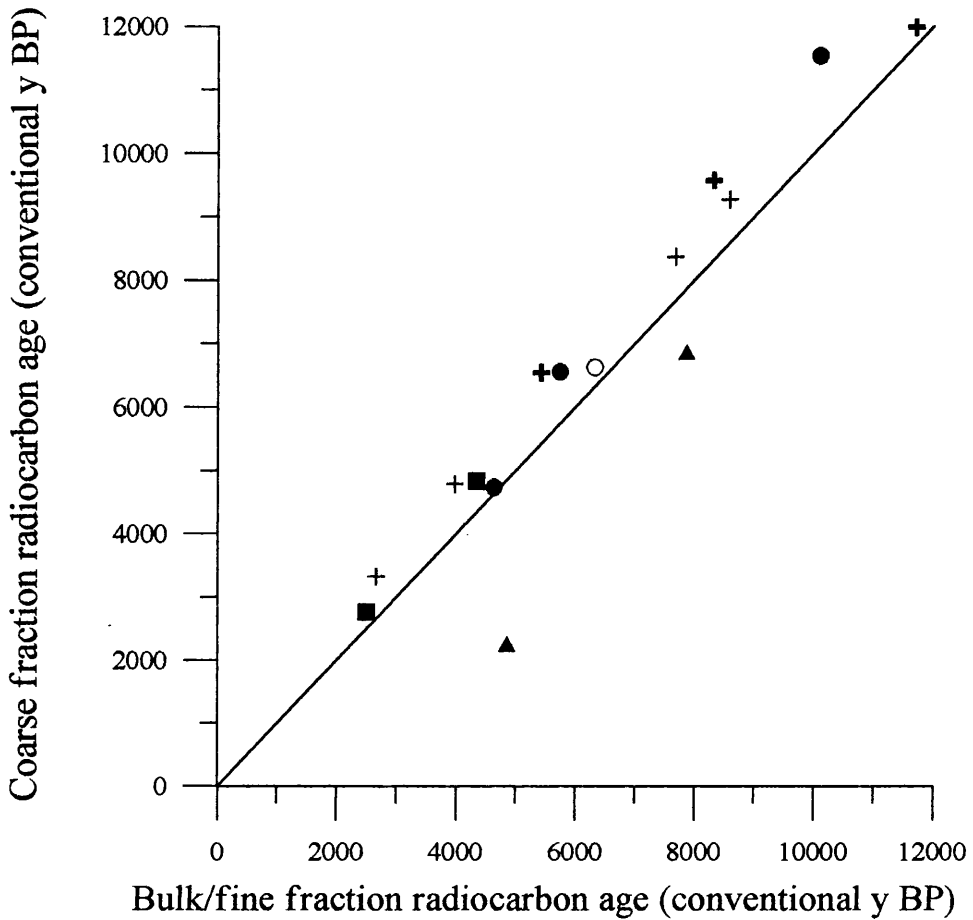


Fig. 1.6: Examples of Holocene-age size fraction ^{14}C age offsets found in previous studies. Data is taken from the following sources: + = Thomson *et al.* 1995; ■ = Jones *et al.* 1989; ● = Paull *et al.* 1991; ▲ = Berger *et al.* 1985; ○ = Andree *et al.* 1984. Additional offsets have also been reported for older sediments.

and samples of planktonic foraminiferal calcite were analysed, and the authors found that the foram material was consistently older than the bulk carbonate at the same depth. The age range and water depth were such that bioturbation-abundance or bioturbation-dissolution effects could not be the cause of the offset. In addition, the use of polyspecific samples and fractionation correction by means of stable isotope measurements should ensure that small-scale carbon isotope fractionation or species vital effects would be accounted for. Thomson *et al.* (1995) concluded that the remaining possibility was particle-size differential mixing by benthic organisms - a mechanism also used to explain the presence of 'lag layers' of coarse (>2 mm) particles from Heinrich layers several centimetres above the original horizon of deposition (McCave 1988). Whilst it is possible these layers may result from millennial-scale climate fluctuations recently observed in North Atlantic Holocene sediments (Bond *et al.* 1997; Bianchi and McCave 1999), this study proposes a biological cause. In essence, when burrowing organisms encounter large sediment grains, mixing ceases to be completely random, as less energy is required to move such grains upwards than to push them downwards, whilst fine sediment then falls into the void thus created. If this mechanism is applicable to the coarse grained foram fraction of deep sea sediment, differing rates of transport out of the SML for the fine and coarse fractions will result in an age offset.

1.4.2 $^{210}\text{Pb}_{\text{excess}}$

1.4.2.1 *Production and behaviour in the marine environment*

^{210}Pb is a product of the ^{238}U natural series decay chain (Fig. 1.7). It is formed from the decay of ^{226}Ra , via five short half life intermediate radionuclides, and has a half life of

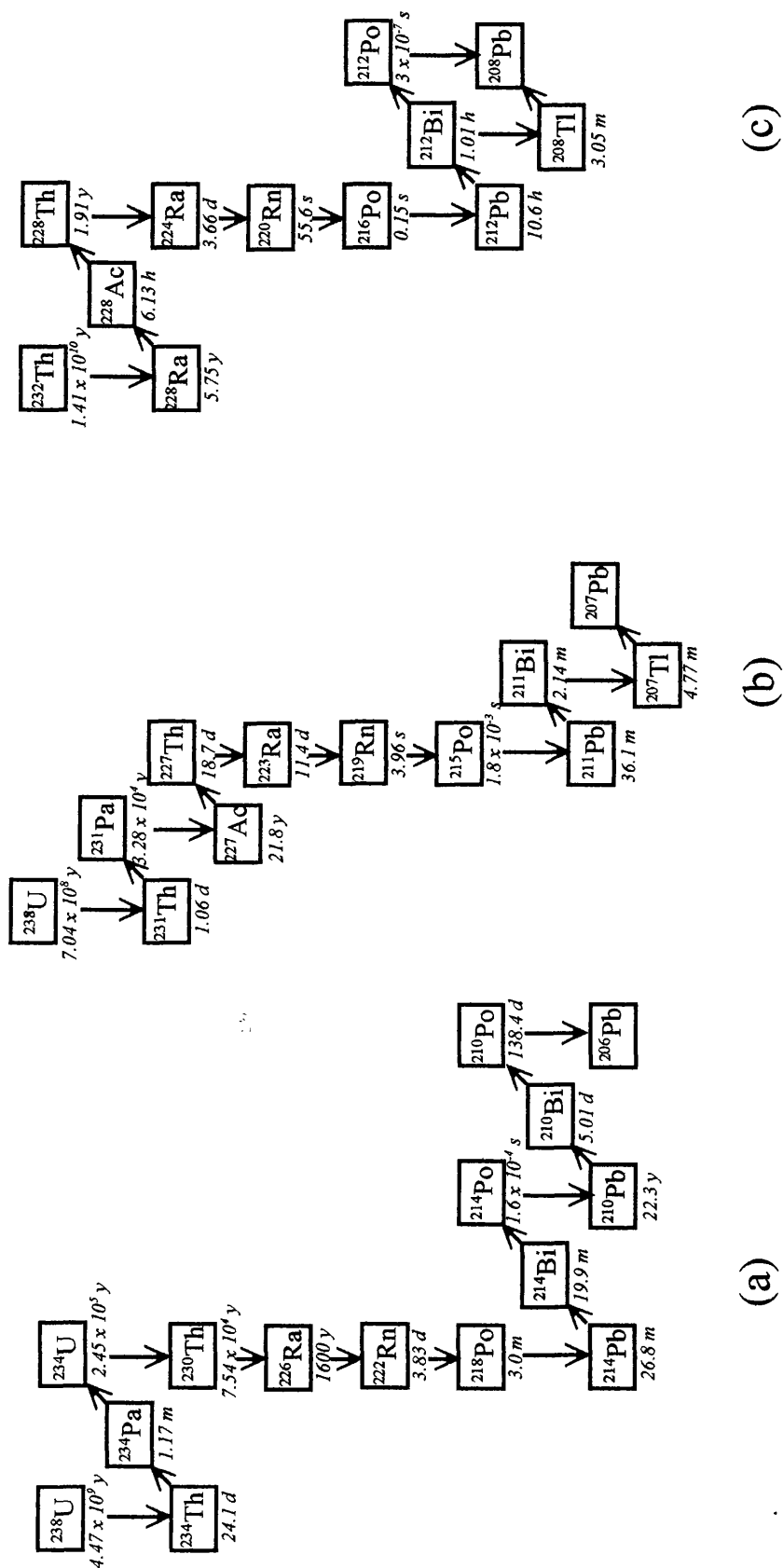


Fig. 1.7: The natural radioactive decay series. (a) Uranium series, (b) Actinium series, (c) Thorium series. Downwards movement indicates alpha decay, diagonal arrow indicates beta decay. The radionuclides analysed in determination of $^{210}\text{Pb}_{\text{excess}}$ are highlighted.

22.3 y. ^{210}Pb decays to ^{210}Bi by beta emission, with two beta groups, $E_{\text{max}} = 15 \text{ keV}$ (81% of ^{210}Pb decay) and $E_{\text{max}} = 61 \text{ keV}$ (19%) (Weast 1981).

^{210}Pb in the marine water column has multiple sources because two of the preceding radionuclides in the decay series are mobile in the environment. ^{222}Rn is gaseous, and escapes from terrestrial rocks and soils into the atmosphere. After it decays, the non-gaseous ^{210}Pb will be rained out over land or the surface ocean. A second component is the decay of ^{226}Ra dissolved in the ocean. The relative importance of these two components to the total ^{210}Pb activity in the ocean will vary with location of a site relative to continents and water depth. The atmospheric supply of ^{210}Pb is more important in coastal locations, and in the surface ocean, whereas in the open ocean, particularly deep waters, ^{210}Pb production from dissolved ^{226}Ra may be 2-20 times greater than the atmospheric supply (Cochran 1982; Thomson *et al.* 1995).

In environments where $\text{pH} > 4$, ^{210}Pb is strongly particle reactive (Lewis 1977) and it is rapidly scavenged from the water column onto both organic detrital particles (Moore and Dymond 1988) and inorganic particles, including iron and manganese oxyhydroxides (Bacon *et al.* 1976; Carpenter *et al.* 1981). This results in radioactive disequilibrium with its parent, ^{226}Ra , from which ^{210}Pb deep sea residence times of the order of 20-100 y have been determined (Craig *et al.* 1973; Bacon *et al.* 1976). Particulate ^{210}Pb activity in the water column has been shown to correlate well with total SPM concentration (Benninger *et al.* 1978), and a good correlation between ^{210}Pb flux to the sediments and the organic carbon flux has also been noted (Moore and Dymond 1988). Comparison of $^{210}\text{Pb}_{\text{excess}}$ profiles with laminated sediments (Crusius and Anderson 1991), artificial radionuclide

profiles (Cochran and Krishnaswami 1980) and laboratory studies of ^{210}Pb mobility (Santschi *et al.* 1983) have concluded that there is little post-depositional remobilisation of ^{210}Pb in marine sediments. The total activity of ^{210}Pb in marine sediments is the sum of the ^{210}Pb scavenged by particles in the water column (also referred to as ‘unsupported’ ^{210}Pb) plus the *in situ* production from decay of its U-series parents in the sediment itself (the ‘supported’ ^{210}Pb component). The activity of ^{210}Pb in excess of the *in situ* fraction is the scavenged fraction and is termed $^{210}\text{Pb}_{\text{excess}}$, i.e. $^{210}\text{Pb}_{\text{total}} - ^{210}\text{Pb}_{\text{in situ}} = ^{210}\text{Pb}_{\text{excess}}$

1.4.2.2 Sediment $^{210}\text{Pb}_{\text{excess}}$ inventories

It has been demonstrated that in shelf and slope areas, $^{210}\text{Pb}_{\text{excess}}$ inventories are inversely related to water depth (Buesseler *et al.* 1985), primarily because of higher suspended particulate matter in nearshore waters due to terrestrial input and resuspension. In the open ocean, Cochran *et al.* (1990) observe that there is a direct positive relationship between water depth and $^{210}\text{Pb}_{\text{excess}}$ inventory. This is explained by the scavenging model of Bacon and Anderson (1982), whereby small, slowly sinking particles would scavenge particle-reactive radionuclides such as ^{210}Pb . As they sink to the sea floor, these particles continually aggregate into large, rapidly sinking particles, then disaggregate into smaller particles, enabling more particle-reactive radionuclides to be scavenged from the water column. Since ^{210}Pb is continually being produced by its parent, the deeper the water column, the more ^{210}Pb should be scavenged. However, the $^{210}\text{Pb}_{\text{excess}}$ inventory of an open ocean site is determined only in part by the vertical input of ^{210}Pb from atmospheric and oceanic sources. Bacon *et al.* (1976) found that 90-95% of the $^{210}\text{Pb}/^{226}\text{Ra}$ disequilibrium in the water column was unaccounted for in particulate matter, thus suggesting there must be some other sink for ^{210}Pb in addition to *in-situ* scavenging. The deep ocean residence

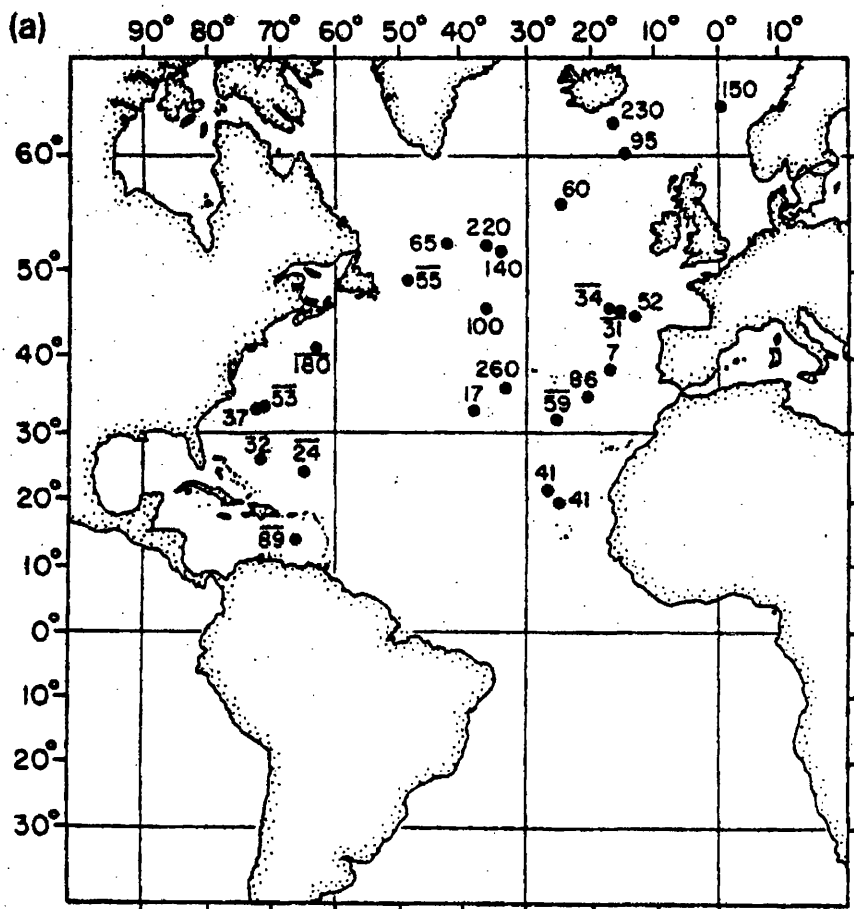


Fig. 1.8: Sediment inventories of $^{210}\text{Pb}_{\text{excess}}$ in the North Atlantic, normalised to the ^{210}Pb scavenged from the overlying water column (Cochran *et al.* 1990). A value of 100 means that all ^{210}Pb scavenged from the overlying water column is present in the underlying sediments. Sites north of 50 °N typically have surplus sediment inventories of $^{210}\text{Pb}_{\text{excess}}$ relative to water column production data, and consequently this area has been suggested as a sink for the ‘missing’ $^{210}\text{Pb}_{\text{excess}}$ from lower latitudes.

time of ^{210}Pb allows sufficient time for the radionuclide to be transported horizontally from areas of low scavenging efficiency to areas of high scavenging efficiency. Areas of high particle flux, such as coastal regions or sediments underlying high-productivity surface waters, might be expected to allow enhanced scavenging. Eastern ocean boundaries appear to be particularly effective sinks because of the high productivity and particle fluxes brought about by upwelling of nutrient-rich waters (Thomson and Turekian 1976; Cochran *et al.* 1983). Resuspension of particles from the sea floor may also result in enhanced ^{210}Pb removal (Spencer *et al.* 1981). Cochran *et al.* (1990) examined the ratio of sediment $^{210}\text{Pb}_{\text{excess}}$ to the water column deficiency, and whilst sediments in the equatorial Pacific contained >80% of the water column deficit, mid-latitude North Atlantic sediments contained only about 40% (Fig. 1.8). The limited data from higher latitudes in the Atlantic led them to suggest that this area constituted a sink for the ^{210}Pb transported out of the mid latitudes, but neither Thomson *et al.* (1993) nor Brand and Shimmiel (1991) found evidence for this in the North East Atlantic BOFS study.

1.4.2.3 $^{210}\text{Pb}_{\text{excess}}$ and bioturbation

The distribution of the activity of a radionuclide tracer in the sediment is a function of SML depth, sedimentation rate, tracer half life and the rate of mixing, described in dimensionless terms in Boudreau (1986a). He states that in order to measure sedimentation rates, the rate of tracer decay must be slow in comparison to the rate of tracer burial. For marine sediments accumulating at a rate of the order of $10^{-3} \text{ cm y}^{-1}$, radionuclides with half lives of several thousand years, such as ^{14}C , are required to establish sedimentation rates. However, bioturbation in most marine sediments is fast enough to homogenise a ^{14}C profile over the SML on such a timescale and no information

as to the processes of mixing can be derived. Similarly, if the tracer half life is short in comparison to the rate of mixing, it will decay before the mixing profile can be superimposed on decay. The particle reactive natural decay series radionuclides ^{234}Th (24 days), ^{228}Th (1.9 y) and ^{210}Pb (22.3 y) have half lives suitable for the study of short term bioturbation processes. The cosmogenic radionuclide ^{32}Si is also potentially useful in this context (DeMaster and Cochran 1982), but is less frequently applied, as its half life is poorly defined (variously reported as being between 130-270 y) and its low natural abundance means analysis is difficult.

At typical open ocean sedimentation rates, ^{210}Pb activity in an unbioturbated sediment should decay to the supported level within the top few millimetres; however, biological activity ensures that it is distributed throughout the SML. The processes which mix $^{210}\text{Pb}_{\text{excess}}$ through the sediment may thus be identified. Many studies of bioturbation employ steady state diffusion as an analogue for biological mixing in the SML (e.g. Peng and Broecker 1979; Boudreau 1986a), characterizing bioturbation as frequent, small-step, random direction movement of particles, and resulting in a profile in which radionuclide activity decreases exponentially with depth. This approach allows the downcore distribution of $^{210}\text{Pb}_{\text{excess}}$ to be quantified as a biodiffusion coefficient, D_B ($\text{cm}^2 \text{y}^{-1}$) (Nozaki *et al.* 1977). The general equation for $0 \leq x \leq L$ is:

$$D_B \cdot \rho \cdot \left(\partial^2 A' / \partial x^2 \right) - \rho \cdot S \cdot \left(\partial A' / \partial x \right) - \rho \cdot \lambda \cdot A' + \rho \cdot P - R = 0 \quad (1.6)$$

Where L is the SML depth in cm; ρ is dry bulk density of sediment (g cm^{-3}); A' is the specific activity of the radionuclide (Bq.g^{-1}); x is the depth in the sediment (cm); S is the sediment accumulation rate (cm y^{-1}); λ is the decay constant of radionuclide (y^{-1}); P is the production rate of the radionuclide ($\text{Bq g}^{-1} \text{y}^{-1}$) and R is the removal rate of the radionuclide

by dissolution ($\text{Bq cm}^3 \text{ y}^{-1}$). Under ideal conditions, ρ , P , R and D_B are assumed to be constant within the SML, and the slow deep sea sedimentation rates are assumed to have negligible effects on the profile. Nozaki *et al.* (1977) give the approximate solution to equation (1.6), for $A' = A_0$ at $x = 0$, and $A' = P/\lambda$ as $x \rightarrow \infty$, as:

$$A' = A_0 \cdot e\left[\left(-\lambda/D_B\right)^{1/2} \cdot x\right] \quad (1.7)$$

A compilation of published data (Middelburg *et al.* 1997) shows a general decrease in D_B with increasing depth of the overlying water column, from rates of the order of $10^2 \text{ cm}^2 \text{ y}^{-1}$ in shallow (few hundred metres) coastal waters, to $10^{-2} \text{ cm}^2 \text{ y}^{-1}$ in the deep sea. This observation is confirmed by Soetaert *et al.* (1995), who found that D_B decreased by three orders of magnitude with increasing depth along the OMEX (Ocean Margin Exchange Project) transect. This decrease in D_B also corresponded to a decrease in benthic biomass. Data for sites from 400-1500 m depth off the Little Bahama Bank also show decreasing D_B with deeper water columns (Henderson *et al.* 1999). In the EUMELI (EUtrophic, MEsotrophic, oLIgotrophic) study, Legeleux *et al.* (1994) reported a threefold difference in $^{210}\text{Pb}_{\text{excess}}$ -derived D_B values in sediments underlying high productivity surface waters and those in areas of low surface productivity.

Depth-zoned models of bioturbation include two or more sublayers within the SML in which biodiffusive mixing occurs, but with a different rate of exponential decrease of tracer activity (and therefore D_B) in each layer. Aller and DeMaster (1984) found two layer mixing in a Panama basin core, consisting of rapidly bioturbated sediment, almost homogenised with respect to $^{210}\text{Pb}_{\text{excess}}$ activity, from 0-6 cm ($D_B = 23 \text{ cm}^2 \text{ y}^{-1}$, from ^{234}Th data), overlying more slowly mixed sediment from 6-20 cm ($D_B = 1.2 \text{ cm}^2 \text{ y}^{-1}$). This rapid

surface mixing has also been found in cores from the Peru Margin (Kim and Burnett 1988) and the Laurentian Trough (Silverberg *et al.* 1986). Conversely, studies by Li *et al.* (1985) and Jahnke *et al.* (1986) report radionuclide profiles which appear to demonstrate less intense mixing in the surface layer and rapid bioturbation below. Legeleux *et al.* (1994) adopted a three-layer bioturbative model to explain $^{210}\text{Pb}_{\text{excess}}$ profiles in meso- and eutrophic sites, with a rapidly mixed middle layer sandwiched between two zones of slower bioturbation. This depth zonation of radionuclide profiles is usually ascribed to specific biological activities, such as head-down deposit feeding (Jahnke *et al.* 1986) or relative activities of epifauna and infauna (Legeleux *et al.* 1994).

In bioturbation studies, it is commonly assumed that mixing is homogeneous and independent of the tracer used to calculate it. This was confirmed at the HEBBLE (High-Energy Benthic Boundary Layer Experiment) sites using the natural decay series radionuclides, where D_B values calculated using $^{210}\text{Pb}_{\text{excess}}$ and $^{234}\text{Th}_{\text{excess}}$ agreed within a 95% confidence limit (DeMaster *et al.* 1991). Comparison of D_B rates from the two nuclides were also generally consistent in the Panama Basin (Aller and DeMaster 1984). At the EUMELI sites, Legeleux *et al.* (1994) found that mixing rates from $^{210}\text{Pb}_{\text{excess}}$, $^{234}\text{Th}_{\text{excess}}$ and $^{228}\text{Th}_{\text{excess}}$ agreed to within a factor of three in four out of five cores. In the fifth core, the three profiles differed dramatically, which the authors ascribed to the non-steady state nature of bioturbation at this site due to the presence of a large infaunal organism. However, Smith *et al.* (1993) found a negative correlation between mixing rate and tracer half life in cores from the Santa Catalina Basin. This, they conjectured, was a result of age dependent mixing of sediments, where the youngest, most nutrition-rich particles with which the short half life radionuclide is most likely to be associated, are

preferentially ingested and mixed faster than older particles, which may still contain



Where macrofauna are present in the sediment, the distance a single particle is moved by bioturbation (the step length) may be large in relation to the the SML. This type of mixing is termed ‘non-local’ or ‘advective’ mixing (Boudreau 1986b). In some instances, the sediment movement is unidirectional rather than random, and may form pronounced subsurface maxima of radionuclide activity. For example, infaunal organisms such as siphunculid and echiuran worms live in burrows at depth, but use a whip-like invert to feed on freshly deposited surface sediment, which is shortly afterwards deposited in the burrow as faeces. This mixing mechanism was proposed to explain the subsurface peaks in $^{210}\text{Pb}_{\text{excess}}$ and $^{239,240}\text{Pu}$ activity in North Atlantic sediments, which had previously been explained as post-depositional remobilisation (Smith *et al.* 1986).

Quite clearly, directional non-local mixing cannot be approximated by the biodiffusive model presented above, and more complex models which allow a direct injection of some of the surface flux of $^{210}\text{Pb}_{\text{excess}}$ are required (e.g. Boudreau and Imboden 1987). Soetaert *et al.* (1996) have modelled the intensity of this type of mixing at the OMEX sites by including an injection flux of $^{210}\text{Pb}_{\text{excess}}$ from either surface or suspended sediment, to depth. Applying this model to those OMEX sites that demonstrated subsurface mixing, they found that between 8% and 86% of the $^{210}\text{Pb}_{\text{excess}}$ flux penetrated the sediment by means of non-local mixing. They noted that the importance of non-local mixing relative to biodiffusive transport decreased with water depth, most probably due to a decreasing supply of labile organic carbon to the sediment with increasing water depth.

Despite the improvements in modelling, any individual core provides only an instantaneous picture of mixing over a very limited (usually less than 1 m²) site, and perhaps particularly where non-local mixing is known to occur, may vary significantly over short spatial and temporal periods. Smith and Schafer (1984) examined three dimensional mixing variations in a 1 m³ box core from the Newfoundland continental slope and demonstrated that significant variations on the ²¹⁰Pb_{excess} tracer timescale occur over short distances. They concluded from X-ray evidence from the box core that this was the result of inclined burrows introducing a horizontal component to bioturbation, rather than purely vertical mixing. The spatial and temporal frequency of non-local mixing events is still uncertain due to potential misinterpretation of ²¹⁰Pb_{excess} profiles. The peak profile of a historical subsurface mixing event, which has been smoothed out by biodiffusion and radioactive decay, may equally be interpreted as the product of multi-layer diffusive mixing (Boudreau 1986b). There is little real understanding of the lifespan and relative mobility of echurian worms, and thus the frequency and overall importance of non-local bioturbation in the deep sea is difficult to ascertain. Smith *et al.* (1986) modelled the erosion of a hypothetical ²¹⁰Pb_{excess} peak by biodiffusive mixing at 0.1 cm² y⁻¹, estimating that the peak would be smoothed out after about 4 years. In summary, whilst bioturbation is a key mechanism in controlling the fate of material entering the sediment column, it is not yet possible to model the effects of bioturbation accurately, due to the lack of information on biological processes in benthic environments.

1.4.3 Man-made Radionuclides

1.4.3.1 Production of man-made radionuclides

The release of radioactive elements from atmospheric nuclear weapons testing

commenced in 1945. Input of radionuclides from atmospheric testing fallout peaked in 1963, after which the subsequent atmospheric weapons test ban treaty between the U.K., U.S A, and U.S.S.R. led to the suspension of atmospheric weapons testing by these nations. Although atmospheric releases from Chinese and French testing continued until 1980, these tests contributed a comparatively minor amount of radioactivity in relation to the total fallout activity. Low energy explosions release radionuclides into the troposphere where they are scavenged by rain or snow within a few tens of days, before being deposited fairly close to the site of the explosion. However, high-energy atmospheric testing leads to injection of weapons testing radionuclides into the stratosphere, where it has a halving-time (time require for activity to fall to half the initial value) of about 1 year. This time is sufficient to allow mixing throughout the atmosphere before fallout, resulting in global contamination with low levels of weapons testing radionuclides (Perkins and Thomas 1980). As such, this is the most important source of man made radionuclides to the open ocean environment.

Nuclear power generation and fuel reprocessing activities result in localised areas of relatively high levels of contamination from man made radionuclides where low level liquid wastes and cooling waters are discharged into the coastal environment. The first of these discharges took place in 1944 from the Hanford plutonium production plant in the USA. However, the most important with respect to the North East Atlantic are the low level liquid radioactive effluent discharges from the nuclear fuel reprocessing facilities at Sellafield in the UK, which began in 1952, and to a lesser extent, Cap de la Hague in France, which has been releasing low activity effluent since 1966. Changes in operations at Sellafield and developments in reprocessing

facilities mean that the activities and ratios of radionuclides discharged as liquid effluent have varied over time (Gray *et al.* 1995). Whilst much of the activity has been shown to stay within the proximity of the nuclear facilities (Woodhead 1988), reprocessing-derived radionuclides are detected in the North Sea (Beks 2000) and Arctic (Nies *et al.* 1999; Cooper *et al.* 2000). Sellafield radionuclides incorporated into local Irish Sea sediments may be transported out of the area either by redistribution of the sediment or by redissolution from the sediment (Hunt and Kershaw 1990; MacKenzie *et al.* 1998). In time, cross-shelf currents and cascades of water over the shelf may transport Sellafield-derived radionuclides away from the coastal waters and into the deep North East Atlantic. The NEA dumpsite, at 4700 m depth off the Iberian coast and containing approximately 42 000 TBq of packaged solid waste, may represent another localised source of radionuclides to the North Atlantic. However, as yet there is no evidence of any of this material entering the sediments surrounding the dumpsite (Kershaw 1985). Finally, accidental releases may contribute to the inventories of radionuclides in the marine environment. The most significant for the open ocean environment was the burn up of the satellite SNAP 9A in 1964, which released significant quantities of ^{238}Pu , mostly in the southern hemisphere (Hardy *et al.* 1973). The 1986 accident at the Chernobyl nuclear reactor in the Ukraine released a large amount of radiocaesium (3.8×10^{16} Bq ^{137}Cs and 1.49×10^{16} Bq ^{134}Cs), but the fraction of this which entered the open North Atlantic is assumed to be inconsequential in comparison to the radionuclides present from weapons testing fallout.

Radionuclides produced either by anthropogenic or natural processes can be divided into three categories. Fission products are those elements which are produced by the splitting of the fissile material. Radionuclides may also be formed by nuclear fusion of two atomic nuclei, for example, the fusion of hydrogen to form helium is process sustaining stars throughout most of their existence. The final category consists of those radionuclides formed by activation by thermal neutrons, such as the transuranic elements formed by anthropogenic activities, or activation of environmental materials by cosmogenic neutrons, for example ^{14}C , ^{10}Be or ^3H .

1.4.3.2 *Geochemistry of artificial radionuclides used in this study*

The man-made radionuclides examined in this study are ^{137}Cs (half life 30.1 y), ^{241}Am (241 y), ^{238}Pu (87.7 y) and $^{239,240}\text{Pu}$ (6560 and 24 100 y respectively). The radionuclides ^{239}Pu and ^{240}Pu are considered as a single entity as it is not possible to determine them individually using the alpha spectrometric method applied in this study.

As with NDS radionuclides, man-made radionuclides exhibit a wide range of geochemical behaviour. The uptake of radionuclides by particulate material relative to the concentration in the dissolved phase is governed mainly by the ionic potential of the element. Particulate uptake of radionuclides may occur by a number of mechanisms, including adsorption to a solid surface, chemical bonding, ion exchange and coprecipitation. Assuming chemical equilibrium, the degree of solubility or particle reactivity can be described by an equilibrium constant, the distribution coefficient, K_D :

$$K_D = \frac{A_{(s)}}{A_{(d)}} \quad (1.8)$$

where $A_{(s)}$ is the activity of the radionuclide in the solid phase and $A_{(d)}$ is the activity of the radionuclide in the dissolved phase. K_D values for a radionuclide vary depending on the geochemistry of the environment in question, e.g. the Eh, pH, chemical composition of the water, suspended particle concentration, and physical and chemical characteristics of the suspended particulate matter, such as size or mineralogy. Highly soluble radionuclides have K_D values less than about 10^{-2} , whilst those for strongly particle reactive species greater than 10^6 .

Caesium in the marine environment behaves largely as a soluble constituent (Sholkovitz 1983; Li and Gregory 1984), as a consequence of the low ionic potential (ionic charge/ionic radius) of the Cs^+ ion, resulting in hydration. This conservative behaviour has enabled radioisotopes of caesium to be employed as tracers of water circulation (e.g. McKinley *et al.* 1981 Kershaw *et al.* 1997; Aarkog *et al.* 1999). However, the hydrated Cs^+ ion has a high affinity for illitic clays, and may become particle-bound by interaction with ion exchange sites in the clay (Francis and Brinkley 1976). This mechanism, combined with the large quantities of radiocaesium which entered the marine environment, means detectable activities of ^{137}Cs are present in sediments.

Plutonium exists in the marine environment in a range of oxidation states, from Pu(III) through to Pu(VI), which complicates the understanding of its geochemical behaviour. The more reduced species, Pu (III) and (IV), are found as insoluble hydroxides, $\text{Pu}(\text{OH})_n$, whilst Pu(V) and (VI) form soluble anions. The K_D of the more reduced Pu species is therefore greater than that of the higher oxidation states. According to Santschi *et al.* (1980), 15-20% of Pu in the New York Bight exists as particle-bound Pu, a value which is

thought to reflect the distribution of the various Pu oxidation states. However, Cochran *et al.* (1987) suggested that high K_D values for Pu in the northwest Atlantic were a result of adsorption of oxidised Pu onto mineral surfaces over long timescales.

Unlike caesium, plutonium is bound not to clay mineral sites, but by adsorption onto biogenic particles in the upper water column (Higgo *et al.* 1977; Livingston and Anderson 1983; Fisher *et al.* 1988). It may also be scavenged by precipitating Mn and Fe hydroxides at the water-sediment interface (e.g. Carpenter *et al.* 1987). Much like ^{210}Pb , scavenging of Pu in areas of high particle flux, such as ocean margins, will result in higher than expected inventories in the sediment (Koide and Goldberg 1982; Carpenter *et al.* 1987).

Americium is also a highly particle reactive radionuclide, existing in the marine environment predominantly as insoluble Am(III), although a more soluble Am(V) is also present. Malcolm *et al.* (1990) demonstrated that more than 99% of Am in sediment pore waters was in the reduced form. K_D values for Am in the open ocean are of the order 10^5 - 10^6 (Van Dalen and Wijkstra 1986; Cochran *et al.* 1987), slightly higher than for Pu. Evidence for preferential scavenging of Am relative to Pu, as a result of its higher particle reactivity was also found in Washington Slope sediments (Carpenter *et al.* 1987). In addition to the direct ^{241}Am input from nuclear weapons testing and nuclear fuel reprocessing, ^{241}Am also has an *in situ* production source from beta decay of ^{241}Pu (half life 14.4 y), also released from anthropogenic nuclear activities.

1.4.3.3 Bioturbation of man-made radionuclides

The approximate 50 y presence of artificial radionuclides in the oceans means that they may be employed to examine bioturbation over a similar timescale to $^{210}\text{Pb}_{\text{excess}}$. Like $^{210}\text{Pb}_{\text{excess}}$, they should only be present in the top few millimetres of the surface sediment unless mixed downwards over the last few decades by bioturbation. Mixing models similar to those described for natural decay series radionuclides are employed, although since input has not been steady state, a different input function is required. Cochran (1985) modelled ^{137}Cs and $^{239,240}\text{Pu}$ profiles using both an instantaneous input in the year of peak fallout, 1963, and a continuous input since initiation of weapons testing. He noted that the 'instantaneous input' model gave a better agreement with the D_B calculated from $^{210}\text{Pb}_{\text{excess}}$. In contrast, Legeleux *et al.* (1994) argued that the presence of detectable activities of artificial radionuclides on sinking particles collected in sediment traps during their study was justification for assuming a continuous input function.

Bioturbation profiles and sedimentation histories determined using artificial radionuclide profiles may be influenced by the post-depositional behaviour of the radionuclides in question. Cochran (1985) and Stordal and Johnson (1985) suggested that post-depositional mobility of artificial radionuclides could be responsible for contrasting SML depths and D_B values found using these tracers and the immobile $^{210}\text{Pb}_{\text{excess}}$. Livingston and Bowen (1979) attributed the changing $^{239,240}\text{Pu}/^{137}\text{Cs}$ ratio in western Atlantic coastal sediments to the preferential remobilisation of Pu relative to Cs in the sediments, whilst Sayles and Livingston (1983) detected $^{239,240}\text{Pu}$ up to 10 cm deeper than $^{210}\text{Pb}_{\text{excess}}$. ^{137}Cs mobility relative to $^{210}\text{Pb}_{\text{excess}}$, $^{239,240}\text{Pu}$ and ^{241}Am has been demonstrated in Washington slope sediments (Carpenter *et al.* 1987) and in lake sediments (Crusius and Anderson 1995).

Diffusion of ^{137}Cs from sediments has also been shown in the MERL artificial ecosystem (Santschi *et al.* 1983) and sediment tank experiments (Sholkovitz *et al.* 1983). In contrast, a good correlation between ^{210}Pb and ^{137}Cs profiles has been reported in the tropical Atlantic (Legeleux *et al.* 1994), and between ^{210}Pb and $^{239,240}\text{Pu}$ in the northeastern Atlantic (Smith *et al.* 1986). A ten year time-series study of ^{137}Cs and $^{210}\text{Pb}_{\text{excess}}$ also concluded that the artificial radionuclide was immobile in the anoxic sediments of Skan Bay (Sugai *et al.* 1994). Both laboratory (Santschi *et al.* 1983; Sholkovitz *et al.* 1983) and *in situ* studies (Buesseler and Sholkovitz 1987; Malcolm *et al.* 1990) appear to indicate no active diagenesis of Pu in a range of marine environments.

These conflicting reports of potential effects of remobilisation on radionuclide profiles highlight the importance of a multi-tracer approach to sediment bioturbation studies. However, other possibilities remain for the explanation of disparate profiles between tracers. The first concerns the analytical uncertainty with which $^{210}\text{Pb}_{\text{excess}}$ and artificial radionuclides may be detected. Since artificial radionuclides are measured against an environmental background of zero, it is possible to confirm their presence at much lower activities than $^{210}\text{Pb}_{\text{excess}}$, where the supported activity must be subtracted from the total. A second possibility for reconciling differences in radionuclide profiles is the size-differential mixing of particles by bioturbation. The discriminatory feeding of benthic organisms has been highlighted in section 1.1.3, and size-selective mixing of foraminifera and fine sediment was discussed in section 1.4.1.4. Size differential mixing was also suggested as a cause for the faster mixing rates of $^{210}\text{Pb}_{\text{excess}}$ relative to ^{32}Si , where the latter is incorporated in coarse grained radiolarian tests, and the former is associated with finer detrital material (DeMaster and Cochran 1982). Similarly, Cochran (1985) suggested that

^{137}Cs , which is attached primarily to the fine-grained clay fraction of the sediment, could be mixed faster than $^{210}\text{Pb}_{\text{excess}}$ bound to a coarser detrital component.

1.4.3.4 Radionuclide Activity Ratios

The differences in radionuclide releases from weapons testing, fuel reprocessing, and accidental releases, combined with their different geochemical behaviours, allows information to be derived on the sources and means of transport of radionuclides to a site. The radionuclides produced differ between sources because of variables such as the type of fuel used and its burn up time. Table 1.3 lists some of the major radionuclides produced in weapons tests, fuel reprocessing, and the Chernobyl accident. From this, it is apparent that the radioisotope and radionuclide activity ratios may be used to identify the source of artificial radionuclides to a site.

The $^{238}\text{Pu}/^{239,240}\text{Pu}$ activity ratio is a frequently used tracer of the source of plutonium at a site. The ratio should be dependent solely on the input since there will be no geochemical fractionation between isotopes of such a heavy element. In the case of atmospheric deposition, the distribution pattern of Pu isotopes varies between the hemispheres, with the northern hemisphere being dominated by weapons fallout, and the southern hemisphere being heavily influenced by SNAP 9A. Northern hemisphere $^{238}\text{Pu}/^{239,240}\text{Pu}$ activity ratios from weapons testing fallout were determined as 0.03-0.04 (Hardy *et al.* 1973). The value for time-integrated Sellafield discharges to 1998 is 0.182 (MacKenzie *et al.* 1998), and that from Chernobyl fallout is 0.49 (Pentreath 1988).

In contrast, variations in $^{239,240}\text{Pu}/^{137}\text{Cs}$ and $^{137}\text{Cs}/^{241}\text{Am}$ activity ratios are caused by both differences in source output ratio and in geochemical behaviour of the nuclides and may

be used to gather information on, e.g. particle scavenging processes and water transport in the area of study. Cochran (1985) found that the $^{239,240}\text{Pu}/^{137}\text{Cs}$ ratio along a Pacific Ocean transect decreased from 5.7 to 0.06 from 1°N to 30°N . The highest inventory was a result of rapid scavenging of the particle reactive $^{239,240}\text{Pu}$ from close-in fallout from weapons testing at Christmas Island. Elsewhere, the changing ratio was a result of decreasing ^{137}Cs activity with latitude due to the increasing distance from the main area of weapons testing. Carpenter *et al.* (1987) found lower ratios on shelf compared to slope sediments, which they concluded was due to preferential scavenging of $^{239,240}\text{Pu}$ on the shelf, where concentration of suspended particulate material was highest. $^{137}\text{Cs}/^{241}\text{Am}$ ratios will also reflect such differences in radionuclide behaviour. MacKenzie *et al.* (1998) calculated a time-integrated $^{137}\text{Cs}/^{241}\text{Am}$ Sellafield discharge ratio of 31.1, but reported that sediment ratios in core sections where no redissolution of radionuclides has occurred, were of the order of 5.5. In Washington continental shelf and slope sediments, where the $^{238}\text{Pu}/^{239,240}\text{Pu}$ activity ratio indicates that the plutonium activity is dominated by atmospheric fallout, $^{137}\text{Cs}/^{241}\text{Am}$ core inventory ratios range between 2.7 and 5.3 and $^{239,240}\text{Pu}/^{137}\text{Cs}$ ratios between 0.21 and 0.64 (Carpenter *et al.* 1987). The change in $^{239,240}\text{Pu}/^{137}\text{Cs}$ ratios between the shelf and slope regions is ascribed to additional input of terrestrially-sourced, particle-bound ^{137}Cs in shelf sediments. Since $^{239,240}\text{Pu}$ (and similarly, ^{241}Am) are bound to organic particles, the fate of the terrestrially derived transuranic elements is linked to the biological cycling of the organic material, whilst ^{137}Cs , tightly bound to inorganic particles is more likely to be transported out onto the continental shelf. The more distal slope sediments, however, will receive their radionuclide fluxes primarily from direct fallout. The authors note that the $^{239,240}\text{Pu}/^{137}\text{Cs}$ ratios are much higher than the mean $^{239,240}\text{Pu}/^{137}\text{Cs}$ ratio of 0.17 in Northwestern Atlantic sediments, yet this value is still far higher than the

estimated fallout ratio of 0.012 (Livingston and Bowen 1979) due to the different geochemical behaviour and solubilities of the two radionuclides.

Source			
	Fallout ^a	Reprocessing ^b	Other ^c
^{239,240} Pu	1.2 x10 ¹⁶ Bq	6.1 x 10 ¹⁴ Bq	
²³⁸ Pu	2.9 x10 ¹⁴ Bq	1.1 x 10 ¹⁴ Bq	5.1 x 10 ¹⁴ Bq
²⁴¹ Pu	1.4 x10 ¹⁷ Bq	1.3 x 10 ¹⁶ Bq	
²⁴¹ Am	4.9 x10 ¹⁶ Bq	9.4 x 10 ¹⁴ Bq	
¹³⁷ Cs	1.3 x10 ¹⁸ Bq	3.0 x 10 ¹⁶ Bq	4 x10 ¹⁶ Bq

Table 1.3: Estimated activities of some radionuclides released to the environment by anthropogenic activity (sources: Hardy *et al.* 1973; MacKenzie and Scott 1993; UNSCEAR 1993; Gray *et al.* 1995).

^a Input to the environment from weapons testing fallout. For ²⁴¹Am, the activity presented is that resulting from the decay of ²⁴¹Pu between 1962 (peak testing activity) and 1997. Thus, the present day activity of fallout-derived ²⁴¹Pu will have decreased by a similar amount from that presented in the table.

^b Total effluent from nuclear fuel reprocessing activity at the Sellafield (formerly Windscale) plant, Cumbria, UK, from 1952-1990

^c Refers to atmospheric input of ²³⁸Pu from the SNAP 9A satellite burn up in 1962, and ¹³⁷Cs from the 1986 accident at the Chernobyl nuclear power plant in the Ukraine

Chapter 2 - Methods and Materials

2.1 Sample Collection and Storage

The bulk of the work described in this thesis is based on analyses of sediment from box cores collected from the three BENBO sites on the first BENBO cruise, CD107, in August 1997. A NIOZ box corer of 50 cm diameter x 57 cm length was used to retrieve the sediment cores, which were sub cored using 11 cm diameter plastic core liner.

Immediately after collection, the sub-cores were sealed at both ends. On return to port, the cores were stored at 4 °C in the Southampton Oceanography Centre (SOC) core repository. The sub-cores were sectioned using a precision extruder specially constructed at SOC, and the individual sections weighed wet, dried at 90 °C, and reweighed to determine sediment bulk densities.

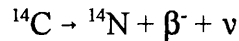
2.2 Radiocarbon Analysis

2.2.1 Methods of detection for ^{14}C dating

Techniques used for analysis of ^{14}C fall into two basic categories. Radiometric analysis involves measurement of the ^{14}C specific activity of a sample with known sample mass. Atom-counting methods, specifically accelerator mass spectrometry (AMS), entail determination of the proportion of ^{14}C atoms relative to the number of stable carbon atoms in a sample. This latter technique has the capability to analyse smaller samples in a much shorter counting time than is possible using radiometric methods, but at present it is also more costly.

2.2.1.1 Radiometric methods

^{14}C decays by pure beta emission, resulting in release of a β^- particle (an electron) and an antineutrino ($\bar{\nu}$) from the ^{14}C nucleus, so that:



The beta decay energy is shared between the β^- particle and the antineutrino, so that the sum of their energies is equal to the E_{max} energy of the beta decay. The beta particles may therefore have any energy between zero and the maximum energy, E_{max} . E_{max} for most beta emitters lies in the range 10 keV to 4 MeV. ^{14}C is a 'soft' beta emitter with $E_{\text{max}} = 156$ keV.

Interaction of beta radiation with matter occurs mainly through ionisation or excitation interactions with electrons. High-energy beta radiation has a specific ionisation of about 10^2 ion pairs mm^{-1} and a range of several metres in air. Energy may also be lost from beta particles as a result of interaction with the nuclei of absorbing atoms, resulting in path deflection and emission of Bremsstrahlung radiation.

Radiometric methods utilise the beta decay of ^{14}C . Initial ^{14}C dating techniques, developed by Libby in the 1940s, measured decay by inserting solid carbon samples in a radiation detector. However, this technique suffered from high self-absorption of beta particles by the sample and interference from background radiation. The gas proportional counting method uses high carbon content gases (e.g. CO_2 , C_2H_2 and CH_4) prepared from the sample as a counting medium. This not only improves detection efficiency due to less self-absorption, but gaseous samples are also easier to prepare than solid carbon. The advent of liquid scintillation counting (LSC) in the 1950s (e.g. Hayes and Gould 1953) offered

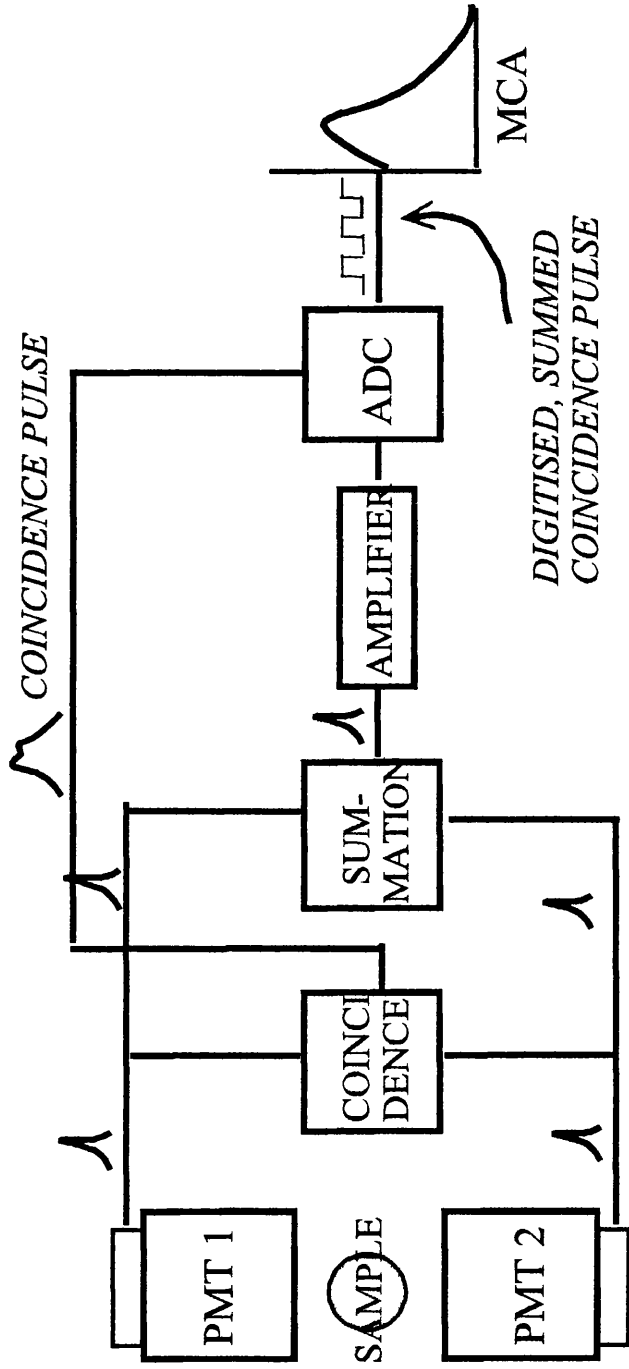


Fig. 2.1: Schematic diagram of a liquid scintillation counter

further improvements in ^{14}C analysis. Samples in liquid form are easier to manipulate, and, because the volume is much less than the corresponding volume of gas, the incidence of background counts is reduced.

The basis for the liquid scintillation technique is the interaction of beta particles with scintillator compounds and detection of the subsequent light pulse. The beta emitter is either dissolved in or chemically prepared as a solvent (typically benzene for radiocarbon dating), in which is also dissolved a quantity of aromatic organic scintillator. The beta particle produced by decay interacts with the surrounding molecules and the energy is transferred to the scintillator. The energy from the beta decay excites the scintillator electrons, then, as they return to ground state, photons are released. The total number of photons released by interaction of the beta particle with the scintillator is proportional to the beta particle energy.

In LSC, the sample and scintillating compounds are dissolved in an aromatic organic solvent and sealed in a glass vial. The vial is placed between two photomultiplier tubes (PMTs), and optical reflectors direct the light energy from the beta particle-scintillator interaction to the PMTs where it is transformed into a voltage signal proportional to the energy of the β^- particle produced (Fig. 2.1). Using two PMTs enables coincidence counting to be applied, which reduces the background from radiation external to the vial. If a signal is registered in both PMTs within a set time period (usually about 25 nanoseconds), the signal is accepted as originating from within the vial. Thus, if the signal occurs only in a single PMT, it is discounted as being external to the sample and therefore a consequence of environmental radiation or detector noise. The problem of cosmic

radiation penetrating the vial and causing ionisation of the scintillator is reduced by application of a number of background-reduction techniques. Passive shielding of a few centimetres of lead is usually incorporated into the detector and will prevent penetration of most low energy environmental radiation. Anti-coincidence counting may also be employed to provide active shielding against high-energy environmental radiation. An anti-coincidence guard incorporates a PMT, or an array of PMTs aligned in the detector guard so that they will record counts from environmental radiation penetrating the lead shielding. If a count is registered simultaneously in both the sample analyser PMTs and the anti-coincidence guard, the count will be rejected as being external to the sample. Modern detectors also possess other anti-coincidence counting techniques such as pulse amplitude comparison or pulse shape analysis. These take advantage of the different signal shape characteristics of the photon pulses produced by beta particles and cosmic radiation to accept or reject signals.

If the signal is accepted by the coincidence circuit, the output from the two PMTs is combined to generate a summed coincident pulse. This accounts for differences in the signal strength measured in the PMTs because of the geometrical location of the pulse in the vial. Following summation, the analogue pulse is transformed to a digital signal by an analogue-digital converter. This digital signal is linearly related to the beta particle energy, and is stored in a channel corresponding to that energy in a multichannel analyser. The spectrum produced from the multichannel analyser enables detailed information to be gathered on the energy distribution of the pulses. Rather than being referred to as liquid scintillation counters, detectors employing this type of spectral analysis are more correctly called liquid scintillation spectrometers; however for consistency, the method will

continue to be abbreviated in this paper as LSC.

A number of factors must be taken into account to optimise the components of the liquid scintillation system and obtain accurate and precise analysis within a reasonable counting time. . These are outlined below:

Counting windows - For a number of reasons, it is not practical to use the entire ^{14}C spectrum to determine the count rate. At the lower end of the spectrum, there may be interference from tritium ($E_{\text{max}} = 18.6 \text{ keV}$) in the sample, solvent or scintillator.

Quenching (see below) may affect the apparent energy of a photon and move signals in or out of the area defined by the ^{14}C spectrum. As a result, only a part of the spectrum is analysed. The lower window limit is generally chosen as where $<1 \%$ of ^3H counts would interfere with the ^{14}C spectrum, whilst the upper window is chosen so that slight variations in quench between samples, as measured by the transformed index of the external standard (tSIE) has the least effect on count rate, but without substantially reducing counting efficiency. This is termed balance-point counting.

Counting interferences - Quenching is the term given to the reduction in PMT output caused by processes occurring during or after deposition of energy in the scintillant by ionising particles, resulting in a shift in distribution of the ^{14}C energy spectrum. There are essentially two types of quenching; colour quench and chemical quench. Colour quench results from the absorption of photons as they travel through a coloured sample, whilst chemical quench is the consequence of absorption of beta energy by impurities in the sample or scintillation cocktail medium. As the counting window does not encompass all

the possible energies of ^{14}C beta particles, this will result in some counts moving into the counting window and some moving out, and hence a change in counting efficiency.

Chemical quench is more important than colour quench in LSC analysis of benzene, and the extent of quenching is primarily dependent on the purity of the benzene and scintillators and the oxygen content of the sample. The choice of vial material may also affect the energy of photons reaching the PMT, although not directly quenching the sample.

Chemoluminescence is the result of random chemical interactions between sample components, each resulting in the generation of a single photon. Likewise, photoluminescence generates photons when the sample solvent is excited by ultraviolet radiation. Whilst the coincidence circuit will exclude single photon events, occasionally the rate of photon production by these means is sufficient that two individual events occur within the time window allowed by the coincidence circuit. Photoluminescence can be eliminated by delaying the start of counting by about 1 hour after placing the sample in the counter, by which time most photoluminescence will have disappeared.

Chemiluminescence is accounted for by means of a second coincidence circuit involving PMT 2 and a 'delayed response' signal from PMT 1. True beta events will not be recorded in this second circuit, and the chemiluminescence effect can be eliminated. Static electricity in samples, counter and vial materials may also result in photon emissions. In modern counters, this is neutralized by electrical discharge of counter ions to discharge the static.

Background - There are several sources of background radiation which could affect the observed count rate in an LSC. The detector is protected from external environmental radiation by several centimetres of lead shielding, whereas that introduced by cosmic rays is excluded by an anti-coincidence guard, coincidence counting or pulse shape analysis. Background counts from radioactivity in the counter, vial or scintillation cocktail materials is minimised by choice of low activity materials for these components, and background from chemiluminescence and photoluminescence in the sample are eliminated as outlined above. Electrical noise introduces mostly low energy background, and is kept to a minimum by maintaining stable temperature, humidity and electricity supply. Optical cross talk between the left and right PMTs is another source of low energy background. Imperfect vacuum in a PMT means that ionisation occurring within one tube may be recorded as a count in the opposing tube, if there is no barrier between them. This can be reduced by masking the area of the PMT that is not exposed to the sample (Gupta and Polach 1985). Electrostatic discharge from sample, vial, and detector materials may also produce low energy photons, and is controlled as outlined above.

Scintillation cocktail - This is the term given to the combination of organic solvent and the solute or organic scintillator. Benzene (C_6H_6), synthesised from the sample carbon, is almost exclusively used as the solvent in modern liquid scintillation practice for ^{14}C analysis (Polach, 1987). Synthesis of benzene directly from sample material enables quantitative transfer of carbon from sample to solvent. Benzene is used in preference to other organic solvents because of its excellent energy transfer properties, capability to dissolve scintillators, and resistance to quenching. In addition, benzene has a high carbon content, thus reducing the volume of liquid required for high accuracy counting, and is

easily synthesised in high purity form from sample carbon. The scintillation solute should have a high solubility in the chosen solvent, a high conversion of energy to light pulses, be available in pure form free of radionuclides, be resistant to quenching, and have long term stability. Polach *et al.* (1983) tested a range of scintillants in benzene and concluded that butyl-PDB, at a concentration of 15 g l⁻¹ of benzene, was the most efficient scintillator for low level ¹⁴C analysis using Wallac Quantulus counters. Secondary fluors may also improve efficiency by modification of pulse shape or suppression of afterpulses. This is important in counters with low level counting options which differentiate between sample and background counts on the basis of pulse shape (Anderson and Cook 1991). Different combinations of cocktail may therefore be required for different types of counter.

Vials - The shape and material from which vials are constructed are important in maximising transmission efficiency of photons. For practical and economical reasons, commercially available cylindrical vials are most frequently used, although square or spherical vials theoretically have a higher probability of photon detection (Gupta and Polach 1985). Optimal vial materials should have low natural radionuclide content, high photon transmission efficiency, and uniform dimensions within a batch to reduce variations in counting efficiency. Borosilicate glass vials with low ⁴⁰K and ²²⁶Ra content are low background, non-reactive, inexpensive, and can be manufactured with consistent dimensions. Quartz glass vials are free of radionuclides, but more expensive and thus more problematic to obtain a batch of uniform size. Plastic vials are cheap and have low background and standard geometry, but due to problems with water absorption or interaction with scintillation cocktails, most plastics are unsuitable and only Teflon is routinely used in ¹⁴C analysis.

2.2.2.2 Atom Counting Methods

In the AMS method, radiocarbon concentrations are determined by measuring the ratio of ^{14}C to ^{13}C atoms in a sample. Conventional mass spectrometry is unsuitable for radiocarbon analysis because of a high background from other mass-14 atoms or molecules, such as ^{14}N , $^{12}\text{CH}_2$ and ^{13}CH , which are also present in the sample or are created in the mass spectrometer. However, in 1977, it was demonstrated that these interferences could be eliminated by the use of a particle accelerator (Nelson *et al.* 1977; Bennet *et al.* 1977).

A schematic diagram of the University of Arizona AMS facility, which was installed in 1981, is shown in Fig. 2.2 (Donahue 1990). Samples are prepared as graphite targets of a fixed geometry and loaded onto a wheel for automatic sample processing. The wheel is then inserted into an ion source. Most AMS facilities use a Cs sputter source, in which a beam of Cs^+ ions is fired at the graphite target, ‘sputtering’ negative ions from the target surface. The Cs source is efficient in terms of ionising carbon, and has a low memory of previous samples.

The negative ions from the target are accelerated to 25 keV, and the mass-14 ions are focussed into the high voltage terminal of the accelerator. The ions are accelerated to 2 MeV into a stripper tube containing argon gas. When the negative ions collide with the gas, they lose electrons and are discharged from the stripper with a positive charge, and are accelerated to ground potential. An electrostatic deflector at the end of the accelerator allows only the ions with a charge of 3^+ and an energy of 8 MeV to pass through. The hydrocarbon molecules are unstable and are eliminated at this stage. Two magnets placed

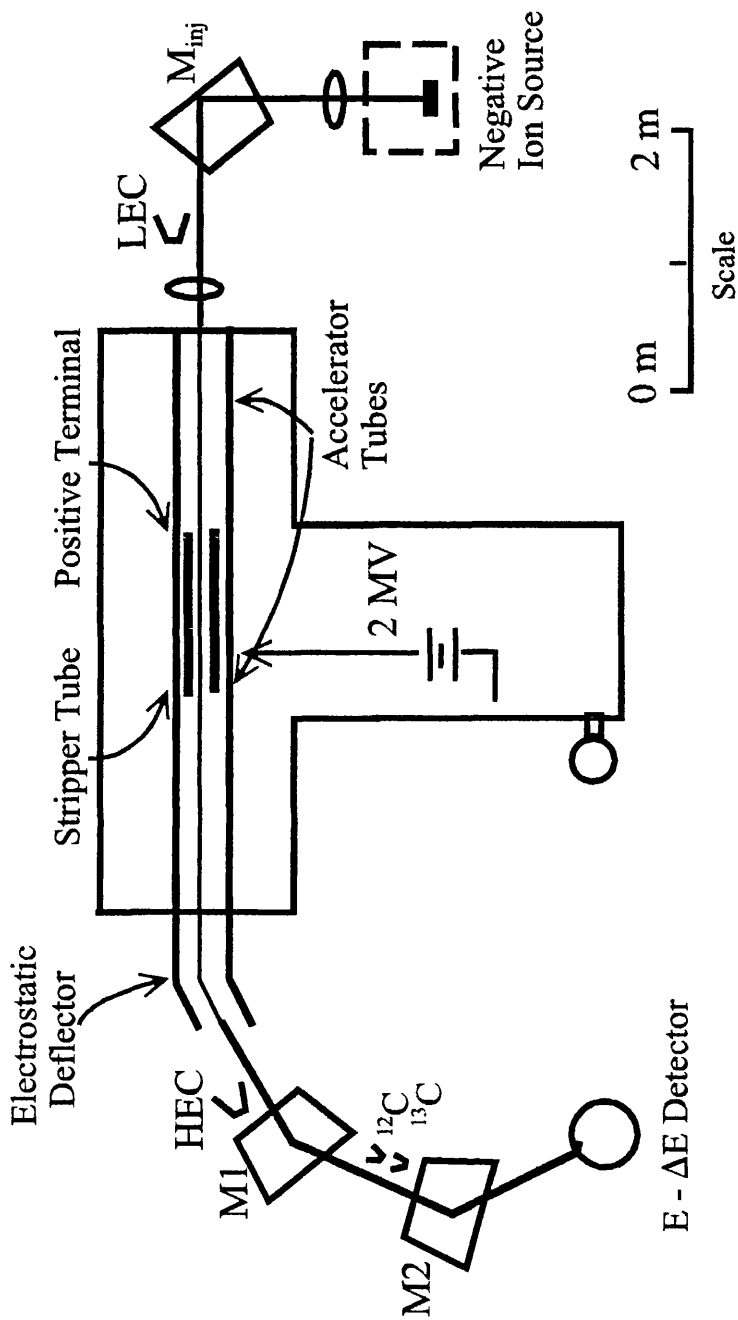


Fig. 2.2: Schematic diagram of the University of Arizona AMS (Donahue 1990). M_{inj} = injection magnet; *LEC*, *HEC* = low- and high-energy Faraday cups; ^{12}C , ^{13}C = fixed Faraday cups for collection of stable carbon isotopes; *M1* and *M2* = analysing magnets.

before the detector are set to pass ions with a known value for $M \cdot E/q^2$, where M is mass, E is energy and q is charge. The mass of any stable C or N atoms reaching the detector can be identified by the channel number at which they appear on a detector spectrum. Once sufficient ^{14}C counts have been recorded to provide a statistically acceptable value, the potential in the injection magnet is raised to +2 keV. The change in energy allows ions of mass 13 rather than mass 14 to pass through the injection magnet, and these are collected in the Faraday cup. Thus, the measurement of ^{13}C enables determination of the $^{14}\text{C}/^{13}\text{C}$ ratio and an age calculation. The ^{14}C analysis runs for 50 seconds and the ^{13}C for five seconds, and both measurements are repeated eight times to yield a statistical precision of 0.5 %.

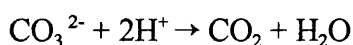
2.2.2 ^{14}C analysis by liquid scintillation counting - method

2.2.2.1 Sample preparation

Initial ^{14}C age-depth profiles were determined using 20-60 g of sediment from sub cores A(i), B(i) and C(ii). Sections of 0.5-2.0 cm thickness were required, depending on the CaCO_3 content and the anticipated age of the sample. The sediment was extruded using the SOC precision extruder, dried at 90 °C and ground to a homogeneous powder in a TEMA mill.

2.2.2.2 Synthesis of benzene from sediment carbonate for LSC analysis

CO_2 is readily generated from inorganic carbonate in sediment by acid hydrolysis using 4 M HCl, the reaction being:



The dry sample is placed in the reaction vessel shown in Fig. 2.3 and the lid replaced. An

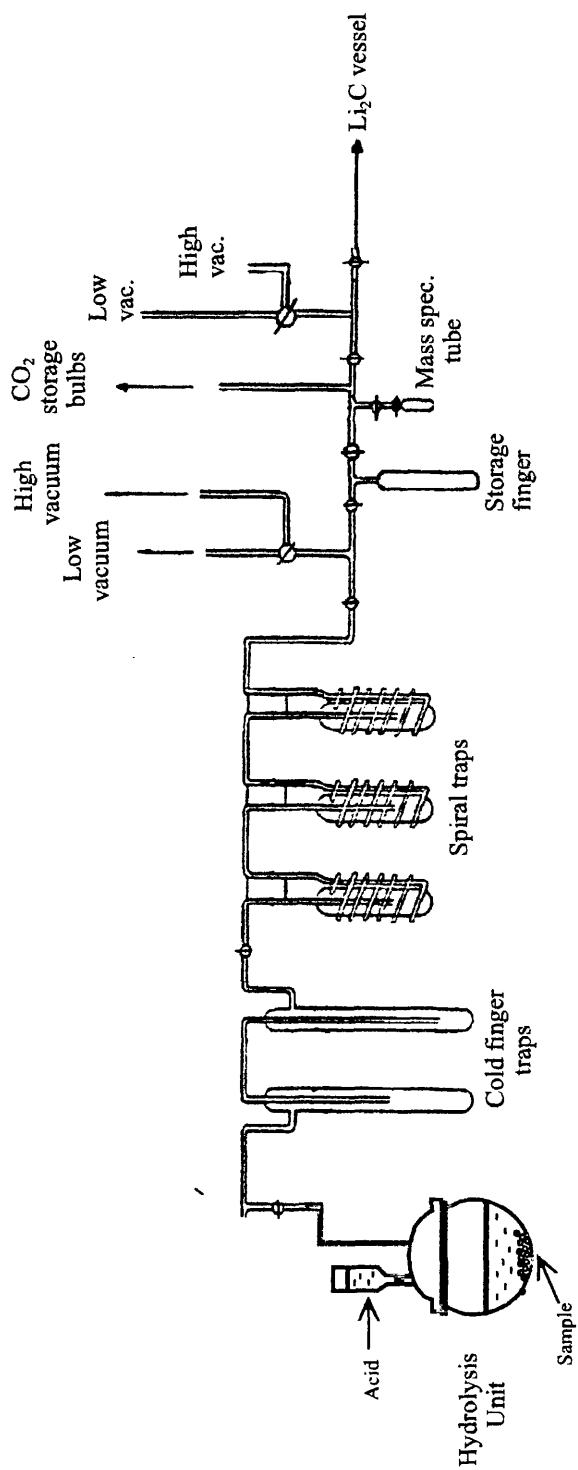


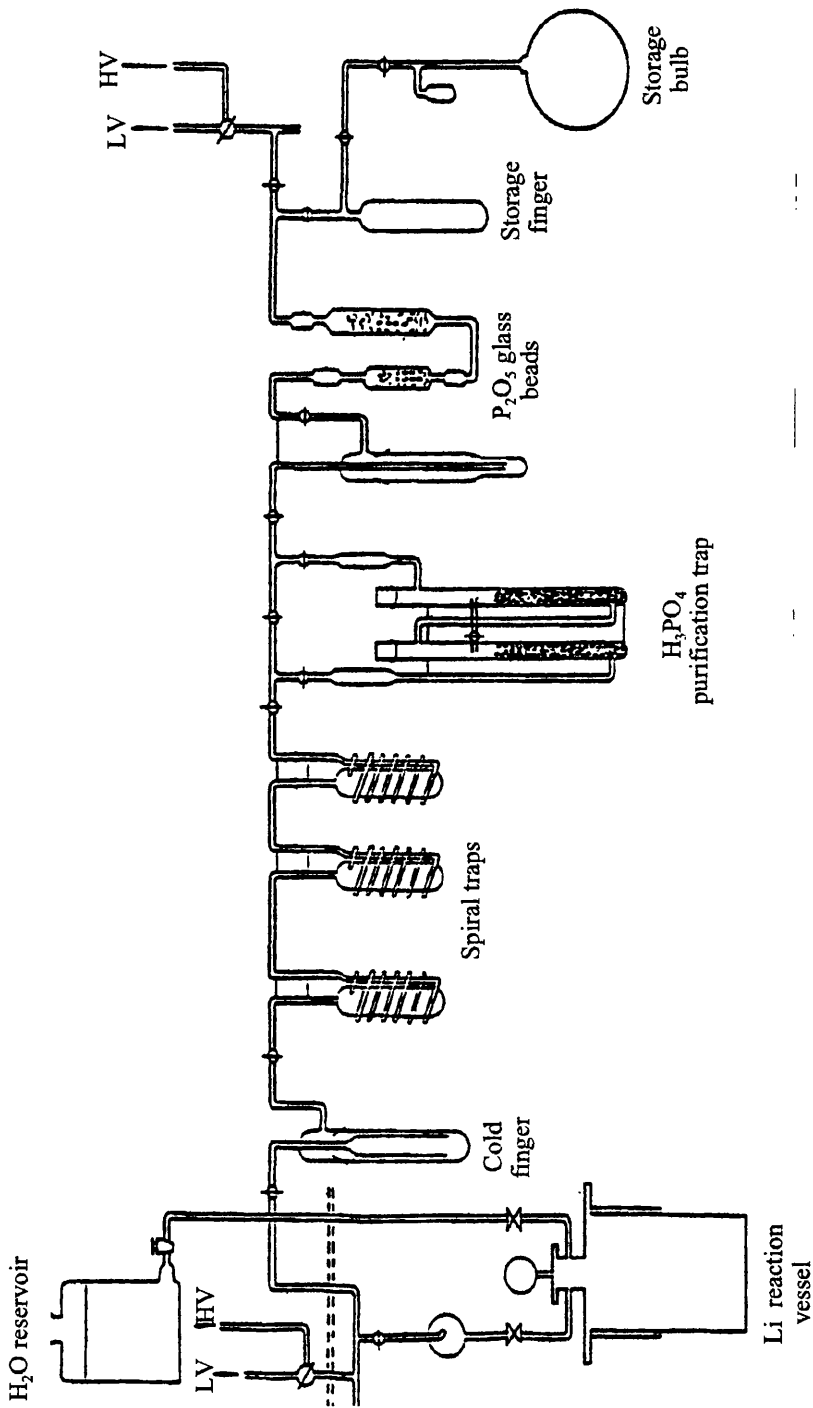
Fig. 2.3: Vacuum system for CO₂ production from inorganic carbonates - radiometric analysis

airtight seal between the vessel and lid is obtained by smearing a small quantity of silicon grease around the ground glass seal. The vessel is connected via two ports to the vacuum line and a reservoir of acid. The reaction vessel is evacuated by briefly opening the tap to the low vacuum manifold.

'Slush traps' consisting of a mixture of methanol and solid CO_2 in a glass Dewar flask are placed around the two finger traps to freeze down any water vapour from the hydrolysis. The three spiral traps are surrounded by Dewar flasks containing liquid nitrogen to trap CO_2 from the reaction by freezing. Any other gases evolved are pumped away by the low vacuum pump.

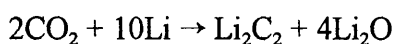
A small quantity of 4 M HCl is added gradually to the sample. Once a pressure has built up in the reaction vessel, the tap connecting the vessel to the vacuum line is opened briefly to allow CO_2 to pass into the vacuum line and freeze down in the spiral traps. Acid is added until all the carbonate has reacted. The tap to the high vacuum manifold is opened, allowing gaseous impurities to be pumped away whilst the CO_2 remains frozen. The CO_2 is then transferred to a storage finger by removing the liquid N_2 from the spiral traps and placing a Dewar flask of liquid N_2 around the storage finger. The sample is then again pumped using the high vacuum. The CO_2 is allowed to expand into one or more 5 l storage bulbs, and the volume of CO_2 generated is calculated using the pressure reading from the mercury manometer.

In the second stage of benzene preparation, the CO_2 is converted to lithium carbide. An excess of Li (approx. 2.5 g Li is used for every litre of CO_2) is placed in the reaction vessel



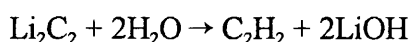
ig 2.4: Vacuum system for Li_2C_2 production and ethyne production - radiometric analysis. HV = high vacuum; LV = low vacuum.

(Fig. 2.4), which is evacuated using low vacuum. The Li is melted by heating to 900 °C, and evacuation of the vessel is continued using high vacuum, to $<10^{-1}$ mbar. A sub sample of CO₂ is taken for stable isotope analysis, then CO₂ is slowly allowed into the Li reaction vessel. The reaction is as follows:



Once all the CO₂ has been transferred into the vessel, it is shut off from the vacuum line and heating of the vessel is continued for 45 minutes to ensure complete reaction. The vessel is then left to cool.

The lithium carbide thus generated is used to synthesise ethyne (acetylene) by means of a hydrolysis reaction:



Collection and purification of ethyne is carried out using a second vacuum system (Fig. 2.4) On the vacuum line, the first finger is surrounded by a solid CO₂ - methanol slush trap to collect water vapour, and the spiral traps surrounded by liquid N₂ to collect the ethyne. While in use, this system is continuously pumped by the low vacuum pump to remove hydrogen gas generated by the reaction with excess lithium. A 2.5 l reservoir of water is connected to the reaction vessel and a small amount of water is added. As pressure builds up, the tap connecting the vessel to the collection system is opened to allow ethyne to transfer to the vacuum line. Water is added incrementally until all lithium carbide has reacted.

The ethyne is purified by passing the gas through an orthophosphoric acid trap to remove impurities. Any remaining moisture is removed by a slush trap and a further trap

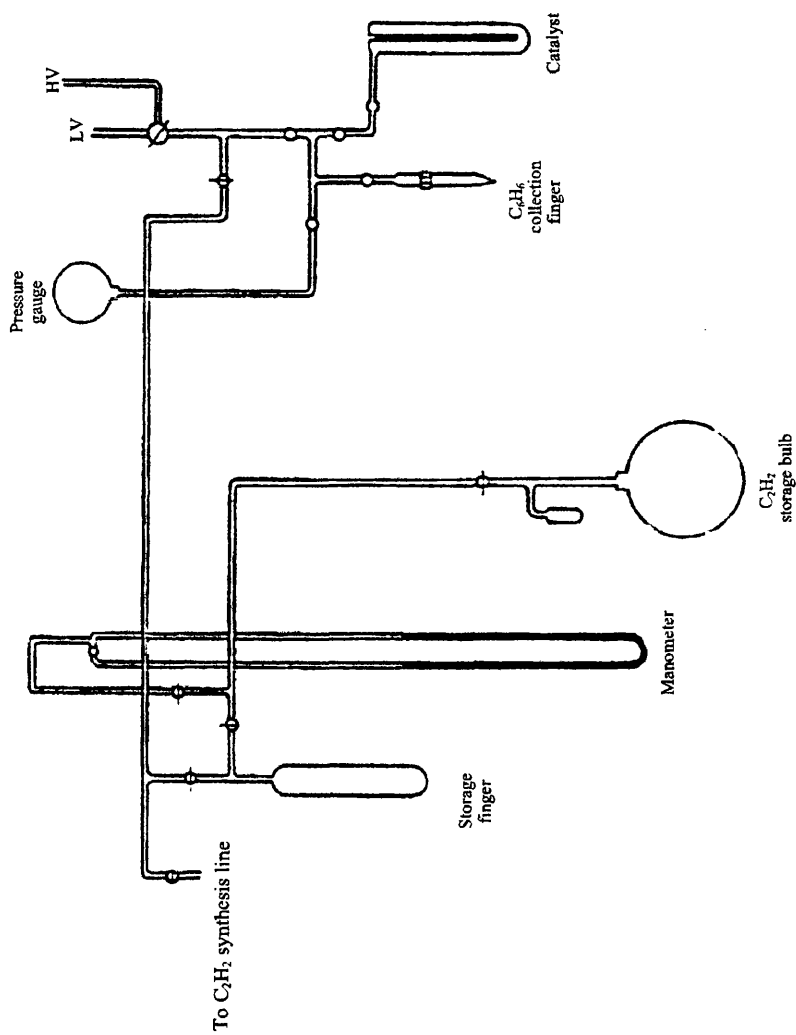


Fig. 2.5: Vacuum line for benzene synthesis - radiometric analysis. HV = high vacuum; LV = low vacuum.

containing phosphorus pentoxide-coated glass beads. The purified acetylene is frozen into a storage finger and purified using high vacuum before being stored in 5 l storage bulbs.

Finally, benzene is synthesised on another vacuum system (Fig. 2.5) by trimerization of ethyne on a chromium oxide catalyst within the temperature range 120-160 °C.

Maintaining the system within this range is critical, as higher temperatures promote the formation of side chains on the benzene. The catalyst is heated to 350 °C to drive off any moisture, which is removed by pumping on low vacuum; then, as the catalyst cools, it is fully pumped down using high vacuum. When the catalyst reaches 120 °C, ethyne is released from the storage bulbs as far as the manometer and the yield of ethyne from CO₂ calculated. A small amount of ethyne is then introduced to the catalyst. The pressure in the catalyst falls as benzene is formed, enabling more ethyne to be introduced to the catalyst. The exothermic nature of the reaction means that the temperature rises with each addition, and the final addition should take place at about 150 °C. The catalyst is allowed to cool, whilst benzene, along with any unreacted ethyne in the catalyst, is frozen into the collection finger. Once the catalyst has cooled to 120 °C, the collection finger is thawed to allow any unreacted ethyne back onto the catalyst. This process of ethyne addition and freezing over benzene is repeated until all ethyne has reacted. Once all the benzene has frozen in the collection finger, it is allowed to melt, then the finger is unscrewed from the line and capped. The weight of benzene is recorded and the yield from ethyne calculated.

2.2.2.3 Preparation of benzene for analysis by LSC

Natural decay series radionuclides are ubiquitous in the environment, and thus will be present in both the sample and in chemicals and materials used in the preparation of

sample benzene, e.g. the glass in the vacuum line. One of the NDS radionuclides, ^{222}Rn , decays to ^{218}Po by emission of alpha particles of energy 5.49 MeV, which may act as a potential interference to ^{14}C . The half life of ^{222}Rn is 3.8 days, so a storage time of three weeks is necessary for the ^{222}Rn and its daughters to have decayed to insignificant levels.

After this storage period, the samples are added to scintillation vials in preparation for counting. The quantity of benzene generated from these samples was generally of the order of 1-3 g. In order to maintain constant counting conditions for each sample, 2 g of benzene was counted in 7 ml glass vials with silicon rubber and indium-lined brass caps, designed to minimise weight changes by evaporative loss of benzene or absorption of water from the atmosphere. Where less than 2 g of sample benzene was available, a known quantity of ^{14}C -free benzene was added to make up the volume, and final results were adjusted accordingly.

The fluor mixture providing optimal performance of the scintillation counters is 2-(4-biphenyl)-5-(4-tert-butyl-phenyl)-1,3,4-oxadiazole (or butyl-PDB) and 1,4-bis(2-methylstyryl)-benzene (or bis-MDB), at concentrations of 2.8 mg g⁻¹ benzene and 3.0 mg g⁻¹ benzene (Anderson and Cook 1991; Cook and Anderson 1992). To achieve maximum reproducibility in dispensing the fluors, 2 g aliquots of a bulk scintillation cocktail solution prepared using ^{14}C -free benzene are pipetted into the scintillation vials and freeze-dried, removing the benzene whilst the fluors remain in the vials.

The sample benzene is air purged to remove any residual ethyne and added to the vial by pipette to a weight of 2 g. The vial is capped and the total weight recorded. Sample

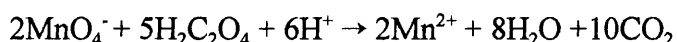
weights are checked on a weekly basis before and during counting to ensure there has been no evaporative loss of benzene.

2.2.2.4 *Liquid Scintillation Counting of Samples*

Samples were counted using a Packard Tri-Carb 2260 XL counter for a minimum of 2000 minutes. In addition to samples synthesised from BENBO sediments, each counting batch contained the following:

Background - Benzene was synthesised from ^{14}C -free marble chips in the same manner as described above for inorganic sediments to determine the effect of background radiation or contamination during sample preparation. Background samples were prepared before and after a series of samples.

Modern Reference Standards - Radiocarbon ages are calculated relative to an international standard (Stuiver and Polach 1977; Mook and Van der Plicht 1999). The standard in current use is a secondary standard produced by the National Institute of Standards and Technology (NIST), Oxalic Acid II SRM-4990C. CO_2 is generated from 28 g of Oxalic Acid II, by the addition of 112 ml of 6M sulphuric acid, followed by addition of an excess of a hot, saturated potassium permanganate solution. The reaction is as follows:



CO_2 collection, ethyne and benzene synthesis are as described previously.

Known Age Samples - Evaluation of results from the worldwide radiocarbon community is achieved by participation in intercomparison exercises (Rosanski *et al.* 1992; Gulliksen

and Scott 1995), enabling a check on the accuracy and precision of radiocarbon dates from a laboratory. Each batch of samples also included benzene synthesized from the TIRI K turbidite utilized in the Third International Radiocarbon Intercomparison (Gulliksen and Scott 1995), which has a consensus age of $18\,155 \pm 34$ conventional radiocarbon years.

¹⁴C and ³H spikes - The high activity spikes are not required for age calculation, but are counted with each sample batch and the activities recorded as a measure of counter stability.

2.2.2.5 Correction factors and age calculations

The effect of quenching on the beta spectrum has been discussed above. The amount of quenching undergone by a sample is assessed by a quench indicating parameter (QIP), in this study, the transformed index of the external standard (tSIE). This is determined by shining a gamma emitting source (e.g. ¹³³Ba) through the sample and measuring the activity, and is carried out automatically by the LSC. The source is moved to a fixed position close to the vial. The gamma photons interact with the vial and its contents, producing Compton electrons, which are subject to the same quenching effect as the beta particles. The Compton spectrum thus produced will reflect the degree of quenching and is subject to mathematical transformation to generate a tSIE value. The tSIE scale ranges from 0-1000, with 1000 being a completely unquenched sample. Calibration of tSIE with counting efficiency under a specific set of counting conditions is carried out by preparing a quench curve. A series of vials are spiked with a known high activity ¹⁴C, scintillation cocktail is added, and incremental amounts of a quenching agent are added (examples are nitromethane and acetone) to produce a range of quenched standards. The quenched

standards are counted and the efficiency for each determined by dividing the count rate from the detector by the known activity. The equation of the best-fit line through the plot of efficiency against tSIE is obtained and used to determine the quench correction for unknown activity samples.

Isotopic fractionation during biological or physical processes (e.g. photosynthesis, gas exchange) may result in disequilibrium the environment and ^{14}C dateable materials. A correction factor must be introduced to compensate for fractionation in materials relative to the primary dating standard of 1890 wood. For radiometric ^{14}C analysis, this is achieved by measuring the carbon isotopic composition of a subsample of CO_2 by mass spectrometry. The ratio is reported as a $\delta^{13}\text{C}$ value, relative to the $^{13}\text{C}:^{12}\text{C}$ ratio for a belemnite fossil from the Cretaceous Peedee formation (PDB):

$$\delta^{13}\text{C} = \left[\frac{\left(\frac{^{13}\text{C}}{^{12}\text{C}} \right)_{\text{sample}}}{\left(\frac{^{13}\text{C}}{^{12}\text{C}} \right)_{\text{PDB}}} - 1 \right] \cdot 1000 \quad (2.1)$$

The ^{14}C fractionation factor (FF) is used to correct for deviations from the 1890 wood $\delta^{13}\text{C}$ of -25‰, assuming the fractionation of ^{14}C is twice that of ^{13}C :

$$FF = \left[\frac{1 + \frac{-25}{1000}}{1 + \frac{\delta^{13}\text{C}_{\text{sample}}}{1000}} \right]^2 \quad (2.2)$$

The correction factors FF and QF are required for both the sample and the modern standard. In order to calculate the sample age, the count rate (cpm) and weight (g) of

benzene for both the sample and modern, and a background count rate are also required for age calculation.

Net sample activity (A_s) is derived by subtracting the background count rate (B) from the gross sample count rate (A_G), and dividing by sample weight (W_s) to give counts per minute per gram. Activity is then corrected for sample quenching by multiplying by the quench factor (QF):

$$A_s = \frac{A_g - B}{W_s} \cdot QF \quad (2.3)$$

The activity is normalised for fractionation by multiplying by the fractionation factor (FF):

$$A_{SN} = A_s \cdot FF \quad (2.4)$$

Normalised net modern activity, A_{ON} , is also derived by correcting for quench and fractionation as above and a factor of 0.7459 to account for difference in ^{14}C activity between the oxalic acid standard and the 'modern' value of the 1890 wood activity corrected to its hypothetical value in 1950. The conventional radiocarbon age of the sample, in years before present, is then calculated from:

$$t = (1 / \lambda) \cdot \ln(A_{SN} / A_{ON}) \quad (2.5)$$

where $\lambda = \ln 2 / 5568$ (the Libby half life of ^{14}C)

2.2.3 Radiocarbon dating by Accelerator Mass Spectrometry - method

2.2.3.1 Sample preparation

The samples analysed by AMS were size-fractionated, hand-picked, polyspecific

foraminifera, and associated fine fraction material from 1 cm increments from sub cores A(iii), B(iv) and C(vi). The depth increments from which the samples were collected were chosen on the basis of the bulk carbonate ^{14}C age profiles obtained by LSC. Samples of $>150\ \mu\text{m}$ hand-picked polyspecific foraminifera from the BOFS cores utilised in Thomson *et al.* (1995) were also analysed.

Approximately a quarter of the wet sediment was weighed and dried at a temperature of 50-60 °C, to ensure that the foram tests did not break through expansion and contraction caused by temperature changes. The dried sediment was re-weighed, disaggregated in 200 ml reverse osmosis water, and stirred gently using a magnetic stirrer for 30 minutes to break up clay aggregates and wash matrix material from within the foram tests. The wet sediment was washed through a series of Endecott 7" diameter brass sieves of mesh sizes 250 μm , 150 μm and 63 μm , with the $< 63\ \mu\text{m}$ fraction and excess water collected in a 1500 ml beaker. The sediment was then washed with a further 500 ml of reverse osmosis water. A peristaltic pump transferred this water back to the top sieve to wash the sediment through until all material smaller than the sieve diameter had passed through. Samples were then dried at 50 °C. The $<63\ \mu\text{m}$ fraction was collected by filtration through a 47 mm diameter GFF filter paper, dried and then ground to a homogenous powder. The best preserved planktonic forams were then picked out from the larger size fractions using fine tweezers. Each analysis required 10-15 mg of forams (approximately 1000 specimens for the 150-250 μm fraction), which were stored in 2 ml glass vials until required.

2.2.3.2 *Synthesis of graphite for AMS analysis*

CO_2 is generated from inorganic carbonate by acid hydrolysis using 6 M H_3PO_4 . Two types

of reaction vessel were used; one for foraminiferal samples, usually 10-20 mg sample size, and one for $<63 \mu\text{m}$ size fraction samples, where 80 mg of sediment was hydrolysed. The small sample vessel consists of a single glass finger with a rubber septum, through which acid may be injected. The large sample vessel has two connected glass fingers, the larger of which is used to contain the sample and the smaller, angled finger used to hold acid prior to hydrolysis, which is effected by tipping the vessel so the acid runs into the sample finger.

The foram sample was added to the lower tube of the reaction vessel and weighed before connecting to the rest of the reaction vessel and micro-rig (Fig. 2.6). The vessel was evacuated, then closed off from the vacuum line, and 1 ml of acid was added by injection with a syringe through the rubber septum. For the larger samples, an 80 mg sub sample was placed in the first finger of the reaction vessel. 9 ml of 6 M H_3PO_4 was placed in the side finger using a long plastic pipette. The reaction vessel was connected to the micro-rig and evacuated. The tap to the vacuum line was then closed and the reaction vessel removed from the line so that the acid could be poured into the main finger from the side chamber before replacing the vessel on the line and evacuating the small part of the line left open to atmosphere by this process.

A Dewar flask containing solid CO_2 -methanol slush was placed around the first spiral trap and a second Dewar flask containing liquid N_2 placed around the second trap. Once the hydrolysis reaction was complete, the CO_2 was allowed to pass through and freeze down in the liquid N_2 trap. The frozen CO_2 was pumped briefly on high vacuum to remove impurities. The CO_2 was then transferred to the storage finger and allowed to sublime so

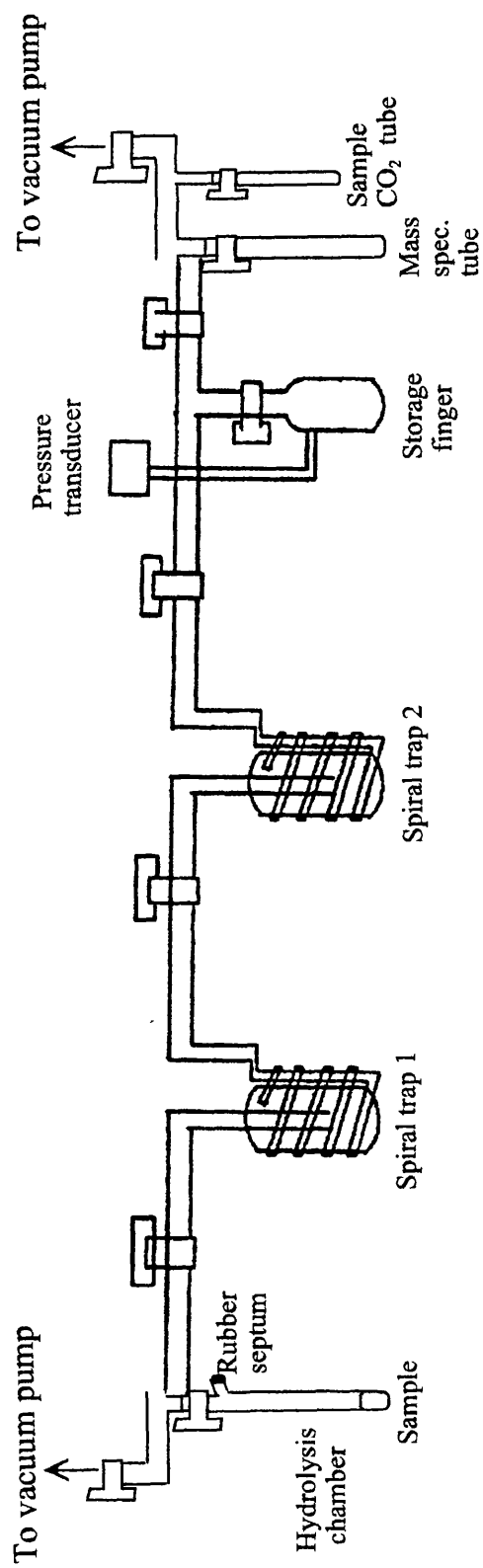


Fig. 2.6. Vacuum system for production of CO_2 from inorganic carbonate - AMS analysis. The system is shown with the reaction vessel for small samples attached.

the volume of CO₂ could be calculated from the gas pressure.

A small Dewar flask containing liquid N₂ was placed around the tube at the end of the line and the micro rig closed off from the vacuum pump at the final tap. Sufficient CO₂ to make a 1-2 mg graphite target was frozen down in the sample collection tube. The remaining CO₂ was then frozen down in the second tube for stable isotope analysis by mass spectrometry.

The CO₂ from the hydrolysis reaction was then used to prepare graphite for AMS analysis. Graphite is prepared using heated zinc and iron powder on a micro-rig system (Fig. 2.7). The procedure is based on the method of Slota *et al.* (1987), in which the zinc reduces the CO₂ to CO, while Fe-catalysed decomposition of CO leads to formation of pure C as graphite.

The amount of iron powder required for a ratio of 2:1 with carbon is calculated and weighed out into a closed-end precombusted quartz tube and an excess (50 mg) of zinc powder weighed out into another tube. These are then fitted onto the graphite preparation apparatus, along with the tube containing the sample CO₂. The Fe- and Zn-containing tubes are then evacuated. The furnace for the Fe-tube is preheated to 550 °C, and the furnace for the Zn-tube is heated to 450 °C. Both furnaces are positioned around the tubes for 30 minutes, after which the furnaces are removed and the tubes allowed to cool to room temperature. A liquid N₂-filled Dewar flask is placed around the Fe-containing tube and the tap to the sample CO₂ is opened, allowing the CO₂ to freeze down in the tube. The tube is closed off from the vacuum line and the Dewar flask is removed and the gas allowed to sublime in the Fe tube. The Zn furnace is replaced over the Zn-containing tube and heated for one hour, then the furnace is replaced over the Fe-containing tube until the

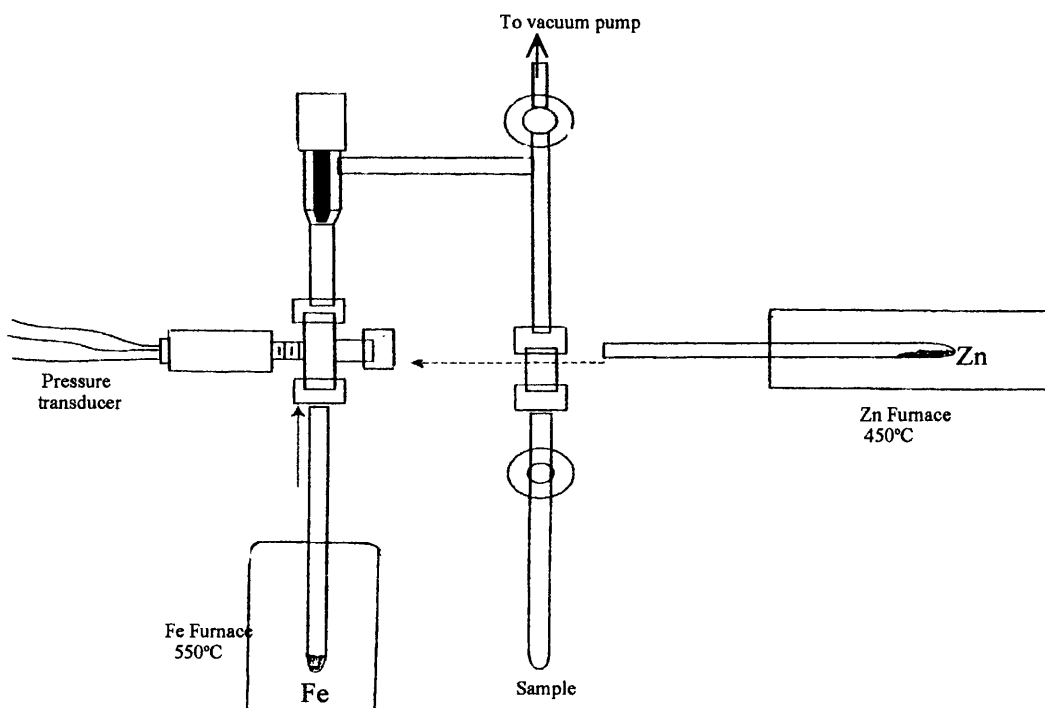


Fig 2.7: Vacuum system for preparation of graphite from CO_2 - AMS analysis

graphitisation reaction is complete. The yield of graphite is calculated by the reduction in gas pressure in the tube. The graphite is weighed and stored in a 2 ml glass vial to be sent for analysis at the University of Arizona AMS facility.

As with radiometric methods, known age standards and infinite age marble standards were prepared with a batch of samples. Some samples were also analysed by both LSC and by AMS to assess whether there were any systematic differences between results obtained using the different methods. The results, given in Table 2.1, show there is no systematic bias in the results from the two methods of analysis.

2.2.3.3 *Pretreatment of small AMS samples*

The small size of foraminifera creates an inherent problem in any attempt to clean or pretreat these samples before ^{14}C analysis. In order to compare this study directly with the preceding work by Thomson *et al.* (1995), it was decided that no pretreatment should be attempted for the majority of samples. However, the work of Schleicher *et al.* (1998) demonstrated that pretreatment could remove surficial contamination and fine carbonate trapped within the foram tests, significantly altering the ^{14}C age determined for a background sample of Eemian (>100 ky) foraminifera. Two samples from this study were given a simple acid wash pretreatment to assess whether *in situ* contamination might be of importance and if development of a pretreatment method is necessary for Holocene-age inorganic carbonates.

The samples chosen for pretreatment were > 150 μm mixed planktonic forams from BOFS core 11881 0-1 cm and 26-27 cm depth increments, for which bulk carbonate and foram

Sample	LSC sample I.D.	Age $\pm 1\sigma$	AMS sample I.D.	Age $\pm 1\sigma$
B(iv) 0-1 cm	GU-8258	2180 \pm 50	GU-8265	2120 \pm 50
B(iv) 29-30 cm	GU-8260	5100 \pm 70	GU-8267	5120 \pm 60
C(vi) 0-1 cm	GU-8261	2860 \pm 50	GU-8268	2940 \pm 50
C(vi) 30-31 cm	GU-8264	5620 \pm 90	GU-8271	5180 \pm 50

Table 2.1 Comparison of the radiocarbon ages of four samples dated by both liquid scintillation and AMS methods. Ages are in conventional radiocarbon years BP.

^{14}C ages had already been characterised (Thomson *et al.* 1995). Approximately 50 mg of well-preserved planktonic forams were collected, and the sample was split so that 12 mg could be measured without pretreatment and the remainder used for the pretreatment experiment. The pretreatment chosen was a dilute acid wash to remove the outer 20% of sample carbonate, as is commonly used for larger inorganic carbonates (Gupta and Polach 1985). HCl was chosen for the acid wash rather than H_3PO_4 as the latter is hygroscopic, making it difficult to prepare and keep a solution of known molarity.

40 mg of forams were weighed out into the reaction vessel tube and a small amount of RO water added, ensuring the acid would spread throughout the sample. The system was connected to the vacuum line and evacuated. The vessel was closed off from the vacuum and removed from the line. 1 ml of 0.16 M HCl was injected into the vessel to remove the outer 20% carbonate and the vessel shaken gently to distribute the acid throughout. The vessel was reconnected to the line and the region of the line which had been open to the

atmosphere was evacuated before the CO₂ generated by the acid hydrolysis reaction was collected. Once the gas evolved from pretreatment was collected, 0.5 ml of 9 M HCl was added to complete the hydrolysis reaction. The CO₂ gas was collected as before. Graphite was prepared from both CO₂ fractions.

2.2.3.4 Age calculations

Age calculations from AMS ¹⁴C:¹³C ratios can be derived from a modified version of the equation used for radiometric analysis (Donahue *et al.* 1990). The normalised specific activity of a sample is proportional to the atomic ratio of ¹⁴C:C_{total}, corrected for fractionation and normalised to δ¹³C = -25 of the standard 1890 wood, as is required for radiometric analysis. This correction is:

$$\left({}^{14}\text{C}/{}^{13}\text{C} \right)_{\text{SN}} = \left({}^{14}\text{C}/{}^{13}\text{C} \right)_{\text{s}} \cdot \left[\frac{1 + (-25 / 1000)}{1 - (\delta^{13}\text{C}_s / 1000)} \right] \quad (2.6)$$

where (¹⁴C/¹³C)_{SN} is the ¹⁴C to ¹³C ratio of the sample corrected for isotopic fractionation relative to the atmospheric δ¹³C value of -25‰, (¹⁴C/¹³C)_s is the measured ¹⁴C to ¹³C ratio of the sample, and δ¹³C_s is the stable isotope ratio (¹³C to ¹²C) of the sample.

The ¹⁴C/¹³C ratio of the modern standard is corrected back to the hypothetical 1950 activity of the 1890 wood standard with δ¹³C = -25‰ using the formula:

$$\left({}^{14}\text{C}/{}^{13}\text{C} \right)_{\text{ON}} = 0.7404 \cdot \left({}^{14}\text{C}/{}^{13}\text{C} \right)_{\text{OX}} \quad (2.7)$$

where (¹⁴C/¹³C)_{ON} is the modern standard corrected for fractionation and (¹⁴C/¹³C)_{OX} is the measured value for the oxalic standard. The value 0.7404, therefore is the decay correction of the oxalic standard back to 1950 (0.7459) corrected for isotopic fractionation

as shown for the sample in equation (2.6). Fraction modern, F , is then calculated from:

$$F = \frac{\left({}^{14}\text{C} / {}^{13}\text{C} \right)_{\text{SN}}}{\left({}^{14}\text{C} / {}^{13}\text{C} \right)_{\text{ON}}} \quad (2.8)$$

Finally, radiocarbon age, t , is determined using:

$$t = (1 / \lambda) \cdot \ln F \quad (2.9)$$

2.3 Gamma Spectrometry

Gamma spectrometry was used in this study to determine ^{137}Cs , ^{241}Am , and $^{210}\text{Pb}_{\text{excess}}$ activities in the sediments. This method enables simultaneous analysis of the three nuclides, requires little in the way of sample preparation, and is more rapid than other techniques, which require time-consuming sediment digestion and radiochemical separation (e.g. Smith and Hamilton 1984; Graham 1993). Gamma spectrometry is non-destructive, allowing subsequent analyses to be carried out on the same sample. Another advantage with respect to $^{210}\text{Pb}_{\text{excess}}$ analysis is that the supported ^{210}Pb activity can also be measured simultaneously rather than estimated, as is often the case with the alpha-spectrometry method of determining ^{210}Pb activity from its alpha-emitting daughter, ^{210}Po . Since ^{226}Ra , which precedes ^{210}Pb in the ^{238}U decay chain, may be mobile in marine sediments, this may be important in calculating inventories, or modelling sedimentation or bioturbation rates. The main disadvantage is the lack of sensitivity of this technique relative to the alpha-spectrometric method; the low ionisation of gamma photons and hence low probability of interaction with detector materials, together with the sample-detector geometry means only a few percent will be detected and long counting times may be required for low activity samples.

2.3.1 Gamma decay and interaction with matter

Gamma radiation is the result of excess energy released by the rearrangement of the nuclear particles within the daughter radionuclide following radioactive decay. This occurs when radioactive decay produces a nuclide that is not in its lowest possible energy state. The gamma energy is emitted as photons of high-energy electromagnetic radiation. Each daughter radionuclide emits gamma radiation at one or more distinctive energies, from which it may be identified.

Gamma photons have a low probability of interaction with surrounding matter (once every 10^6 atoms) and may travel large distances before the energy is absorbed. Interaction is mainly with electrons, and takes one of the following forms:

Photoelectric effect - the incoming photon transfers all of its energy to a K- or L-shell electron, which is ejected from the atom as a photoelectron. The vacancy left by the ejected electron is filled by an electron from a higher orbital, resulting in a 'cascade' of electrons and the emission of x-rays. The energy of the emitted photoelectron (E_{e^-}) is the difference between the energy of the gamma radiation (E_γ) and the binding energy of the electron in the atom; i.e. (E_{binding}); i.e. $E_\gamma = E_{e^-} + E_{\text{binding}}$.

Compton scattering - an outer shell electron is ejected from the atom by interaction with a photon. The binding energy of an outer electron is much lower than for an inner electron, and the gamma photon also travels onwards, but with a lower energy and in a different direction. In this case, $E_\gamma = E_{e^-} + E_{\gamma'} + E_{\text{binding}}$, where $E_{\gamma'}$ is the energy of the deflected gamma photon. The maximum energy transfer to the electron occurs when the gamma

photon is deflected through an angle of 180° .

Pair production - the spontaneous production of an electron - positron pair by high energy (>1.022 MeV) gamma radiation passing close to a nucleus. The energy of the gamma photon is completely absorbed by the neutron.

These different interaction types result in the following features in the energy spectrum of gamma-emitting radionuclides:

Photopeak - the signal derived from photoelectric interaction of a gamma photon with a K-shell electron in the semiconductor. This generates the identifying energy peak from which the activity of the radionuclide is calculated.

Compton edge - the upper energy limit of electrons excited by Compton interaction with the semiconductor.

Compton continuum - caused by the excitation of electrons which have absorbed only part of the energy of the gamma radiation, and are thus represented at energies lower than the Compton edge in the spectrum.

Annihilation peak - occurs where a positron combines with an electron in the absorbing material, resulting in production of two photons, each with energy 0.511 MeV.

2.3.2 Gamma detection by semiconductor detectors

The electrons of a semiconductor material can occupy one of two bands; the valence band or the conduction band. In the valence band, electrons are bound to specific atoms and are not mobile, whilst in the conduction band electrons are not associated with a specific atom and may move freely. The distribution of electrons between the two bands is dependent on the crystal temperature and the energy gap between the conduction and valence bands.

Semiconductor crystals contain impurities which substitute for semiconductor atoms in the crystal lattice. If the dominant impurity has more valence electrons than the semiconductor, it is an electron donor and the weakly bound valence electrons from the impurity require only a small amount of energy to transfer into the conduction band of the semiconductor. This is known as an n-type semiconductor, as charge is transferred through the crystal by electrons. Conversely, if the impurity has fewer valence electrons than the semiconductor, it is an electron acceptor, and electrons from the semiconductor valence band can transfer into it. This creates positively charged 'holes' in the valence band to carry the charge through the crystal and the semiconductor is p-type.

Semiconductor diodes are constructed by fusing n-type and p-type semiconductor material, which has the effect of creating a central intrinsic (*i*) region with extremely low concentrations of charge carriers and which exhibits semiconductor characteristics.

Gamma photon detectors are based on semiconductor diodes having a p-*i*-n structure in which the intrinsic region is sensitive to ionising radiation. Under reverse bias, an electric field extends across the intrinsic region. Cooling the crystal with liquid nitrogen causes the electrons to remain in the valence band and no current will flow, even with a high voltage across the crystal. However, the interaction of photons with electrons in the *i*-region of a

semiconductor imparts sufficient energy to the electrons to enable them to overcome the relatively small (0.75 eV for germanium) energy gap between the bands in the semiconductor, producing charge carriers. These are swept to the p and n electrodes, producing a current proportional to the energy deposited in the crystal by the initial radiation. This signal is converted to a voltage pulse by a charge-sensitive pre-amplifier, then the voltage pulse is shaped and the gain increased further by an amplifier. The voltage pulse is transformed into a digital signal by an analogue-to-digital converter and transmitted to a multi-channel analyser, where each digital signal is stored in one of many (typically around 4000) energy channels (Choppin *et al.* 1995).

The high energy of gamma radiation means that background counts from environmental radiation can significantly affect the count rate. To minimise this effect, a lead shield of approximately 10 cm thickness surrounds the detector to attenuate external radiation. X-rays from gamma excitation of the lead shield are absorbed by a cadmium lining within the detector, whilst the X-rays generated by gamma excitation of the cadmium shield are in turn absorbed by an inner copper lining.

Fig.2.8 shows a schematic diagram of a high-purity germanium (HPGe) semiconductor detector for gamma spectrometry. The high density and Z value of Ge result in a large number of interactions between the gamma radiation and detector material and a relatively high detection efficiency for gamma radiation (section 2.3.4). Although less efficient than solid scintillation detectors (e.g. NaI(Tl) detectors), HPGe detectors provide superior resolution of the energy spectrum, with typical full width half-maximum values for the 1332 keV ^{60}Co peak of the order of 2 keV. Germanium semiconductor detectors provide

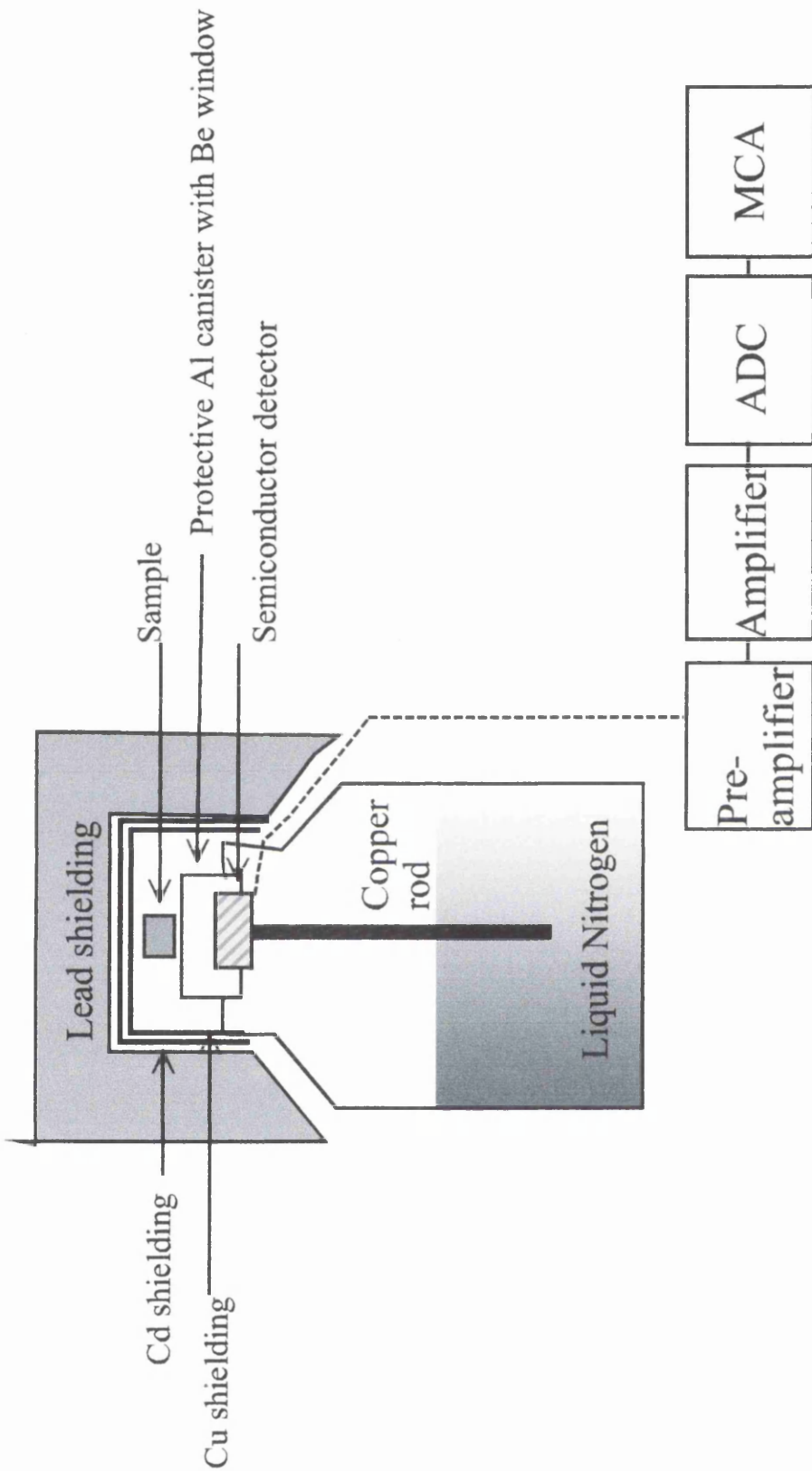


Fig. 2.8: Schematic diagram of a HPGe semiconductor detector for gamma spectroscopy. ADC - analogue-digital converter; MCA-multi-channel analyser

high resolution spectra over a 0.02-2 MeV energy range, enabling ready identification of peaks. The ability to grow large, virtually impurity-free Ge crystals has enabled development of intrinsic semiconductor detectors, which require less maintenance than the older, lithium-drifted detectors.

The size and shape of the semiconductor crystal are important factors when considering the detection efficiency of a semiconductor detector. Crystals may be planar, coaxial or well-shaped. Coaxial detectors are cylinders with a hole drilled in the lower surface, where one of the electrical contacts is located. Planar detectors are much thinner, with the n-contact located on the lower surface and the p-contact on the upper surface. The positive contact is typically ion-implanted boron or a thin gold layer, whilst the negative contact is Li^+ diffused over the n surface of the detector. The difference in crystal thickness means that coaxial detectors will have higher detection efficiency for high-energy gamma photons than planar detectors. In contrast, the thinner planar detectors will detect fewer high-energy photons and have a lower Compton continuum. Planar detectors also have better charge collection characteristics and thus better peak resolution. In planar and coaxial detectors, location of the sample above the semiconductor crystal means most gamma photons from a sample are emitted in directions outwith the angle subtended by the sample at the detector surface, and detection efficiency is relatively low. Higher detection efficiencies are obtained by using well detectors, where the sample sits inside a U-shaped crystal. These are appropriate for small, low activity samples, but have poorer spectral resolution than coaxial and planar detectors.

The crystal is kept under vacuum in an aluminium canister to protect it from dirt and damage. N-type detectors also typically have a thin counting window of beryllium or carbon epoxy resin. These materials are chosen because of their low Z value, which allows all but the lowest energy gamma photons to reach the detector. Ultra-thin Be windows of less than 0.025 mm thickness are available to enable high transmission efficiencies at low photon energies.

2.3.3 Sample preparation for gamma spectrometry

Initial analyses were carried out on sub cores A(i), B(i) and C(ii), and replicate analyses on B(vi) and C(iv), sectioned at 0.5 cm vertical resolution to a depth of 20 cm. The dried sediment was homogenised by grinding in an agate TEMA mill. Fixed diameter (4.7 cm) pellets were made from 20 g sub samples of the homogenised sediment using a hydraulic press at 10 tons pressure for 90 seconds. The pellets were sealed using Araldite glue in airtight plastic petri dishes and set aside for 21 days to allow the activity of ^{222}Rn and its daughter radionuclides to equilibriate with that of its parent, ^{226}Ra .

$^{210}\text{Pb}_{\text{excess}}$ analysis was also carried out on small samples (0.3-2 g) of faecal material from open subsurface burrows, burrow lining material, sediment from the depth adjacent to the burrow, and surface sediment, obtained from BENBO cruises CD111 and CD113. These samples were dried, homogenised and stored in small airtight plastic tubs for counting.

All samples were analysed using low-background planar semiconductor gamma photon detectors with typical counting times of 3-7 days. Counting times varied because the artificial radionuclides, where present, were detected at very low activities, and long

Table 2.2: Radionuclides measured by gamma spectrometry in this study.

Radionuclide	²¹⁰ Pb	²¹⁴ Pb	²¹⁴ Bi	¹³⁷ Cs	²⁴¹ Am
Photopeak Energy, keV	46.5	295.2 and 351.9	609.3	661.6	59.5
Half Life	22.3 y	26.8 min	19.7 min	30.2 y	458 y

counting times were required to reduce the statistical error to an acceptable value. Table 2.2 lists the energies of the radionuclides analysed.

The ²²⁶Ra peak at 185 keV cannot readily be analysed due to interferences from a ²³⁵U peak of similar energy. However, if the radionuclides from ²²⁶Ra onwards are allowed to reach secular equilibrium before counting, ²²⁶Ra can be determined from the activities of the gamma emissions of ²¹⁴Pb at 295.2 keV and 351.9 keV, and ²¹⁴Bi at 609.3 keV, which are not subject to interference from other radionuclides. The mean value of these three peaks is used to estimate the activity of ²²⁶Ra.

2.3.4 Detector calibration and intercomparison studies

The relationship between gamma photon energy and the MCA channel number is linear, and the energy-channel number relationship for each detector is calibrated using a ¹⁵⁵Eu point source. The known energy of the radionuclide corresponds with the peak maximum channel.

Detection efficiency (E), in percent, is defined as:

$$E = \frac{C}{A} \cdot 100 \quad (2.10)$$

where C is observed count rate in counts per second (cps), and A is the known source activity. The photoelectric gamma detection efficiency, E_γ , is also dependent on the intensity of the gamma peak, and is determined by:

$$E_\gamma = \frac{C}{A \cdot I} \cdot 100 \quad (2.11)$$

where I is the gamma intensity. The detection efficiency varies depending on the characteristics of both the sample, (e.g. volume, density, heavy mineral content), and the detector (e.g. crystal thickness). Efficiency losses result from self-absorption or scattering by the sample matrix, absorption of gamma photons by the air space between the detector and the sample, gamma photons passing through the detector crystal with no interaction, and gamma photons emitted outwith the angle subtended by the sample to the detector.

Pellets prepared from 20 g samples of homogenised Aegean Sea sediment spiked with known activities of ^{210}Pb , ^{226}Ra , ^{137}Cs and ^{241}Am standard solutions, and an unspiked pellet, were used to calibrate detection efficiency. The pellets were counted for 24 hours each, and the net count rates attributable to the known-activity spikes were determined by subtracting the count rates of the unspiked pellet from the corresponding count rates of the spiked samples. Total detection efficiency for each radionuclide was calculated by dividing the measured count rate by the known activity of the pellet (equation 2.10).

Table 2.3: Total detection efficiencies (%) for 20 g sediment pellets, counted on SURRC HPGe detectors (LEGe 3 and 4) and co-axial detectors (Tennelec2 and Det 1.2). The errors quoted are 1 σ error reported as a percentage of the detection efficiency. Efficiencies of the small samples of burrow material, counted on an EG&G Lo-AX detector, were determined individually due to the variable weights of the samples.

Gamma Detector				
Radionuclide	LEGe 3	LEGe 4	Tennelec2	Det 1.2
²¹⁰ Pb@ 46.5 keV	0.449 ± 1.39	0.348 ± 1.28	0.665 ± 1.19	0.487 ± 1.54
²¹⁴ Pb@ 295 keV	0.559 ± 2.00	0.352 ± 1.78	1.630 ± 1.47	0.930 ± 1.64
²¹⁴ Pb@352 keV	0.885 ± 1.62	0.52 ± 1.64	2.500 ± 1.43	1.520 ± 1.48
²¹⁴ Bi@609 keV	0.489 ± 1.78	0.278 ± 2.22	1.604 ± 1.46	1.00 ± 1.55
¹³⁷ Cs@662 keV	0.95 ± 0.05	0.650 ± 0.02	4.150 ± 1.05	2.470 ± 1.26
²⁴¹ Am@59.5 keV	3.91 ± 0.005	2.94 ± 0.05	6.940 ± 0.22	4.13 ± 0.62

The Aegean Sea sediment was of similar composition to the BENBO sediments, and a self absorption experiment (Cutshall *et al.* 1983) confirmed that no correction for density or mineral content was necessary. The detection efficiencies for each radionuclide used in the experiment are shown in Table 2.3 above.

Initial data from gamma spectrometry analysis were required relatively quickly, in order to make material available for ¹⁴C analyses, and to judge which samples would be analysed for plutonium. Rapid sample turnaround was achieved by analysing sub cores A(i) and B(ii) at SURRC, whilst sub core C(ii) was simultaneously analysed by S. Nixon at SOC. To ensure comparable results were obtained between laboratories and detectors, a number of 20 g pellets were exchanged between the laboratories and recounted on different

detectors. Table 2.4 lists the activities determined for the exchanged samples. In general, ^{210}Pb and ^{226}Ra values obtained at SURRC are about 10 Bq kg^{-1} higher than those counted at SOC. The values for ^{210}Pb , and consequently $^{210}\text{Pb}_{\text{excess}}$, are within 1σ error, but the difference between ^{226}Ra activities from the two laboratories is larger, sometimes outwith 3σ . One possible reason for this is that different methods were used to calibrate detection efficiency; the method at SURRC, described above uses a standard activity solution of the radionuclide in question mixed with the sediment, whereas the SOC calibration employs a high activity mineral ^{238}U spike (DH-1a, supplied by the Canadian Centre for Mineral and Energy Technology) added to a 20 g pellet of BENBO sediment. It is not clear why this should make a difference, although other factors in determining detection efficiency, e.g. accuracy of pipette in spiking sample, may be important. The good agreement between values for sub core A(i) for the two SURRC detectors (Fig 2.9) also suggests calibration of detection efficiency is the cause of the offset. It may also be worth noting that the error for ^{226}Ra may be underestimated, as the error was simply taken as the mean of the 1σ errors for each of the 295, 342 and 609 keV peaks. However, regardless of individual offsets between the ^{210}Pb and ^{226}Ra activities, the resultant $^{210}\text{Pb}_{\text{excess}}$ values between the two laboratories are comparable. The values for the artificial radionuclides from the two laboratories, where both laboratories determined efficiency by spiking with liquid standards, fall within 1σ error, although the percentage error is much larger than for the natural decay series. A comparison was also made at the SOC laboratory between the gamma spectrometry method and the alpha spectrometry method outlined in Smith and Hamilton (1984) (J. Thomson pers. comm.). The alpha spectrometry method produced slightly higher activities of $^{210}\text{Pb}_{\text{excess}}$ than those from gamma spectrometry (SOC analysis).

Table 2.4: Comparison of results, shown with 1σ errors, derived from SOC and SURRC gamma analysis. N/A represents where the pellets had been destroyed for ^{14}C analysis before it was possible to recount them. BDL indicates where the measured activities were below detection limits (2σ of the detector background).

Sample						
	A(i) 0.0-0.5 cm	A(i) 4.0-4.5 cm	A(i) 8.0-8.5 cm	A(i) 11.0-11.5 cm	C(ii) 0.0-0.5 cm	C(ii) 9.0-9.5 cm
<i>SOC</i>						
^{210}Pb	289.0 ± 11.2	84.2 ± 4.3	37.5 ± 2.2	40.3 ± 3.2	99.2 ± 5.0	88.6 ± 4.5
^{226}Ra	30.8 ± 0.7	38.2 ± 0.8	39.5 ± 0.8	44.3 ± 0.8	54.5 ± 1.0	43.8 ± 0.9
$^{210}\text{Pb}_{\text{excess}}$	258.2 ± 11.2	46.0 ± 4.4	-2.0 ± 2.3	-4.0 ± 3.3	44.7 ± 5.1	44.8 ± 4.6
^{137}Cs	1.33 ± 0.33	0.91 ± 0.35	BDL	BDL	0.94 ± 0.34	1.39 ± 0.37
^{241}Am	0.78 ± 0.17	0.33 ± 0.17	BDL	BDL	0.52 ± 0.22	0.40 ± 0.16
<i>SURRC Tennelec</i>						
^{210}Pb	299.3 ± 9.2	N/A	N/A	57.4 ± 7.3	107.0 ± 6.4	98.2 ± 7.9
^{226}Ra	43.0 ± 1.6	N/A	N/A	50.7 ± 1.0	60.0 ± 2.1	49.7 ± 2.2
$^{210}\text{Pb}_{\text{excess}}$	256 ± 9.3	N/A	N/A	6.7 ± 7.4	47.6 ± 6.4	48.5 ± 8.2
^{137}Cs	1.65 ± 0.54	N/A	N/A	BDL	1.02 ± 0.39	1.27 ± 0.50
^{241}Am	1.50 ± 0.45	N/A	N/A	BDL	0.66 ± 0.33	1.62 ± 0.60
<i>SURRC Det 1.2</i>						
^{210}Pb	316.2 ± 18.1	96.1 ± 10.4	49.2 ± 5.2	47.6 ± 8.2	108.2 ± 10.4	97.4 ± 8.4
^{226}Ra	30.2 ± 4.9	50.9 ± 3.7	47.9 ± 2.2	54.5 ± 4.3	68.4 ± 4.0	49.7 ± 3.2
$^{210}\text{Pb}_{\text{excess}}$	286 ± 18.6	45.2 ± 11.0	1.3 ± 5.6	-6.9 ± 9.3	39.8 ± 11.0	47.7 ± 9.0
^{137}Cs	BDL	BDL	BDL	BDL	BDL	BDL
^{241}Am	BDL	BDL	BDL	BDL	BDL	BDL

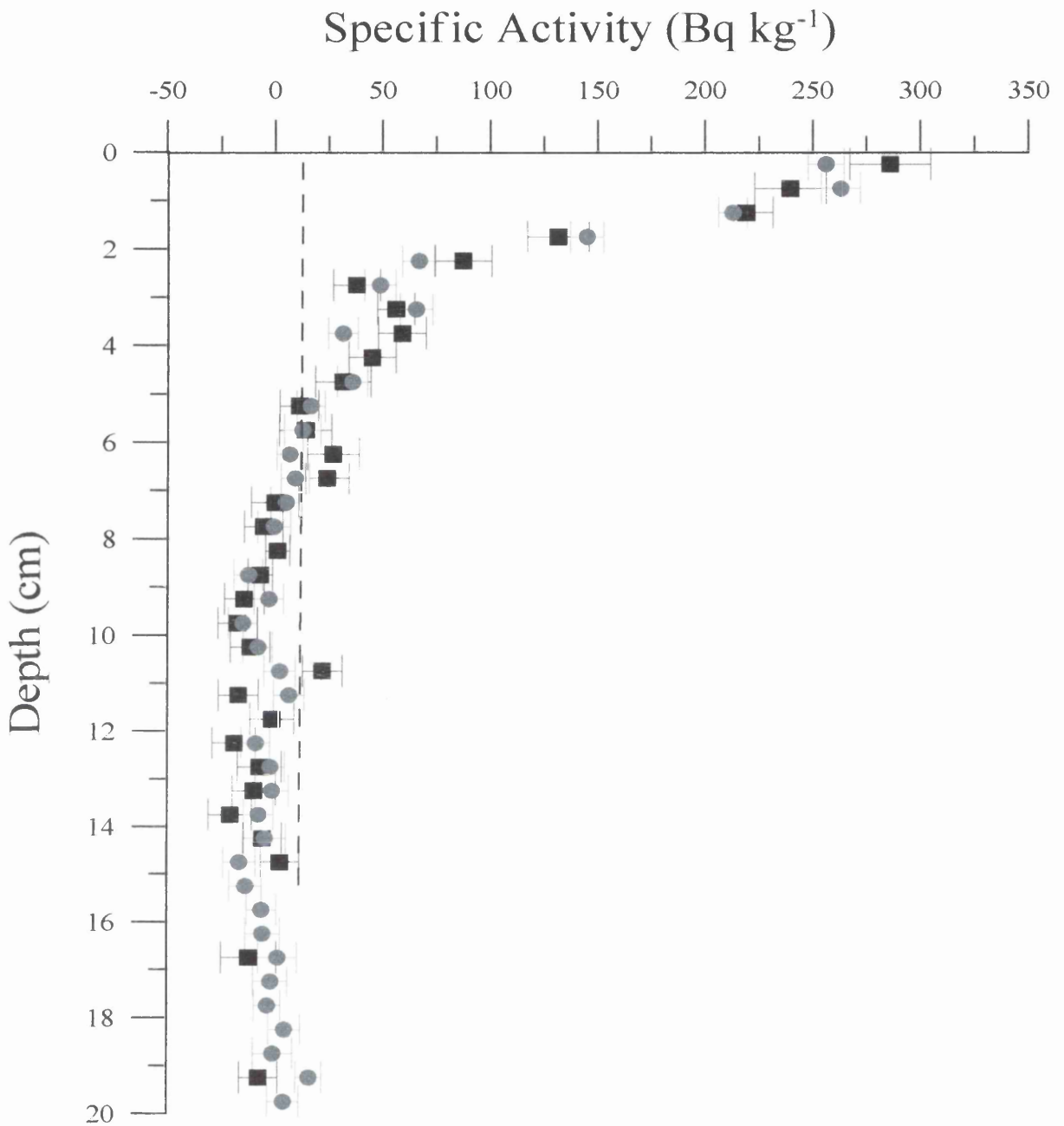


Fig. 2.9: Comparison of the $^{210}\text{Pb}_{\text{excess}}$ profiles from BENBO sub core A(i), measured on two gamma spectrometers at SURRC. ■ = Det. 1.2; ● = Tennelec

Previous studies have indicated that, even on the timescale over which $^{210}\text{Pb}_{\text{excess}}$ may be used to examine biological mixing, bioturbation may be considerably heterogeneous over small distances (Smith and Schafer, 1984). In order to assess the extent to which analysis of a single sub core might represent mixing over the area of sediment retrieved by a box core, gamma spectrometry analysis was undertaken on replicate sub cores from the box cores taken from sites B and C. Pellets were prepared as before from sub cores B(vi) and C(iv) to investigate this phenomenon.

2.3.5 Activity calculations

Determination of the count rate for each radionuclide was performed manually rather than using the available computer software package, GammaVision. Commercial peak search software packages are generally designed for analysis of samples with relatively high count rates and well defined peak shapes, with few interferences. The low levels of activity in deep sea sediment samples, combined with interferences from NDS radionuclides may cause peaks to be rejected by the software package, and manual calculation is the preferred option. This approach also ensured any stability problems with the system would be identified quickly.

The gross peak counts are determined by summing the counts in all channels within the peak area. The Compton background was determined by calculating the mean count rate in four channels on either side of the peak and multiplying this value by the number of channels in the peak. The estimated Compton contribution is subtracted from the gross counts to give net photopeak counts. The error on the Compton contribution is taken as the Poisson error - 1σ of the average Compton counts per channel multiplied by the

number of channels in the peak. The error on the net photopeak counts is:

$$1\sigma_{net} = \sqrt{\left[(1\sigma_{gross})^2 + (1\sigma_{compton})^2 \right]} \quad (2.12)$$

where $1\sigma_{net}$ is the net photopeak count error, $1\sigma_{gross}$ is the total photopeak count error, and $1\sigma_{Compton}$ is the error on the Compton continuum counts under the photopeak area. For the ^{137}Cs and ^{241}Am peaks, only the four channels to the left of the peak were used to calculate the Compton contribution to eliminate the effect of increased Compton counts from NDS series radionuclide peaks on the right hand side. For similar reasons, the background for the ^{210}Pb peak was determined from a single channel to the right of the peak. The net photopeak counts were then converted to counts per second (cps) by dividing by the counting time.

In addition to the Compton continuum contribution, the detector background must also be subtracted. Detector backgrounds, from external gamma radiation or detector contamination, are determined by recording a spectrum in the absence of a sample and calculating the count rate above Compton counts in the region of interest. Table 2.5 lists the backgrounds determined for the SURRC detectors.

Once detector background has been subtracted, the count rate is corrected for detection efficiency to give the activity of the radionuclide in the pellet. Values are reported as specific activity, derived by calculating the activity per kg from the known weight of sample:

$$\text{Specific Activity} = \frac{C}{E} \cdot \frac{100}{1} \cdot \frac{1000}{W_S} \quad (2.13)$$

Table 2.5: Detector backgrounds in counts per second, measured over one week, for the detectors used in this project. The errors quoted are 1σ errors as a percentage of the detector background.

Gamma Detector				
Radionuclide	LEGe 3	LEGe 4	Tennelec 2	Det 1.2
$^{210}\text{Pb}@ 46.5 \text{ keV}$	0	0	0.006 ± 11	0
$^{214}\text{Pb}@ 295 \text{ keV}$	0	0	0.002 ± 19	0
$^{214}\text{Pb}@352 \text{ keV}$	0	0	0.003 ± 22	0.001 ± 27
$^{214}\text{Bi}@609 \text{ keV}$	0	0.001 ± 21	0.003 ± 22	0.002 ± 13
$^{137}\text{Cs}@662 \text{ keV}$	0	0	0.001 ± 28	0
$^{241}\text{Am}@ 58.5 \text{ keV}$	0	0	0	0

where C is the net photopeak count rate in cps, E is the percentage detection efficiency for the radionuclide, and W_s is the sample weight (g). Where calculations involved addition or subtraction, errors were propagated using the general equation:

$$1\sigma_{tot} = \sqrt{\left[(1\sigma_A)^2 + (1\sigma_B)^2 \right]} \quad (2.14)$$

where $1\sigma_{tot}$ is the combined error of the errors on values A ($1\sigma_A$) and B ($1\sigma_B$). If values were divided or multiplied, the following equation was used:

$$\frac{1\sigma_{tot}}{Tot} \cdot \frac{100}{1} = \sqrt{\left[\left(\frac{1\sigma_A}{A} \cdot \frac{100}{1} \right)^2 + \left(\frac{1\sigma_B}{B} \cdot \frac{100}{1} \right)^2 \right]} \quad (2.15)$$

The limit of detection for a radionuclide was taken as 2σ of the background count rate; thus, where activity is below the detection limit, the radionuclide is reported as being $< 2\sigma$.

The non-destructive nature of gamma spectrometry means that salts evaporated from sediment porewaters are incorporated into the sample being analysed. As these will be effectively free of radionuclides, the contribution of the salts to the total sediment weight must be subtracted before specific activities can be determined. As no porewater salinity data were available for these cores, a value of 35‰ was used. The salinity correction applied was therefore:

$$A_{salt} = \frac{W_{pellet}}{W_{pellet} \cdot ((W_{wet} - W_{dry}) \cdot 0.035)} \cdot A_{measured} \quad (2.16)$$

where A_{salt} is the radionuclide specific activity of the sample corrected for the salt content (Bq kg^{-1}); $A_{measured}$ is the specific activity of the radionuclide determined by gamma spectrometry (Bq kg^{-1}); W_{wet} is the wet weight of sediment in depth increment (g); W_{dry} is the dry weight of sediment in depth increment (g); W_{pellet} = weight of pellet used in gamma spectrometry analysis.

The salt-corrected activities fell within 1σ error of the uncorrected values for all samples except for the surface samples from B(i), where the dry bulk density was extremely low. Taking into consideration that the correction was based on an approximation of porewater salinity, it was decided to report data uncorrected for salt content.

2.4 Plutonium

The principal Pu isotopes released by anthropogenic activities are ^{238}Pu , ^{239}Pu , ^{240}Pu and ^{241}Pu (Table 2.6). The first three isotopes decay by alpha emission to isotopes of U, whilst ^{241}Pu is a soft beta emitter that decays to ^{241}Am . Although ^{241}Pu can be determined by liquid scintillation counting (Cook and Anderson 1991), this study is concerned only with analysis of the alpha-emitting radionuclides.

2.4.1 Principles of alpha spectrometry

Alpha decay entails emission of a helium nucleus and production of a daughter radionuclide of $M-4$ and $Z-2$ of that of its parent. Alpha particles have relatively low velocities and thus have a high probability of interaction with matter relative to other forms of nuclear radiation. Interaction of an alpha particle with matter is mainly by attraction of electrons, causing ionisation. Only a tiny amount ($<0.1\%$) of energy is lost with each interaction; however, the high efficiency of interaction means that the distance of penetration of the alpha particle is very short - a few centimetres in air. Alpha-emitting radionuclides are almost all of $Z>200$, and alpha particle energies fall within the range of 3-9 MeV.

Radionuclide	Half life (y)	Decay mode	Alpha particle energy (MeV)
^{238}Pu	87.7	α	5.456 (28.3%); 5.499 (71.6%)
^{239}Pu	24 100	α	5.143 (15.1%); 5.156 (73.2%)
^{240}Pu	6 560	α	5.124 (26.4%); 5.168 (73.5%)
^{241}Pu	14.4	β	$E_{\text{max}} = 20.8 \text{ keV}$

Table 2.6: Decay characteristics of plutonium isotopes

As with gamma photons, alpha radiation can be detected by the use of semiconductor materials; specifically silicon crystals doped with electron acceptor and donor species to form a p-i-n diode (Fig. 2.11). A reverse bias (typically 50-100 V) is applied to the diode by placing a negative electrical contact in the p-type material and a positive contact in the n-type material, increasing the region of charge depletion. This region is generally of the order of 100 μm thickness. The nature of the electrical contact determines the type of detector. Surface barrier detectors have contacts of evaporated Au on one face and Al on the other, whilst passivated ion implanted planar detectors (PIPS) have a passivated outer oxide layer and implanted B and As for electrical contacts. The protective oxide layer of PIPS detectors renders them less fragile than surface barrier detectors, and enables them to be cleaned if accidentally contaminated.

In the detection process, alpha particles are stopped in the depletion region, forming electron-hole pairs. The energy necessary to form a single electron-hole pair depends on the detector material, but is essentially independent of the energy of the incoming particle. The number of electron-hole pairs ultimately formed is thus directly proportional to the energy of the particle. The electric field in the depletion region sweeps the electrons to one terminal and the holes to the other. The resultant charge pulse is integrated in a charge sensitive pre-amplifier to produce a voltage pulse, amplified and digitised, and stored in a multi channel analyser.

The short penetration distance of alpha particles means there is no requirement for shielding since the detector walls will exclude any alpha and low energy beta radiation originating outside the chamber. As the intrinsic region of the semiconductor crystal is only of the order of 100 μm thick, gamma radiation is also unlikely to interact with the

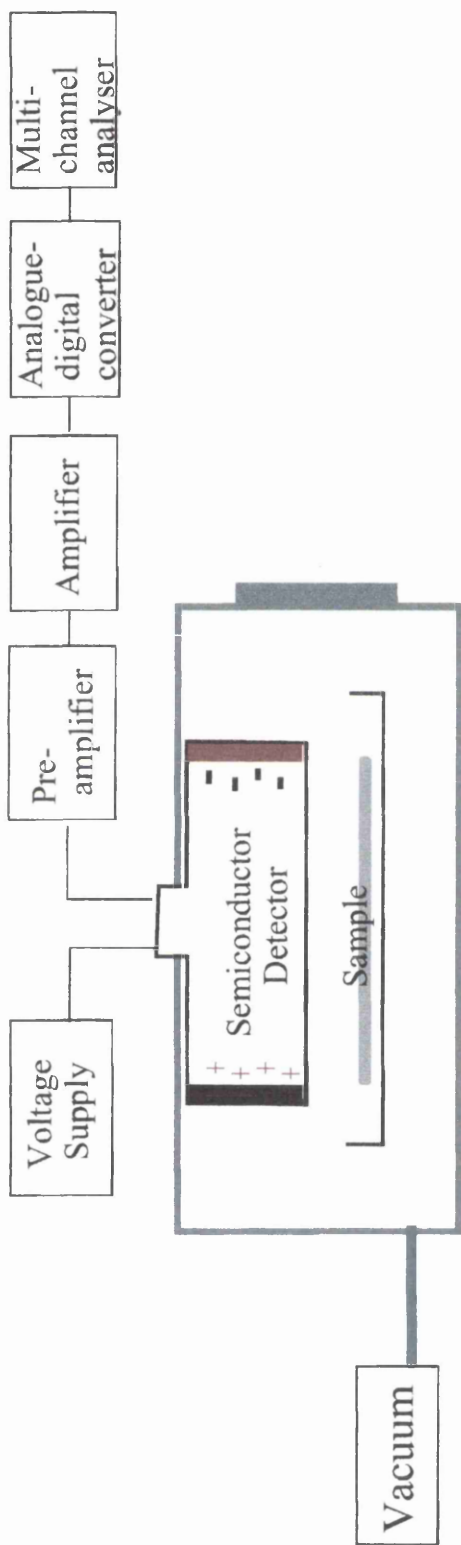


Fig 2.10: Schematic diagram of an alpha spectrometry system.

detector. The counting chamber is maintained under vacuum and the sample placed within a few centimetres of the detector to minimise attenuation of alpha particle energy by residual air in the gap between the sample and the detector.

One disadvantage of alpha spectrometry is that detector resolution is insufficient to determine ^{239}Pu and ^{240}Pu separately, and the combined activity is usually reported as $^{239,240}\text{Pu}$. Mathematical techniques may be used to discriminate between the two radioisotopes in high resolution spectra (Bland *et al.* 1992; LaMont *et al.* 1998). More sensitive methods for Pu analysis, including thermal ionisation mass spectrometry (e.g. Kersting *et al.* 1999), inductively coupled plasma mass spectrometry (e.g. Kershaw *et al.* 1995), and AMS (e.g. McAninch *et al.* 2000) are also able to resolve ^{239}Pu and ^{240}Pu .

2.4.2 Sample preparation

The non-destructive nature of the gamma spectroscopy technique permitted the same sediment to be used for Pu analysis, and thus a direct comparison with ^{241}Am , ^{137}Cs and $^{210}\text{Pb}_{\text{excess}}$ profiles can be made. However, in contrast to gamma spectroscopy, accurate measurement of low activity alpha emissions requires both a thin sample source to prevent attenuation of alpha radiation by the source itself, and chemical separation from other radionuclides to prevent interferences from alpha emitters of similar energy (Fig. 2.11).

The preparation of a sediment sample for Pu analysis by alpha spectrometry has three main steps: dissolution of the sample matrix, separation of Pu from interfering species by solvent extraction (e.g. Ramanujam *et al.* 1978) or ion exchange techniques (e.g. Chen *et al.* 1993), and source preparation by electrodeposition (Talvitie 1972). This method is a modified version of the ion-exchange method of Wong (1971)

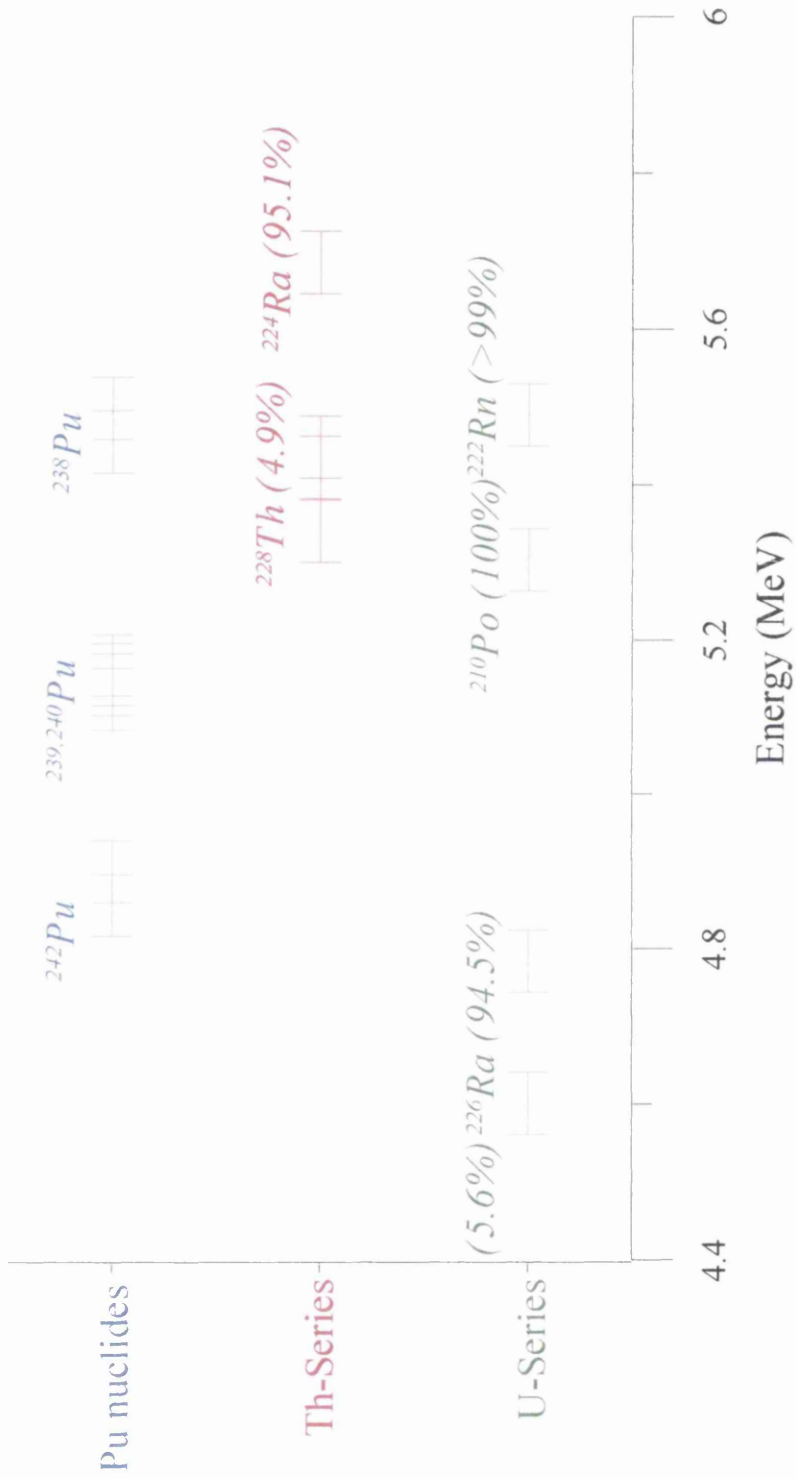


Fig. 2.11: Potential interferences in plutonium alpha spectra from the natural decay series radionuclides

Radionuclide extraction

Fallout Pu in the open ocean is associated mainly with organic detritus (e.g. Higgs *et al.* 1977), so partial digestion should be sufficient to extract plutonium from the sediment matrix. The 20 g sediment pellet was ground to a homogeneous powder, then furnace for 12 h at 450 °C to remove organic material. A chemical yield tracer of ^{242}Pu (0.073 Bq ml⁻¹) was added to the sample. Any carbonate in the sample was hydrolysed by the gradual addition of 100 ml of 9 M HCl. The sample was taken to near dryness on a hotplate and 50 ml of 30 % H₂O₂ added to oxidise any remaining organic material. After again taking to dryness, the sample was digested with 100 ml aqua regia, made from 50% v/v each of 12 M HCl and 12 M HNO₃. The sample was again taken to near dryness and 200 ml of 9 M HCl added. The solution and solids were separated by centrifugation (10 minutes at 3000 rpm), and the sediment washed twice with 9 M HCl and finally with reverse osmosis (RO) H₂O to ensure all the Pu was collected.

Ammonia was added to the liquid phase from the centrifugation stage until a ferric hydroxide precipitate formed at approximately pH 9. The solution and precipitate were stirred well, then allowed to stand for at least one hour to allow all the particle-reactive radionuclides to be adsorbed by the precipitate. The solid phase was again separated using centrifugation, and the precipitate washed five times with RO H₂O to remove salts. The precipitate was redissolved in concentrated HNO₃, taken to dryness and finally taken up in 50 ml of 9 M HCl.

The high Fe content of BENBO sediments interfered with the isolation of Pu by ion exchange; therefore the Fe was first removed by solvent extraction with 50 ml of diisopropyl ether (DIPE). The Fe-containing DIPE was discarded, and the process repeated

using fresh DIPE until most of the Fe had been removed. The residual DIPE in the sample was removed by evaporation, and the sample was redissolved in 50 ml of 9 M HCl.

Ion-exchange processes

Ion exchange resins are composed of an insoluble hydrocarbon network to which is attached a large number of either acidic (anion exchange) or basic (cation exchange) functional groups. If a solution is passed through the ion exchange resin, the H^+ and OH^- ions in the resin can be replaced by other ions for which the resin has a stronger affinity. Different ions will have different selectivity coefficients for the resin, and by altering the oxidation state or ionic complex of a particular element, ion exchange techniques may be used for the separation of ions in a solution (e.g. Saito 1984). This method uses anion exchange resin to isolate the plutonium.

An ion exchange column of approximately 6 cm length x 1 cm² area was prepared from BioRad AG1 x8 chloride form anion exchange resin. The column was preconditioned by passing through 50 ml of 1.2 M HCl, followed by 20 ml of 9 M HCl, after which the sample solution was passed through the column. In 9 M HCl, Pu exists mainly in the Pu(IV) oxidation state, and forms the anionic complex $PuCl_6^{2-}$, which is held on the resin along with anionic complexes of U and Fe, whilst the cationic Am, Th and Ra pass through. The column was then rinsed twice with 50 ml of 9 M HCl to ensure complete removal of these species. The Pu was eluted from the column by reducing Pu(IV) to Pu(III), using 6 x 20 ml of a solution containing 15 ml of 9 M HCl and 5 ml of 1 M NH_4I . After elution, iodine was removed from the sample solution by evaporation, followed by addition of 2-3 ml of 12 M HNO_3 to ensure Pu was oxidised back to Pu(IV). The solution was transferred to a clean beaker, where the HNO_3 was evaporated and the Pu redissolved in 50 ml of 8 M HNO_3 .

Elimination of U and Fe was achieved using a second BioRad AG1 x8 column of similar dimensions to the first, pretreated with 20 ml of 0.1 M HNO₃ and 20 ml of 8 M HNO₃ before addition of the sample. In 6-10 M HNO₃, Pu(IV) is retained on the column as Pu(NO₃)₆²⁻, whilst U and Fe pass through. The column is rinsed twice with 50 ml of 8 M HNO₃, and Pu is eluted as for the first column. Following evaporation of iodine and transfer of the Pu solution to a clean beaker, Pu was redissolved in 8 drops of 12 M HCl and 50 ml of 3.75% w/v NH₄Cl solution in preparation for electrodeposition.

Source preparation

The solution was placed into an electrolysis cell attached to a direct current voltage supply unit, with a 2.5 cm stainless steel planchette acting as the cathode. The Pu was plated onto the planchette for one hour at a current of 3 A and a voltage of 10-15 V, after which approximately 5 ml of ammonia was added to prevent redissolution of the Pu, and the current immediately switched off. The planchette was removed from the electrolysis cell, washed with RO H₂O and dried before alpha counting

2.4.3 Alpha counting and calculations

The samples were counted using four low-background Canberra passivated implanted planar silicon (PIPS) detectors for 1-3 weeks or until 500 counts were recorded in the ^{239,240}Pu energy region. Energy calibrations were made using a three-point alpha emitter source and calibrating the known energy peaks to the detector channel number.

The use of the ²⁴²Pu yield tracer eliminates the need for determination of chemical

recovery and detection efficiency, and the activities of Pu isotopes in the sample were obtained from:

$$A_{sample} = \frac{A_{spike} \cdot C_{sample}}{C_{spike}} \cdot \frac{1000}{W_S} \quad (2.17)$$

where A_{sample} is the activity of either the ^{238}Pu or combined $^{239,240}\text{Pu}$ in the sample (Bq), A_{spike} is the known activity of the ^{242}Pu spike added to the sample prior to the chemical processing, and C_{sample} and C_{spike} are the count rates (cps) determined for the radionuclide peaks for the ^{238}Pu or $^{239,240}\text{Pu}$ species in the sample and the ^{242}Pu spike respectively.

Results were reported as specific activities (Bq kg^{-1}) by adjusting for sample weight (W_S).

The planchettes generally produced clean, well-defined spectra, but trace activities of NDS radionuclides persisted in some spectra despite the ion-exchange purification steps. The presence of the ^{232}Th -series radionuclides ^{228}Th , at 5.42 MeV and ^{224}Ra , at 5.45 MeV results in spectral interferences with the ^{238}Pu energy peaks at 5.45 and 5.49 MeV (Fig. 2.11) Where activities of plutonium were low, these interferences would result in significant errors in calculated ^{238}Pu activities if no correction was applied to observed count rates. Therefore, in order to obtain the true ^{238}Pu count rate, corrections for these interferences were made by reference to related, well-resolved peaks for other radionuclides in the ^{232}Th decay series.

Chapter 3 - Results

3.1 Radiocarbon

3.1.1 Bulk carbonate results and box models

The bulk carbonate radiocarbon age-depth profiles for sub cores A(i), B(i) and C(ii) are reported in Tables A1-A3 in Appendix I. ^{14}C ages are reported as conventional radiocarbon years BP $\pm 1\sigma$. No correction for the reservoir age of the surface ocean has been applied.

The profiles for BENBO sites B and C approximate the idealised profile of a homogeneously mixed SML underlain by a zone of constant accumulation (Erlenkeuser 1980). The long-term sediment accumulation and bioturbation characteristics at these two sites were modelled using the parameters outlined in Section 1.4.1.2. The results of this modelling are reported in Table 3.1, and the age models shown in Fig. 3.1. Mean sediment accumulation fluxes are determined by dividing accumulation rate, s , by the mean core dry bulk density (DBD), giving values of $3.1 \text{ g cm}^{-2} \text{ ky}^{-1}$ for site B(i), and $4.5 \text{ g cm}^{-2} \text{ ky}^{-1}$ for site C(ii). Mean DBD was used for this calculation since, with the exception of the water-rich surface sections, DBD varied little over the length of the 40-50 cm cores.

The profile for BENBO A is irregular, with a sharp hiatus between 12 cm and 16 cm, over which range the ^{14}C age increases from $6120 \pm 70 \text{ y}$ to $19\,860 \pm 250 \text{ y}$, and an age inversion at 22 cm. The age anomaly corresponds to a sharp change in sediment carbonate content, from 60-75% in the upper part of the core to 20% in the lower section,

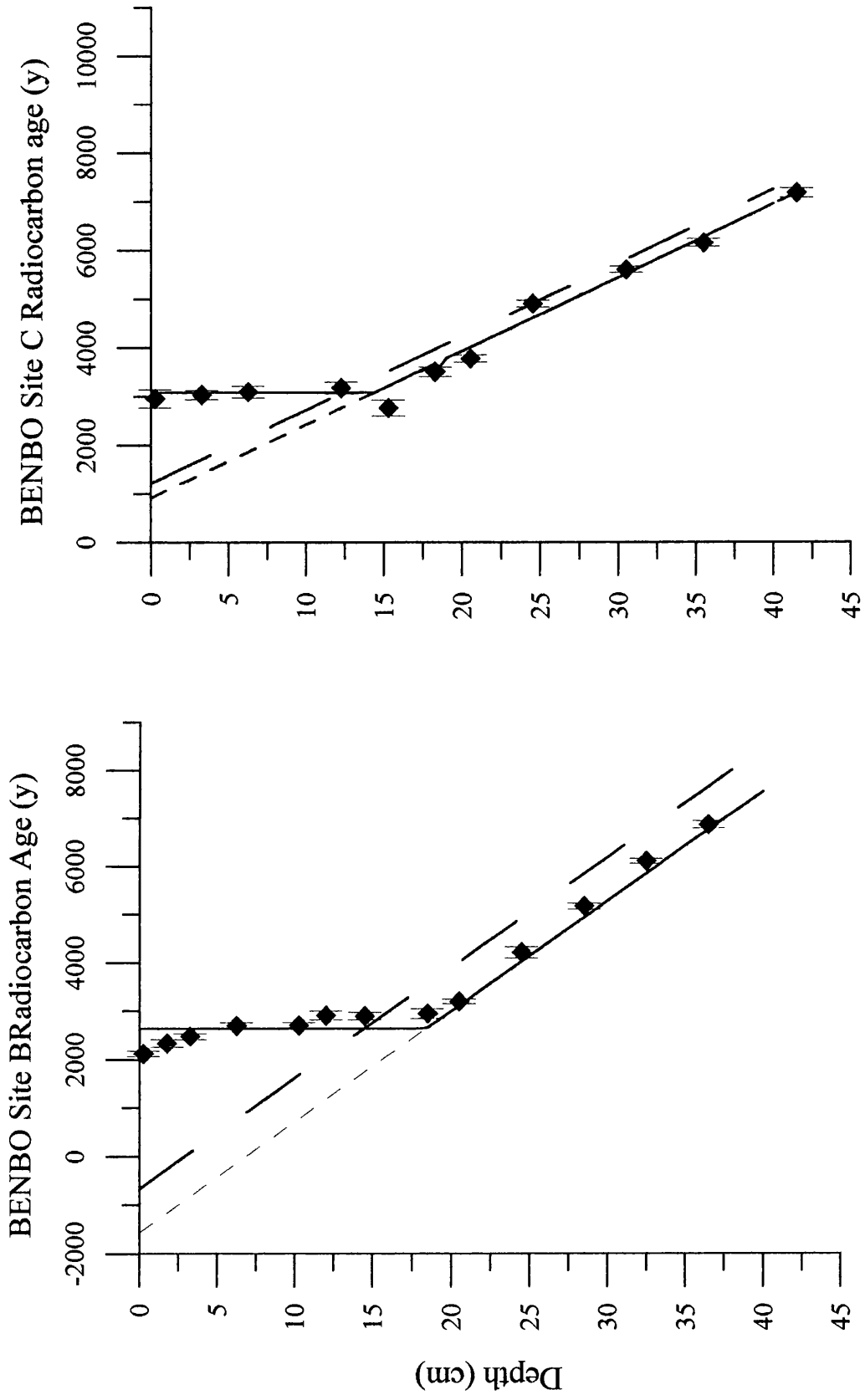


Fig 3.1: Modelling of radiocarbon data from BENBO sites B and C using the parameters of Erlenkeuser (1980). \blacklozenge = BENBO radiocarbon data; — = modelled radiocarbon profile; - - - = accumulation extrapolated to surface; - - - = unbioturbated profile

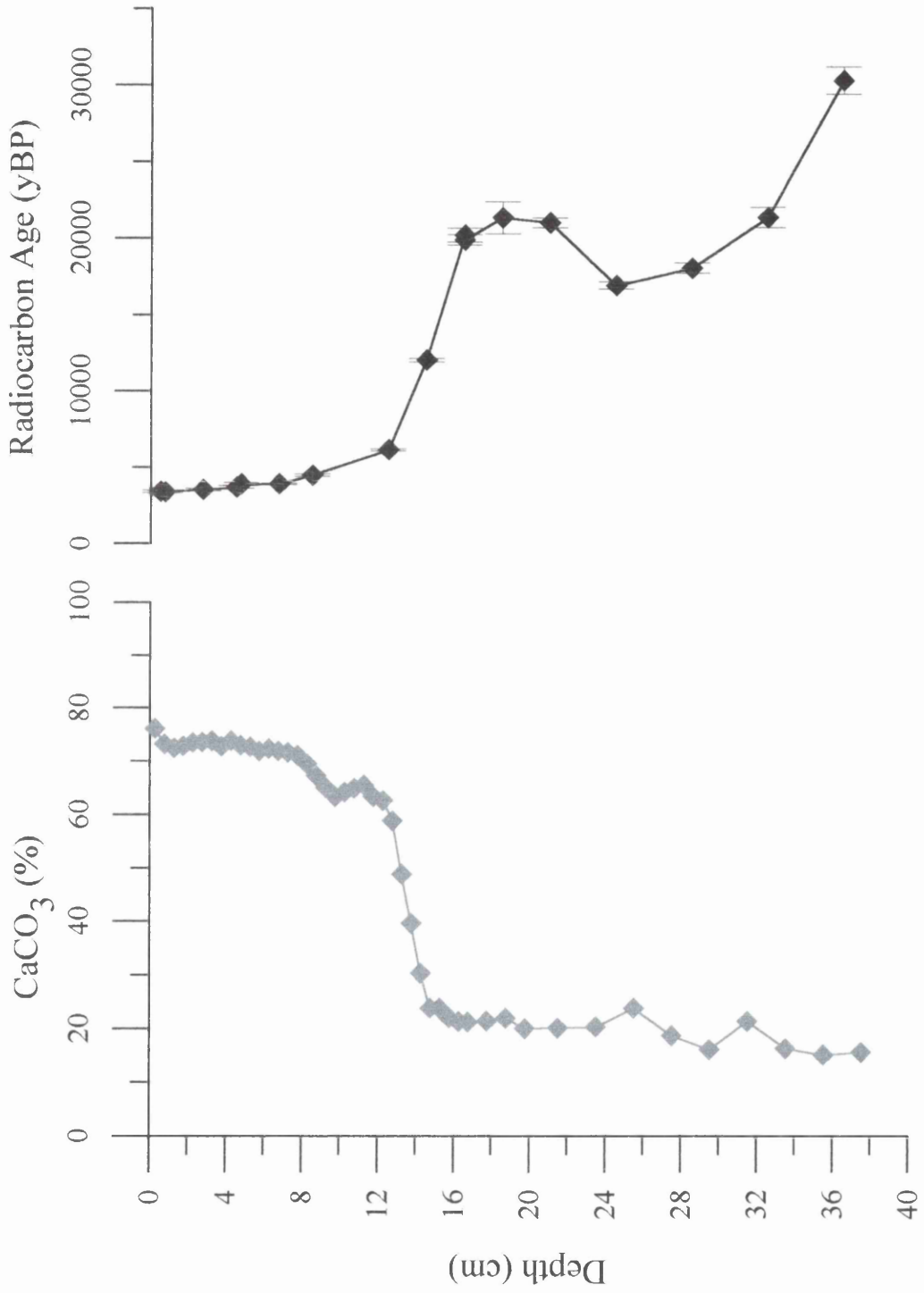


Fig. 3.2: Carbonate content and radiocarbon age profiles for BENBO site A, sub core (i)

Site	s (cm ky ⁻¹)	X (cm)	T_{ML} (y)	T_{SF} (y)	T_0 (y)	R (y)
BENBO B	4.3	18	2640	-1570	-660	4190
BENBO C	6.5	15.5	3000	810	1100	2460

Table 3.1: Bulk sediment radiocarbon data from BENBO sites B and C modelled according to Erlenkeuser (1980). s = sediment accumulation rate; X = SML depth; T_{ML} = SML average age; T_{SF} = sediment surface age; T_0 = age of freshly arriving sediment; R = average residence time of sediment in the mixed layer. The coefficient of determination (R^2) values of the fit of the best straight line through the data points below the SML are 0.99 and 0.98 for sites B and C respectively.

representing a junction between Holocene and glacial age sediments (Fig. 3.2). The implications of this will be discussed more fully in the following chapter.

3.1.2 Size fraction analysis - BENBO samples

Radiocarbon ages for the polyspecific planktonic foram samples and the $<63 \mu\text{m}$ fraction are listed in Tables A4-A6 in the Appendix and presented with the bulk carbonate profiles for comparison in Figs. 3.3-3.5.

The initial purpose of these analyses was to study the extent and development of size differential bioturbation, which had been observed previously in BOFS cores for which a steady state accumulation regime had already been determined (Thomson *et al.* 1995).

The irregular profile for bulk carbonate ^{14}C ages at site A (Fig. 3.3) clearly indicates that it is not suitable for this purpose; however, a limited number of analyses were undertaken to see if an offset could be identified in the upper region, and to see if the larger size fraction could provide any information as to the cause of the offset. In the disturbed part of the

core, the foraminifera ages follow no identifiable trend and bear little relation to that of the bulk carbonate. In contrast, two of the three $<63 \mu\text{m}$ samples are in good agreement with the bulk carbonate. In the third size fractionated sample from A(iii), at 25-26 cm, the foraminifera and $< 63 \mu\text{m}$ samples are within 2σ of each other, possibly indicating heterogeneity between the sub cores A(i) and A(iii). In the undisturbed upper section, the four foraminifera sample ages are within 2σ error of the bulk carbonate profile. However, the foram ages are on average 660 y older than the $< 63 \mu\text{m}$ fraction from the same core, ranging between 340 - 885 y older. The direction of this offset is in agreement with that from the BOFS cores of Thomson *et al.* (1995).

At site B (Fig. 3.4), 150-250 μm foram sample ages fall into two distinct groups relative to the bulk carbonate profiles. From 0-9 cm the foram samples are 560-1415 y younger than the bulk carbonate, with no obvious pattern with depth. Below 9 cm, the foram samples and bulk carbonate ^{14}C ages agree within 2σ . Two of the $< 63 \mu\text{m}$ fraction samples are in good agreement with the bulk carbonate, the other is approximately 500 y older. The $> 250 \mu\text{m}$ foraminifera are 215-610 y younger (average 370 y) than the 150-250 μm foram fraction, with the exception of one sample at 24-25 cm where the ages of the two size fractions are well within 1σ error.

At site C (Fig. 3.5), the foram samples are again younger than the bulk carbonate in the upper core. The age difference from 0-26 cm depth in the core ranges between 840-1400 y with the exception of the sample at 15-16 cm, where an age inversion in the bulk carbonate profile reduces the offset to 365 y. For the deepest samples, at 30-31 cm and 37-39 cm, the foram ages are within 2σ error of the bulk carbonate. Three of the four $<63 \mu\text{m}$

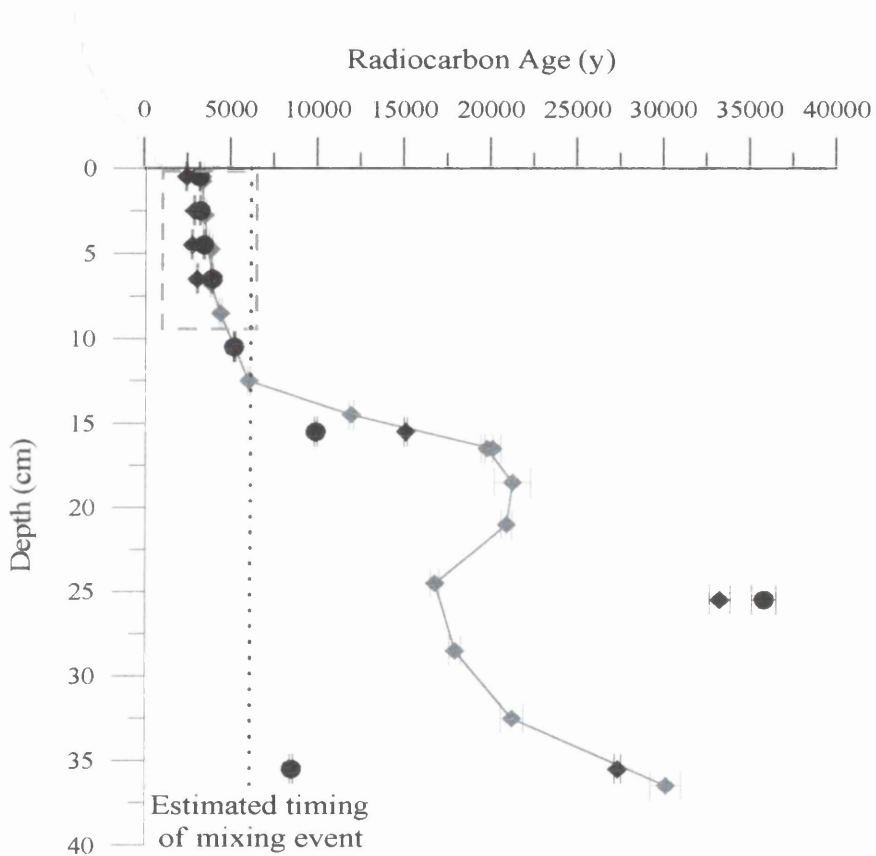
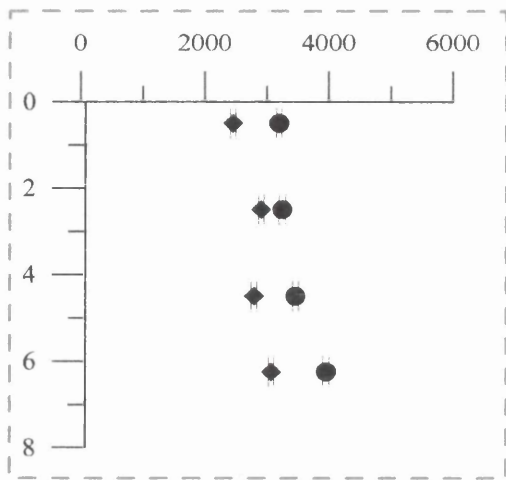


Fig. 3.3: BENBO site A 150-250 μm planktonic forams and $<63 \mu\text{m}$ carbonate radiocarbon profiles. The bulk carbonate profile generated by radiometric dating is also shown for comparison. The upper 8 cm is highlighted to emphasise the apparent age offset between the two size fractions. ● = 150-250 μm forams; ◆ = $<63 \mu\text{m}$ carbonate; ◆ = bulk carbonate

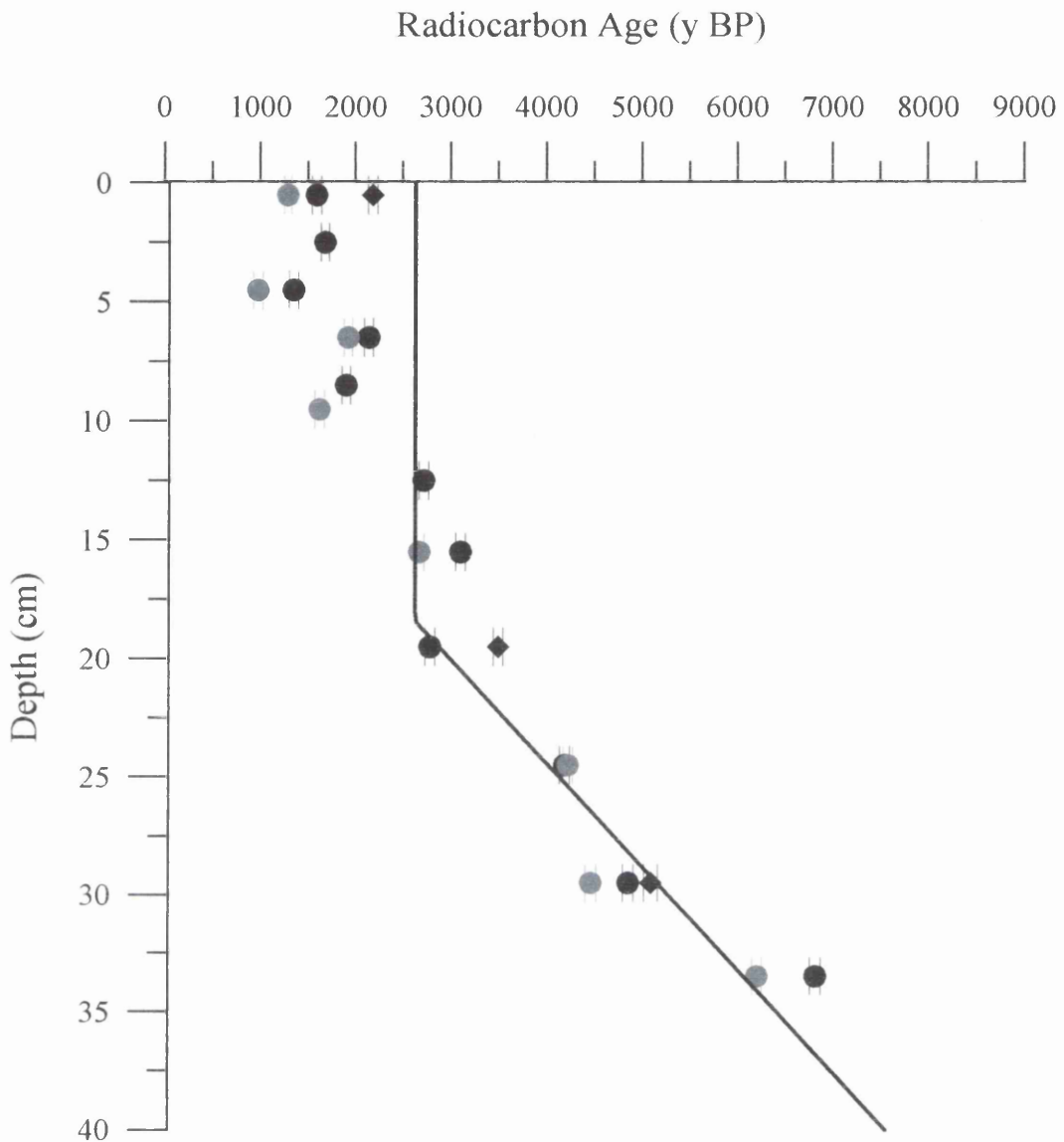


Fig. 3.4: BENBO site B (sub core (iv)) 150-250 μ m hand-picked planktonic forams and < 63 μ m sediment fraction radiocarbon ages. The size fractionated material is derived from subcore B(iv). The model profile from the bulk carbonate radiocarbon data is shown for comparison. ● = 150 - 250 μ m forams; ◆ = <63 μ m fraction; ○ = >250 μ m forams; — = bulk carbonate age model.

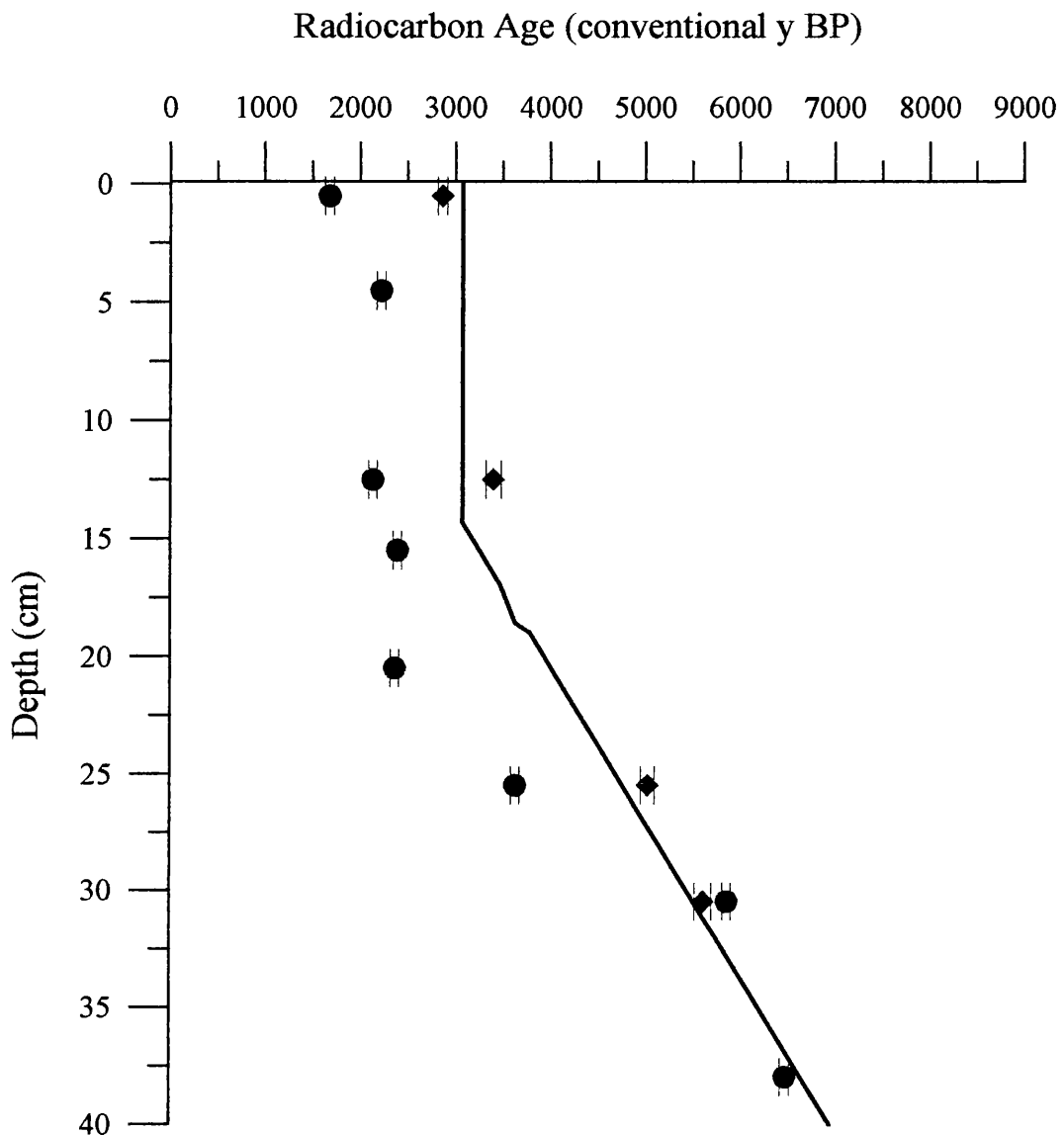


Fig. 3.5: BENBO site C 150-250 μ m hand-picked planktonic forams and < 63 μ m sediment fraction radiocarbon ages. The size fractionated material is derived from subcore C(vi). The model profile from the bulk carbonate radiocarbon data is shown for comparison. \bullet = 150 - 250 μ m forams; \blacklozenge = <63 μ m fraction; — = bulk carbonate age model.

fraction samples lie within 1σ error of the bulk carbonate, the exception being near the age inversion at 12-13 cm, where the $<63\ \mu\text{m}$ sample is within 2σ of the bulk.

3.1.3 Size fraction analysis - BOFS samples

The ^{14}C ages for the $>150\ \mu\text{m}$ hand-picked polyspecific planktonic foram samples are shown in Table A7 in the Appendix and illustrated in Fig. 3.6, with the published data for bulk carbonate and foraminiferal calcite (Thomson *et al.* 1995). Data were modelled using the Erlenkeuser box model, and the results are compared with those from the previously published data in Table 3.2.

Table 3.2: ^{14}C age-depth profiles for BOFS cores 11881 and 11886, modelled using the Erlenkeuser box model. As the foraminiferal carbonate samples of Thomson *et al.* (1995) were all below the SML, the depth of the bulk carbonate SML was used to calculate T_{ML} and T_0 for these samples. The asterisk in the fit to data column indicates where the best fit line has been calculated based on only two data points.

Profile	s (cm ky^{-1})	fit to data (R^2)	X (cm)	T_{ML} (y) data mean	T_{ML} (y) calculated	T_0 (y)
11881 bulk carbonate	3.0	0.988	9.3	3090	—	370
11881 hand-picked forams	3.0	1.00*	8.9	3620	—	900
11881 foram. carbonate	3.0	1.00*	—	—	4180	1800
11886 bulk carbonate	5.9	0.996	9.3	2350	—	840
11886 hand-picked forams	6.1	0.998	10.0	2690	—	1200
11886 foram. carbonate	5.9	0.998	—	—	3060	1830

Omitting the data point at 10 - 11 cm, the ^{14}C profile for hand-picked forams in BOFS 11881 generates the same SML depth and accumulation rate as both the bulk carbonate and foraminiferal calcite profiles of Thomson *et al.* (1995). However, the hand-picked foram profile is offset from the bulk carbonate profile by + 0.6 ka, and from that of the foraminiferal calcite by about 0.5 ka. The data point at 10-11 cm lies on the line described by the two points from the foraminiferal calcite. In BOFS 11886, the hand-picked foram profile coincides almost exactly with the profile for bulk carbonate. The average age of the hand-picked foram SML is 340 y older than that calculated for the bulk carbonate, which makes a minor difference of 0.7 cm in the calculated depth of the SML. The sediment accumulation rate determined from the hand-picked foram profile is also slightly higher, although still easily within 1σ error of that for the bulk carbonate.

The radiocarbon ages of both the pre-treated sample and the carbon removed during pre-treatment of BOFS core 11881 samples 0-1 cm and 26-27 cm are also highlighted in Fig. 3.6. The 26 - 27 cm pre-treated sample lies on the line described by the two points from the foraminiferal calcite (and the 10 - 11 cm hand-picked foram sample). If the SML depth of the foraminiferal calcite profile is assumed to be 9 cm, similar to those calculated for the bulk carbonate and hand-picked foram profiles, the age of the pre-treated sample at 0-1 cm is similar to the foraminiferal calcite T_{ML} . The carbon removed during pre-treatment of the 0-1 cm sample is close in age to the bulk carbonate. Recalculating the age of the total sample using the percent modern values reported for the samples ($[0.2 \times 0.7244] + [0.8 \times 0.5943]$) gives a value of 3840 ± 75 , in reasonable agreement with the 3630 ± 40 determined for the untreated sample. The age of carbon removed during pre-treatment of the 26-27 cm sample is older than the pre-treated sample by about 200 years.

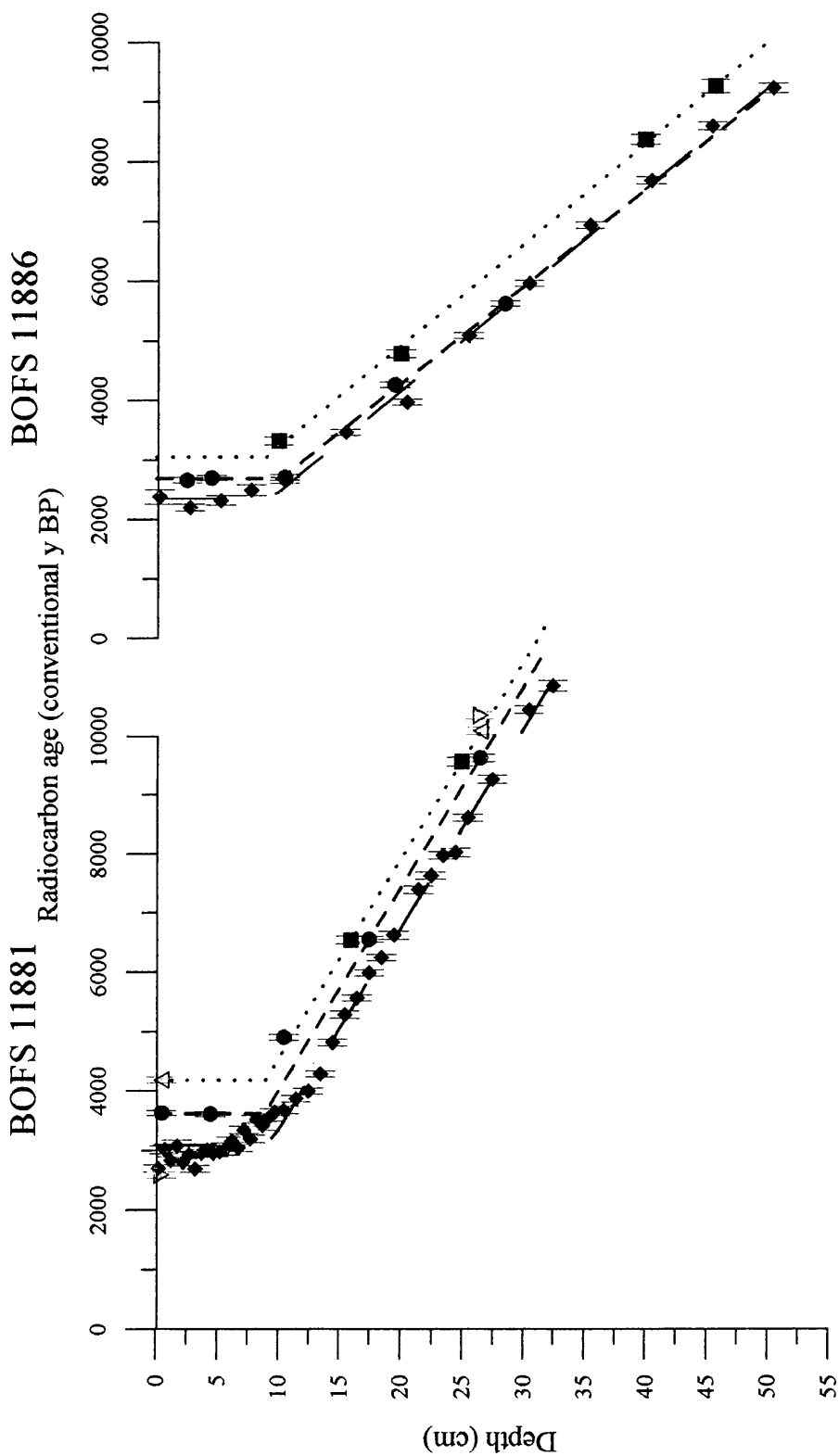


Fig. 3.6. Radiocarbon results for hand-picked polyspecific planktonic foraminifera, shown with the bulk carbonate and >150 μm foraminiferal carbonate data of Thomson *et al.* (1995). The lines represent the data modelled using the Erlenkeuser (1980) box model. The data for the pretreated samples are also shown. \blacklozenge = >150 μm foraminiferal calcite; \bullet = 150 μm hand-picked foraminifera; \triangle = pretreated forams; ∇ = carbonate released during foram pretreatment.

3.2 $^{210}\text{Pb}_{\text{excess}}$

3.2.1 SML depths and mixing rates

The $^{210}\text{Pb}_{\text{excess}}$, $^{210}\text{Pb}_{\text{total}}$, and ^{226}Ra profiles for the sub cores A(i), B(i) and C(ii) are shown in Figs. 3.7-3.9. The data are presented in full in Tables A8-A10 in the Appendix. The ^{226}Ra profiles of sub core C(ii) and to a lesser extent, B(i) indicate there has been some diffusion of ^{226}Ra , and thus the direct analysis of this parameter by gamma spectroscopy has provided a more reliable evaluation of $^{210}\text{Pb}_{\text{excess}}$ than assumption of a constant value throughout.

The $^{210}\text{Pb}_{\text{excess}}$ profiles of sub cores A(i) and B(i) decrease approximately exponentially, in the manner expected for biodiffusive-type mixing. The simplified equation (Nozaki *et al.* 1977) for uniform, biodiffusive mixing of a relatively short-lived tracer is:

$$A_x = A_0 \cdot e^{-(\lambda/D_B)^{1/2} \cdot x} \quad (3.1)$$

where A_x is the radionuclide activity at a depth, x , A_0 is the activity of the tracer at $x = 0$, λ is the decay constant of the radionuclide, and D_B is the biodiffusion coefficient. Only the data where $^{210}\text{Pb}_{\text{excess}} > 1\sigma$ error were included in the calculation. This precaution was taken to prevent an artificial deepening of the SML by inclusion of data points in which counting error produced a positive value for $^{210}\text{Pb}_{\text{excess}}$. Using this approach, the bioturbation mixing coefficients are $0.088 \text{ cm}^2 \text{ y}^{-1}$ for subcore A(i) and $0.045 \text{ cm}^2 \text{ y}^{-1}$ for sub core B(i). The depth of the SML in these profiles is defined as $A_0/100$ of the best fit exponential curve through the data, corresponding to a 10 cm thick SML in subcore A(i) and 8 cm for subcore B(i).

The $^{210}\text{Pb}_{\text{excess}}$ profile in sub core C(ii) contains subsurface peaks as are observed as a result of advective mixing (Smith *et al.* 1986). Approximately a quarter of the total $^{210}\text{Pb}_{\text{excess}}$ is found in a surface layer from 0 cm to 3 cm, whilst the remainder is located in the region from 6 cm to 16 cm. Software capable of modelling the effect of subsurface mixing on the $^{210}\text{Pb}_{\text{excess}}$ profile (<http://www.nioo.knaw.nl/homepages/soetaert/Soetaert.htm> and accompanying paper by Soetaert *et al.* 1996) is available; however, the maximum depth at which injection of the tracer by advective mixing is possible is set at 10 cm in this model; since a subsurface peak in sub core C(ii) is observed at 16 cm depth, it was not possible to apply this model.

In view of the unusual $^{210}\text{Pb}_{\text{excess}}$ profile at site C, and the contrasting SML depths between ^{14}C and $^{210}\text{Pb}_{\text{excess}}$ profiles at site B, replicate analyses of the gamma-emitting radionuclides were repeated on sub cores B(iv) and C(vi). The initial and replicate sub core $^{210}\text{Pb}_{\text{excess}}$ profiles are compared in Fig 3.10; replicate sub core data are listed in Tables 11 and 12 in the Appendix. In the upper 7 cm, the replicate profile at site B appears superficially similar to the initial profile, however, in the lower part of the core, a subsurface peak in activity is present from 8-14 cm. At site C, sub core(vi), the subsurface peak is present only from 11-16 cm, and contains 25% of the total $^{210}\text{Pb}_{\text{excess}}$, compared with 75% of total $^{210}\text{Pb}_{\text{excess}}$ in subsurface peaks in C(ii).

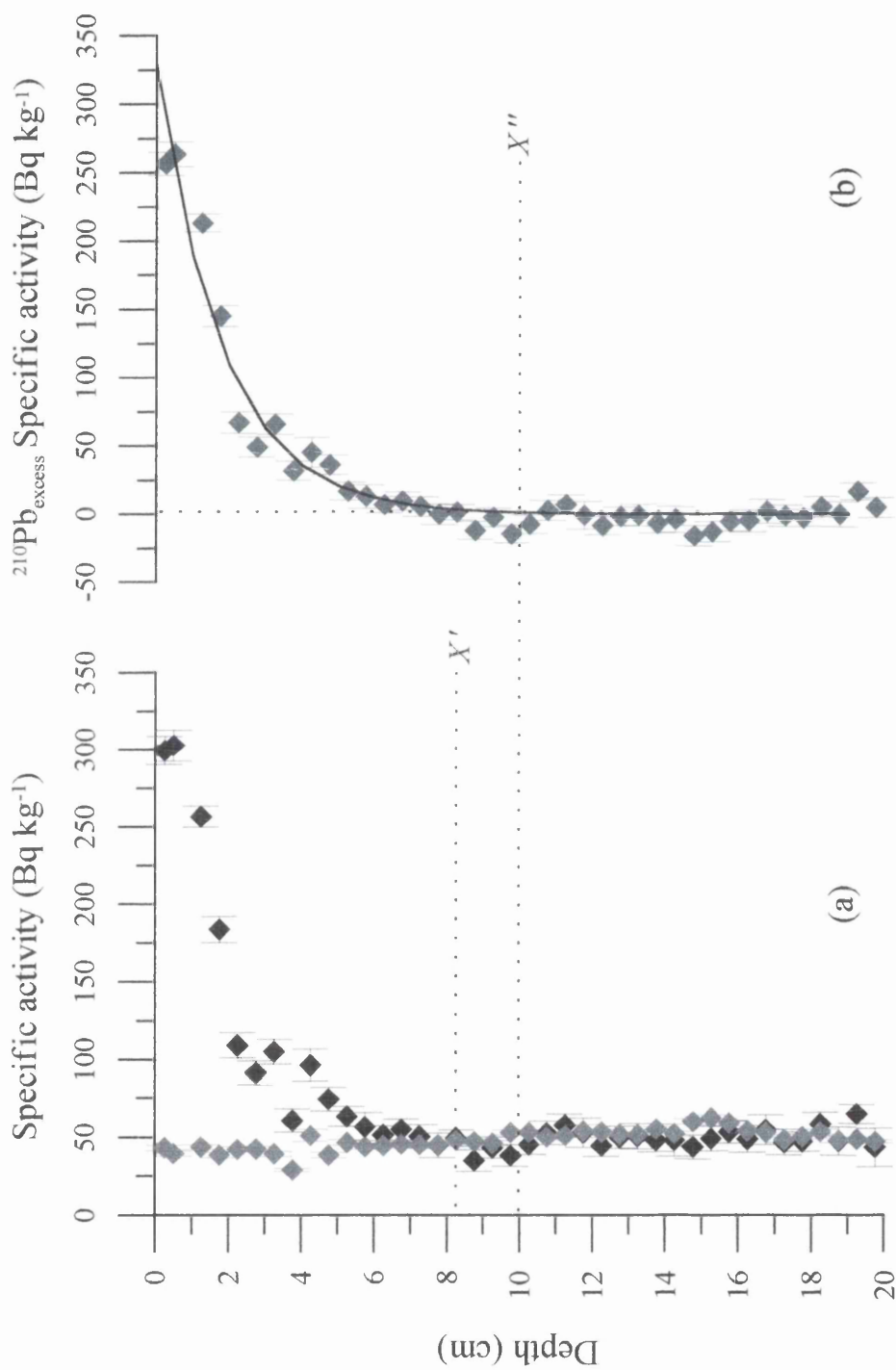


Fig. 3.7: (a) Total ²¹⁰Pb (♦) and ²²⁶Ra (♦) specific activity profiles, and (b) ²¹⁰Pb_{excess} specific activity profiles for sub core A(i), shown with the best fit exponential curve. X' and X'' represent the visual SML depth estimate and that estimated from $A = A_0/100$ of the best fit curve.

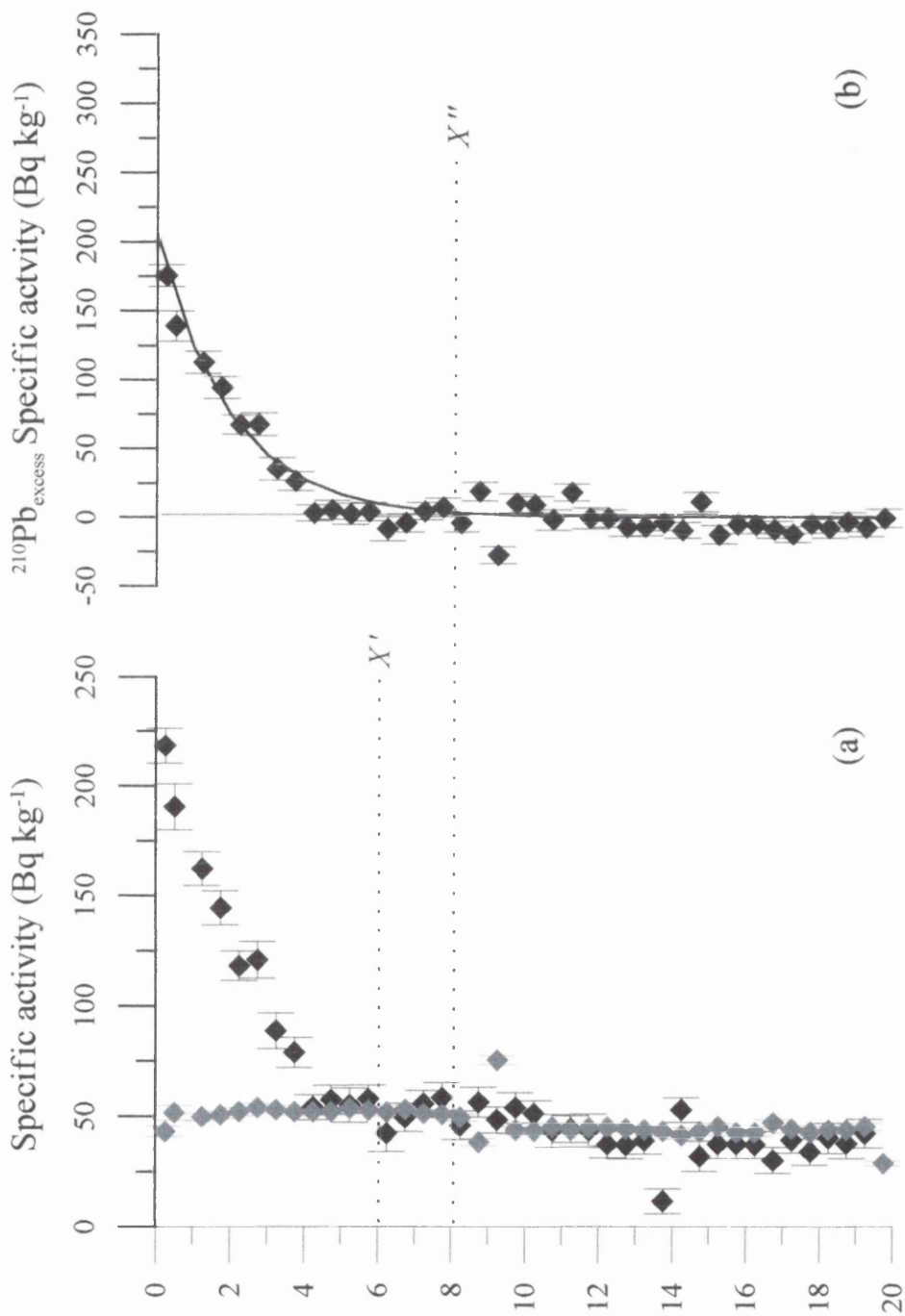


Fig. 3.8: (a) Total ^{210}Pb (\blacklozenge) and ^{226}Ra (\blacklozenge) specific activity, and (b) $^{210}\text{Pb}_{\text{excess}}$ specific activity profiles for sub core B(i), shown with the best fit exponential curve. X' and X'' represent the visual SML depth estimate and that estimated from $A = A_0/100$ of the best fit curve.

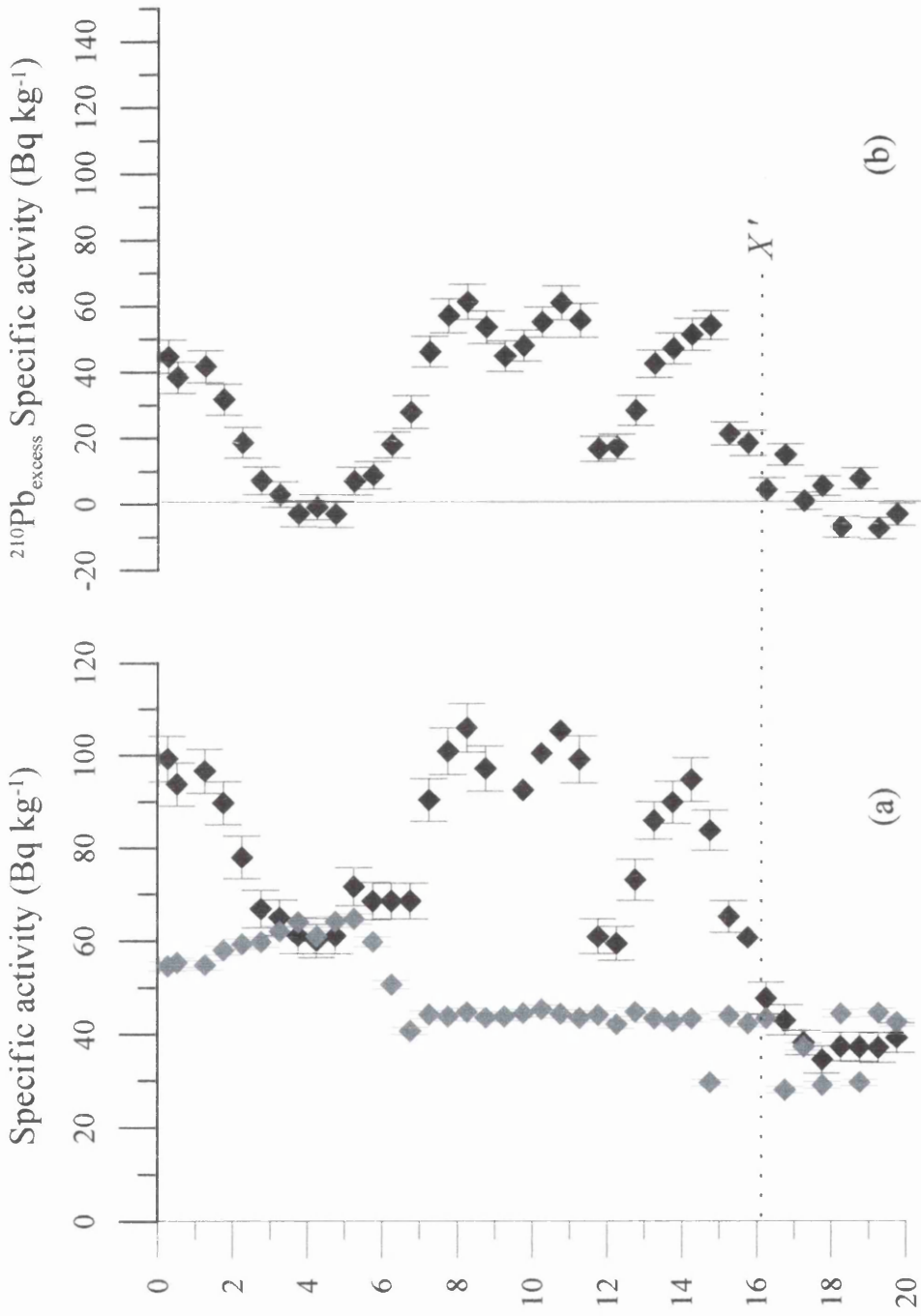


Fig. 3.9: (a) Total ²¹⁰Pb(♦) and ²²⁶Ra (♦) specific activity, and (b) ²¹⁰Pb_{excess} specific activity profiles for sub core C(ii). X' represents the best visual estimate of the depth of the mixed layer. The profile shows subsurface peaks in activity and is not suitable for calculation a D_B value.

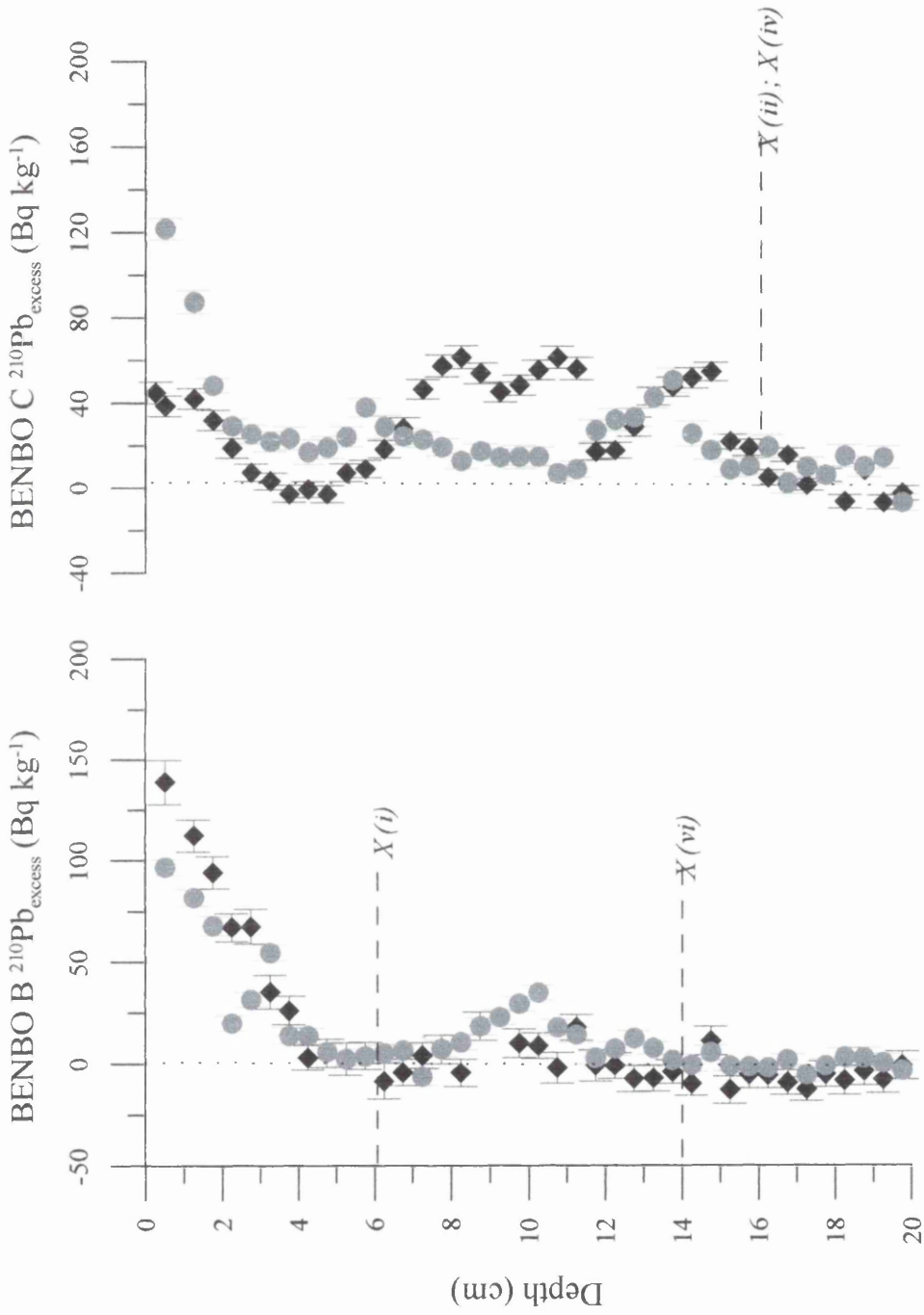


Fig. 3.10: Comparison between the initial (\blacklozenge) and replicate (\bullet) $^{210}\text{Pb}_{\text{excess}}$ profiles from BENBO sites B and C. Visual estimates for the SML depth are shown for all sub cores.

3.2.2 Inventory and flux calculations

Inventories of $^{210}\text{Pb}_{\text{excess}}$ in deep sea sediments are calculated using the equation:

$$I = \sum (\rho_i \cdot A^i_{\text{xs}} \cdot \Delta X_i) \quad (3.2)$$

Where I is the inventory of $^{210}\text{Pb}_{\text{excess}}$ (Bq cm^{-2}); ρ_i is the sediment dry bulk density of depth interval i (g cm^{-3}); A^i_{xs} is $^{210}\text{Pb}_{\text{excess}}$ specific activity of depth interval i (Bq g^{-1}); ΔX_i is the thickness of depth interval i (cm). This is related to the flux to the sediment by:

$$J = I \cdot \lambda_{\text{Pb-210}} \quad (3.3)$$

Where J is the mean annual $^{210}\text{Pb}_{\text{excess}}$ flux ($\text{Bq cm}^{-2} \text{y}^{-1}$) and $\lambda_{\text{Pb-210}}$ is the decay constant of $^{210}\text{Pb}_{\text{excess}}$ ($\ln 2/22.3 \text{y}^{-1}$). The inventories and fluxes from all sub cores are presented in Table 3.3. The variation between sites is consistent with the hypothesis that $^{210}\text{Pb}_{\text{excess}}$ inventory should increase with increasing water depth. The differences in inventory between sub cores of the same box core are smaller and most likely attributable to small-scale horizontal variations in bioturbation.

Table 3.3: $^{210}\text{Pb}_{\text{excess}}$ inventories and fluxes from BENBO sub cores. The water column depths from the sites are also shown.

Sub core	A(i)	B(i)	B(vi)	C(ii)	C(iv)
Inventory (Bq cm^{-2})	0.420	0.211	0.204	0.329	0.344
Flux ($\text{Bq cm}^{-2} \text{y}^{-1}$)	0.0131	0.0066	0.0063	0.0102	0.0106
Water depth (m)	3570	1100	1100	1925	1925

3.3 Man-made Radionuclides

3.3.1 ^{241}Am and ^{137}Cs

In sub cores A(i) and B(i), artificial radionuclides are above detection limits only in the uppermost samples, and as such, apparently penetrate only a few centimetres (Figs. 3.11 and 3.12; Appendix Tables A8 and A9). Maximum activities in A(i) are $1.65 \pm 0.54 \text{ Bq kg}^{-1}$ for ^{137}Cs and $1.50 \pm 0.45 \text{ Bq kg}^{-1}$ for ^{241}Am , and in B(i), $2.28 \pm 0.52 \text{ Bq kg}^{-1}$ for ^{137}Cs and $1.77 \pm 0.56 \text{ Bq kg}^{-1}$ for ^{241}Am . The apparent reappearance of ^{241}Am activity in some samples in the lower section of A(i) is attributed to a higher activity of NDS radionuclides in the clay-rich sediment. Specifically, increases in the activity of the ^{234}Th peak at 63 keV may interfere with the ^{241}Am energy region.

The artificial radionuclides in sub core C(ii) closely follow the distribution pattern established by $^{210}\text{Pb}_{\text{excess}}$ (Fig. 3.13; Appendix Table A10). The highest activities, of $3.04 \pm 0.42 \text{ Bq kg}^{-1}$ for ^{137}Cs and $0.84 \pm 0.18 \text{ Bq kg}^{-1}$ for ^{241}Am , are found within the region of the $^{210}\text{Pb}_{\text{excess}}$ subsurface peak. The artificial radionuclides in the replicate sub cores B(vi) and C(iv) also reappear in concordance with the $^{210}\text{Pb}_{\text{excess}}$ profiles (Figs. 3.14 and 3.15; Appendix Tables A11 and A12).

The low activities and high errors of the ^{137}Cs and ^{241}Am measurements imply that the calculation of the inventories and fluxes of these radionuclides using equations (3.2) and (3.3) above will be somewhat uncertain. Estimates of the range of inventories and fluxes are made in Chapter 4, section 4.1.4.

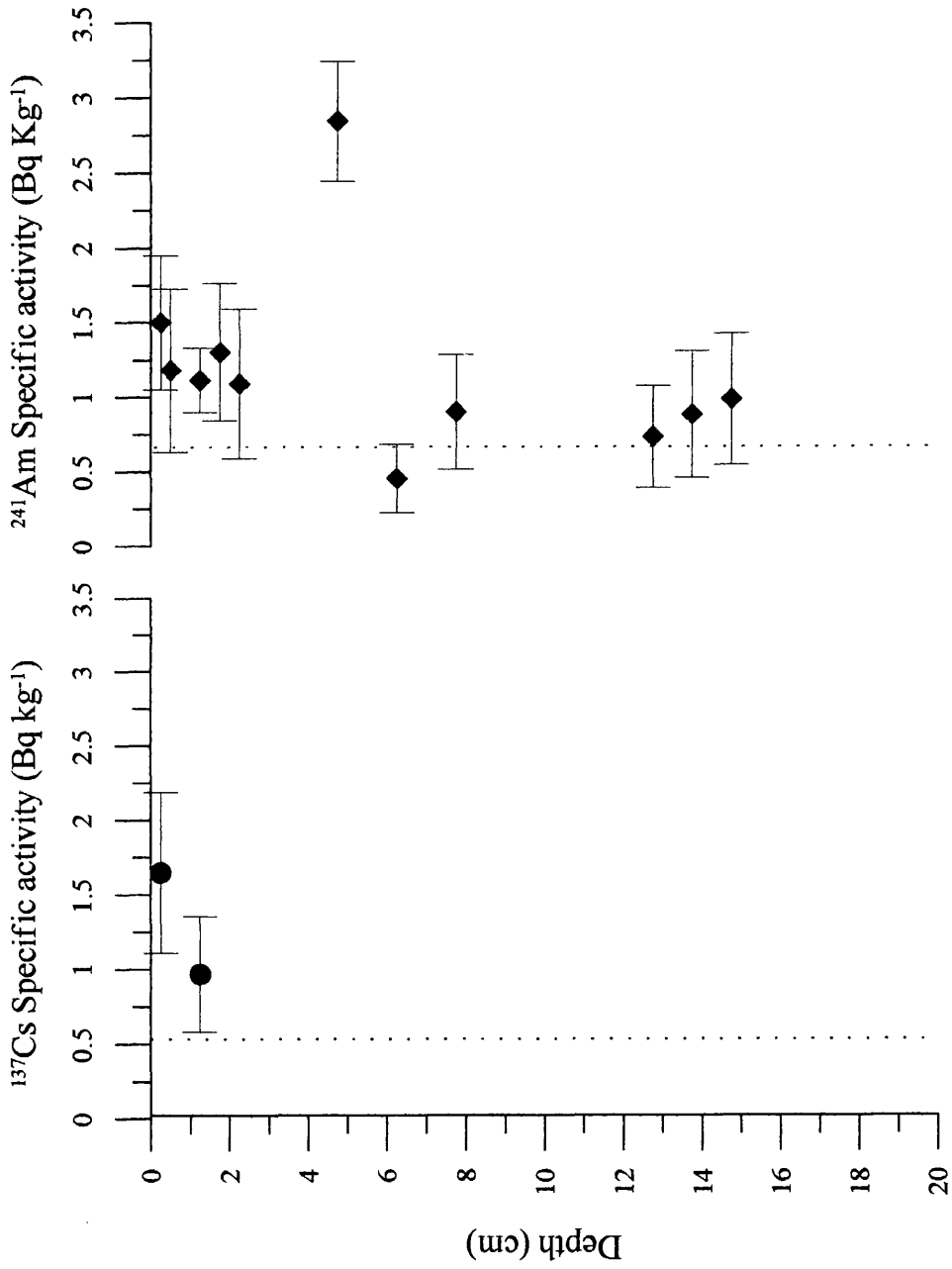


Fig. 3.11: Man-made radionuclides ^{137}Cs (●) and ^{241}Am (◆) specific activities in sub core A(i). Absence of data indicates that measured activities are below detection limits, which are indicated by the dotted lines on the profiles.

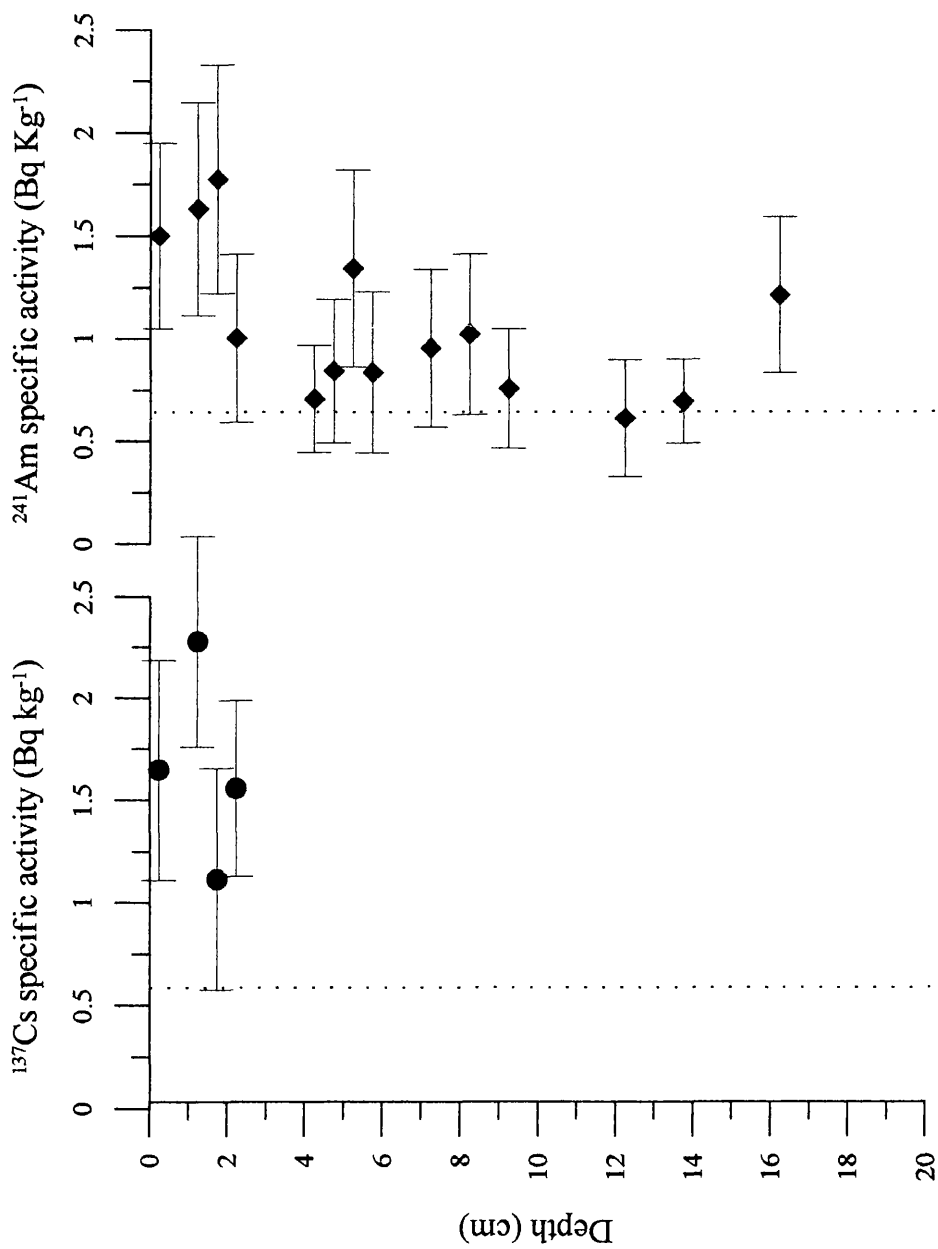


Fig. 3.12: Man-made radionuclides ^{137}Cs (●) and ^{241}Am (◆) specific activities in sub core B(i). Absence of data indicates that measured activities are below detection limits, which are indicated by the dotted lines on the profiles.

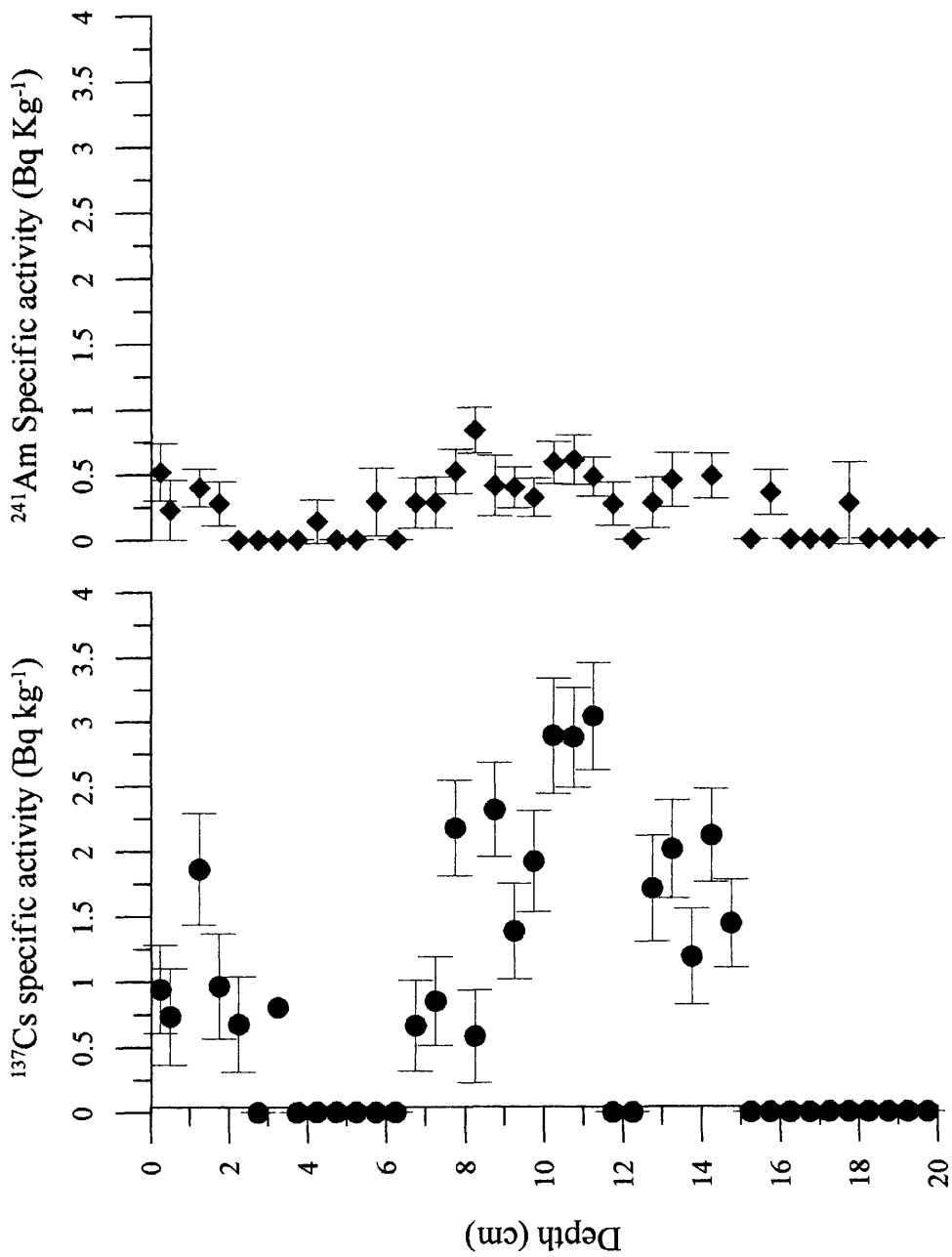


Fig. 3.13: Man-made radionuclides ^{137}Cs (●) and ^{241}Am (◆) specific activities in sub core C(ii). Data where the activity is below the detection limits is shown on the plot as zero activity...

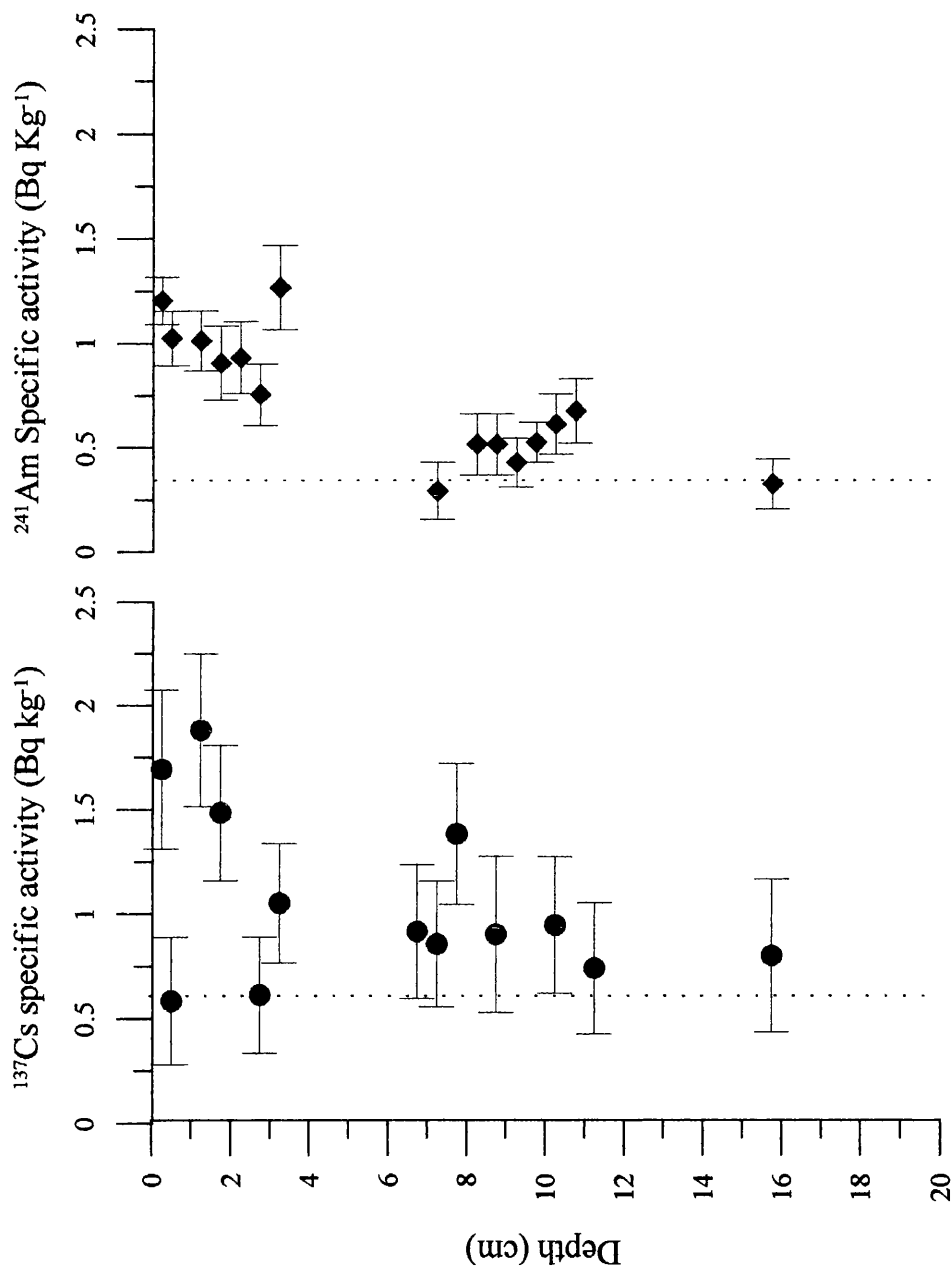


Fig. 3.14: Man-made radionuclides ^{137}Cs (\bullet) and ^{241}Am (\blacklozenge) specific activities in the replicate sub core B(vi). Absence of data indicates that measured activities are below detection limits, which are indicated by the dotted lines on the profiles.

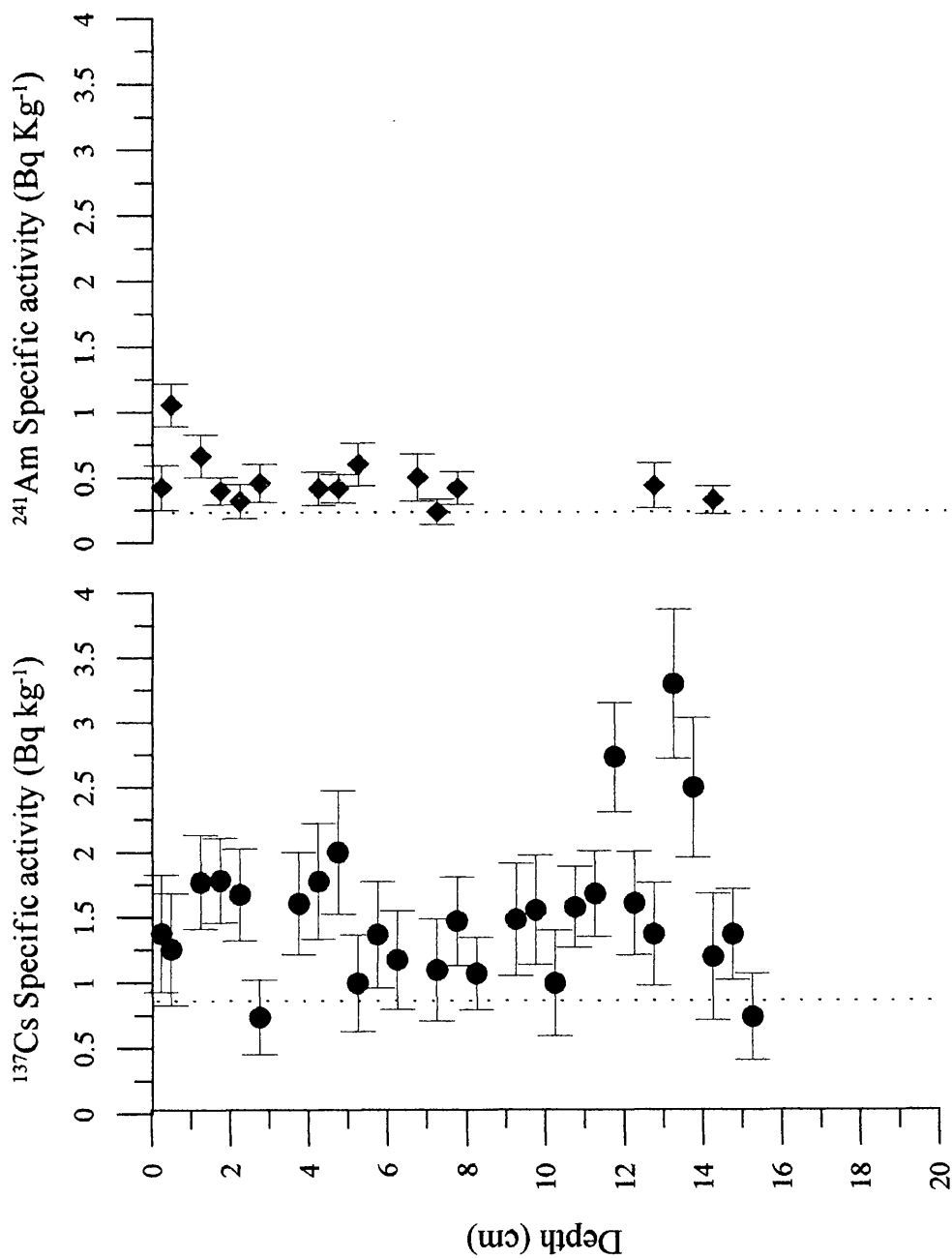


Fig. 3.15: Man-made radionuclides ^{137}Cs (●) and ^{241}Am (◆) specific activities in the replicate sub core C(iv). Absence of data indicates that measured activities are below detection limits, which are indicated by the dotted lines on the profiles.

3.3.2 ^{238}Pu and $^{239,240}\text{Pu}$

The plutonium analyses were not completed on all cores due to the timescale of the project. The available data, from sub cores B(i) and C(ii), are tabulated in Table A13 in the Appendix, and the $^{239,240}\text{Pu}$ and ^{238}Pu profiles for B(i) are shown in Fig 3.16.

At site B, the profile is initially similar to that of $^{210}\text{Pb}_{\text{excess}}$, but a small subsurface peak in activity of both $^{239,240}\text{Pu}$ and ^{238}Pu is evident at a depth of 12 cm. Plutonium activity is detectable to a depth of 14 cm, so that the depth of the SML determined from this method is midway between that determined from $^{210}\text{Pb}_{\text{excess}}$ and ^{14}C .

The presence of the subsurface peak implies advective mixing has occurred. However, the absence of $^{210}\text{Pb}_{\text{excess}}$ to this depth in the core suggests that the peak is relict. Therefore, despite this evidence of subsurface mixing, the D_B was determined for both pulse input and constant input functions. For pulse input, the radionuclide profile is determined from:

$$A_x = \frac{M}{(\pi \cdot D_B \cdot t)^{1/2}} \cdot e^{(-x^2/4 \cdot D_B \cdot t)} \quad (3.4)$$

Where A_x is the radionuclide activity at depth x , M is the total activity of the radionuclide deposited per unit area, and t is the time between radionuclide input and sample collection.

Where the radionuclide input is constant over time, the equation is:

$$A_x = 2 \cdot q \cdot \left(\frac{t}{D_B \cdot \pi} \right)^{1/2} \cdot \left[e^{(-x^2/4 \cdot D_B \cdot t)} - \frac{x}{2} \cdot \left(\frac{\pi}{D_B \cdot t} \right)^{1/2} \cdot \text{erfc} \left[x / 2(D_B \cdot t)^{1/2} \right] \right] \quad (3.5)$$

where q is the annual radionuclide input and erfc is the error function complement. Both equations are modified from Cochran (1985).

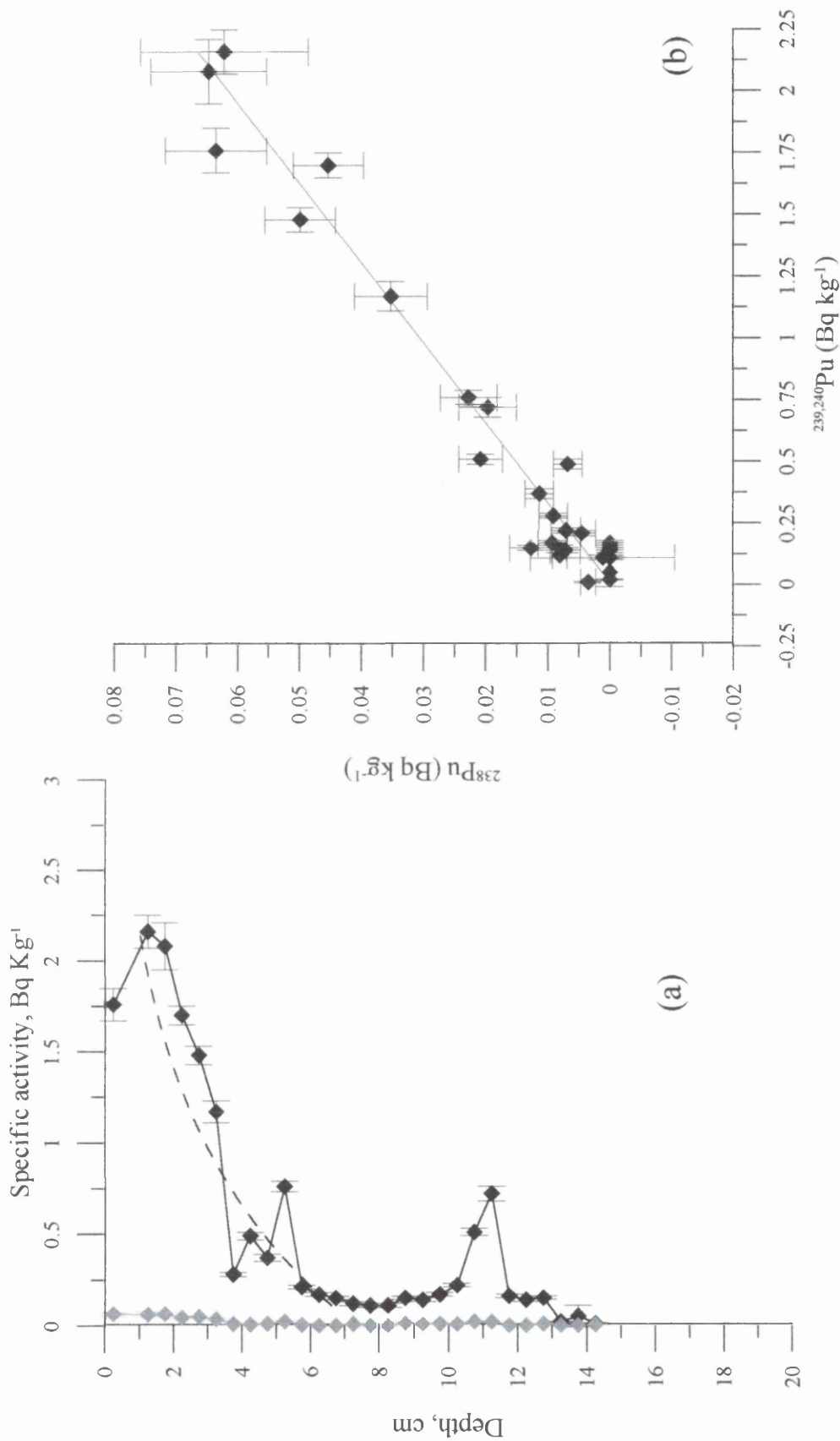


Fig 3.16: (a) ^{239,240}Pu (◆) and ²³⁸Pu (♦) activity profiles for BENBO sub core B(i). The dashed line represents the best exponential fit of the ^{239,240}Pu in the upper 8 cm. (b) Plot of ^{239,240}Pu specific activity to ²³⁸Pu specific activity in sub core B(i). The gradient of the best fit straight line is 0.0309; $R^2 = 0.96$

In order to determine values of D_B which best fit the sub core B(i) data, models of A_x versus depth were generated using both methods above for different values of D_B . These curves were compared with the best fit curve generated from an exponential fit of the $^{239,240}\text{Pu}$ data with depth in the top 8 cm (Fig. 3.16); i.e. the region identified by $^{210}\text{Pb}_{\text{excess}}$ as the SML. The D_B values obtained were $0.0136 \text{ cm}^2 \text{ y}^{-1}$ for the pulse input model and $0.0645 \text{ cm}^2 \text{ y}^{-1}$ for the continuous input model.

3.4 Burrow Sediments

Table 3.4 illustrates the ^{14}C and $^{210}\text{Pb}_{\text{excess}}$ activities of faecal material belonging to infaunal burrowing organisms, and associated material from the burrow linings, surrounding sediment and surface sediment. It is clear that the $^{210}\text{Pb}_{\text{excess}}$ specific activity in the faecal material in all three cores is at least an order of magnitude higher than the surrounding ambient sediment. At site C, the specific activity of the faecal material was 50-70% of that of the surface activity, whilst at site B, faecal pellet activity exceeded that of the surface sediment. Sediment rich in $^{210}\text{Pb}_{\text{excess}}$ was also incorporated into burrow lining material at site B.

The results of AMS ^{14}C analysis of faecal pellets and surrounding sediment from cruise CD113, site C are shown in relation to the bulk carbonate profile for CD107 C(ii) in Fig. 3.19. The surface sediment and faecal pellet material radiocarbon ages agree well with those of the bulk carbonate at the corresponding depth in CD107 C(ii). However, the surrounding sediment from the same depth as the faecal pellets is 1310 y older.

Table 3.4: $^{210}\text{Pb}_{\text{excess}}$ and radiocarbon analyses of material derived from biological structures and deposits found in box cores from BENBO sites B and C, collected on cruises CD111 and CD113. ‘Surrounding sediment’ refers to the well-mixed sediment collected from the same depth as the biological materials. *BDL* = below detection limit

Cruise/Site	CD111 site C	CD113 site C	CD113 site B
Sample description			
$^{210}\text{Pb}_{\text{excess}}$ (Bq kg^{-1})			
Surface sediment	402 ± 14	401 ± 54	260 ± 50
Faecal pellets	220 ± 29	274 ± 117	351 ± 78
Surrounding sediment	<i>BDL</i>	<i>BDL</i>	<i>BDL</i>
Green burrow lining			142 ± 26
<i>Radiocarbon</i> (γ BP)			
Surface sediment	2780 ± 50		
Faecal pellets	2700 ± 50		
Surrounding sediment	4070 ± 50		

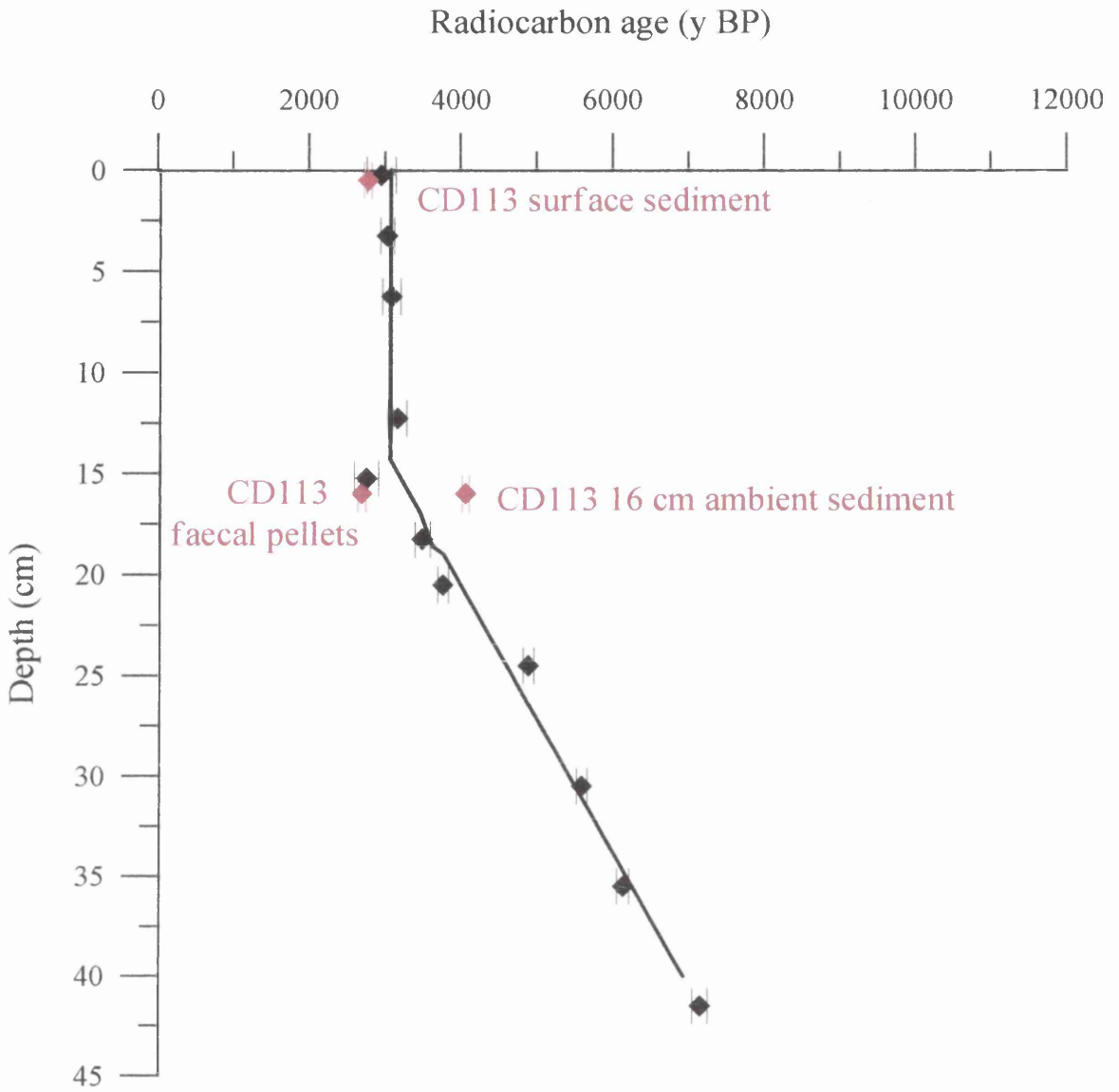


Fig. 3.17: Comparison of ^{14}C data from faecal pellets and associated material from BENBO site C, collected on cruise CD113, with the bulk carbonate data from subcore BENBO C(ii), collected on cruise CD107. The black line indicates the ^{14}C age model for site C as determined from the bulk carbonate data from C(ii) using the model of Erlenkeuser (1980).

Chapter 4 - Discussion

4.1 Sedimentary processes and fluxes to sediment

4.1.1 Sedimentation - BENBO B and C

The bulk carbonate radiocarbon profiles of BENBO B and C are, on first inspection, typical of model deep sea carbonate profiles with uniform sedimentation rates and homogenous mixed layers (Fig. 3.1). Taking bioturbation into account (Table 3.1), deposition of all the material in the BENBO B and C box cores occurred within the Holocene. This is in agreement with the uniform sediment accumulation rates established for these cores. The sediment accumulation rate at BENBO site B is 4.4 cm ky^{-1} , at the upper end of the range quoted by Balsam and McCoy (1987) as being typical of the North East Atlantic, whilst that at BENBO C is 6.5 cm ky^{-1} , comparable to the faster accumulation rates measured in the Rockall Plateau area (e.g. Thomson *et al.* 1993; Keigwin and Jones 1989; Duplessey *et al.* 1986). Sediment composition data (Thomson *et al.* 2000) indicate that BENBO B sediment is a carbonate ooze, with a mean CaCO_3 content of $79.6 \pm 1.9 \%$, typical of North East Atlantic Holocene sediments, however, BENBO C is a marl, with only $54.0 \pm 2.6 \%$ mean CaCO_3 content (Fig. 4.1). Similar low carbonate contents have been recorded in other samples from the Feni Drift (Keigwin and Jones 1989). The carbonate fluxes are similar for both sites, at $2.56 \text{ g cm}^{-2} \text{ ky}^{-1}$ for B and $2.43 \text{ g cm}^{-2} \text{ ky}^{-1}$ for C; thus, the additional flux to site C must be predominantly non-carbonate, lithogenic material. Selected samples from the three BENBO cores were analysed for particle size distribution and composition (Table 4.1; I.N. McCave, pers. comm.). The sortable silt (*ss*) ($10\text{-}63 \text{ }\mu\text{m}$) content and mean diameter have been used as a

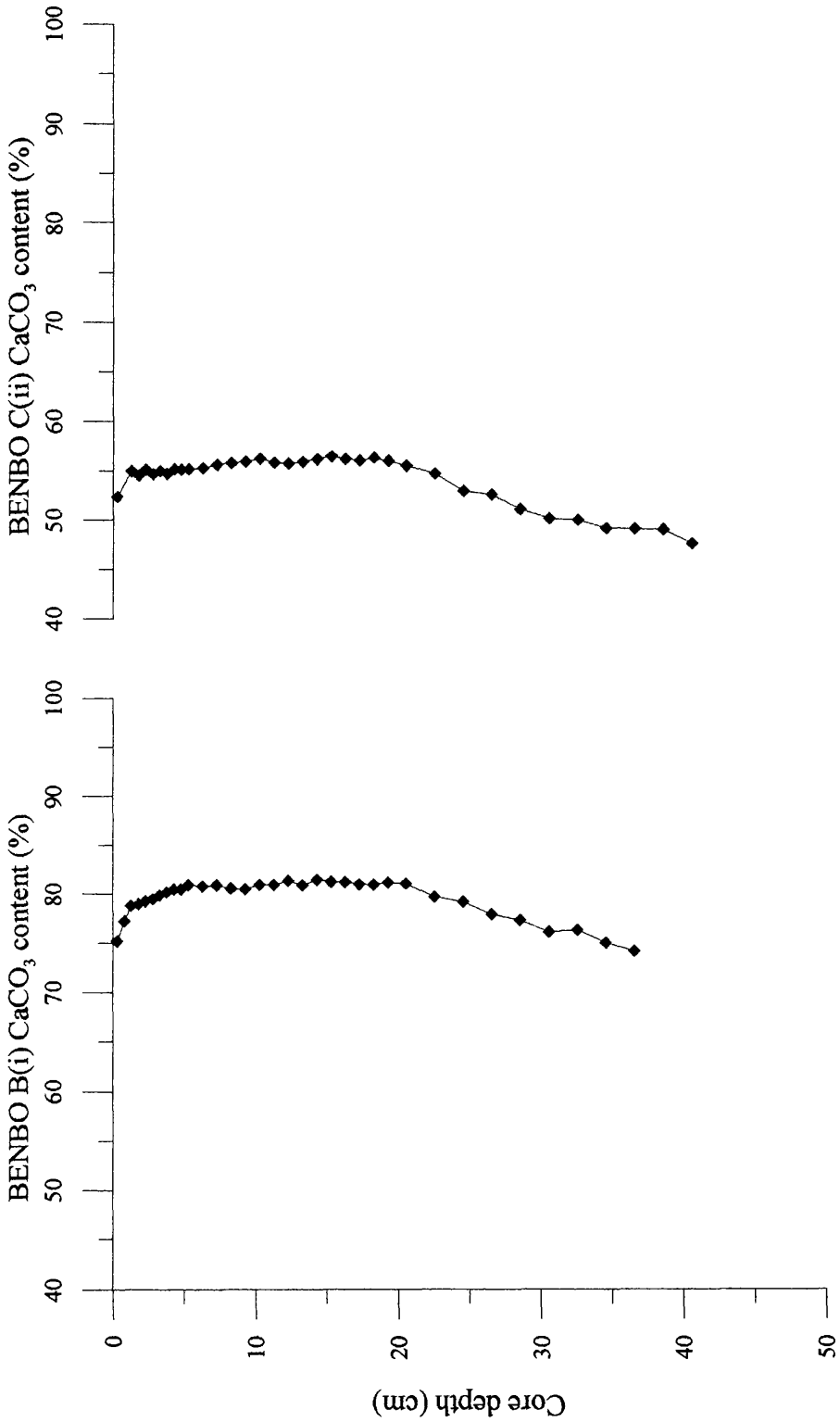


Fig 4.1: Calcium carbonate content in BENBO sub cores B (i) and C (ii). CaCO₃ content was determined from the quantity of CO₂ evolved from hydrolysis of the sediment with 10% (v/v) H₃PO₄. Data supplied by S.Nixon and J.Thomson, Southampton Oceanography Centre.

guide to estimate qualitatively the bottom current strength (Wang and McCave 1990; McCave *et al.* 1995). The underlying principle of this approach is that faster bottom currents both deposit less fine sediment and are more likely to winnow previously deposited sediment, resulting in lower *ss* content and a higher mean grain size diameter. The low percentage of *ss* and mean diameter of sediment at BENBO site C, relative to BENBO B, thus indicates weaker current control and thus a greater propensity to deposit fine silt and clay-sized material. Bottom currents in the Feni Drift region are dominated by the northward-flowing AABW (Antarctic Bottom Water) and southward-flowing NADW (North Atlantic Deep Water); however, the initial growth of Feni Drift has been linked with increased flow of Norwegian Sea Deep Water (NSDW) over the Wyville-Thomson Ridge. Howe (1996) notes that increased sedimentation on the drift occurred at the beginning of the Holocene as the NSDW increased as a result of surface warming. Therefore, it seems likely that the source of additional sediment to site B is deposited by southward-flowing bottom currents slowing at the boundary of the Rockall Bank, as described in Section 1.3.

The SML depths at BENBO sites B and C, as defined by the radiocarbon profiles (i.e. on the thousand-year timescale), are 18 cm and 16 cm respectively. This is significantly deeper than the global mean SML thickness of 9.8 ± 4.5 cm (Boudreau 1994), and the apparent 8 cm SML at site A. Trauth *et al.* (1997) demonstrated a 2 cm increase in SML thickness for every $1 \text{ g C m}^{-2} \text{ y}^{-1}$ increase in organic carbon flux. Empirically, the positive

Table 4.1 (overleaf): Particle size distribution and characteristics of selected sediment depths from the three BENBO sites. Analyses carried out by Prof. I.N. McCave, University of Cambridge.

Sample	total >63 μm	total <63 μm	total % CaCO ₃	>63μm % CaCO ₃	<63μm % CaCO ₃	total ss mean wt.%	total ss mean diam.μm	total silt/clay	CO ₃ -free ss mean wt.%	CO ₃ -free ss mean diam.μm	CO ₃ -free silt/clay
A-1.5	55.82	44.18	72.64	80.48	62.7	11.3	15	0.85	15.3	15.7	2.35
A-9.5	34.95	65.05	64.13	76.56	57.5	12.9	18.2	0.87	11.6	22.8	0.67
A-17.5	9.17	90.83	31.34	16.21	21.9	22.9	23.2	2.01	8.8	16.8	0.85
A-26.5	33.5	66.5	31.16	28.77	17.3	21.9	23.7	2.15	14.2	19.6	0.61
A-33.5	0.1	99.9	16.22	indet.	14.4	4.5	17.1	0.47	1.5	indet.	0.27
B-1.5	55.82	44.18	72.64	80.48	62.7	11.3	15	0.85	15.3	15.7	2.35
B-10.5	34.95	65.05	64.13	76.56	57.5	12.9	18.2	0.87	11.6	22.8	0.67
B-17.5	9.17	90.83	31.34	16.21	21.9	22.9	23.2	2.01	8.8	16.8	0.85
B-25.5	33.5	66.5	31.16	28.77	17.3	21.9	23.7	2.15	14.2	19.6	0.61
B-32.5	0.1	99.9	16.22	indet.	14.4	4.5	17.1	0.47	1.5	indet.	0.27
C-1.5	9.77	90.23	54.72	69.38	53.1	10.8	17	1.24	13.4	16	1.35
C-9.5	12.79	87.21	55.84	70.44	53.7	10.8	15.6	1.02	13.8	17	0.88
C-17.5	11.23	88.77	55.98	88.76	51.8	11.6	17.2	1.35	11.2	14.1	0.85
C-26.5	9.82	90.18	52.57	98.76	47.5	15.7	19.9	0.97	14	18.1	0.8
C-33.5	10.65	89.35	49.53	74.31	46.6	11	16.3	1.03	15.7	18.1	1.5

relationship between C_{org} and SML depth holds for BENBO sites. Higher C_{org} fluxes would be expected at BENBO B and C relative to A, as less degradation of organic material should occur at intermediate water depths (Sarnthein *et al.* 1992), and the flux to site C is augmented by current deposition, as discussed above. Table 4.2 shows the relationship between C_{org} fluxes and SML depth for BENBO sites, calculated from material collected in BENBO water column traps for sites A and B. Both sites have deeper SML depths than predicted by this model (Fig. 4.2), and the BENBO data also suggest a larger increase in SML per unit increase in C_{org} . However, Trauth *et al.* (1997) estimated their C_{org} fluxes from a productivity-water depth equation (Sarnthein *et al.* 1992), whereas the C_{org} data used in this study were derived directly from sediment traps. Furthermore, Trauth *et al.* (1997) considered only data from sites below 2000 m water depth, and it may be that the relationship does not hold for shallower depths.

The age of freshly arriving material at the sediment surface, T_0 , for sub core C(ii) is 1100 y, older than the 400 y expected from the reservoir age of pelagic carbonates in this region. This is consistent with the input of current redistributed sediment with a carbonate component in excess of that of the pelagic flux. Assuming the radiocarbon age of the direct pelagic flux to the sediment has the surface ocean reservoir age of 400 y, the percentage of redistributed carbonate can be estimated from:

$$e^{-\lambda \cdot T_0} = (1 - f) \cdot e^{-\lambda \cdot T_{pelagic}} + f \cdot e^{-\lambda \cdot T_{old}} \quad (4.1)$$

Table 4.2: Organic carbon fluxes and SML depths for BENBO sites A and B. The C_{org} fluxes were calculated from sediment trap fluxes at 100 metres above bottom (m.a.b), supplied by Emily Good, University of Edinburgh. Mean and maximum values for C_{org} flux are shown because of the seasonal nature of North East Atlantic primary productivity. The irregular ^{14}C profile of site A means the SML depth is the visual estimate from the $^{210}Pb_{excess}$ profile - this is therefore a minimum value for the long term (^{14}C) SML. The SML depth quoted for site B is that derived from bulk carbonate radiocarbon data.

Mean A 100 m.a.b. C_{org} flux ($g\ C\ m^{-2}\ y^{-1}$)	0.643
Max A 100 m.a.b C_{org} flux ($g\ C\ m^{-2}\ y^{-1}$)	0.913
A SML depth ^a (cm)	8
Mean B 100 m.a.b C_{org} flux ($g\ C\ m^{-2}\ y^{-1}$)	1.396
Max B 100 m.a.b C_{org} flux ($g\ C\ m^{-2}\ y^{-1}$)	2.114
B SML depth ^b (cm)	18
Mean A/B C_{org}	0.46
Max A/B C_{org}	0.43
A/B SML depth	0.44

where λ is the ^{14}C decay constant determined from $\ln 2$ /Libby half life; f is the fraction of the sediment composed of old carbonate, $T_{pelagic}$ the conventional radiocarbon age of the pelagic carbonate, and T_{old} the conventional radiocarbon age of the old carbonate.

To estimate the fraction of 'old' carbonate flux to the site, two circumstances will be considered. In the first, T_{old} consists of eroded infinite age sediment, i.e. $T_{old} = \infty$. For site C, with a T_0 age of 1110 y, 8 %, or $0.2\ g\ cm^{-2}\ ky^{-1}$, of the total carbonate flux is T_{old} . In the

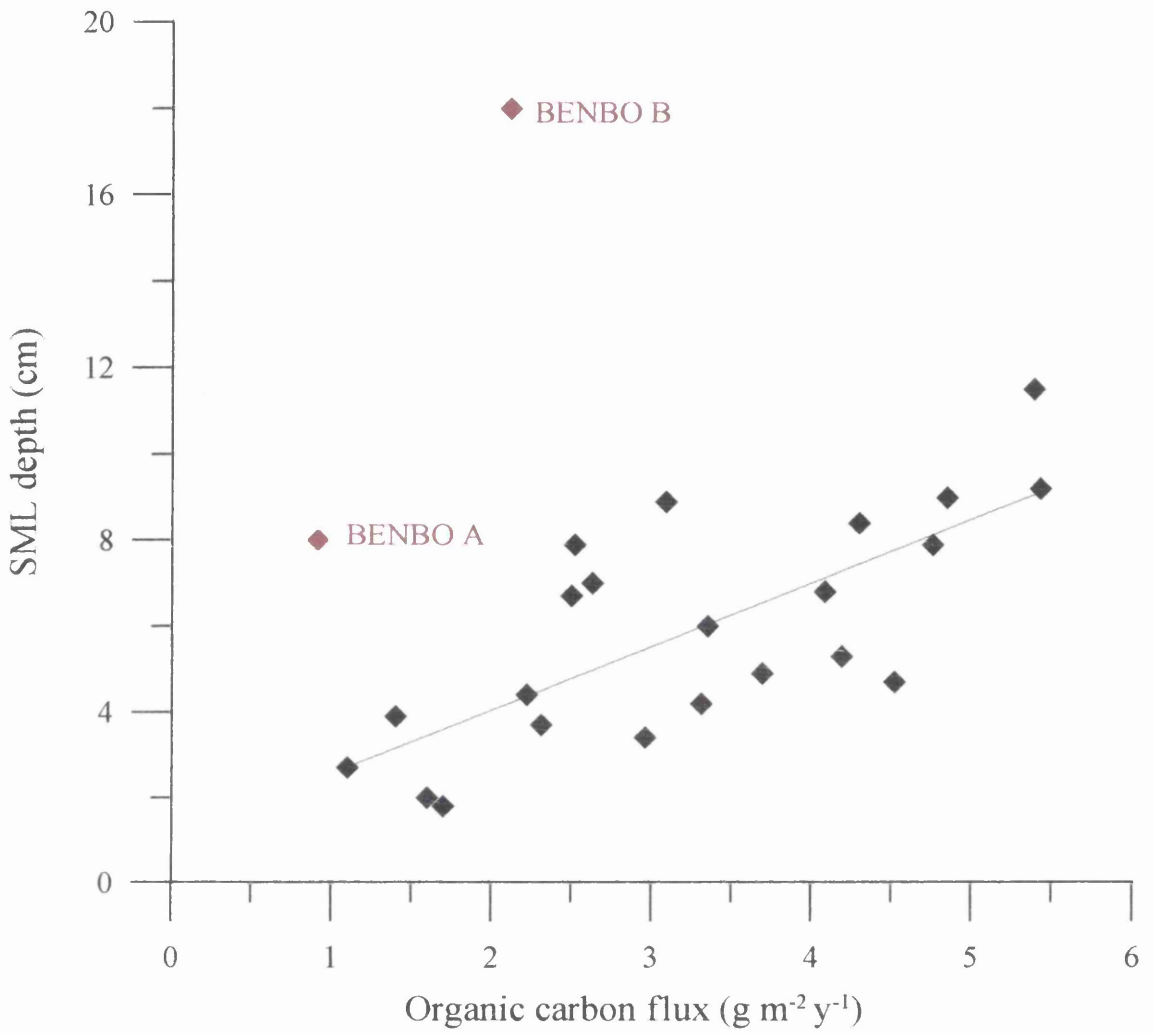


Fig 4.2: The relationship of mixed layer thickness versus organic carbon flux at BENBO sites (highlighted in red), compared with data from previously published studies summarised in Trauth *et al.* (1995). No sediment trap data was available for site C.

second situation, the redistributed sediment is eroded from a model North East Atlantic site with a 10 cm homogenised SML and sedimentation rate of 4 cm ky^{-1} . The age of T_{old} in this case would be equal to the T_{ML} of 2900 y of the hypothetical site (calculated from $X/s + \text{reservoir age}$). In this scenario, 31% of the carbonate flux is derived from T_{old} .

The radiocarbon profile from B(i) gives a T_0 value of -660 y, rather than the expected age of 400 y. Unusually low T_0 values have been observed in a few other cores (e.g. Erlenkeuser 1980; Trauth *et al.* 1995), but no explanation as to the cause has been offered. Analysis of recognised standard materials during the sample run produced acceptable values, and it can be inferred that there is no sample contamination or other analytical interferences (TIRI K turbidite = $18\,080 \pm 110$ y BP (lab ID number GU-8847), compared with consensus value of 18 115 y BP; doublespar calcite background sample = $>45\,000$ y BP (lab ID number BK-44)). Rather, the negative T_0 age must indicate that, despite the apparently steady state ^{14}C profile, sediment accumulation at this site is subject to non-steady state processes. A possible interpretation of this result is given in section 4.2.3.

4.1.2 Sedimentation - BENBO A

The ^{14}C age-depth and CaCO_3 content-depth profiles from BENBO A (Fig. 3.2 and Table A1) indicate glacial-age sediments composed primarily of non-carbonate material overlain disconformably by Holocene carbonate ooze. This dissimilarity in composition between Holocene and glacial sediments has been noted at other locations in the North East Atlantic (Balsam and McCoy 1987; Bacon 1984). The hiatus between the two sediment components implies that either sedimentation ceased for a period of time, or that deposited

BENBO site A sub core i

BENBO site A sub core iii

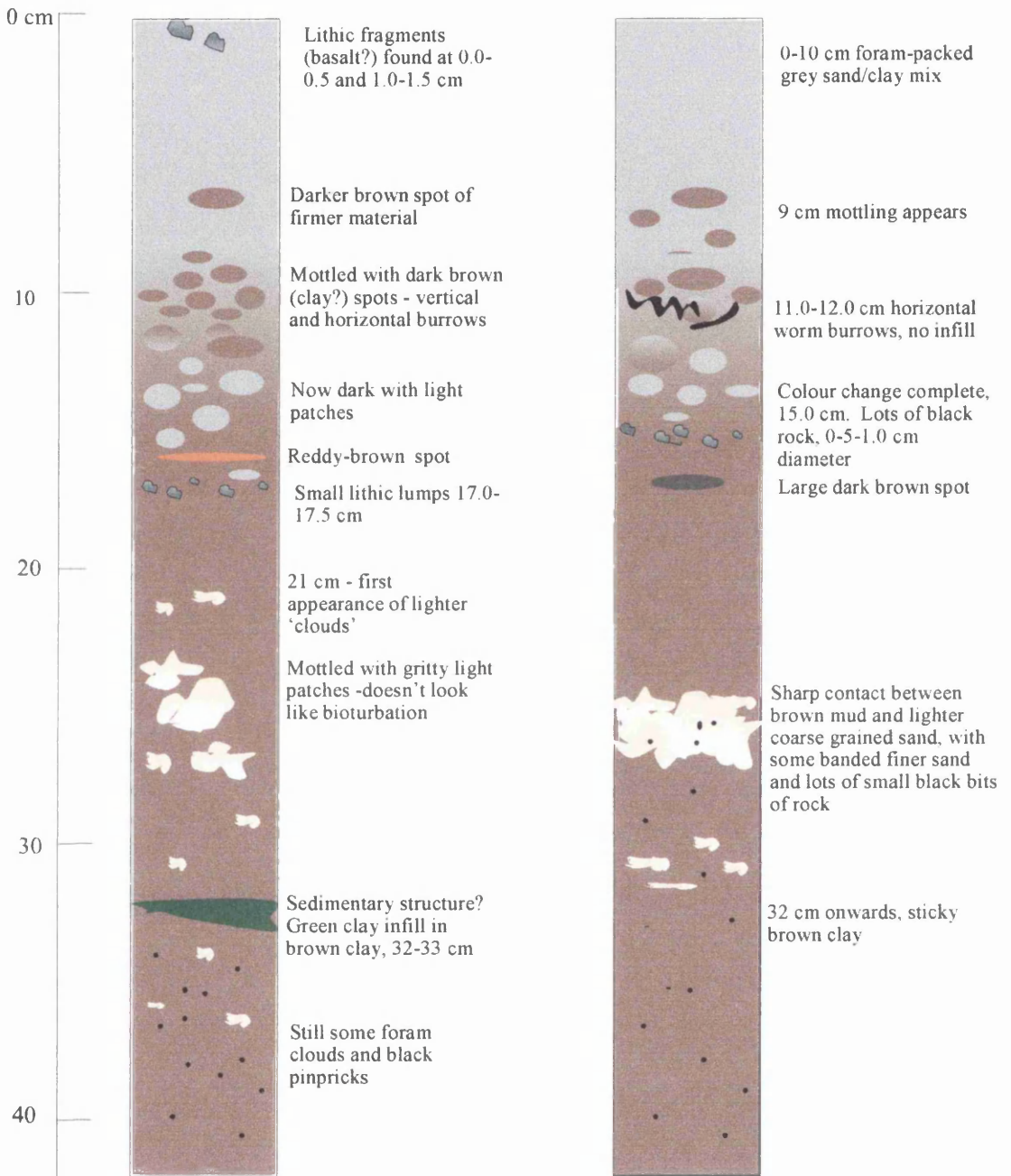


Fig. 4.3: Core logs recorded during extrusion of sub cores at 0.5 cm resolution from 0 cm to 20 cm, and 1 cm resolution thereafter, showing sedimentary structures, compositional changes and redox changes.

sediment has been removed.

The particle size and composition data (Table 4.1) for samples below the radiocarbon age hiatus at Site A (17-18 cm and 26-27 cm) do not show a typical size distribution signature of sediment winnowing, although the relatively low fraction of sortable silt may be a result of strong currents preventing silt deposition. However, these samples are unusual in that the coarse ($> 63 \mu\text{m}$) fractions contain only 16.2 % and 28.8 % CaCO_3 respectively, so over 70% of the coarse fraction below the unconformity has a terrigenous source. The logs for the two BENBO A sub cores (Fig. 4.3) show foram 'clouds' embedded in the clay between 24 cm and 28 cm. Deposition (and preservation - indicating the disturbance has a Holocene origin) of marine carbonates must have occurred, but then been disturbed by benthic currents. A 2 m long Kastenlot core from the same site also contained a turbidite at a depth below that to which the box cores extended (J. Thomson, pers. comm.), confirming this type of disturbance occurred in this area previously. It seems most likely that the sediment between 17 000 and 6000 y BP has been removed by an erosive event such as slumping or a turbidity current. Above the unconformity, the particle size analyses reveals that the 1-2 cm and 9-10 cm increments are also coarse grained, but in these samples the coarse fraction is $>75\%$ carbonate, more typical of modern deep ocean sediments. The sortable silt content in these two samples is low, at 11.3% and 12.9% respectively, and may indicate winnowing and strong currents in the area at present.

Bioturbation between the Holocene and glacial age sediment resulted in mixing of the two sediment types. This is evident from the excellent correlation seen between 0-22 cm on a

plot of CaCO₃ content against Ti content (Fig. 4.4a), where Ti is assumed to represent the proportion of lithogenic material in the sediment. The timing of resumption of sedimentation can be estimated from the mixing of the carbonate and clay sediments, if it is assumed the age of each depth increment is a composite of the ‘new’ Holocene carbonate and the ‘old’ glacial clay. The ¹⁴C age and CaCO₃ content of the glacial end member are 20 580 y and 21.1 %, determined from the mean of the four points from 16-22 cm which fit well to the CaCO₃-Ti regression line. The CaCO₃ content of the Holocene end-member is taken as 76.1 %, the value for the uppermost data point at 0-1 cm. The fraction of new sediment in a layer can then be calculated using:

$$f = \left[\frac{(\%CaCO_3)_{\text{sample}} - (\%CaCO_3)_{\text{old}}}{(\%CaCO_3)_{\text{new}} - (\%CaCO_3)_{\text{old}}} \right] \quad (4.2)$$

where (%CaCO₃)_{sample} is the percentage carbonate composition of the sample sediment, (%CaCO₃)_{new} represents the percentage of CaCO₃ in the ‘new’ end-member, and (%CaCO₃)_{old} represents the percentage of CaCO₃ in the ‘old’ end-member. The age of the new fraction is then be determined from:

$$e^{-\lambda \cdot t_{\text{new}}} = \frac{\left[e^{-\lambda \cdot t_{\text{measured}}} - (1-f) \cdot e^{-\lambda \cdot t_{\text{old}}} \right]}{f} \quad (4.3)$$

where t_{measured} is the radiocarbon age of the sample, t_{new} is the mean radiocarbon age of the bioturbated Holocene sediment found in the upper core, and t_{old} is the mean radiocarbon age of the four points between 15 and 22 cm which lie on the CaCO₃-Ti regression line. The ‘new’ fraction radiocarbon ages thus determined for 0-12.5 cm lie between 2970 y and 3380 y, with no obvious trend with depth (Fig. 4.4b). The time since the resumption of sediment deposition is estimated at twice the mean value of the new fraction age,

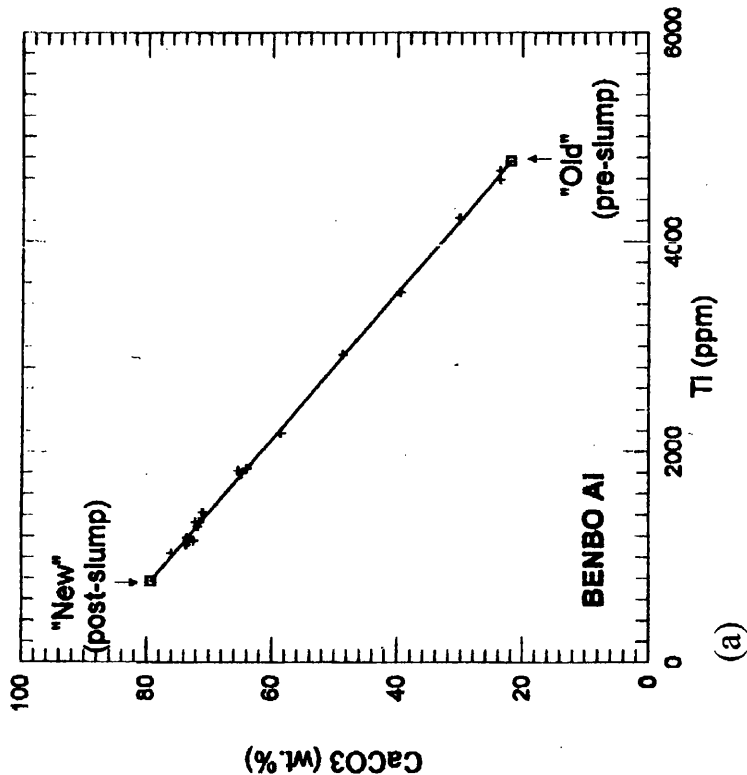
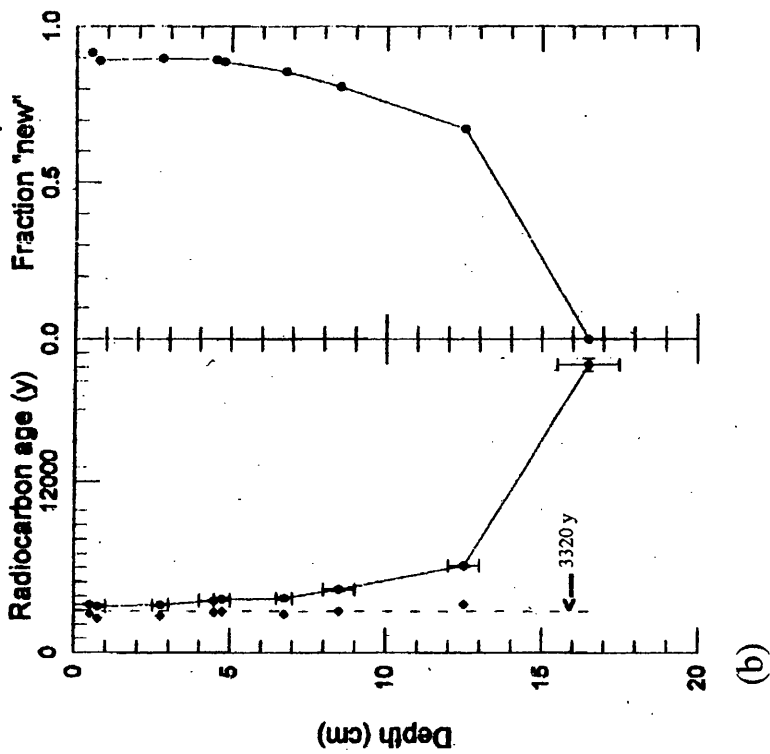


Fig. 4.4: (a) BENBO site A, plot of CaCO₃ content against titanium content for samples in the depth range 0 cm to 22 cm. It is assumed that the sediment in these sections is a composite of the new, carbonate-rich end member, and the old, clay rich end member.

(b) The fraction 'new' sediment and deconvoluted radiocarbon age of samples from 0-17 cm in BENBO core A(i). Radiocarbon ages, in y BP, are determined from equation (4.3). Both figures are derived from Thomson *et al.* 2000.

corrected for the surface ocean reservoir effect, i.e. $2 \cdot (3320 - 400) = 5840$ y BP.

Using a mean sediment density of 0.71 g cm^{-3} from the 0 cm to 12.5 cm section, it can be calculated that 8.7 g cm^{-2} of sediment has been deposited since this time, corresponding to a mean sediment flux of $1.5 \text{ g cm}^{-2} \text{ ky}^{-1}$ or a sedimentation rate of 2.1 cm ky^{-1} . Therefore, approximately 30 cm of glacial and early Holocene sediment, accumulated between 20580 y and 5840 y, has been removed. This value is likely to be a lower estimate, as North Atlantic glacial-age sedimentation rates are typically higher than those in the present day.

4.1.3 $^{210}\text{Pb}_{\text{excess}}$ and sediment fluxes

The $^{210}\text{Pb}_{\text{excess}}$ inventories calculated for the BENBO sites are listed in Table 3.3, and show increasing $^{210}\text{Pb}_{\text{excess}}$ inventory with increasing water depth. This is in agreement with the hypothesis that the approximately 10^2 year residence time of ^{210}Pb in the deep water column enables scavenging of the radionuclide onto sinking particles. There is close agreement between the $^{210}\text{Pb}_{\text{excess}}$ inventories determined for the sub core pairs at sites B (0.211 and $0.204 \text{ Bq g}^{-1} \text{ y}^{-1}$) and C (0.329 and $0.344 \text{ Bq g}^{-1} \text{ y}^{-1}$). Other studies have explained a variation between replicate sub cores as a result of heterogeneous horizontal redistribution of $^{210}\text{Pb}_{\text{excess}}$ by bioturbation, (Brand and Shimmiel 1991), but the similarity between the replicates at the BENBO sites suggests that this is not important at these sites over the scale of a single box core.

The absence of $^{210}\text{Pb}/^{226}\text{Ra}$ water column data for the BENBO sites means that the scavenging efficiency - the fraction of the water column ^{210}Pb inventory which is adsorbed

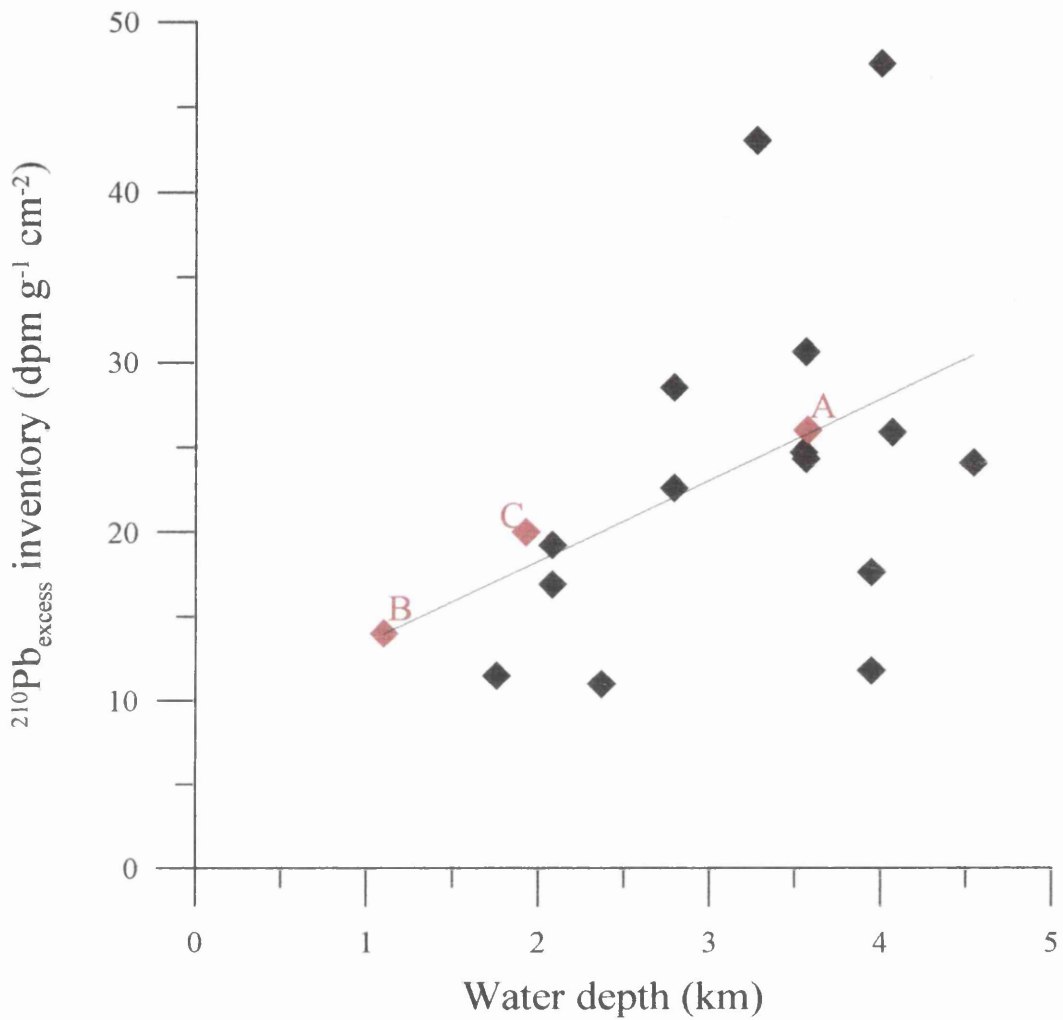


Fig. 4.5: BOFS and BENBO $^{210}\text{Pb}_{\text{excess}}$ data, plotted against the depth of the overlying water column. The black line denotes the best-fit relationship between the two parameters for the BOFS data. \blacklozenge = BOFS data (Thomson *et al.* 1993; Brand and Shimmiel 1991); $\color{red}\blacklozenge$ = BENBO data, this study (sites B and C -mean of two cores)

by particulate material in the water column and delivered to the underlying sediment - cannot be directly determined. However, the correlation of the BENBO data with the best-fit line of the BOFS water depth/ $^{210}\text{Pb}_{\text{excess}}$ inventory data (Fig. 4.5) is probably sufficient to suggest that, as with the BOFS transect, the BENBO sites are not regions of enhanced radionuclide scavenging.

The total flux of ^{210}Pb to the sediment from the overlying water is a function of the flux of ^{210}Pb from the atmosphere to the ocean and of the decay of dissolved ^{226}Ra in the water column (Section 1.4.2.1). Water column production fluxes of ^{210}Pb are determined using the formula:

$$J = I \cdot \lambda_{210-Pb} \quad (4.4)$$

where J is the ^{210}Pb production flux ($\text{Bq cm}^{-2} \text{y}^{-1}$), I is the ^{226}Ra water column inventory (Bq cm^{-2}), and λ_{210} is the ^{210}Pb decay constant (y) (Bacon *et al.* 1976). The good agreement of the BENBO data to the BOFS best fit equation in Fig. 4.6 suggests that, in the absence of BENBO ^{226}Ra water column data, it is reasonable to estimate I for each of the sites by integrating the BOFS station 3 ^{226}Ra profile (Thomson *et al.* 1993) over the depths of the three BENBO sites' water columns. This calculation provides water column ^{210}Pb production fluxes of $0.0192 \text{ Bq cm}^{-2} \text{y}^{-1}$ for site A, $0.005 \text{ Bq cm}^{-2} \text{y}^{-1}$ for site B, and $0.0088 \text{ Bq cm}^{-2} \text{y}^{-1}$ for site C.

Thomson *et al.* (1993) then estimated the atmospheric contribution to the ^{210}Pb flux to the sediment by comparing the water column flux, calculated from the ^{226}Ra water column data, and the flux determined from the sediment $^{210}\text{Pb}_{\text{excess}}$ inventory. The water column

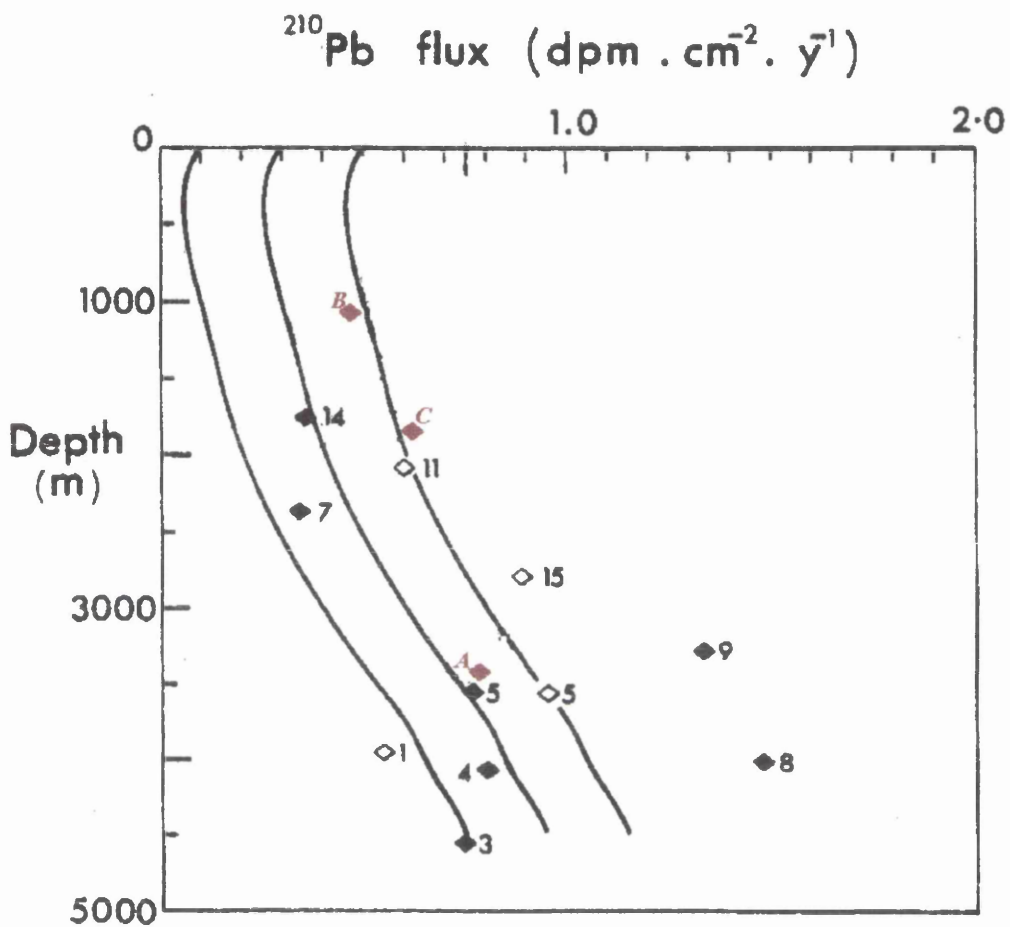


Fig. 4.6: ^{210}Pb removal fluxes from the water column estimated from the water column ^{210}Pb deficit relative to ^{226}Ra at BOFS site 3, and sediment $^{210}\text{Pb}_{\text{excess}}$ inventories. From left to right, the three curves represent the sedimentary flux necessary to maintain the observed ^{226}Ra - ^{210}Pb disequilibrium with atmospheric ^{210}Pb inputs of 0.1, 0.3 and 0.5 $\text{dpm} \cdot \text{cm}^{-2} \cdot \text{y}^{-1}$. BENBO data are shown by the red symbols; BOFS data (Thomson *et al.* 1993, black symbols; Brand and Shimmiel 1991, open symbols) are shown for comparison.

flux for any depth was determined by calculating the flux required to maintain the deficit of ^{210}Pb to ^{226}Ra in the water column, and including an additional flux of ^{210}Pb from atmospheric input. Fig 4.6, modified from Thomson *et al.* (1993) shows the ^{210}Pb removal fluxes thus derived for atmospheric inputs of $0.1 \text{ dpm cm}^{-2} \text{ y}^{-1}$ ($0.0017 \text{ Bq cm}^{-2} \text{ y}^{-1}$), $0.3 \text{ dpm cm}^{-2} \text{ y}^{-1}$ ($0.005 \text{ Bq cm}^{-2} \text{ y}^{-1}$) and $0.5 \text{ dpm cm}^{-2} \text{ y}^{-1}$ ($0.0083 \text{ Bq cm}^{-2} \text{ y}^{-1}$). The ^{210}Pb flux determined from the $^{210}\text{Pb}_{\text{excess}}$ sediment data was then plotted against water column depth and compared to that from the water column deficit plus atmospheric input curves to estimate the atmospheric contribution. Using this approach, the atmospheric ^{210}Pb fluxes to BENBO B and C are estimated as being of the order of $0.5 \text{ dpm cm}^{-2} \text{ y}^{-1}$ ($0.0083 \text{ Bq cm}^{-2} \text{ y}^{-1}$), and $0.3 \text{ dpm cm}^{-2} \text{ y}^{-1}$ ($0.005 \text{ Bq cm}^{-2} \text{ y}^{-1}$) to BENBO A. Thus, the atmospheric and water column fluxes at the mid depth sites are of approximately equal importance in determining the flux to the sediment, whereas the water column flux is of increased importance relative to atmospheric input at the deeper site, BENBO A.

Moore and Dymond (1988) found that the flux of organic carbon to the sediments was related to the ^{210}Pb flux by:

$$\text{Flux } C_{\text{org}} = 8.5 + 430 \cdot (F/P) \quad (4.5)$$

where F/P is the ratio of the ^{210}Pb flux to the sediment (calculated from the $^{210}\text{Pb}_{\text{excess}}$ sediment inventory) to the ^{210}Pb production flux (including both atmospheric and water column contributions). Using the production fluxes estimated above, the C_{org} fluxes to the BENBO sites should be $240 \mu\text{g cm}^{-2} \text{ y}^{-1}$ for site A, $217 \mu\text{g cm}^{-2} \text{ y}^{-1}$ for site B, and $269 \mu\text{g cm}^{-2} \text{ y}^{-1}$ for site C. These values are in contrast to the order expected from the water depths, as the C_{org} flux is generally expected to decrease with increasing water depth, and

the data from the sediment traps at sites A and B (Table 4.2). It also conflicts with the evidence of enhanced biological activity as evinced from the deeper ^{14}C SML, and organism density (D. Hughes, pers. comm.) at site B relative to A, which would be expected to result from a higher C_{org} flux. The estimates of C_{org} flux from the 100 m.a.b. sediment traps at BENBO sites A and B are $64 \mu\text{g cm}^{-2} \text{y}^{-1}$ and $140 \mu\text{g cm}^{-2} \text{y}^{-1}$ - much lower than predicted from the ^{210}Pb F/P ratios. It may be significant that the F/P values for the BENBO sites are higher than any ratios obtained by Moore and Dymond at their Sargasso Sea and Pacific Ocean sites, and that they restricted their study to sites of water depth >3000 m. Thus the contrast between the predicted C_{org} fluxes and that expected from the sediment trap data and other evidence may be due to the relatively crude method used to estimate the ^{210}Pb production at BENBO sites, or simply that there are different controls on the flux of C_{org} relative to ^{210}Pb at these sites.

4.1.4 Man-made radionuclides - fluxes and source inputs

The fact that the activities of ^{137}Cs and ^{241}Am in the BENBO sediments are close to the limits of detection for the gamma spectrometry method, and consequently have large errors associated with them means that the values determined for sediment inventories and fluxes also have a large error. As a result, the upper and lower limits of fluxes and inventories from each of the five sub cores analysed for these radionuclides are presented in Table 4.3 below. The upper limit for the inventory is calculated as:

$$I_{\text{max}} = \sum \left[(A_i + 1\sigma) \cdot \rho_i \cdot \Delta X_i \right] \quad (4.6)$$

where I_{max} is the inventory of the radionuclide in Bq cm^{-2} , A_i is the activity of the

radionuclide in depth increment i , 1σ is the error on activity A_i , ρ_i is the dry bulk density of depth increment i (g cm^{-3}), and ΔX_i is the thickness of the depth increment i (cm). Where the activity is below the detection limit the detection limit activity is used for A_i . The minimum inventory, I_{min} is calculated from:

$$I_{min} = \sum [(A_i - 1\sigma) \cdot \rho_i \cdot \Delta X_i] \quad (4.7)$$

In this case, where activity is below the detection limit, that depth increment is assigned an activity of zero. Annual fluxes (J) of the man made radionuclides are calculated using the assumption of Cochran (1985) of constant input since the height of atmospheric weapons testing in 1962; i.e.:

$$J = \frac{I}{1997 - 1962} \quad (4.8)$$

The 30 year half life of ^{137}Cs requires that a decay correction from the time of input - assumed to be the time of peak weapons testing in 1962 - to the time of sample collection in 1997, must be applied. The better precision of the Pu radionuclide data relative to ^{137}Cs and ^{241}Am enables the calculation of the inventory using equation (3.2). The inventory of ^{238}Pu is also decay corrected back to the time of peak input in 1962.

The maximum and minimum inventories calculated for ^{137}Cs and ^{241}Am differ by a factor of between two and ten, with the largest variation being found in sub cores A(i) and B(i), where there are the least data points above detection level. For the purposes of comparison, the mean of the maximum and minimum values will used.

Inventories reported for man-made radionuclides in open waters vary by several orders of

magnitude. For ^{137}Cs , values range from 0.01-0.08 Bq cm^{-2} for the Washington slope and shelf (Carpenter *et al.* 1987) to a low of 0.0001-0.0006 Bq cm^{-2} at the MANOP Pacific sites (Cochran 1985). The mean BENBO values of 0.0197 (sub core A(i)), 0.0178 (B(i)), 0.018 (B(vi)), 0.0235 (C(ii)), and 0.0353 (C(iv)) Bq cm^{-2} , are more analogous to those reported for the Washington slope rather than the deeper abyssal plain sites. The BENBO ^{241}Am inventory data (0.0188, 0.0166, 0.0091, 0.0061 and 0.0068 Bq cm^{-2} for A(i) to C(iv)) are also more comparable to the Washington slope (0.0032-0.020 Bq cm^{-2}) than true open ocean sites (3.3×10^{-4} and 9.3×10^{-5} Bq cm^{-2} for Nares and Hatteras abyssal plains - Cochran *et al.* 1987). The $^{239,240}\text{Pu}$ inventory of 0.0049 Bq cm^{-2} at site B(i) however, is somewhat below those found on the Washington slope (lowest value 0.0075 Bq cm^{-2}), but within the range quoted for the New York Bight area by Santschi *et al.* (1980), and an order of magnitude above those found at deeper sites .

The estimated average global fallout deliveries of $^{239,240}\text{Pu}$ and ^{137}Cs at 55 °N - the BENBO sites lie between 52 and 57°N - are 0.00481 (± 0.0044) and 0.146 Bq cm^{-2} respectively, if ^{137}Cs is corrected for decay to 1997 (Bowen *et al.* 1980). From this, it is clear that almost all of the $^{239,240}\text{Pu}$ has been incorporated into the sediments, but only 12-25 % of the ^{137}Cs inventory anticipated from fallout is present in the particulate-bound form in sediments. This is in agreement with the known geochemical behaviour of these elements. However, as with the ^{210}Pb data, there is no evidence that the BENBO sites are areas of enhanced particulate scavenging.

Site					
Radionuclide	BENBO A(i)	BENBO B(i)	BENBO B(vi)	BENBO C(ii) *	BENBO C(iv)
<i>Inventory</i> (Bq cm ⁻²)					
¹³⁷ Cs max	0.0370	0.0323	0.0288	0.0289	0.0476
¹³⁷ Cs min	0.0023	0.0032	0.0072	0.018	0.023
²⁴¹ Am max	0.0311	0.0273	0.0128	0.0086	0.0110
²⁴¹ Am min	0.0027	0.0059	0.0053	0.0036	0.0025
^{239,240} Pu	----	0.0049	----	----	----
²³⁸ Pu	----	0.00028	----	----	----
<i>Flux</i> (Bq cm ⁻² y ⁻¹)					
¹³⁷ Cs max	0.0011	0.0009	0.0008	0.0008	0.00136
¹³⁷ Cs min	6.43 E-05	9.06 E-05	0.00021	0.0005	0.00065
²⁴¹ Am max	0.00088	0.00078	0.00036	0.0002	0.00032
²⁴¹ Am min	0.00018	0.00017	0.00015	0.0001	7.01 E-05
^{239,240} Pu	----	0.00014	----	----	----
²³⁸ Pu	----	8.13 E-06	----	----	----

Table 4.3: Inventories of man-made radionuclides measured in BENBO sub cores. Maximum and minimum inventories for ¹³⁷Cs and ²⁴¹Am were determined for all sub cores except C(ii), using formulae 4.9 and 4.10. The inventories of ¹³⁷Cs and ²³⁸Pu were back-corrected for decay from the collection date to the time of peak atmospheric fallout. Average annual fluxes were calculated by dividing inventory by time elapsed between peak fallout and sample collection.

* For sub core C(ii), no values for gamma spectrometry detection limit were available and a value of zero was applied in calculation of both maximum and minimum values where activities were below detection limit.

There is little variation in the ^{137}Cs inventories between sites A and B, but at site C, the mean values for sub cores C(ii) and C(iv) are approximately 25% and 75% higher than the other two sites. However, the ^{241}Am inventory at site C is lower than the other two sites.

The activity ratios of $^{238}\text{Pu}/^{239,240}\text{Pu}$ and $^{137}\text{Cs}/^{241}\text{Am}$, $^{239,240}\text{Pu}/^{137}\text{Cs}$ and $^{241}\text{Am}/^{239,240}\text{Pu}$ should aid identification of the source of these radionuclides to the sediment. Bioturbation of marine sediments, combined with slow sedimentation rates, ensures that any variations in radionuclide inputs over time will be averaged, so that the ratios will be representative of the integrated input of radionuclides to the site from the first releases to the date of sampling. Ratios of $^{238}\text{Pu}/^{239,240}\text{Pu}$ should reflect the integrated ratio of the nuclides from the source, whilst the $^{137}\text{Cs}/^{241}\text{Am}$ ratio may be modified by the differential geochemical behaviour of the two nuclides (section 1.4.3.2).

No plutonium radionuclide data was available for site A at the time of thesis submission. The $^{137}\text{Cs}/^{241}\text{Am}$ ratio determined from the mean of the maximum and minimum inventories in Table 4.3 is 1.16, which is in fairly good agreement with the values of 1.09 and 0.87 determined for the two points in the profile at which ^{137}Cs and ^{241}Am activities are above detection limit.

At site B, the mean $^{238}\text{Pu}/^{239,240}\text{Pu}$ ratio in sub core B(i) is 0.032 (± 0.003), which agrees well with the estimated fallout ratio at this latitude of 0.03-0.04 (Hardy *et al.* 1973). The activity ratio expected from reprocessing operations would be 0.182 (MacKenzie *et al.* 1998). The mean $^{137}\text{Cs}/^{241}\text{Am}$ inventory ratios are 1.06 for sub core B(i), and 1.99 in sub core B(iv) - this difference may be reasonably attributed to the large errors inherent in the

inventory calculations. Mean $^{137}\text{Cs}/^{241}\text{Am}$ ratios, determined using only the data where both ^{137}Cs and ^{241}Am activities are above the detection limit, are 0.97 for sub core B(i), based on four points, and 1.45 for sub core B(vi), based on 11 points.

There are five data points in sub core C(ii) for which $^{238}\text{Pu}/^{239,240}\text{Pu}$ activity ratios are available. One of these (15.5-16.0 cm, $^{238}\text{Pu}/^{239,240}\text{Pu} = 0.13$) appears anomalous, and has been rejected as there is no conceivable mechanism by which this ratio could occur at this point in the core, other than by contamination. The mean of the other four points is 0.039 (± 0.004), which is slightly higher than the mean $^{238}\text{Pu}/^{239,240}\text{Pu}$ ratio obtained for site B(i), but still within the range quoted for fallout ratios at this latitude. Whilst the high clay content of the sediment might suggest input of material from the continental shelf, it is not possible to conclusively state whether this site shows the influence of Sellafield-derived radionuclides.

The $^{137}\text{Cs}/^{241}\text{Am}$ mean inventory ratios are 3.84 and 5.82 for BENBO C(ii) and C(iv) respectively, and 3.64 and 3.35 if determined only from the mean of the points where the activity of both radionuclides was above detection limit. These values are higher than those found at the other two sites, and more in line with the ratios determined from the Washington slope (Carpenter *et al.* 1987). One possible reason for the higher ratios at site C may be the different sediment composition at this site in comparison with sites A and B (Figs 3.2 and 4.1). At site B the carbonate content is over 75% throughout the core, and is of a similar value in the surface layer of core A(i) where the man-made radionuclides are distributed by bioturbation. However, the mean carbonate content of site C is closer to

50%, with the remainder of the sediment being composed of clay. Since ^{137}Cs is known to bind to clay rather than organic detritus, the additional clay flux must also contribute to the ^{137}Cs flux to the site. This theory is also in agreement with the higher inventory of ^{137}Cs found at site C relative to sites A and B.

4.2 Bioturbation processes

4.2.1 Biodiffusive mixing - cores A(i) and B(i)

The biodiffusion coefficients determined from the $^{210}\text{Pb}_{\text{excess}}$ profiles for site A(i) ($0.088 \text{ cm}^2 \text{ y}^{-1}$) and B(i) ($0.045 \text{ cm}^2 \text{ y}^{-1}$) lie in the range observed at other open ocean sites (Middelburg 1997). However, the difference between the sites disagrees with the general observation of decreasing D_B with increasing water depth, and with the relative abundance of benthic macrofauna at the two sites (D. Hughes, pers. comm.). Two empirical formulae have been developed to describe the relationship between water depth and mixing rate; these are:

$$D_B = 6330 \cdot (x^{-1.65}) \quad (4.9)$$

where x is water depth in metres, (Soetaert *et al.* 1996), and:

$$\log(D_B) = 0.7624 - 39720 \cdot x \quad (4.10)$$

(Middelburg *et al.* 1997). The D_B determined for B(i), at 1100 m water depth, is fitted reasonably well by the model of Soetaert *et al.* (1996) (Fig. 4.7), but that determined for the 3570 m site A(i) is an order of magnitude greater than the predicted value. However, Soetaert *et al.* (1996) acknowledge that their D_B values from deep water sites are low in comparison to published values. The D_B rates predicted by the Middelburg model are

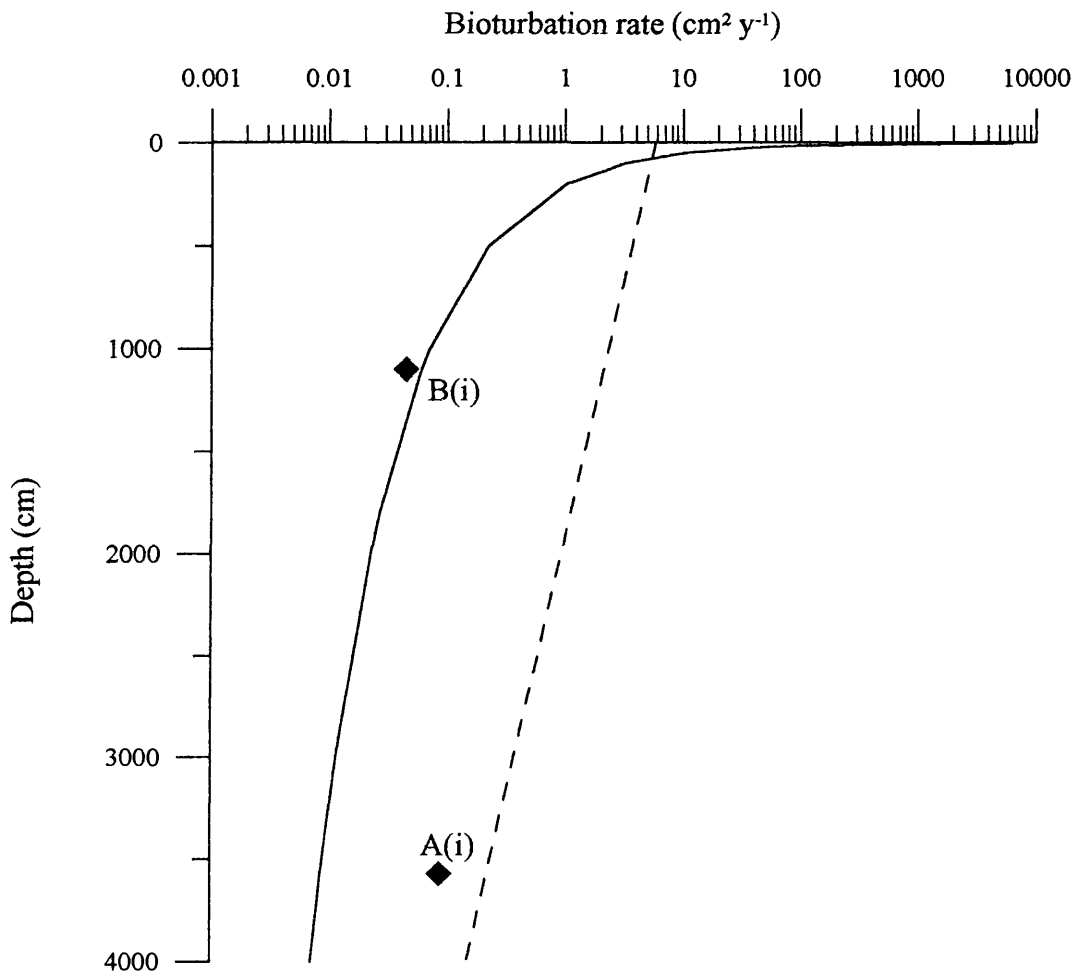


Fig. 4.7: Comparison of BENBO D_B mixing rates with the water depth-dependent models of D_B of Soetaert *et al.* (1996) (solid line) and Middelburg *et al.* (1997) (dashed line).

higher than the measured values, by a factor of 2.5 and 10 for sites A and B respectively.

The fit of the $^{210}\text{Pb}_{\text{excess}}$ data to the best fit exponential curve is good - $R^2 = 0.95$ for both site A and site B. However, between 4-8 cm in sub core B(i), the measured data are noticeably and consistently lower than the values generated using the best-fit curve of all the data where $^{210}\text{Pb}_{\text{excess}}$ is less than 1σ (Fig. 3.8). Including this data in the calculation of the best fit curve significantly lowers the goodness of fit ($R^2 = 0.79$). This suggests that bioturbation in this sub core is not best modelled as uniform biodiffusive mixing - a hypothesis which would explain the low D_B value at the shallow site B relative to the deeper site A, when the opposite trend would be expected. One explanation is that two-layer biodiffusive mixing exists at this site, with a faster mixing rate below 4 cm. Alternatively, Boudreau (1986b) demonstrated how non-local mixing could, over time, produce profiles similar to those generated by biodiffusive mixing.

4.2.2 Non-local (advective) mixing - cores B(vi), C(ii) and C(iv)

Sub cores B(iv), C(ii) and C(vi) contain subsurface peaks in $^{210}\text{Pb}_{\text{excess}}$ activity. These are typical profiles generated by large infaunal 'head up' deposit feeders, such as siphunculid and echiurid worms (Smith *et al.* 1986), created by the rapid transport of fresh material to depth via the organisms' digestive systems. The presence of these organisms at the mid depth sites, BENBO B and C, rather than the deep water site A, is consistent with the observation of Soetaert *et al.* (1996) that the importance of this type of mixing, relative to biodiffusion, decreases with increasing water depth.

Post-depositional remobilisation has also been suggested as being responsible for the appearance of subsurface peaks in $^{210}\text{Pb}_{\text{excess}}$ activity (e.g. Koide *et al.* 1973), and is linked to sulphate cycling in anoxic or seasonally anoxic conditions - conditions which are not generally applicable in the deep sea. However, Gobeil and Silverberg (1989) also noted paired subsurface peaks in porewater Pb concentrations in Laurentian Trough sediments. The upper peak was attributed to release of Pb during organic carbon degradation, and the lower peak to redox cycling of Fe. Data from the subsequent BENBO cruises CD111 and CD113 indicates high $^{210}\text{Pb}_{\text{excess}}$ activities found in burrow lining and faecal material relative to the surrounding sediment (Table 3.4). This clearly demonstrates that advective bioturbation is responsible for the high subsurface activities at these sites, rather than post-depositional remobilisation. In addition, the core logs for all site B and C sub cores (Fig.4.8) indicate textural or colour changes at depths concurrent with the increased radionuclide activity, which are the result of the physical effects of bioturbation or by biological introduction of oxic waters to depth. Fig. 4.9 also shows evidence of macrofaunal activity at sites B and C in the form of large burrows and faecal deposits in dissected box cores.

4.2.3 Temporal and spatial variations in bioturbation

Under model conditions of continuous biological mixing at typical deep sea rates, the SML depths derived from ^{14}C and $^{210}\text{Pb}_{\text{excess}}$ should agree. This condition has been observed in a number of studies (Nozaki *et al.* 1977; Peng and Broecker 1979; Buffoni *et al.* 1992), as well as at BENBO site C in this study. According to this evidence, where it is not possible to determine the long term SML from the ^{14}C data - for example the disturbed profile at site A - $^{210}\text{Pb}_{\text{excess}}$ data should provide an equally reliable estimate.

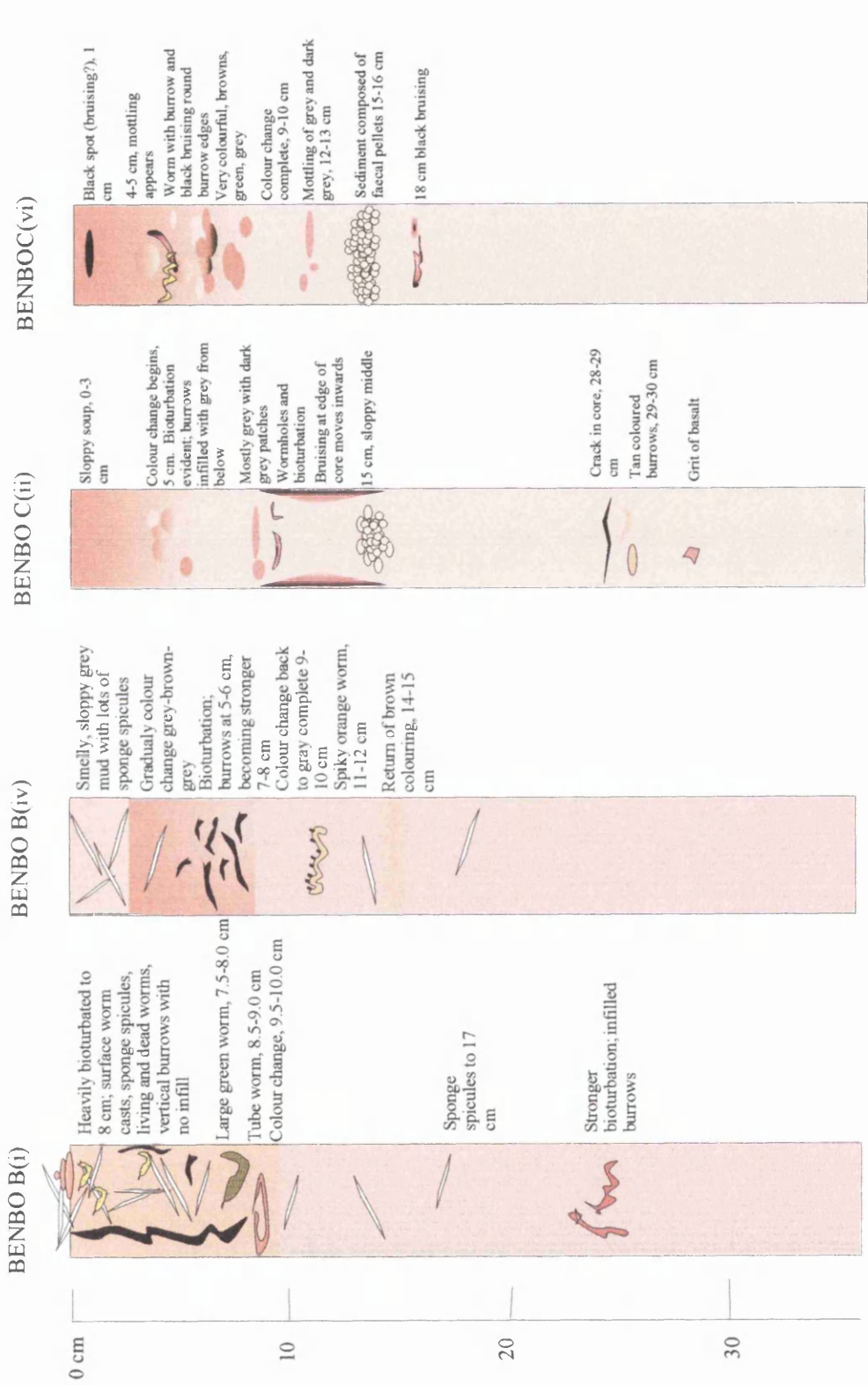


Fig. 4.9: The core logs recorded during extrusion of initial (B(i) and C(ii)) and replicate (B(vi) and C(iv)) sub cores from BENBO sites B and C, showing the major sedimentary structures and compositional changes.

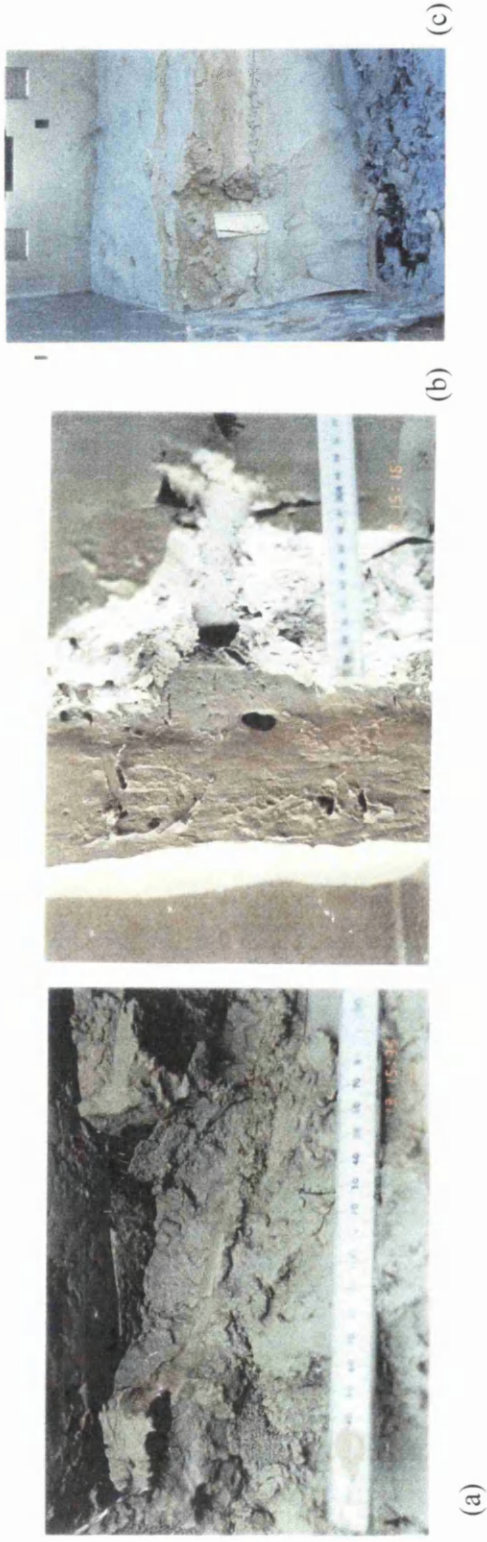


Fig. 4.8: Biogenic structures and organisms in BENBO sediments. (a) Cruise CD111 site C – faecal pellets in burrow, 16 cm depth; (b) Cruise CD111 site C - large horizontal tunnel at 16 cm depth; (c) Cruise CD113 site B – siphuncular worm in situ (photographs courtesy of D. Hughes, Dunstaffnage Marine Laboratory)

In sub core B(i), however, ^{14}C and $^{210}\text{Pb}_{\text{excess}}$ provide SML depths of 18 cm and 8 cm respectively, despite the analyses being carried out on material from the same sub core. However, the $^{210}\text{Pb}_{\text{excess}}$ profile derived from replicate sub core B(vi), taken from within a few tens of centimetres of sub core B(i), appears to show that biological mixing extends to a depth of 14 cm. The presence of live specimens of siphunculids and echurids found in later BENBO cruises to site B, and the high $^{210}\text{Pb}_{\text{excess}}$ activity in faecal material relative to surrounding sediment as discussed in section 4.2.2 indicates that unidirectional non-local mixing is also active at this site. The most likely explanation for the contradictory ^{14}C and $^{210}\text{Pb}_{\text{excess}}$ SML depths from BENBO B(i) is that the biodiffusive mixing, indicated by the exponentially decreasing $^{210}\text{Pb}_{\text{excess}}$ activity, is being intermittently disturbed by advective bioturbation to depth by deposit feeding organisms. In sub core B(i), the contrasting values for SML depth are interpreted as being produced by an advective mixing event which occurred sufficiently long ago that the $^{210}\text{Pb}_{\text{excess}}$ introduced to depth has since decayed, whilst the signal from ^{14}C is preserved due to its longer half life. For all $^{210}\text{Pb}_{\text{excess}}$ to have decayed away, the subsurface mixing must have occurred more than 100 y ago, but less than 4090 y - the time required to generate an SML of 18 cm with an accumulation rate of 4.4 cm ky^{-1} . This discrepancy between the short- and long-term SML thicknesses may explain the negative T_0 age of -660 y (Fig. 3.1; Table 3.14). Bioturbation at the site can be partitioned into two layers; a surface layer 0-8 cm with uniform, rapid (on the $^{210}\text{Pb}_{\text{excess}}$ timescale) biodiffusive mixing, and a lower layer 8-18 cm where mixing is intermittent and advective. Comparison of radiocarbon ages from BENBO site C burrow material and ambient sediment from the same depth (Fig. 3.17; Tables A3 and 3.4) confirms that this type of advective mixing can 'short-circuit' the biodiffusive mixing, directly injecting young material to the well-mixed material at depth to form the lower

mixed layer (Fig. 4.10).

Fig. 4.11 shows the radiocarbon age profile for sub core B(i) with the effects of the secondary, advective mixing removed. This model profile was determined using the SML depth of 8 cm determined from the $^{210}\text{Pb}_{\text{excess}}$ profile, with the sediment accumulation rate of 4.4 cm ky^{-1} derived from the radiocarbon data from this core. The overall, long term sediment accumulation rate will apply, regardless of which bioturbation mechanism is operating, as long as there is no net horizontal movement of sediment in or out of the region. According to the model, the 'real' profile below the SML is 2.4 ky older than the measured profile, and the T_0 value is 1040 y, close to the T_0 of 1110 y at site C. The fraction of sediment which has been transported by advective rather than biodiffusive mechanisms, to any depth in the lower (8-18 cm) SML, can be determined using a version of equation (4.1) in section 4.1.1. This model assumes the sediment age is a composite of biodiffusively mixed sub-SML sediment, whose age is determined from the hypothetical ^{14}C age-depth profile, and fresh material, age T_0 , advected directly to the lower SML. This results in 25% of fresh material being directly injected to depth at 10.25 cm and 12.0 cm, and 35% at 14.5 cm. If this hypothesis is correct, the good fit of the historical layer age-depth data to the regression line ($R^2=0.997$) must mean that this two-layer mixing has occurred regularly and at a similar rate over the last 8000 y. *

*Despite the evidence presented in section (4.2.5) showing that $^{239,240}\text{Pu}$ is present to a depth of 14 cm and that advective mixing must have occurred < 50 y ago, the argument for intermittent advective mixing at this site still holds for the following reasons. Firstly, in cores where advective mixing was active, there was invariably textural or biological evidence, e.g. faecal pellets. Secondly, the ^{14}C SML was 18 cm; 14 cm deeper than the $^{239,240}\text{Pu}$ SML. The presence of the small $^{239,240}\text{Pu}$ activity peak is therefore most likely to indicate a relict mixing event.

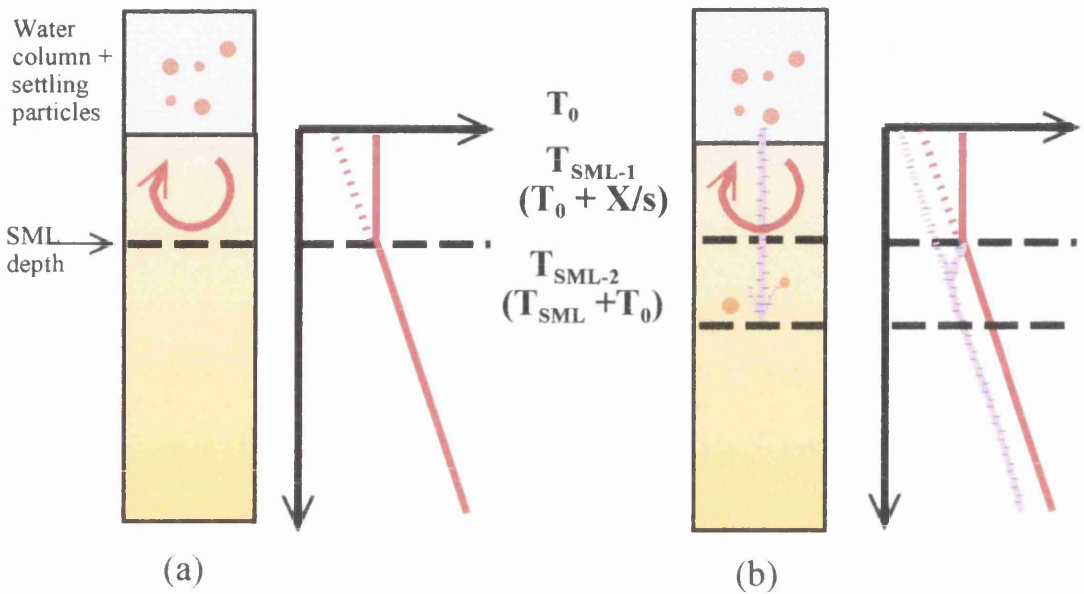


Fig 4.10: Schematic diagram of how the negative T_0 age at site B could have been formed. In (a) and the upper SML region in (b), sediment arriving at the surface is mixed homogeneously. The resultant age of this homogenised sediment, T_{SML} , is a function of the age on arrival at the sediment surface (T_0), and the residence time in the SML (X/s , where X is SML depth and s is sedimentation rate). In the lower SML of (b), a fraction of the sediment arriving at the surface is intermittently transported directly to depth by a subsurface burrower, such as a siphunculid. The age is then a function of the relative proportions of T_{SML-1} and T_0 contributing to the sediment at this depth, and the frequency and depth of injection of T_0 , controlling the amount of ^{14}C decay undergone in the historical layer affected by the subsurface mixing.

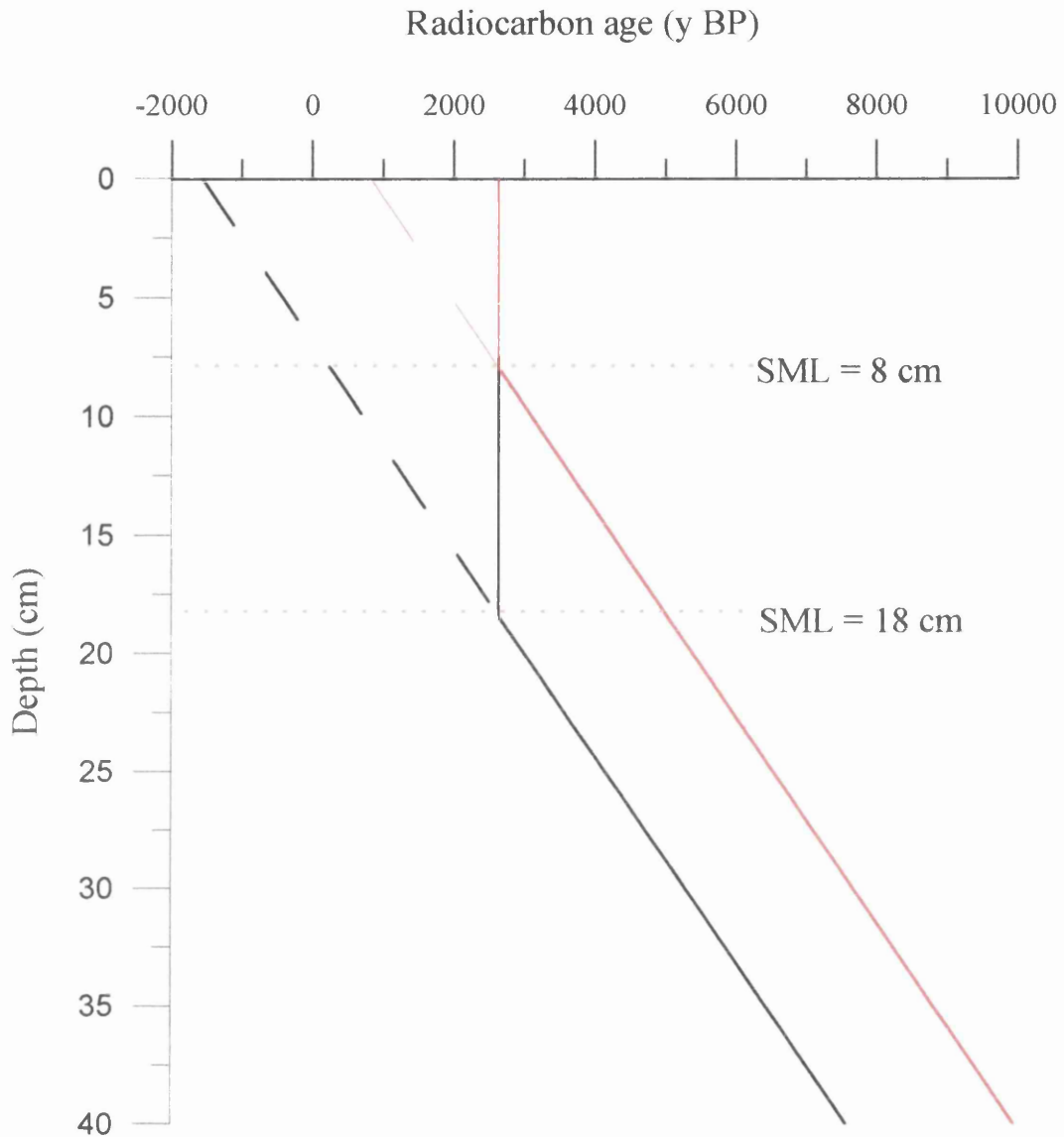


Fig. 4.11: A hypothetical model of the BENBO site B bulk carbonate radiocarbon profile without the influence of the deep advective mixing of siphunculids. The black line shows the profile generated from the site B bulk carbonate data, whilst the red line indicates the profiles expected if the SML depth was 8 cm, as indicated by the $^{210}\text{Pb}_{\text{excess}}$ profile from sub core B(i)

Broecker *et al.* (1991) showed that homogeneous dissolution of CaCO_3 grains in the mixed layer could decrease the age of the SML. This process could also potentially result in a negative age for T_0 . However, the water depth at site B is well above the North Atlantic lysocline (approximately 3500 m), and the CaCO_3 content, at around 80%, is typical for North East Atlantic pelagic sediments, suggesting dissolution is insignificant. It is also worth observing that in sample collection for foram analysis, there were abundant whole, well-preserved specimens, which would not be the case if homogeneous dissolution was operating.

The extent to which analysis of a single sub core can accurately represent bioturbation over a larger area has previously been questioned (e.g. Smith *et al.* 1984). The replicate sub core measurements at sites B and C demonstrate that bioturbation is heterogeneous on the $^{210}\text{Pb}_{\text{excess}}$ timescale. Within a 1 m² box core, the $^{210}\text{Pb}_{\text{excess}}$ SML depth at site B varies at least between 8 cm and 14 cm. Only sub core B(vi), with an SML of 14 cm, contains a subsurface peak in $^{210}\text{Pb}_{\text{excess}}$ activity. The $^{210}\text{Pb}_{\text{excess}}$ -derived SML depths for sub cores C(ii) and C(iv) are identical, but C(ii) contains two major zones of subsurface activity, whereas C(iv) contains only one, so that the relative importance of biodiffusive and non-local mixing apparently varies between sub cores. However, the depth and activity of the lower peak in C(ii) corresponds almost exactly with that in C(iv), implying that this bioturbation structure is present in both sub cores. Indeed, vertically sliced box cores from cruise CD113 exposed a horizontal sipunculid burrow structure filled with faecal pellets extending at least 20 cm (Fig. 4.9).

4.2.4 Variation in bioturbation models from man-made and NDS radionuclides

The half life of $^{210}\text{Pb}_{\text{excess}}$ and the period of time elapsed since the introduction of man made radionuclides are of a similar magnitude, so it might be expected that the depths and rates of biological mixing determined from these tracers should be similar. However, previous studies have highlighted contrasting SML depths and bioturbation rates determined from $^{210}\text{Pb}_{\text{excess}}$ and man-made radionuclides in a single core. This has been attributed to factors such as preferential post-depositional remobilisation of certain man-made radionuclides (Sayles and Livingston 1983; Stordal and Johnson 1985), differences in modelling mixing by continuous input (NDS radionuclides) and instantaneous input (man made radionuclides) tracers (Cochran 1985), or preferential adsorption of radionuclides on to different sediment components (Cochran 1985).

Gamma spectroscopy analysis of sub cores A(i) and B(i) appear to indicate that at the BENBO sites A and B, the natural radionuclide $^{210}\text{Pb}_{\text{excess}}$ penetrates deeper into the sediment than the man-made radionuclides ^{137}Cs and ^{241}Am . At BENBO site C, the man-made radionuclide profiles are similar in shape and penetration depth to that of $^{210}\text{Pb}_{\text{excess}}$. In the replicate sub cores analysed by gamma spectroscopy, B(vi) and C(iv), the man made radionuclides are also present to similar depths as $^{210}\text{Pb}_{\text{excess}}$. Thus, the reason for the disparity in SML depths between the natural and man-made radionuclides analysed by gamma spectroscopy in sub cores A(i) and B(i) seems more likely to be due to the low activities of the man-made radionuclides than post-depositional remobilisation. In sub cores A(i) and B(i), biodiffusive mixing soon dilutes the low activities of man-made

radionuclides to below detection limits, whilst in the sub cores dominated by advective mixing, significant quantities of sediment with measureable activity of ^{137}Cs or ^{241}Am are delivered straight to depth. With detection limits of around 1 Bq kg^{-1} and 0.8 Bq kg^{-1} for ^{137}Cs and ^{241}Am respectively for the analytical conditions used for sub cores A(i) and B(i), it can be appreciated that under a biodiffusive mixing regime, activities will soon fall below these limits.

In contrast to the data from gamma spectrometry, $^{239,240}\text{Pu}$, which was analysed by alpha spectrometry, for site B(i) is detectable to 14 cm depth, with a subsurface peak at 11-12 cm. Particle-bound $^{210}\text{Pb}_{\text{excess}}$ and $^{239,240}\text{Pu}$ are both thought to be associated predominantly with organic detrital material, so it is unlikely that particle-differential mixing is responsible for the contrasting profiles. The subsurface mixing observed in the replicate sub core B(vi) $^{210}\text{Pb}_{\text{excess}}$ analysis, and the enhanced activity burrow material from the later BENBO cruise suggest that the peak in $^{239,240}\text{Pu}$ activity is evidence of advective mixing occurring in this sub core rather than geochemical remobilisation of Pu. The presence of $^{239,240}\text{Pu}$ at this depth when the radionuclides analysed by gamma spectrometry are absent is therefore certainly due to the greater sensitivity of alpha spectrometry relative to gamma spectrometry.

The biodiffusion coefficients calculated from the $^{239,240}\text{Pu}$ data in the top 8 cm of the core are $0.0136 \text{ cm}^2 \text{ y}^{-1}$ for the pulse input model and $0.0645 \text{ cm}^2 \text{ y}^{-1}$ for the continuous input model. Cochran (1985) notes that higher values are expected from the continuous input

model because faster mixing would be required to transport a given fraction of the tracer to depth. Samples from North East Atlantic sediment traps demonstrated that sinking particles continued to contribute significant activities of man-made radionuclides in 1992 (Legeleux *et al.* 1994), although the actual method of delivery is probably a combination of the two end-member models. Bearing this in mind, the $^{239,240}\text{Pu}$ and $^{210}\text{Pb}_{\text{excess}}$ -derived D_B values for the BENBO sites agree well, within about 30%, in comparison to other studies where the D_B values differ by an order of magnitude or more.

4.2.5 Size selective mixing

4.2.5.1 Causes of bulk carbonate - foram age offsets

Radiocarbon age offsets between bulk carbonate and planktonic forams were observed in all three BENBO cores, but only the upper section of site A has an offset with magnitude and direction consistent with that anticipated from the BOFS study (Thomson *et al.* 1995). Consequently, the possible explanations for the offset which were discounted by Thomson *et al.* (1995) will be reconsidered. These were:

1. A systematic difference between ^{14}C analysis in LSC and AMS methods was ruled out by analysing BOFS subsamples and known age TIRI standards in the SURRC (LSC) and University of Arizona (AMS) laboratories. The values agreed well, both between the two laboratories and with the TIRI consensus values.
2. Differences in 'vital effects' - the fractionation of carbon isotopes during skeletal uptake (e.g. Kahn and Williams 1981; Bouvier-Soumagnac and Duplessey 1985).

Foraminifera and coccolithophores (which contribute most of the fine fraction carbonate) may differently fractionate the carbon isotopes in seawater when secreting their carbonate tests. The incorporation of isotopically light, metabolic CO₂ from algal symbionts into foram tests (Erez 1978) is another possible source of fractionation of foram carbonate relative to seawater. However, both of these potential offsets are accounted for by the $\delta^{13}\text{C}$ correction in the radiocarbon age calculation.

3. Some foraminifera secrete a proportion of their shell calcite in water below the ocean surface layer, whereas the photosynthesising coccoliths must live permanently in the surficial photic zone. Whilst this offset is in the right direction to produce the foram-bulk carbonate discrepancy observed in the BOFS study, the age difference from 0-3000 m in the North Atlantic is only 250 y (Broecker *et al.* 1988) - much smaller than the observed age offset.
4. The effect of dissolution on ¹⁴C ages of any CaCO₃ component should be unimportant, as the sites are all above the North East Atlantic lysocline.
5. Input of re-distributed old carbonate to the BOFS sites is dismissed because the direction of the age offset is in the opposite direction to that expected for input of fine, easily winnowed carbonate.

The first three of these reasons can also be rejected for the BENBO samples, as the same conditions apply. The water depths, high carbonate fluxes to the sediments, and excellent preservation of the foram tests from BENBO sites suggest that calcite dissolution can also

be rejected as a cause of the offset.

The foram-bulk carbonate age offset in the upper section of both cores B and C is in the right direction to be explained by the input of older, fine-grained carbonate. Whilst site B has already been shown to be non-steady state, modelling of bulk carbonate at site C indicated a T_0 age of 1100 y, which could be explained by the input of a small amount of old carbonate. Should this be the cause of the offset, similar treatment of the foram data might be expected to reveal a T_0 age of about 400 y, the reservoir age of the surface ocean. T_0 was thus calculated using T_{ML} of the four foram ages from 0-16 cm, and because of the elimination of the offset below 30 cm depth, the bulk carbonate sediment accumulation rate of 6.5 cm ky^{-1} . However, the foram T_0 value thus obtained was only 20 y, and it was inferred that fine sediment redistribution was not the cause of the offset at these sites.

Broecker *et al.* (1999) demonstrate that radiocarbon age profiles generated by different species of planktonic foraminifera vary considerably, even within the supposedly stable Holocene. They propose that this is the result of changes in abundance of the different species to the sediment, occurring both across the glacial-interglacial boundary, and throughout the Holocene. Whilst we expected to eliminate this factor by employing polyspecific samples (i.e. the sample should be dominated by the most abundant species at any depth and bioturbation-abundance biases should not be an issue), if the total rain rate of forams to the sediment changed relative to total carbonate, then perhaps bioturbation-abundance coupling could affect the radiocarbon profiles. This could perhaps explain the

change in offset direction observed in the lower section of BENBO C and in the BOFS samples older than 10 000 y. However, if this effect were indeed the cause, it seems highly unlikely that the Holocene offsets in the BOFS and BENBO cores should be in the opposite direction, even if the different sampling strategies are accounted for.

The reworking of foraminifera in medium to high energy environments has been shown to produce unreliable radiocarbon ages (Heier-Nielsen *et al.* 1995; Cearreta and Murray 2000). Although in principle, the use of AMS-dated forams in core stratigraphies eliminates the age effect of reworked sediment, Oehmig (1993) highlighted the fact that planktonic foraminifera are more readily transported than similar sized lithogenic grains, because the water-filled foram tests have lower bulk densities than solid grains and can be resuspended under lower current strengths. Heier-Nielsen *et al.* (1995) observed that samples of polyspecific or certain species of benthic forams from a shallow coastal marine core were up to 4000 y older than the more reliable chronology constructed from macrofossil dates. They attributed this to the input of species of benthic forams whose size or shape rendered them more susceptible to current redistribution. The possibility therefore exists that redistribution of foram shells is responsible for the age offset in the open ocean cores from BENBO site A and from the BOFS study. From the grain size distribution, the top of BENBO core A(i) is known to have low sortable silt content, indicative of relatively strong currents which may be sufficient to resuspend forams (section 4.1.2). The T_0 age of bulk carbonate from BOFS core 11886 is 840 y, about double the North Atlantic reservoir age, which also suggests some current redistribution of

carbonate. However, the T_0 age of BOFS core 11881 suggests that the bulk of the carbonate is derived directly from overlying surface waters, yet this core has the largest foram-bulk carbonate radiocarbon age offset of the three. Despite the fact that the >150 μm foram fraction is only a small component of the total carbonate, and would not by itself have a large effect on the sediment age, it is difficult to imagine that silt-sized carbonate would not also be transported under the influence of such strong currents.

4.2.5.2 Pretreated samples

The potential effect of the exchange of sample carbon with modern atmospheric carbon has been noted on background-age samples of both foram (Schleicher *et al.* 1998) and coral (Burr *et al.* 1992) samples. The aim of the pretreatment experiment carried out in this study was to ascertain if contamination from non-contemporaneous carbonate is significant in Holocene-age foraminiferal samples, and whether it could be responsible for the age offset. The details of the pretreatment experiment, undertaken on samples from BOFS core 11881, are outlined in section 2.2.3.3, and the results presented in Table A7 and Fig. 3.6. For the 0-1 cm depth sample, the age of the pretreated sample is almost exactly the same as the hypothetical age determined for the SML of foraminiferal calcite, while the age of carbon produced during pretreatment is similar to the age determined for the bulk carbonate at the same depth. This suggests that there may be some fine-grained carbonate trapped within the foram tests which is influencing the age of the untreated sample, assuming that this is the material which dissolves more rapidly. If foram tests are whole rather than fragmented, it may be more difficult to remove trapped fine carbonate

by simply rinsing with water, as in the procedure employed in both this study and by Thomson *et al.* (1995). However, while the datum for the pretreated sample from 26-27 cm depth is also located on the foraminiferal calcite profile, the age of carbon released during pretreatment is older than the sample age. The older age of the carbon released during pretreatment means that the cause of the difference between the pretreated and untreated samples at this depth is less clear than in the 0-1 cm sample. Sample size and representation should not be an issue as the analyses were carried out on splits from the same 50 mg sample, unless some fractionation of older and younger forams could have occurred during the process of splitting the sample. The possibility of contamination introduced during sample preparation is discounted, as a background sample of infinite age marble and a known-age turbidite from the TIRI study (Gulliksen and Scott 1995), which underwent the same procedure as the foram samples yielded satisfactory ages (see section 4.1.2). One possible explanation may be the presence of calcite overgrowths which can be deposited on foram test from dissolved bottom water or pore water carbonate. The age difference between the pretreated and sample carbonate is +270 y, which is consistent with the difference between surface and deep waters in this region (Broecker *et al.* 1988). The absence of these overgrowths in the 0-1 cm sample can be attributed to the shorter time these specimens have spent in the SML, and therefore have had less time to develop these overgrowths.

This effect may have implications for the difference in the hand-picked forams versus the foram carbonate age offsets in the BOFS samples, if choosing the best-preserved

specimens has eliminated the specimens with the most extensive overgrowths. However, given the elementary nature of the pretreatment technique, it is unwise to extrapolate too much from a single result, either in the context of the foram-bulk-carbonate age offset or in obtaining the most appropriate radiocarbon age for a sediment horizon in any particular study, but obviously further work is required in this area.

4.2.5.3 Reasons for differences in age offset between sites

From the above discussion, it appears that bioturbation must also be responsible for the age offsets observed at the BENBO sites as well as the BOFS sites. However, the offsets observed at BENBO sites B and C are in the opposite direction to those at the BOFS sites, and the offset at A is fairly inconclusive, owing to the disturbed nature of the core. One possible reason for the opposing offset directions at BENBO sites B and C and the BOFS and BENBO A sites may be the different sampling strategies employed in the two studies. The BOFS coarse fraction consisted of $>150\ \mu\text{m}$ foraminiferal calcite, consisting of all pelagic foraminiferal material in the sample (Thomson and Weaver 1994). However, the BENBO study used samples consisting of 150-250 μm hand picked, well-preserved forams, which were regarded as being more representative of samples used in other palaeoceanographic techniques.

Two means exist by which the differences between the two methods could influence the age offset. In the first instance, the different size fractions used in the two studies could affect the amount of size-differential bioturbation undergone by the particles sampled. McCave (1988) places the limit of size-differential mixing for an organism as where the

sediment grain size exceeds the diameter of the organism. It could be argued that the 150-250 μm forams used in the BENBO study were below the size threshold at which size-differential mixing takes place, particularly with regard to the greater density of macro- and megafauna at sites B and C relative to that expected at the deeper BOFS sites. However, the larger $>250 \mu\text{m}$ foram fraction ages from site B are offset by an average of 320 y (younger) from the 150-250 μm fraction in the upper section of site B, with no consistent age offset below the SML (Table 3.6; Fig. 3.4). This appears to be further evidence that whatever process causes the offset is indeed size-dependent.

The second possibility is that the strategy of picking only the best-preserved specimens and rejecting those which were chemically or physically degraded may have led to the preferential selection of only the youngest forams in any depth horizon. Simple bioturbative mixing results in the random distribution of particles throughout the SML, so that the age of any depth horizon is a product of the particle age distribution spectrum, defined by SML depth and sediment accumulation rate (Fig. 4.12). Since dissolution and abundance changes are not important at this water depth and age range, it is proposed that the longer a foram remains in the SML, the greater the probability will be that it may have been damaged by chemical or physical processes. These damaged specimens would be included in the foraminiferal calcite fraction (Thomson *et al.* 1995), but rejected for a best-preserved foram sample (this study), assuming sufficient well-preserved specimens were available. The age of the best-preserved foram sample would therefore be shifted systematically towards a younger ^{14}C age than that of a less well preserved sample. The

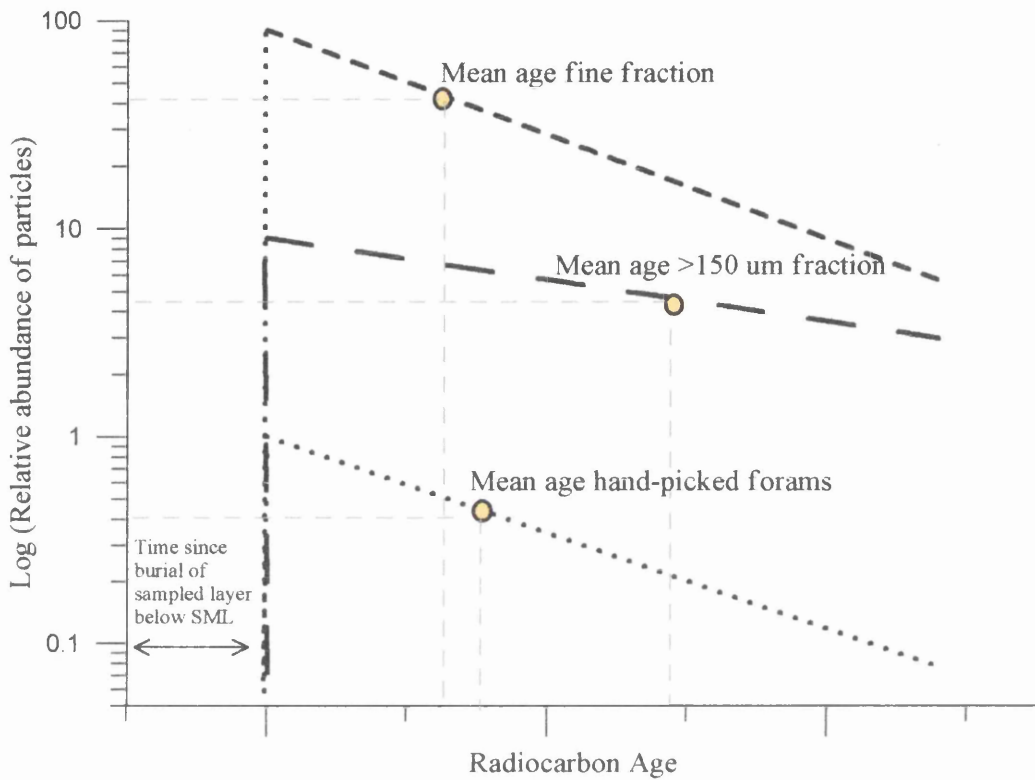


Fig 4.12: Schematic diagram of how sampling strategy might affect the radiocarbon age in a core with constant sediment accumulation and SML depth, instantaneous (c.f. ^{14}C decay) bioturbation, and relative abundances of fine fraction carbonate, coarse fraction carbonate and coarse fraction well-preserved planktonic foraminifera of 90%, 9% and 1% respectively. Size differential mixing causes the coarse fraction to have a longer SML residence time than the fine fraction. Chemical and physical degradation occurring in the SML means that many specimens of foraminifera will be rejected, assuming that the damage incurred to the foram test increases as time spent in the SML increases. A sample of well-preserved forams could therefore have a younger age than the bulk coarse fraction carbonate.

disappearance of the offset with depth may occur when sufficient time has passed outwith the SML that all surviving forams at a particular depth are degraded to about the same extent and younger forams are no longer preferentially selected.

Comparison of the BOFS foraminiferal calcite and well-preserved foram samples (Table 3.9; Fig. 3.6) reveals that in BOFS core 11881, the hand-picked foram-bulk carbonate age offset is in the same direction as, but about half the magnitude of, the foram calcite-bulk carbonate offset, whereas in BOFS core 11886, the hand-picked foram-bulk carbonate offset is observed within the SML but not below it. The selection of best-preserved forams must somehow eliminate a proportion of the forams which have undergone most size-selective mixing. The most obvious reason for this would be on the basis of preferential selection of the youngest, least damaged foram tests, as outlined above. Another possible explanation is that the size spectrum of particles is shifted by selecting only whole foram tests. McCave (1988) has demonstrated that in the range of foram sizes, the biodiffusion coefficient varies inversely with grain size. Therefore, if the smaller, less size-selectively mixed forams are less liable to be damaged by physical mixing than larger specimens, rejection of the large foram fragments would leave a sample of forams from the smaller size range and thus a shorter residence time in the mixed layer. The method of sample preparation has some effect on the ^{14}C age determined for a particular depth horizon, but is in itself not sufficient to create the age offset. The concordance of values for accumulation rate and SML depth between all three profiles suggests that the offset is the result of a physical process rather than sampling or material heterogeneities.

The $^{210}\text{Pb}_{\text{excess}}$ profiles have already indicated heterogeneous bioturbation in sub cores from the same box core for both BENBO site B and site C (Fig. 3.10), and it could be that heterogeneities between sub cores could explain the ^{14}C age offsets found at the BOFS sites. Site A is the most obvious example, with the 24-25 cm depth bulk carbonate from A(i) having a ^{14}C age of $16\,880 \pm 240$ y, but both the $<63\ \mu\text{m}$ fraction and 150-250 μm forams from A(iii) being over 30 000 y. Even in the less disturbed upper section of core A, the apparent age offset is between the $<63\ \mu\text{m}$ and the foram fraction because comparison with the bulk carbonate of A(i) indicates that the $<63\ \mu\text{m}$ material, which constitutes the bulk of the sediment, is younger than A(i) bulk carbonate. However, at sites B and C, there is generally good agreement between the $<63\ \mu\text{m}$ fine fraction of the foram core and the sub core used for bulk carbonate analysis.

The preceding section has already illustrated how bioturbation at the mid-depth sites, BENBO B and C, occurs by different mechanisms from those operating at the deep water site A. The BOFS sites 11881 and 11886 are also deep water sites, from about 4000 m, and are known to have typical SML depths of 10 cm. If bioturbation is indeed the cause of the foram-bulk carbonate offsets, it is perhaps not surprising that the different biological mixing regimes operating at the mid-depth compared to the deep water sites will result in different modes of size-dependent mixing.

According to the hypothesis of Thomson *et al.* (1995), the SML residence time of coarse particles is longer than fine particles because the larger particles are preferentially moved

upwards by bioturbation. For any given particle diameter, this effect decreases with increasing organism size, and the dominance of mega- and macro fauna at BENBO sites B and C may eliminate this preferential upwards mixing of coarse particles.

Paradoxically, the specific feeding strategies of some of the benthic macrofauna may result in the faster transport of coarse particles through the SML relative to fine sediment. Jahnke *et al.* (1986) proposed that steep gradients in $^{210}\text{Pb}_{\text{excess}}$, CaCO_3 content and organic carbon from 0-1 cm were the result of preferential ingestion of 'non- CaCO_3 ' (here used to mean C_{org} -rich, and by default, high radionuclide activity) relative to ' CaCO_3 ' particles. The 'non- CaCO_3 ' particles are preferentially eaten by organisms because of their high food content. Jahnke *et al.* (1986) surmised that the fauna consisted of 'head-down, bottom-up' deposit feeders, which feed on subsurface sediment then deposit faeces on top of the sediment. The 'non- CaCO_3 ' particles therefore have a longer SML residence time, older mean SML age, and greater abundance in the surface layer than the ' CaCO_3 ' particles.

Bock and Miller (1999) observed that certain polychaete species are particle size selective when feeding. Organic matter in deep sea sediment is thought to exist as a monolayer coating on sediment grains (Mayer 1994), and thus the selection of finer particles when feeding provides more surface area and more organic matter per unit volume ingested. If the hypothesis of Jahnke *et al.* (1986) holds for 'large' and 'small' particles instead of ' CaCO_3 ' and 'non- CaCO_3 ', this mechanism would explain the rapid transport of coarse material through the SML. Both sites B and C have lower CaCO_3 content in the top few

centimetres (Fig. 4.1), and the presence of faecal deposits has been recorded on the surface of a site B box core (Fig. 4.9). This explanation would also allow for the differences between the 150-250 μm and $>250 \mu\text{m}$ fractions at site B.

Bioturbation by the large siphunculids which formed the deep mixed layers at sites B and C could eliminate the offset in one of two ways. Bock and Miller (1999) demonstrated that size selectivity decreases as organism size increases, thus, both coarse and fine material would be advected to depth, or the direct advection of fine fraction material only would erode the offset between the bulk carbonate and foram profiles. The age inversion in the bulk carbonate profile at 15-16 cm at site C (Fig. 3.1) suggests the latter. Therefore, changes in the relative importance of the 'head down' and 'head up' feeding mechanisms between sites can account for the variations in particle ages from the same depth horizons.

Chapter 5 - Conclusions

Sediment accumulation rates, determined from bulk carbonate ^{14}C - depth profiles, are 2.1 cm ky^{-1} , 4.3 cm ky^{-1} and 6.5 cm ky^{-1} for BENBO sites A, B and C respectively. The accumulation at sites B and C has been at a constant rate over the Holocene. The carbonate flux to both sites is similar, and the faster sedimentation rate at site C relative to B is therefore mainly the result of an increased flux of fine clay material to this site. In contrast, sedimentation at site A was subject to an interruption by an erosional event, probably a strong current or possibly a sediment slump, after which Holocene carbonate rich sediments were deposited unconformably on the disturbed glacial clays.

Deconvolution of the radiocarbon profile at site A indicated that about 0.3 m of sediment had been removed by erosion, and that resumption of continuous sedimentation occurred at approximately 5840 y.

The SML depths calculated from the ^{14}C data using Erlenkeuser's (1980) box model are 18 cm for site B and 16 cm for site C. These are significantly greater than the global mean value of 9.8 ± 4.5 cm for open ocean sediments (Boudreau 1994). The deep mixed layers are attributed to bioturbation by large infaunal organisms which could be sustained by the higher organic carbon fluxes anticipated at these mid-depth sites relative to deep water sites. The box model was also applied to determine the age of freshly arriving material at the sediment surface, T_0 . At site B, T_0 was calculated as -660 y rather than the expected age of 400 y. The negative value clearly indicates that even though the radiocarbon age-depth profile approximates that expected for constant sediment accumulation, the site

cannot be in a steady state. At site C, T_0 is 1000 y, indicating that some of the accumulating carbonate is of a greater age than that derived from carbonate-shelled organisms sinking directly from the overlying surface ocean.

The $^{210}\text{Pb}_{\text{excess}}$ -derived SML depths for the sub cores A(i), B(i) and C(ii) are 10 cm, 8 cm and 15.5 cm respectively. The profiles from A(i) and B(i) approximate to an exponential decrease in activity with depth, implying that mixing is dominated by biodiffusive processes. The D_B values calculated for these profiles are $0.088 \text{ cm}^2 \text{ y}^{-1}$ for sub core A(i) and $0.045 \text{ cm}^2 \text{ y}^{-1}$ for sub core B(i). These results disagree with the general observation of decreasing D_B as water depth increases, but despite the approximate exponential shape of the B(i) profile, there is evidence to suggest mixing is not truly biodiffusive. The D_B values calculated from the $^{239,240}\text{Pu}$ at site B(i) are $0.0136 \text{ cm}^2 \text{ y}^{-1}$ for the pulse input model, and $0.0645 \text{ cm}^2 \text{ y}^{-1}$ if assuming a continuous input $^{239,240}\text{Pu}$ over time, and agree reasonably well with the D_B value determined from $^{210}\text{Pb}_{\text{excess}}$. The BENBO D_B values lie within the range of observed measurements in the deep sea under similar water depths. At site C, 70% of the $^{210}\text{Pb}_{\text{excess}}$ activity is present in subsurface peaks, indicating that bioturbation occurs mainly by unidirectional, advective processes. This observation is given further credence by the presence of faecal pellet deposits and live specimens of infaunal organisms (siphunculids) which are known to feed at the surface but excrete at depth. The ability of this feeding mechanism to produce subsurface peaks in radionuclide activity was confirmed by $^{210}\text{Pb}_{\text{excess}}$ analysis of faecal pellet samples and burrow matrix sediment. These samples demonstrated much higher $^{210}\text{Pb}_{\text{excess}}$ activities relative to the surrounding sediment.

$^{210}\text{Pb}_{\text{excess}}$ was analysed in replicate sub cores B(vi) and C(iv) to examine the small scale spatial variation in bioturbation. Sub core B(vi) showed a subsurface peak in activity and an SML of 14 cm, in comparison to the biodiffusive-type profile and 8 cm SML of sub core B(i). This indicated heterogeneity in the depth and mechanisms of mixing at this site. Sub core C(iv) had an identical SML depth to the first sub core, C(ii), but the distribution of $^{210}\text{Pb}_{\text{excess}}$ showed only one subsurface peak in activity rather than the two peaks observed in C(ii), also indicating heterogeneity at this site.

As with $^{210}\text{Pb}_{\text{excess}}$, the $^{239,240}\text{Pu}$ profile in sub core B(i) exhibits approximately exponential decay in the top 8 cm, but also contains a small (approximately 10% total activity) subsurface peak in activity at 11-12 cm. The SML depth is 14 cm, deeper than the 8 cm SML from $^{210}\text{Pb}_{\text{excess}}$ but less than the 18 cm SML from the ^{14}C profile. It is proposed that the discrepancy between SML depths derived from $^{210}\text{Pb}_{\text{excess}}$ and $^{239,240}\text{Pu}$ is the result of better analytical sensitivity in determination of $^{239,240}\text{Pu}$ rather than geochemical remobilisation or differential mixing of particles on the basis of food value or size. In contrast, the relatively high detection limits for ^{137}Cs and ^{241}Am mean that where mixing is biodiffusive, the low initial activity of these radionuclides soon decreases to below detection levels. ^{137}Cs , ^{241}Am and $^{210}\text{Pb}_{\text{excess}}$ SML depths are only comparable in those sub cores where a significant amount of surface sediment is advected to depth. This study has highlighted the spatial and temporal variability in bioturbation which must be taken into account in modelling benthic boundary processes and in reconstruction of palaeoenvironmental records. The variation in the biological mixing parameters determined from the man-made radionuclides and $^{210}\text{Pb}_{\text{excess}}$ in a single core also emphasizes the importance of a multi-tracer approach to bioturbation studies, or at the very least, an appreciation of the

potential errors inherent in the different methods.

The difference in SML depth between these short-term tracers and ^{14}C at sub core B(i) is attributed to intermittent advective mixing, such as is observed in sub core B(vi), and at site C. This mechanism could explain the negative value for T_0 at this site, if biodiffusive mixing homogenises the sediment (with respect to ^{14}C age) to a depth of 8 cm, and then a large infaunal organism injects fresh, zero age sediment to depth somewhere below the depth to which biodiffusive mixing occurs. If this hypothesis is correct, between 25 and 35% of the sediment must be injected directly to depth to account for the site B T_0 age of -660 y.

Particle size differential mixing was examined by comparison of the ^{14}C age of hand picked pelagic foraminifera with the bulk carbonate profile. In a previous study (Thomson *et al.* 1995), the large size fraction had an older ^{14}C age than the bulk carbonate at the same depth. At site A, the direction of the age offset was consistent with this observation in the Holocene-age sediment. In BENBO B and C, however, the age offset is generally in the opposite direction. The effect of the sampling method was considered as a possible reason for the contrasting age offsets, but examination of material from the BOFS cores used in the previous study indicated that sampling technique could modify the extent, but not the direction, of the offset. Instead, the reversal in offset direction at sites B and C was attributed to the different biological mixing mechanisms observed at the two mid depth sites B and C relative to the deep water sites. One explanation is that organisms preferentially consumed smaller, more nutritious particles below the sediment surface, then deposited these as faecal pellets on the surface, whilst the large, nutritionally inferior

foraminifera tests were ignored and thus were buried faster. Again, the offset could be modified by the large infaunal siphunculid-type organisms which would be less selective in feeding.

The $^{210}\text{Pb}_{\text{excess}}$ inventories at the BENBO sites are 0.42 Bq cm^{-2} at site A, 0.208 Bq cm^{-2} (mean of two sub cores) at site B, and 0.335 Bq cm^{-2} (mean of two sub cores) at site C. The inventories increase with increasing water depth, as has been previously observed. The BENBO inventory-depth data also correlate well with the data from the BOFS study area. Comparison with the BOFS data suggests the BENBO sites are not areas of enhanced radionuclide scavenging. The estimated atmospheric ^{210}Pb flux to site A is $0.005 \text{ Bq cm}^{-2} \text{ y}^{-1}$, compared to a water column flux of $0.0192 \text{ Bq cm}^{-2} \text{ y}^{-1}$. At sites B and C, the atmospheric flux is calculated as $0.0083 \text{ Bq cm}^{-2} \text{ y}^{-1}$ whilst the water column fluxes are 0.005 and $0.0088 \text{ Bq cm}^{-2} \text{ y}^{-1}$ respectively.

The mean activity ratios of $^{238}\text{Pu}.$ $^{239,240}\text{Pu}$ were 0.032 at site B and 0.039 at site C. This clearly indicates that atmospheric weapons testing fallout is the source of radionuclides to site B, and probably to site C. Differences in the $^{137}\text{Cs}.$ ^{241}Am ratio between sites were attributed to the varying sediment composition between sites. Inventories of ^{137}Cs , ^{241}Am , $^{239,240}\text{Pu}$ and ^{238}Pu were also determined. A maximum and minimum value was calculated for ^{137}Cs and ^{241}Am because of the high limits of detection of gamma spectroscopy relative to the activity present. Inventories of all radionuclides were more akin to those found in shelf and slope sediments than those at open ocean sites. The high flux of clay to site C is considered to be the cause of the higher ^{137}Cs inventory at this site relative to sites A and B, as ^{137}Cs is known to adsorb preferentially to clay particles, whereas the other man-made

radionuclides in this study have a stronger affinity for adsorption by organic matter. Comparison of the site B inventories with the estimated fallout delivery of ^{137}Cs and $^{239,240}\text{Pu}$ to the overlying water column showed that almost all of the $^{239,240}\text{Pu}$ was transferred to the sediment, whilst less than a quarter of ^{137}Cs delivered to the surface ocean was present in sediments.

Appendix - Results

Table A1: Bulk carbonate radiocarbon ages, in y BP, for BENBO site A. Samples were from sub core A(i), or if marked *, from sub core A(vi). The GU- sample identification number is that assigned to the sample by the SURRC radiocarbon laboratory.

Sample I.D.	Depth (cm)	Age (y BP)	1 σ Error
GU-7411	0.0-1.0	3380	70
GU-8077	0.5-1.0	3360	80
GU-8078	2.5-3.0	3510	80
GU-7410	4.0-5.0	3660	80
GU-8079	4.5-5.0	3880	90
GU-8080	6.5-7.0	3890	60
GU-7409	8.0-9.0	4450	80
GU-7408	12.0-13.0	6120	70
GU-8255	14.0-15.0	12010	130
GU-8955	15.0-16.0	19860	250
GU-7407	15.5-17.5	20170	460
GU-8256	16.0-17.0	19850	340
GU-8257	18.0-19.0	21320	1040
GU-7406	20.0-22.0	20980	320
GU-7405	24.0-25.0	16880	240
GU-8956	25.0-26.0*	26510	270
GU-7404	28.0-29.0	18010	340
GU-7403	32.0-33.0	21320	660
GU-8957	35.0-36.0*	31590	520

Table A2: Bulk carbonate radiocarbon ages, in y BP, for BENBO site B. Samples were from sub core B(i), unless marked with *, in which case the samples were derived from B(vi).

Sample I.D.	Depth (cm)	Age (y BP)	1σ Error
GU-8081	0.0-0.5	2110	60
GU-8082	1.5-2.0	2330	110
GU-8083	3.0-3.5	2500	120
GU-8958	4.0-5.0*	2770	50
GU-8111	6.0-6.5	2700	130
GU-8112	10.0-10.5	2560	120
GU-7596	11.5-12.5	2900	90
GU-7597	14.0-15.0	2890	80
GU-7598	18.0-19.0	2940	100
GU-7416	20.0-21.0	3190	50
GU-7415	24.0-25.0	4210	120
GU-7414	28.0-29.0	5170	60
GU-7413	32.0-33.0	6100	50
GU-8960	33.0-34.0*	7426	60
GU-7412	36.0-37.0	6860	80

Table A3: Bulk carbonate radiocarbon ages, in y BP, for BENBO site C. All samples were collected from sub core C(ii).

Sample I.D.	Depth (cm)	Age (y BP)	1σ Error
GU-7838	0.0-0.5	2950	180
GU-7837	3.0-3.5	3030	80
GU-7836	6.0-6.5	3090	110
GU-7834	12.0-12.5	3170	120
GU-7833	15.0-15.5	2760	160
GU-7832	18.0-18.5	3500	100
GU-7494	20.0-21.0	3770	70
GU-7493	25.0-26.0	4900	70
GU-7492	30.0-31.0	5600	70
GU-7491	35.0-36.0	6150	80
GU-7490	41.0-42.0	7170	100

Table A4: BENBO site A radiocarbon ages (y BP) for samples of 150-250 μm diameter well-preserved planktonic foraminifera, and fine fraction ($<63 \mu\text{m}$) sediment. All samples were from sub core A(ii).

Depth (cm)	150-250 μm Forams	Age (y BP)	1σ Error	<63 μm sediment	Age (y BP)	1σ Error
0.0-1.0	GU-8688	3200	45	GU-8696	2460	45
2.0-3.0	GU-8689	3255	55	GU-8697	2915	45
4.0-5.0	GU-8690	3470	50	GU-8698	2800	45
6.0-7.0	GU-8691	3965	50	GU-8699	3080	45
10.0-11.0	GU-8692	5230	50	GU-8700	5265	50
15.0-16.0	GU-8693	9945	65	GU-8701	15155	95
25.0-26.0	GU-8694	35900	720	GU-8702	33340	610
35.0-36.0	GU-8695	8605	95	GU-8703	27420	190

Table A5: BENBO site B radiocarbon ages (y BP) for samples of 150-250 μm diameter well-preserved planktonic foraminifera, >250 μm diameter well-preserved planktonic foraminifera and fine fraction (<63 μm) sediment. All samples were from sub core B(iv).

Depth (cm)	150-250 μm Forams	Age (y BP)	1 σ Error	>250 μm Forams	Age (y BP)	1 σ Error	<63 μm sediment	Age (y BP)	1 σ Error
0.0-1.0	GU-8086	1590	45				GU-8258	2180	50
2.0-3.0	GU-8413	1680	45						
4.0-5.0	GU-8087	1355	50		1290	40			
6.0-7.0	GU-8414	2140	45		980	50			
8.0-9.0	GU-8415	1905	45		1625	50			
12.0-13.0	GU-8088	2720	50						
15.0-16.0	GU-8089	3105	50		2680	45			
19.0-20.0	GU-8090	2790	50				GU-8259	3500	50
24.0-25.0	GU-8091	4195	55		4230	50			
29.0-30.0	GU-8092	4860	55		4470	55	GU-8260	5100	70
33.0-34.0	GU-8416	6830	55		6220	50			

Table A6: Site C radiocarbon ages for samples of 10-12 mg 150-250 μm diameter well-preserved planktonic foraminifera, and fine fraction ($<63 \mu\text{m}$) sediment. All samples were from sub core C(iv).

Depth (cm)	150-250 μm Forams	Age (y BP)	1σ Error	<63 μm sediment	Age (y BP)	1σ Error
0.0-1.0	GU-8224	1675	45	GU-8261	2860	50
4.0-5.0	GU-8225	2220	45			
12.0-13.0	GU-8227	2135	45	GU-8262	3400	80
15.0-16.0	GU-8228	2395	45			
20.0-21.0	GU-8229	2365	45			
25.0-26.0	GU-8230	3630	45	GU-8263	5040	70
30.0-31.0	GU-8231	5870	45	GU-8264	5620	90
37.0-39.0	GU-8832	6485	50			

Table A7: Radiocarbon ages (y BP) for samples of 150-250 μm diameter well-preserved planktonic foraminifera, and fine fraction (<63 μm) sediment from BOFS stations 11881 and 11886. The pretreated samples refer to those samples in which 20% of the carbonate was removed by acid hydrolysis before dating. The prefixes *a* and *b* refer to the residue from pretreatment and the pretreated sample respectively.

Depth (cm)	Sample ID	Age (y BP)	1 σ Error	<63 μm sediment	Age (y BP)	1 σ Error
11881						
0.0-1.0	GU-8740	3630	40			
4.0-5.0	GU-8741	3610	45	GU-8761	2590	40
10.0-11.0	GU-8742	4900	45			
17.0-18.0	GU-8743	6550	50			
26.0-27.0	GU-8744	9630	60	GU-8762	6525	50
<i>pre-treated</i>						
0-1	GU-8745 <i>a</i>	2590	55			
0-1	GU-8745 <i>b</i>	4181	50			
26-27	GU-8746 <i>a</i>	10355	60			
26-27	GU-8746 <i>b</i>	10085	60			
11886						
1.0-2.0	GU-8735	2660	45			
4.0-5.0	GU-8736	2700	40	GU-8763	2200	40
10.0-11.0	GU-8737	2710	50			
19.0-20.0	GU-8738	4260	45	GU-8764	3375	50
28.0-29.0	GU-8739	5620	45			

Table A8: Sub core A(i) - ^{210}Pb , ^{226}Ra , $^{210}\text{Pb}_{\text{excess}}$, ^{137}Cs and ^{241}Am results from gamma spectroscopy analysis of sealed 20 g pellets. All results are reported as specific activity in Bq kg^{-1} , with 1σ error. Where the measured activity of a radionuclide is less than twice the background error, the result is presented as *< detection limit*.

Depth	^{210}Pb total	^{226}Ra	$^{210}\text{Pb}_{\text{excess}}$	^{137}Cs	^{241}Am
0.0-0.5	299.3 ± 9.2	43.0 ± 1.6	256.3 ± 8.4	1.6 ± 0.5	1.5 ± 0.5
0.5-1.0	302.5 ± 10.0	39.3 ± 1.6	263.2 ± 9.1	<1.06	1.2 ± 0.5
1.0-1.5	256.3 ± 6.7	43.4 ± 1.6	213.0 ± 6.6	1.0 ± 0.4	1.1 ± 0.2
1.5-2.0	183.2 ± 8.3	38.2 ± 1.6	145.0 ± 7.8	<1.1	1.3 ± 0.5
2.0-2.5	108.9 ± 8.1	41.9 ± 1.6	66.7 ± 7.7	<1.1	1.1 ± 0.5
2.5-3.0	91.1 ± 7.5	42.1 ± 1.6	49.0 ± 7.3	<1.0	<0.7
3.0-3.5	104.8 ± 7.8	39.1 ± 1.6	65.7 ± 7.5	<1.0	<0.8
3.5-4.0	60.5 ± 7.7	28.8 ± 0.9	31.7 ± 6.9	<1.0	<0.9
4.0-4.5	96.1 ± 10.4	50.9 ± 3.7	45.2 ± 11.0	<0.9	<0.8
4.5-5.0	74.2 ± 7.4	38.2 ± 1.6	36.0 ± 7.1	<0.9	2.8 ± 0.4
5.0-5.5	63.1 ± 6.6	46.4 ± 1.6	16.7 ± 6.5	<1.2	<0.9
5.5-6.0	56.5 ± 9.0	43.6 ± 1.7	12.9 ± 8.6	<0.8	<0.2
6.0-6.5	51.3 ± 5.9	44.4 ± 1.6	6.9 ± 6.0	<0.8	0.5 ± 0.2
6.5-7.0	54.8 ± 6.8	45.2 ± 1.7	9.5 ± 6.9	<1.1	<0.8
7.0-7.5	50.3 ± 7.5	44.9 ± 1.7	5.4 ± 7.3	<1.0	<1.0
7.5-8.0	44.5 ± 8.0	44.9 ± 0.9	-0.3 ± 7.6	<1.1	0.9 ± 0.4
8.0-8.5	49.2 ± 5.2	47.9 ± 2.2	1.3 ± 5.7	<0.8	<0.7
8.5-9.0	34.8 ± 6.9	46.9 ± 1.7	-12.1 ± 6.7	<1.1	<0.9
9.0-9.5	43.1 ± 6.9	45.7 ± 1.6	-2.6 ± 6.8	<0.9	<0.7
9.5-10.0	38.0 ± 6.9	52.8 ± 1.7	-14.8 ± 6.8	<1.2	<0.9
10.0-10.5	45.1 ± 6.5	52.7 ± 1.7	-7.7 ± 6.8	<1.2	<0.9
10.5-11.0	52.3 ± 7.5	49.9 ± 1.7	2.5 ± 7.2	<1.0	<1.0
11.0-11.5	57.4 ± 7.3	50.7 ± 1.0	6.7 ± 7.0	<0.9	<0.9
11.5-12.0	52.6 ± 9.3	53.6 ± 4.2	-1.1 ± 10.2	<1.0	<0.9
12.0-12.5	44.3 ± 6.9	53.0 ± 1.7	-8.7 ± 6.7	<1.0	<0.9

12.5-13.0	49.6 ± 6.9	51.6 ± 1.7	-2.0 ± 6.8	<0.9	0.7 ± 0.3
13.0-13.5	50.2 ± 8.1	51.2 ± 1.7	-1.0 ± 7.8	<1.1	<1.0
13.5-14.0	47.4 ± 7.1	54.7 ± 1.7	-7.2 ± 6.9	<1.1	0.9 ± 0.4
14.0-14.5	47.5 ± 10.1	51.8 ± 1.7	-4.3 ± 9.7	<1.2	<1.0
14.5-15.0	43.5 ± 7.8	59.6 ± 1.7	-6.1 ± 7.6	<1.0	1.0 ± 0.4
15.0-15.5	48.9 ± 7.8	62.1 ± 1.8	-13.2 ± 7.5	<1.1	<1.0
15.5-16.0	52.9 ± 7.2	58.9 ± 1.7	-5.8 ± 7.0	<1.0	<0.9
16.0-16.5	48.4 ± 8.5	53.7 ± 1.7	-5.3 ± 8.1	<1.3	<0.9
16.5-17.0	54.4 ± 9.5	52.7 ± 1.7	1.7 ± 9.0	<1.1	<0.9
17.0-17.5	46.4 ± 8.3	48.0 ± 1.7	-1.6 ± 7.8	<1.1	<1.2
17.5-18.0	46.9 ± 6.3	50.1 ± 1.7	-3.1 ± 6.2	<1.0	<1.0
18.0-18.5	58.0 ± 7.6	53.1 ± 1.7	4.9 ± 7.4	<1.0	<0.8
18.5-19.0	47.0 ± 9.0	47.5 ± 1.7	-0.5 ± 9.2	<1.4	<0.8
19.0-19.5	64.6 ± 6.1	48.3 ± 1.6	16.3 ± 6.1	<0.8	<0.7
19.5-20.0	43.1 ± 12.3	46.9 ± 1.0	4.4 ± 12.3	<0.9	<1.0

Table A9: Sub core B(i) - ^{210}Pb , ^{226}Ra , $^{210}\text{Pb}_{\text{excess}}$, ^{137}Cs and ^{241}Am results from gamma spectroscopy analysis of sealed 20 g pellets. All results are reported as specific activity in Bq kg^{-1} , with 1σ error. Where the measured activity of a radionuclide is less than twice the background error, the result is presented as *< detection limit*.

Depth	^{210}Pb total	^{226}Ra	$^{210}\text{Pb}_{\text{excess}}$	^{137}Cs	^{241}Am
0.0-0.5	218.3 ± 7.9	43.0 ± 2.4	175.2 ± 8.0	1.6 ± 0.5	1.5 ± 0.5
0.5-1.0	190.3 ± 10.5	51.4 ± 3.3	138.9 ± 11.0	<1.1	<1.0
1.0-1.5	162.2 ± 7.7	49.6 ± 1.7	112.3 ± 7.9	2.3 ± 0.5	1.6 ± 0.5
1.5-2.0	144.4 ± 7.8	50.5 ± 1.7	94.1 ± 7.9	1.1 ± 0.5	1.8 ± 0.6
2.0-2.5	118.0 ± 6.7	52.0 ± 1.7	67.0 ± 6.9	1.6 ± 0.4	1.0 ± 0.4
2.5-3.0	120.8 ± 8.3	53.8 ± 1.7	68.0 ± 8.5	<1.2	<1.0
3.0-3.5	88.6 ± 8.2	52.8 ± 1.7	35.2 ± 8.4	<1.0	<0.9
3.5-4.0	78.9 ± 6.7	51.9 ± 1.7	26.0 ± 6.9	<0.9	<0.8
4.0-4.5	54.1 ± 5.8	51.9 ± 1.6	2.2 ± 6.0	<0.9	0.7 ± 0.3
4.5-5.0	57.4 ± 6.6	52.0 ± 1.7	5.4 ± 6.8	<0.9	0.8 ± 0.4
5.0-5.5	55.1 ± 7.7	53.7 ± 1.7	1.4 ± 7.9	<1.1	1.3 ± 0.5
5.5-6.0	57.8 ± 6.5	52.7 ± 1.7	4.1 ± 6.7	<1.0	0.8 ± 0.4
6.0-6.5	42.3 ± 8.5	51.8 ± 1.7	-8.5 ± 8.6	<1.1	<1.1
6.5-7.0	49.4 ± 6.4	53.0 ± 1.7	-3.6 ± 6.6	<1.1	<0.9
7.0-7.5	55.1 ± 6.1	51.3 ± 1.7	3.8 ± 6.3	<1.0	1.0 ± 0.4
7.5-8.0	58.3 ± 6.7	50.9 ± 1.7	7.4 ± 6.9	<1.0	<0.9
8.0-8.5	45.8 ± 6.5	49.4 ± 1.7	-3.6 ± 6.7	<1.0	1.0 ± 0.4
8.5-9.0	56.2 ± 6.7	38.1 ± 1.6	8.1 ± 6.9	<1.0	<0.9
9.0-9.5	48.3 ± 5.9	75.2 ± 1.9	-27.9 ± 6.2	<0.9	0.8 ± 0.3
9.5-10.0	53.9 ± 6.8	43.6 ± 1.6	10.3 ± 7.0	<1.0	<0.8
10.0-10.5	51.0 ± 6.0	43.2 ± 1.6	6.8 ± 6.2	<0.9	<0.9
10.5-11.0	43.5 ± 7.3	45.0 ± 1.6	-1.5 ± 7.5	<1.0	<0.9
11.0-11.5	44.2 ± 6.1	43.6 ± 1.6	0.6 ± 6.3	<1.0	<0.8
11.5-12.0	43.5 ± 7.5	44.8 ± 1.6	-1.3 ± 7.6	<1.1	<0.9
12.0-12.5	37.3 ± 6.1	44.9 ± 1.6	-7.6 ± 6.3	<0.9	0.6 ± 0.3

12.5-13.0	37.0 ± 6.2	44.9 ± 1.6	-7.9 ± 6.4	<0.8	<0.6
13.0-13.5	38.9 ± 6.2	43.8 ± 1.6	-4.9 ± 6.4	<0.8	<0.6
13.5-14.0	41.5 ± 5.6	43.1 ± 1.6	-1.6 ± 5.8	<0.7	0.7 ± 0.2
14.0-14.5	52.8 ± 5.5	41.3 ± 1.6	11.5 ± 5.7	<0.8	<0.6
14.5-15.0	31.8 ± 6.8	43.8 ± 1.6	-12.0 ± 7.0	<1.0	<0.9
15.0-15.5	37.4 ± 6.5	45.2 ± 1.6	-7.8 ± 6.7	<1.0	<0.8
15.5-16.0	37.3 ± 6.4	45.2 ± 1.6	-8.9 ± 5.6	<0.9	<0.8
16.0-16.5	37.0 ± 6.1	42.2 ± 1.6	-5.2 ± 6.3	<1.0	1.2 ± 0.4
16.5-17.0	29.9 ± 5.9	46.9 ± 1.6	-13.0 ± 6.7	<0.9	<0.6
17.0-17.5	39.0 ± 5.6	44.0 ± 1.6	-5.0 ± 5.8	<0.9	<0.5
17.5-18.0	33.8 ± 6.0	42.6 ± 1.6	-8.8 ± 6.2	<1.0	<0.6
18.0-18.5	39.9 ± 6.9	43.7 ± 1.6	-3.8 ± 7.1	<1.0	<0.9
18.5-19.0	37.5 ± 6.8	43.6 ± 1.6	-6.1 ± 7.0	<1.0	<0.9
19.0-19.5	42.1 ± 6.5	45.2 ± 1.6	-3.1 ± 6.7	<1.0	<0.8
19.5-20.0	27.4 ± 6.7	28.5 ± 1.0	-1.1 ± 6.8	<0.9	<0.9

Table A10: Sub core C(ii) - ^{210}Pb , ^{226}Ra , $^{210}\text{Pb}_{\text{excess}}$, ^{137}Cs and ^{241}Am results from gamma spectroscopy analysis of sealed 20 g pellets. All results are reported as specific activity in Bq kg^{-1} , with 1σ error. Unlike the other cores, where the measured activity of a radionuclide is less than twice the background error, the result is presented as zero (core measured at SOC; detection limit data not available).

Depth	^{210}Pb total	^{226}Ra	$^{210}\text{Pb}_{\text{excess}}$	^{137}Cs	^{241}Am
0.0-0.5	99.2 ± 4.9	54.5 ± 1.0	44.7 ± 5.0	0.94 ± 0.34	0.52 ± 0.22
0.5-1.0	93.7 ± 4.7	55.3 ± 1.0	38.5 ± 4.8	0.73 ± 0.37	0.23 ± 0.23
1.0-1.5	96.5 ± 4.7	54.7 ± 1.0	41.8 ± 4.9	1.86 ± 0.42	0.40 ± 0.14
1.5-2.0	89.7 ± 4.6	57.9 ± 1.0	31.7 ± 4.7	0.97 ± 0.40	0.28 ± 0.17
2.0-2.5	77.9 ± 4.6	59.2 ± 1.1	18.7 ± 4.7	0.68 ± 0.36	0
2.5-3.0	66.8 ± 4.0	59.7 ± 1.1	7.1 ± 4.1	0	0
3.0-3.5	64.9 ± 3.8	62.0 ± 1.1	2.9 ± 4.0	0.80 ± 0.38	0
3.5-4.0	61.1 ± 3.8	64.0 ± 1.1	-2.9 ± 4.0	0	0
4.0-4.5	60.0 ± 3.6	60.9 ± 1.1	-0.9 ± 3.8	0	0.14 ± 0.17
4.5-5.0	60.9 ± 3.8	64.0 ± 1.2	-3.1 ± 4.0	0	0
5.0-5.5	71.6 ± 4.1	64.6 ± 1.1	7.0 ± 4.2	0	0
5.5-6.0	68.5 ± 6.5	59.7 ± 1.1	8.7 ± 4.1	0	0.29 ± 0.26
6.0-6.5	68.5 ± 3.9	50.5 ± 0.9	18.0 ± 4.0	0	0
6.5-7.0	68.6 ± 6.4	40.6 ± 0.8	28.0 ± 4.9	0.66 ± 0.35	0.29 ± 0.19
7.0-7.5	90.3 ± 4.6	44.1 ± 0.8	46.2 ± 4.7	0.85 ± 0.34	0.29 ± 0.19
7.5-8.0	100.8 ± 5.1	43.7 ± 0.9	57.1 ± 5.2	2.18 ± 0.37	0.53 ± 0.17
8.0-8.5	105.9 ± 5.2	44.6 ± 0.9	61.2 ± 5.3	0.58 ± 0.36	0.84 ± 0.18
8.5-9.0	97.1 ± 4.8	44.4 ± 0.9	48.0 ± 4.7	2.32 ± 0.36	0.42 ± 0.23
9.0-9.5	88.6 ± 4.5	43.7 ± 0.9	44.8 ± 4.6	1.39 ± 0.37	0.40 ± 0.16
9.5-10.0	92.4 ± 4.6	45.2 ± 0.9	55.1 ± 4.6	1.92 ± 0.39	0.32 ± 0.15
10.0-10.5	100.3 ± 4.5	45.22 ± 1.6	6.8 ± 6.2	2.89 ± 0.44	0.59 ± 0.16
10.5-11.0	105.2 ± 5.1	44.2 ± 0.9	61.0 ± 5.2	2.88 ± 0.39	0.61 ± 0.19
11.0-11.5	99.0 ± 5.1	43.3 ± 0.9	55.7 ± 5.2	3.04 ± 0.42	0.48 ± 0.15
11.5-12.0	60.8 ± 3.7	44.1 ± 0.8	16.7 ± 3.8	0	0.27 ± 0.17
12.0-12.5	59.4 ± 3.7	42.0 ± 0.9	17.4 ± 3.8	0	0

12.5-13.0	73.0 ± 4.4	44.6 ± 0.9	28.4 ± 4.5	1.71 ± 0.41	0.28 ± 0.20
13.0-13.5	85.8 ± 4.0	43.3 ± 0.9	42.5 ± 4.1	2.01 ± 0.37	0.46 ± 0.20
13.5-14.0	89.7 ± 4.6	42.6 ± 0.8	47.1 ± 4.6	1.19 ± 0.37	0.77 ± 0.24
14.0-14.5	94.6 ± 4.7	43.3 ± 0.8	51.3 ± 4.8	2.12 ± 0.36	0.49 ± 0.17
14.5-15.0	83.7 ± 4.4	29.5 ± 0.7	54.2 ± 4.4	1.44 ± 0.34	0.80 ± 0.23
15.0-15.5	65.1 ± 3.4	43.8 ± 0.9	21.3 ± 3.5	0	0
15.5-16.0	60.6 ± 3.7	42.2 ± 0.8	18.4 ± 3.8	0	0.36 ± 0.17
16.0-16.5	47.6 ± 3.4	43.3 ± 0.9	4.3 ± 3.6	0	0
16.5-17.0	42.8 ± 3.2	27.9 ± 0.7	14.9 ± 3.3	0	0
17.0-17.5	38.1 ± 2.6	37.2 ± 0.8	0.9 ± 2.7	0	0
17.5-18.0	34.4 ± 2.9	29.0 ± 0.7	5.4 ± 3.0	0	0.27 ± 0.32
18.0-18.5	37.2 ± 3.1	44.3 ± 0.8	-7.1 ± 3.2	0	0
18.5-19.0	37.1 ± 3.1	29.5 ± 0.7	7.6 ± 3.2	0	0
19.0-19.5	36.9 ± 3.2	44.4 ± 0.9	-7.5 ± 3.3	0	0
19.5-20.0	39.1 ± 3.2	42.4 ± 0.8	-3.3 ± 3.3	0	0

Table A11: Replicate sub core B(vi) - ^{210}Pb , ^{226}Ra , $^{210}\text{Pb}_{\text{excess}}$, ^{137}Cs and ^{241}Am results from gamma spectroscopy analysis of sealed 20 g pellets. All results are reported as specific activity in Bq kg^{-1} , with 1σ error. Unlike the other cores, where the measured activity of a radionuclide is less than twice the background error, the result is presented as zero (core measured at SOC; detection limit data not available).

Depth	^{210}Pb total	^{226}Ra	$^{210}\text{Pb}_{\text{excess}}$	^{137}Cs	^{241}Am
0.0-0.5	175.9 ± 4.7	73.4 ± 1.7	702.5 ± 5.0	1.69 ± 0.38	1.20 ± 0.11
0.5-1.0	152.3 ± 3.8	55.6 ± 1.2	96.7 ± 4.0	0.59 ± 0.30	1.02 ± 0.13
1.0-1.5	137.9 ± 3.9	56.3 ± 1.3	81.6 ± 4.1	1.88 ± 0.37	1.01 ± 0.14
1.5-2.0	126.9 ± 4.4	59.2 ± 1.4	67.7 ± 4.6	1.48 ± 0.32	0.91 ± 0.18
2.0-2.5	76.0 ± 3.4	56.1 ± 1.3	19.9 ± 3.6	<0.57	0.93 ± 0.17
2.5-3.0	89.8 ± 3.4	58.3 ± 1.4	31.4 ± 3.6	0.61 ± 0.28	0.76 ± 0.15
3.0-3.5	110.7 ± 3.5	56.2 ± 1.4	54.5 ± 1.2	1.05 ± 0.29	1.27 ± 0.20
3.5-4.0	67.9 ± 3.8	54.2 ± 1.2	13.7 ± 4.0	<0.7	<0.36
4.0-4.5	69.7 ± 3.5	55.9 ± 1.3	13.8 ± 3.7	<0.64	<0.24
4.5-5.0	61.5 ± 3.4	55.8 ± 1.4	5.7 ± 3.7	<0.68	<0.32
5.0-5.5	60.4 ± 2.9	58.2 ± 1.3	2.2 ± 3.2	<0.70	<0.32
5.5-6.0	61.9 ± 3.5	58.3 ± 1.3	3.6 ± 3.7	<0.64	<0.30
6.0-6.5	61.5 ± 3.6	56.5 ± 1.3	5.0 ± 3.9	<0.76	<0.32
6.5-7.0	62.3 ± 2.7	55.9 ± 1.2	6.4 ± 3.0	0.91 ± 0.32	<0.31
7.0-7.5	49.9 ± 4.1	56.3 ± 1.3	-6.5 ± 4.3	0.86 ± 0.30	0.29 ± 0.14
7.5-8.0	63.0 ± 3.9	55.8 ± 1.4	7.2 ± 4.1	1.38 ± 0.33	<0.24
8.0-8.5	64.0 ± 3.5	53.6 ± 1.3	10.4 ± 3.7	<0.74	0.52 ± 0.15
8.5-9.0	69.0 ± 4.0	50.8 ± 1.2	18.2 ± 4.2	0.90 ± 0.37	0.52 ± 0.15
9.0-9.5	73.1 ± 3.5	50.3 ± 1.2	22.8 ± 3.7	<0.64	0.43 ± 0.12
9.5-10.0	78.7 ± 3.5	49.5 ± 1.2	29.2 ± 3.7	<0.64	0.53 ± 0.09
10.0-10.5	82.8 ± 3.5	48.0 ± 1.2	34.7 ± 3.7	0.95 ± 0.33	0.61 ± 0.14
10.5-11.0	68.3 ± 3.8	50.7 ± 1.2	17.6 ± 4.0	<0.70	0.68 ± 0.16
11.0-11.5	63.7 ± 3.4	49.6 ± 1.2	14.1 ± 3.6	0.74 ± 0.31	<0.24
11.5-12.0	52.7 ± 2.9	50.0 ± 1.3	2.7 ± 3.2	<0.60	<0.21

12.0-12.5	54.6 ± 3.1	47.4 ± 1.1	7.2 ± 3.3	<0.64	<0.28
12.5-13.0	59.6 ± 3.5	47.3 ± 1.1	12.3 ± 3.7	<0.74	<0.25
13.0-13.5	54.2 ± 2.9	46.7 ± 1.1	7.4 ± 3.1	<0.68	<0.30
13.5-14.0	47.4 ± 2.8	45.9 ± 1.2	1.5 ± 3.0	<0.72	<0.28
14.0-14.5	45.7 ± 3.1	46.6 ± 1.1	-0.9 ± 3.3	<0.72	<0.24
14.5-15.0	52.5 ± 3.3	47.2 ± 1.1	5.3 ± 3.5	<0.72	<0.28
15.0-15.5	45.0 ± 2.3	46.3 ± 1.1	-1.3 ± 2.5	<0.72	<0.28
15.5-16.0	60.6 ± 3.7	42.2 ± 0.8	18.4 ± 3.8	0.80 ± 0.36	0.33 ± 0.12
16.0-16.5	44.2 ± 3.2	46.5 ± 1.1	-2.2 ± 3.4	<0.72	<0.24
16.5-17.0	45.8 ± 2.5	44.1 ± 1.1	1.7 ± 2.7	<0.66	<0.24
17.0-17.5	41.5 ± 3.4	47.3 ± 1.2	-5.8 ± 3.6	<0.82	<0.32
17.5-18.0	46.1 ± 3.0	47.3 ± 1.4	-1.2 ± 3.3	<0.98	<0.32
18.0-18.5	51.2 ± 4.2	48.3 ± 1.3	2.9 ± 4.4	<0.88	<0.28
18.5-19.0	51.5 ± 4.7	49.0 ± 1.3	2.5 ± 4.9	<0.90	<0.30
19.0-19.5	48.1 ± 4.2	48.0 ± 1.3	0.1 ± 4.4	<0.98	<0.32
19.5-20.0	46.4 ± 4.6	50.0 ± 1.4	-3.6 ± 4.9	<1.00	<0.32

Table A12: Replicate sub core C(iv) - ^{210}Pb , ^{226}Ra , $^{210}\text{Pb}_{\text{excess}}$, ^{137}Cs and ^{241}Am results from gamma spectroscopy analysis of sealed 20 g pellets. All results are reported as specific activity in Bq kg^{-1} , with 1σ error. Where the measured activity of a radionuclide is less than twice the background error, the result is presented as *< detection limit*.

Depth	^{210}Pb total	^{226}Ra	$^{210}\text{Pb}_{\text{excess}}$	^{137}Cs	^{241}Am
0.0-0.5	227.8 ± 5.7	52.6 ± 1.3	175.1 ± 5.8	1.38 ± 0.44	0.42 ± 0.17
0.5-1.0	178.5 ± 4.8	56.9 ± 1.4	121.6 ± 5.0	1.26 ± 0.42	1.06 ± 0.16
1.0-1.5	148.6 ± 5.2	61.4 ± 1.5	87.2 ± 5.4	1.77 ± 0.36	0.66 ± 0.16
1.5-2.0	113.7 ± 3.2	65.6 ± 1.0	48.1 ± 3.4	1.78 ± 0.35	0.40 ± 0.11
2.0-2.5	94.7 ± 3.3	65.7 ± 1.0	29.0 ± 3.4	1.67 ± 0.35	0.32 ± 0.13
2.5-3.0	86.5 ± 3.6	61.3 ± 2.4	25.3 ± 4.3	0.73 ± 0.28	0.45 ± 0.15
3.0-3.5	90.1 ± 4.7	68.4 ± 2.5	21.7 ± 4.7	<1.14	<0.30
3.5-4.0	91.0 ± 4.7	67.8 ± 2.4	23.2 ± 5.3	1.61 ± 0.39	<0.36
4.0-4.5	90.2 ± 5.3	73.5 ± 2.4	16.7 ± 5.8	1.77 ± 0.44	0.41 ± 0.13
4.5-5.0	95.9 ± 4.4	77.0 ± 2.6	18.9 ± 5.1	2.00 ± 0.47	0.42 ± 0.11
5.0-5.5	95.6 ± 3.9	71.7 ± 2.5	23.9 ± 4.6	1.00 ± 0.37	0.60 ± 0.16
5.5-6.0	101.7 ± 3.6	64.0 ± 2.5	37.7 ± 4.4	1.37 ± 0.41	<0.36
6.0-6.5	87.2 ± 5.0	58.7 ± 2.4	28.5 ± 5.5	1.17 ± 0.38	<0.38
6.5-7.0	74.6 ± 3.1	50.6 ± 2.4	24.0 ± 3.9	<0.84	0.50 ± 0.18
7.0-7.5	72.8 ± 2.9	50.3 ± 2.2	22.5 ± 3.6	1.09 ± 0.39	0.23 ± 0.10
7.5-8.0	69.1 ± 3.5	50.1 ± 2.2	19.0 ± 4.2	1.47 ± 0.34	0.42 ± 0.13
8.0-8.5	64.6 ± 2.9	52.1 ± 2.3	12.5 ± 3.7	1.06 ± 0.27	<0.20
8.5-9.0	63.9 ± 2.7	46.9 ± 2.3	17.0 ± 3.5	<0.84	<0.32
9.0-9.5	57.6 ± 3.1	46.5 ± 2.2	14.1 ± 3.8	1.48 ± 0.43	<0.32
9.5-10.0	63.7 ± 4.9	49.5 ± 2.2	14.3 ± 5.4	1.55 ± 0.42	<0.34
10.0-10.5	66.5 ± 4.1	52.1 ± 2.3	14.4 ± 4.7	0.99 ± 0.40	<0.36
10.5-11.0	55.4 ± 2.9	48.9 ± 2.4	6.5 ± 3.7	1.58 ± 0.30	<0.34
11.0-11.5	59.4 ± 3.0	50.9 ± 2.3	8.5 ± 3.8	1.68 ± 0.32	<0.30
11.5-12.0	77.8 ± 4.5	51.1 ± 2.3	26.7 ± 5.1	2.73 ± 0.42	<0.40
12.0-12.5	78.0 ± 4.6	46.3 ± 2.3	31.7 ± 5.1	1.61 ± 0.40	<0.30

12.5-13.0	83.4 ± 3.5	50.6 ± 2.3	32.8 ± 4.2	1.36 ± 0.39	0.43 ± 0.17
13.0-13.5	92.4 ± 4.3	50.3 ± 2.3	42.1 ± 4.9	3.29 ± 0.58	<0.22
13.5-14.0	101.3 ± 5.3	51.3 ± 2.4	50.0 ± 5.8	2.49 ± 0.54	<0.32
14.0-14.5	75.3 ± 5.4	50.3 ± 2.4	25.0 ± 5.9	1.20 ± 0.48	0.32 ± 0.11
14.5-15.0	68.0 ± 3.6	50.8 ± 2.2	17.2 ± 4.2	1.37 ± 0.35	<0.24
15.0-15.5	58.6 ± 2.8	50.5 ± 2.2	8.1 ± 3.5	0.74 ± 0.33	<0.24
15.5-16.0	62.9 ± 3.2	53.1 ± 2.2	9.8 ± 3.9	<0.71	<0.30
16.0-16.5	61.4 ± 4.9	42.6 ± 2.2	18.8 ± 5.4	<1.00	<0.40
16.5-17.0	52.4 ± 4.4	50.7 ± 2.3	1.7 ± 4.9	<1.00	<0.40
17.0-17.5	59.4 ± 4.3	50.1 ± 1.8	9.3 ± 4.7	<0.62	<0.28
17.5-18.0	56.2 ± 3.7	50.8 ± 1.7	5.4 ± 4.0	<0.82	<0.34
18.0-18.5	63.7 ± 5.1	49.3 ± 1.8	14.4 ± 5.4	<1.06	<0.42
18.5-19.0	59.7 ± 4.3	50.4 ± 1.8	9.3 ± 4.7	<1.22	<0.48
19.0-19.5	64.2 ± 5.0	50.6 ± 1.8	13.6 ± 5.3	<1.20	<0.49
19.5-20.0	49.0 ± 3.5	56.5 ± 1.8	-7.5 ± 3.9	<1.02	<0.44

Table A13: ^{238}Pu and $^{239,240}\text{Pu}$ results for sub cores B(i) and C(ii). Analyses were carried out on the same 20 g pellets used for gamma spectroscopy analysis. All results are reported as specific activity in Bq kg^{-1} , with 1σ error.

Depth	Sub core B(i)			Sub core C(ii)		
	^{238}Pu	$^{239,240}\text{Pu}$	$\frac{^{238}\text{Pu}}{^{239,240}\text{Pu}}$	^{238}Pu	$^{239,240}\text{Pu}$	$\frac{^{238}\text{Pu}}{^{239,240}\text{Pu}}$
0.0-0.5	0.064 ± 0.008	1.76 ± 0.09	0.032 ± 0.005			
0.5-1.0						
1.0-1.5	0.062 ± 0.014	2.16 ± 0.09	0.026 ± 0.006			
1.5-2.0	0.065 ± 0.009	2.08 ± 0.13	0.027 ± 0.005			
2.0-2.5	0.045 ± 0.006	1.70 ± 0.05	0.024 ± 0.003			
2.5-3.0	0.050 ± 0.006	1.48 ± 0.05	0.030 ± 0.004			
3.0-3.5	0.035 ± 0.006	1.17 ± 0.06	0.30 ± 0.005			
3.5-4.0	0.009 ± 0.002	0.28 ± 0.01	0.029 ± 0.007			
4.0-4.5	0.007 ± 0.002	0.49 ± 0.02	0.013 ± 0.004			
4.5-5.0	0.011 ± 0.002	0.37 ± 0.02	0.028 ± 0.006			
5.0-5.5	0.023 ± 0.005	0.76 ± 0.03	0.027 ± 0.005			
5.5-6.0	0.005 ± 0.002	0.21 ± 0.01	0.019 ± 0.010			
6.0-6.5	0	0.17 ± 0.01				
6.5-7.0	0	0.15 ± 0.01				
7.0-7.5	0.008 ± 0.001	0.12 ± 0.01	0.060 ± 0.009			
7.5-8.0	0.001 ± 0.011	0.11 ± 0.01	0.009 ± 0.09			
8.0-8.5	0	0.11 ± 0.01				
8.5-9.0	0.013 ± 0.003	0.15 ± 0.01	0.075 ± 0.020			
9.0-9.5	0.007 ± 0.002	0.14 ± 0.01	0.044 ± 0.010			
9.5-10.0	0.009 ± 0.002	0.17 ± 0.01	0.048 ± 0.010			
10.0-10.5	0.007 ± 0.002	0.22 ± 0.01	0.028 ± 0.010			
10.5-11.0	0.021 ± 0.003	0.51 ± 0.02	0.036 ± 0.010			

Sub core B(i)				Sub core C(ii)		
11.0-11.5	0.020 ± 0.005	0.72 ± 0.04	0.024 ± 0.006			
11.5-12.0	0	0.16 ± 0.01				
12.0-12.5	0	0.14 ± 0.01				
12.5-13.0	0.008 ± 0.001	0.15 ± 0.01	0.048 ± 0.006			
13.0-13.5	0	0.02 ± 0.01				
13.5-14.0	0	0.05 ± 0.06				
14.0-14.5	0.004 ± 0.001	0.01 ± 0.01	0.31 ± 0.006	0.388 ± 0.057	7.86 ± 0.25	0.0494 ± 0.01
14.5-15.0	0	0				
15.0-15.5	0	0				
15.5-16.0	0	0		0.408 ± 0.049	3.14 ± 0.14	0.130 ± 0.020
16.0-16.5	0	0		0.022 ± 0.005	0.72 ± 0.03	0.031 ± 0.008
16.5-17.0	0	0		0.024 ± 0.006	0.72 ± 0.03	0.033 ± 0.008
17.0-17.5	0	0		0.104 ± 0.026	2.55 ± 0.13	0.040 ± 0.011
17.5-18.0	0	0				
18.0-18.5	0	0				
18.5-19.0	0	0				
19.0-19.5	0	0				
19.5-20.0	0	0				

Cited References

- Aarkrog, A., Dahlgaard, H., Nielsen, S.P. 1999 Marine radioactivity in the Arctic: a retrospect of environmental studies in Greenland waters with emphasis on transport of ^{90}Sr and ^{137}Cs with the East Greenland Current. *Science of the Total Environment* **237/238**, 143-151
- Aller, R.C. The effect of macrobenthos on chemical properties of marine sediment and overlying water. In "Animal-Sediment Relations" McCall, P.L. and Tevesz, M.J.S. ed., Plenum, N.Y. 1982
- Aller, R.C. 1984 The importance of relict burrow structures and burrow irrigation in controlling sedimentary solute distribution. *Geochimica et Cosmochimica Acta* **48**, 1929-1934
- Aller, R.C. and DeMaster, D.J. 1984 Estimates of particle flux and reworking at the deep sea floor using $^{234}\text{Th}/^{238}\text{U}$ disequilibrium. *Earth and Planetary Science Letters* **67**, 308-318
- Anderson D.M. 2001 Attenuation of millennial-scale events by bioturbation in marine sediments. *Palaeoceanography* **16**: 352-357
- Anderson, R. and Cook, G.T. 1991 Scintillation cocktail optimization for ^{14}C dating using the Packard 2000CA/LL and 2260XL. *Radiocarbon* **33**: 1-7
- Andree M., Beer J., Oeschger H., Broecker W., Mix A., Ragano N., O'Hara P., Bonani G., Hofman H.J., Morenzoni E., Nessi M., Suter M., Wolfli W. 1984. ^{14}C measurements on foraminifera of deep sea core V28-238 and their preliminary interpretation. *Nuclear Instruments and Methods* **B 5**: 340-345.
- Austin, W.E.N., Bard, E., Hunt, J.B., Kroon, D., Peacock, J.D. 1995 The C-14 age of the Icelandic Vedde Ash - implications for Younger-Dryas marine reservoir corrections. *Radiocarbon* **37**: 53-62
- Bacon, M.P., Spencer, D.W., Brewer, P.G. 1976 $^{210}\text{Pb}/^{226}\text{Ra}$ and $^{210}\text{Po}/^{210}\text{Po}$ disequilibria in seawater and suspended particulate matter. *Earth and Planetary Science Letters* **32**: 277-296
- Bacon, M.P. and Anderson, R.F. 1982 Distribution of thorium isotopes between dissolved and particulate forms in the deep sea. *Journal of Geophysical Research* **87**: 2045-2056

- Bacon, M.P. 1984 Glacial to interglacial changes in carbonate and clay sedimentation in the Atlantic Ocean estimated from ^{230}Th measurements. *Isotope Geoscience* **2**: 97-111
- Balsam, W.L. and McCoy, F.W. 1987 Atlantic sediments: glacial/interglacial comparisons. *Palaeoceanography* **2**: 531-542
- Bard E, Arnold M, Duprat J, Moyes J, Duplessey J-C. 1987 Reconstruction of the last deglaciation: deconvolved records of $\delta^{18}\text{O}$ profiles, micropalaeontological variations and accelerator mass spectrometric ^{14}C dating. *Climate Dynamics* **1**: 101-112.
- Bard, E. 1988 Correction of accelerator mass spectrometry ^{14}C ages measured in planktonic foraminifera: Palaeoceanographic implications. *Palaeoceanography* **3**: 635-645
- Bard, E., Arnold M., Mangerud, J., Paterne, M., Labeyrie, L., Duprat J, Melieres, M-A., Sonstegaard, E., Duplessey J-C. 1994 The North Atlantic atmosphere-sea surface ^{14}C gradient during the Younger Dryas climatic event. *Earth and Planetary Science Letters* **126**: 275-287
- Becker, B. 1993 An 11 000-year German oak and pine dendrochronology for radiocarbon calibration. *Radiocarbon* **35**: 201-213
- Beks, J.P. 2000 Storage and distribution of plutonium, ^{241}Am , ^{137}Cs and $^{210}\text{Pb}^{\text{xs}}$ in North Sea sediments. *Continental Shelf Research* **20**: 1941-1964
- Ben-Shaban, Y.A. 1989 Radionuclide movement and geochemistry in intertidal sediments in south-west Glasgow. PhD thesis, University of Glasgow
- Bennet, C.L., Beukens, R.P., Clover, M.R., Gove, H.E., Liebert, R.B., Litherland, A.E., Purser, K.H., Sondheim, W.E. 1977 *Science* **198**: 508
- Benninger, L.K. 1978 ^{210}Pb balance in Long Island Sound. *Geochimica et Cosmochimica Acta* **42**: 1165-1175
- Berger, W.H and Heath, G.R. 1968 Vertical mixing in marine sediments. *Journal of Marine Research* **26**: 134-143
- Berger W.H. and Johnson R.F. 1978. On the thickness and the ^{14}C age of the mixed layer in deep-sea carbonates. *Earth and Planetary Science Letters* **41**: 223-227
- Berger, W.H., Killingley, J.S., Metzler, C.V., Vincent, E. 1985 Two-step deglaciation: ^{14}C -dated high-resolution $\delta^{18}\text{O}$ records from the tropical Atlantic ocean. *Quaternary Research* **23**, 258-271

- Bianchi, G.G. and McCave, I.N. 1999 Holocene periodicity in North Atlantic climate and deep ocean flow south of Iceland. *Nature* **397**: 515-517
- Bland, C.J., Truffy, J., DeBruyne, T. 1992 Deconvolution of alpha spectra to obtain plutonium isotopic ratios. *Nuclear Instruments and Methods in Physics Research* **43**: 201-209
- Bock, M.J. and Miller, D.C. 1999 Particle selectivity, gut volume and the response to a step-change in diet for deposit-feeding polychaetes. *Limnology and Oceanography* **44**: 1132-1138
- Bond, G., Showers, W., Cheseby, M., Lotty, R., Almasi, P., deMenocal, P., Priore, P., Cullen, H., Hadjas, I., Bonani, G. 1997 A pervasive millennial-scale cycle in North Atlantic Holocene and Glacial climates. *Science* **278**: 1257-1266
- Bondevik, S., Birks, H.H., Gulliksen, S., Mangerud, J. 1999 Late Weichselian marine 14-C reservoir ages at the western coast of Norway. *Quaternary Research* **52**: 104-114
- Boudreau, B.P. 1986a. Mathematics of tracer mixing in sediments I: Spatially dependent, diffusive mixing. *American Journal of Science* **286**: 161-198
- Boudreau, B.P. 1986b. Mathematics of tracer mixing in sediments II: Non-local and conveyor belt mixing. *American Journal of Science* **286**: 199-238
- Boudreau, B.P. and Imboden, D.M. 1987 Mathematics of tracer mixing in sediments III: The theory of nonlocal mixing within sediments. *American Journal of Science* **287**: 693-719
- Boudreau, B.P. 1994 Is burial velocity a master parameter for bioturbation? *Geochimica Cosmochimica Acta* **58**: 1243-1249
- Boudreau, B.P. 1998 Mean mixed depth of sediments: The wherefore and the why. *Limnology and Oceanography* **43**: 524-526
- Bouvier-Soumagnac, Y. and Duplessy, J-C. 1985 Carbon and oxygen isotopic composition of planktonic foraminifera from laboratory cultures, plankton tows and recent sediment: implications for the reconstruction of palaeoclimatic conditions and the global carbon cycle. *Journal of Foraminiferal Research* **15**: 302-320
- Bowen, V.T., Noshkin, V.E., Livingston, H.D., Volchok, H.L. 1980 Fallout radionuclides in the Pacific Ocean: Vertical and horizontal distributions, largely from GEOSECS stations. *Earth and Planetary Science Letters* **49**: 411-434

- Boyle, E.A. and Keigwin, L.D. 1987 North Atlantic thermohaline circulation during the last 20 000 years linked to high latitude surface temperature. *Nature* **330**: 35-40
- Boyle E.A. 1988 Cadmium: Chemical tracer of deepwater palaeoceanography. *Paleoceanography* **3**: 471-489.
- Brand, T. and Shimmield, G. The use of ^{210}Pb as an indicator of biological processes affecting the flux and sediment geochemistry of organic carbon in the NE Atlantic. In "Radionuclides in the Study of Marine Processes" PJ Kershaw and DS Woodhead, ed. Elsevier Science Publishers, 1991
- Broecker, W.S., Gerard, R., Ewing, M., Heezen, B.C. 1960 Natural radiocarbon in the ocean. *Journal of Geophysical Research* **65**: 2903-2931
- Broecker W., Mix, A., Andree, M., Oeschger, H. 1984 Radiocarbon measurements on coexisting benthic and planktic foraminifera shells: Potential for reconstructing ocean ventilation times over the past 20 000 y. *Nuclear Instruments and Methods in Physics Research* **B5**: 331-339
- Broecker, W.S., Peng, T-H., Ostlund, G., Stuiver, M. 1985 The distribution of bomb radiocarbon in the ocean. *Journal of Geophysical Research* **90**: 6953-6970
- Broecker W.S., Andree M., Wolfli W., Oeschger H., Bonani G., Kennet J., Peteet D. 1988a. The chronology of the last deglaciation: Implications to the cause of the Younger Dryas event. *Paleoceanography* **3**: 1-19.
- Broecker, W.S., Andree, M., Bonani, G., Klas, M., Mix, A., Oeschger, H. 1988b Comparison between radiocarbon ages obtained on coexisting planktonic foraminifera. *Paleoceanography* **3**: 647-657
- Broecker, W.S., Andree, M., Bonani, G., Wolfli, W., Oeschger, H., Klas, M., Mix, A., Curry, W.B. 1988c Preliminary estimates for the radiocarbon age of deep waters in the glacial ocean. *Palaeoceanography* **3**: 659-670
- Broecker, W.S., Klas, M., Clark, E., Bonani, G., Ivy, S., Wolfli, W. 1991 The influence of CaCO_3 dissolution on core top radiocarbon ages for deep sea sediments. *Palaeoceanography* **6**: 593-608
- Broecker, W., Matsumoto, K., Clark, E., Hajdas, I., Bonani, G. 1999 Radiocarbon age differences between coexisting foraminiferal species. *Palaeoceanography* **14**: 431-436
- Brown, J., Colling, A., Park, D., Phillips, J., Rothery, D., Wright, J. Ocean Sediments and Deep-Sea Chemistry. 1989 Open University/Pergamon Press

- Brown, T.A., Farwell, G.W., Grootes, P.M., Schmidt, F.H., Stuiver, M. 1993 Intraannual variability of the radiocarbon content of corals from the Galapagos Islands. *Radiocarbon* **35**: 245-251
- Buesseler, K.O., Livingston, H.D., Sholkovitz, E.R. 1985/6 $^{239,240}\text{Pu}$ and excess ^{210}Pb inventories along the shelf and slope of the northeast U.S.A. *Earth and Planetary Science Letters* **76**: 10-22
- Buesseler, K.O. and Sholkovitz, E.R. 1987 The geochemistry of fallout plutonium in the North Atlantic I: A pore-water study in shelf, slope and deep-sea sediments. *Geochimica et Cosmochimica Acta* **51**: 2605-2622
- Buesseler, K.O. 1990 ^{210}Pb scavenging in the North Atlantic and North Pacific Oceans. *Earth and Planetary Science Letters* **97**: 332-352
- Buffoni, G., Delfanti, R., Pappucci, C. 1992 Accumulation rates and mixing processes in near-surface North Atlantic sediments: Evidence from C-14 and Pu-239,240 downcore profiles. *Marine Geology* **109**: 159-170
- Burr, G.S., Edwards, R.L., Donahue, D.J., Druffel, E.R.M., Taylor, F.W. 1992 Mass spectrometric ^{14}C and U-Th measurements in coral. *Radiocarbon* **34**: 611-618
- Carpenter, R., Bennett, J.T., Peterson, M.J. 1981 ^{210}Pb activities in and fluxes to sediments of the Washington continental slope and shelf. *Geochimica et Cosmochimica Acta* **45**: 1155-1172
- Carpenter, R., Beasley, T.M., Zahnle, D., Somayajulu, B.L.K. 1987 Cycling of fallout (Pu, ^{241}Am , ^{137}Cs) and natural (U, Th, ^{210}Pb) radionuclides in Washington continental slope sediments. *Geochimica et Cosmochimica Acta* **51**: 1897-1921
- Cearreta, A. and Murray, J.W. 2000 AMS ^{14}C dating of Holocene estuarine deposits: consequences of high-energy and reworked foraminifera. *The Holocene* **10**: 155-159
- Chen, Q., Aarkog, A., Nielsen, S.P., Dahlgard, H., Nies, H., Yixuan, Y., Mandrup, K. 1993 Determination of plutonium in environmental samples by controlled valence in anion exchange. *Journal of Radioanalytical Chemistry* **172**: 281-288
- Chung, Y. and Craig, H. 1973 Radium-226 in the Eastern Equatorial Pacific. *Earth and Planetary Science Letters* **17**: 306-319
- Cochran, J.K., McKibbin-Vaughan, T., Dornblaser, M.M., Hirschberg, D., Livingston, H.D., Craig, H., Krishnaswami, S., Somayajulu, B.L.K. 1973 ^{210}Pb - ^{226}Ra radioactive disequilibrium in the deep sea. *Earth and Planetary Science Letters* **17**: 295-305

- Cochran, J.K. and Krishnaswami, S. Radium, thorium, uranium and ^{210}Pb in deep sea sediments and sediment porewaters from the north equatorial Pacific. *American Journal of Science* **280**: 849-889
- Cochran, J.K. The oceanic chemistry of U- and Th-series radionuclides. In: "Uranium Series Disequilibrium: Applications to Environmental Problems" Ivanovich, M. and Harmon, R.S., ed. Elsevier Science Publishers, 1992
- Cochran, J.K., Bacon, M.P., Krishnaswami, S., Turekian, K.K. 1983 Po-210 and Pb-210 distributions in the central and eastern Indian Ocean. *Earth and Planetary Science Letters* **65**: 433-452
- Cochran, J.K. 1985 Particle mixing rates in sediments of the eastern equatorial Pacific: Evidence from ^{210}Pb , $^{239,240}\text{Pu}$ and ^{137}Cs distributions at MANOP sites. *Geochimica et Cosmochimica Acta* **49**: 1195-1209
- Cochran, J.K., Livingston, H.D., Hirschberg, D.J., Suprenant, L.D. 1987 Natural and anthropogenic radionuclide distributions in the northwest Atlantic Ocean. *Earth and Planetary Science Letters* **84**: 135-152
- Cochran, J.K., McKibbin-Vaughan, T., Dornblaser, M.M., Hirschberg, D., Livingston, H.D., Buesseler, K.O. 1990 ^{210}Pb scavenging in the North Atlantic and North Pacific Oceans. *Earth and Planetary Science Letters* **97**: 332-352
- Cook, G.T. and Anderson, R. 1991 The determination of ^{241}Pu by liquid scintillation spectrometry using the Packard 2250CA. *Journal of Radioanalytical and Nuclear Chemistry* **154**: 319-330
- Cook, G.T. and Anderson, R. 1992 A radiocarbon dating protocol for use with Packard scintillation counters employing burst-counting circuitry. *Radiocarbon* **34**:381-38
- Cooper, L.W., Kelley, J.M., Bond, L.A., Orlandini, K.A., Grebmeier, J.M. 2000 Sources of the transuranic elements plutonium and neptunium in arctic marine sediments. *Marine Chemistry* **69**: 253-276
- Craig, H., Krishnaswami, S., Somayajulu, B.L.K. 1973 ^{210}Pb - ^{226}Ra radioactive disequilibrium in the deep sea. *Earth and Planetary Science Letters* **17**: 295-305
- Crusius, J. and Anderson, R.F. 1991 Immobility of ^{210}Pb in Black Sea sediments. *Geochimica et Cosmochimica Acta* **55**: 327-333
- Cutshall, N.H., Larsen, I.L., Olsen, C.R. 1983 Direct analysis of ^{210}Pb in sediment samples: self-absorption corrections. *Nuclear Instruments and Methods in Physics Research* **206**: 309
- DeMaster, D.J., and Cochran, J.K. 1982 Particle mixing rates in deep sea sediments

determined from excess Pb-210 and Si-32 profiles. *Earth and Planetary Science Letters* **61**: 257-271

- DeMaster, D.J., Brewster, D.C., McKee, B.A., Nittrouer, C.A. 1991 Rates of particle scavenging, sediment reworking and longitudinal ripple formation at the HEBBLE site based on measurements of ^{234}Th and ^{210}Pb . *Marine Geology* **99**: 423-444
- Dergachev, V. and Chistyakov, V. 1995 Cosmogenic radiocarbon and cyclical natural processes. *Radiocarbon* **37**, 417-424
- Donahue, D.J. 1990 Radiocarbon measurements at the University of Arizona AMS facility. *Nuclear Instruments and Methods in Physics Research* **B52**: 224-228
- Donahue, D.J., Linick, T.W. and Jull, A.J.T. 1990 Isotope -ratio and background corrections for accelerator mass spectrometry radiocarbon measurements. *Radiocarbon* **32**:135-142
- Dowling, L.M. and McCave, I.N. 1993 Sedimentation on the Feni Drift and late Glacial bottom water production in the northern Rockall Trough. *Sedimentary Geology* **82**: 79-87
- Duplessey, J-C., Arnold, M., Maurice, P., Bard, E., Duprat, J., Moyes, J. 1986 Direct dating of the oxygen-isotope record of the last deglaciation by ^{14}C accelerator mass spectrometry. *Nature* **320**: 350-352
- Ellet, D.J. and Martin, J.H. 1973 The physical and chemical oceanography of the Rockall Channel. *Deep-Sea Research* **20**: 585-625
- Emiliani C. 1955 Pleistocene temperatures. *Journal of Geology* **63**: 538-578.
- Erez, J. 1978 Vital effect on stable-isotope composition seen in foraminifera and coral skeletons. *Nature* **273**: 199-203
- Erlenkeuser, H. 1980 ^{14}C age and vertical mixing of deep sea sediments. *Earth and Planetary Science Letters* **47**: 319-326
- Fisher, N.S., Cochran, J.K., Krishnaswami, S., Livingston, H.D. 1988 Predicting the flux of radionuclides on sinking biogenic debris. *Nature* **335**: 622-624
- Fowler, S.W. Noshkin, V.E., La Rosa, J., Gastaud, J. 2000 Temporal variations in plutonium and americium inventories and their relation to vertical transport in the northwestern Mediterranean Sea. *Limnology and Oceanography* **45**: 446-458
- Francis, C.W. and Brinkley, F.S. 1976 Preferential adsorption of ^{137}Cs to micaceous minerals in freshwater sediments. *Nature* **260**: 511-513

- Froelich, P.N., Klinkhammer, G.P., Bender, M.L., Luedtke, N.A., Heath, G.R., Cullen, D., Dauphin, P., Hammond, D., Hartman, B., Maynard, V. 1979 Early oxidation of organic matter in pelagic sediments of the eastern equatorial Atlantic: suboxic diagenesis. *Geochimica et Cosmochimica Acta* **43**: 1075-1090
- Gage, J.D. 1991 Biological rates in the deep sea: A perspective from studies on processes in the benthic boundary layer. *Reviews in Aquatic Sciences* **5**: 49-100
- Gobeil, C. and Silverberg N. 1989 Early diagenesis of lead in Laurentian Trough sediments. *Geochimica et Cosmochimica Acta* **53**: 1889-1895
- Gooday, A.J. 1988 A response by benthic foraminifera to the deposition of phytodetritus in the deep sea. *Nature* **332**: 70-73
- Graham, M.C. 1995 An investigation of actinide interactions with humic substances. PhD thesis, University of Glasgow
- Gray, J., Jones, S.R., Smith, A.D. 1995 Discharges to the environment from the Sellafield Site. *Journal of Radiological Protection* **15**: 99-131
- Gulliksen, S. and Scott, E.M. 1995 Report of the TIRI workshop, Saturday 13 August 1994. *Radiocarbon* **37**:820-821
- Gupta, S.K. and Polach, H.A. "Radiocarbon Dating Procedures at ANU" Radiocarbon Dating Research, 1985
- Hardy, E.P., Krey, P.W., Volchok, H.L. 1973 Global inventory and distribution of fallout plutonium. *Nature* **241**: 444-445
- Hayes, F.N. and Gould, R.C. 1953 Liquid scintillation counting of tritium-labelled water and organic compounds. *Science* **117**: 480-483
- Heier-Neilsen, S., Conradsen, K., Heinemeier, J., Knudsen, K.L., Nielsen, H.L., Rud, N., Sveinbjornsdottir, A.E. 1995 Radiocarbon dating of shells and foraminifera from the Skagen core, Denmark: Evidence of reworking. *Radiocarbon* **37**: 119-130
- Henderson, G.M., Lindsay, F.N., Slowey, N.C. 1999 Variation in bioturbation with water depth on marine slopes: a study on the Little Bahamas Bank. *Marine Geology* **160**: 105-118
- Higgo, J.J.W., Cherry, R.D., Heyraud, M., Fowler, S.W. 1977 Rapid removal of plutonium from the oceanic surface layer by zooplankton faecal pellets. *Nature* **266**: 623-624
- Howe, J.A. 1996 Turbidite and contourite sediment waves in the northern Rockall Trough, North Atlantic. *Sedimentology* **43**: 219-234

- Hughes, R.N. 1980 Optimal foraging theory in the marine context. *Oceanography and Marine Biology Annual Review* **18**: 423-481
- Hunt, G.J. and Kershaw, P.J. 1990 Remobilisation of artificial radionuclides from the sediment of the Irish Sea. *Journal of Radiological Protection* **10**: 147-151
- Hunt, J.B., Fannin, N.G., Hill, P.G., Peacock, J.D. 1995 The tephrochronology and radiocarbon dating of North Atlantic Late Quaternary sediments: An example from the St. Kilda Basin. *Geological Society Special Publication* **90**: 227-248
- Huthnance, J.M. 1986 The Rockall Slope current and other shelf processes. *Proceedings of the Royal Society of Edinburgh* **88**: 83-101
- Jahnke, R.A., Emerson, S.R., Cochran, J.K., Hirschberg, D.J. 1986 Fine scale distributions of porosity and particulate excess ^{210}Pb , organic carbon and CaCO_3 in surface sediments of the deep equatorial Pacific. *Earth and Planetary Science Letters* **77**: 59-69
- Jansen, E. and Veum, T. 1990 Evidence for two-step glaciation and its impact on North Atlantic deep water circulation. *Nature* **343**: 612-616
- Jones G.A., Jull A.J.T., Linick T.W., Donahue D.J. 1989 Radiocarbon dating of deep sea sediments: a comparison of accelerator mass spectrometer and beta decay methods. *Radiocarbon* **31**: 105-116.
- Jumars, P.A. and Wheatcroft, R.A. Responses of benthos to changing food quality and quantity with a focus on deposit feeding and bioturbation. In "Productivity of the Ocean; Present and Past" Berger W.H., Smetacek, V.S. and Wefer, G., ed., John Wiley and Sons Ltd., 1989
- Jumars, P.A., Mayer, L.M., Deming, J.W., Baross, J.A., Wheatcroft, R.A. 1990 Deep-sea deposit feeding strategies suggested by environmental and feeding constraints. *Philosophical Transactions of the Royal Society of London A* **331**: 85-101
- Kadko, D. 1980 ^{230}Th , ^{226}Ra and ^{222}Rn in abyssal sediments. *Earth and Planetary Science Letters* **49**: 360-380
- Kahn, M.I. and Williams, D.F. 1981 Oxygen and carbon isotopic composition of living planktonic foraminifera from the NE Pacific Ocean. *Palaogeography, Palaeoclimatology, Palaeoecology* **33**: 47-69
- Kidd, R.B. and Hill, P.R. 1986 Sedimentation on mid-ocean sediment drifts. In: Summerhayes, C.P and Shackleton, N.J. North Atlantic Palaeoceanography. *Geological Society Special Publication* **21**: 87-102

- Keigwin, L.D. and Jones, G.A. 1989 Glacial-Holocene stratigraphy, chronology and palaeoceanographic observations on some North Atlantic sediment drifts. *Deep Sea Research* **36**: 845-867
- Kershaw, P.J. 1985 ^{14}C and ^{210}Pb in NE Atlantic sediments: Evidence of biological reworking in the context of radioactive waste disposal. *Journal of Environmental Radioactivity* **2**: 115-133
- Kershaw, P.J., Sampson, K.E., McCarthy, W., Scott, R.D. 1995 The measurement of the isotopic composition of plutonium in an Irish Sea sediment by mass spectrometry. *Journal of Analytical and Nuclear Chemistry* **198**: 113-124
- Kershaw, P., Gurbutt, P., Woodhead, D., Leonard, K., Rees, J. 1997 Estimates of fluxes of ^{137}Cs in northern waters from recent measurements. *Science of the Total Environment* **202**: 211-233
- Kersting, A.B., Efurud, D.W., Finnegan, D.L., Rokop, D.J., Smith, D.K., Thompson, J.L. 1999 *Nature* **397**: 56
- Kim, K-H. and Burnett, W.C. 1988 Accumulation and biological mixing of Peru margin sediments. *Marine Geology* **80**: 181-194
- Koide, M., Bruland, K.W. and Goldberg, E.D. 1973 $^{228}\text{Th}/^{232}\text{Th}$ and ^{210}Pb geochronologies in marine and lake sediments. *Geochimica et Cosmochimica Acta* **37**: 1171-1187
- Koide, M. and Goldberg, E.D. 1982 Transuranic radionuclides in two coastal marine sediments off Peru. *Earth and Planetary Science Letters* **57**: 263-277
- Kroon, D., Shimmield, G., Austin, W.E.N., Derrick, S., Knutz, P., Shimmield, T. 2000 Century- to millennial-scale sedimentological-geochemical records of glacial-Holocene sediment variations from the Barra Fan (NE Atlantic). *Journal of the Geological Society, London* **157**: 643-653
- LaMont, S.P., Glover, S.E., Filby, R.H. 1998 Determination of plutonium 239/240 ratios in low activity samples using high resolution alpha spectrometry. *Journal of Radioanalytical and Nuclear Chemistry* **234**: 195-199
- Legeleux, F., Reyss, J-L., Schmidt, S. 1994 Particle mixing rates in sediments of the northeast tropical Atlantic: Evidence from $^{210}\text{Pb}_{\text{xs}}$, ^{137}Cs , $^{228}\text{Th}_{\text{xs}}$ and $^{234}\text{Th}_{\text{xs}}$ downcore distributions. *Earth and Planetary Science Letters* **128**: 545-562
- Lewis, D.M. 1977 The use of ^{210}Pb as a heavy metal tracer in the Susquehanna River system. *Geochimica et Cosmochimica Acta* **41**: 1557-1564
- Libby, W.F., Anderson, E.C., Arnold, J.R. 1949 Age determination by radiocarbon content. *Science* **109**: 227-228

- Li, Y-H, and Gregory, S. 1974 Diffusion of ions in sea water and deep sea sediments. *Geochimica et Cosmochimica Acta* **38**: 703-714
- Li, W.Q., Guinasso, N.L., Cole, K.H., Richardson, M.D., Johnson, J.W., Schink, D.R. 1985 Radionuclides as indicators of sedimentary processes in abyssal Caribbean sediments. *Marine Geology* **68**: 187-204
- Lin, J.C., Broecker, W.S., Anderson, R.F., Hemming, S., Rubenstone, J.L., Bonani, G. 1996 New $^{230}\text{Th}/\text{U}$ and ^{14}C ages from Lake Lahontan carbonates, Nevada USA and a discussion of the origin of original thorium. *Geochimica et Cosmochimica Acta* **60**: 2817-2832
- Livingston, H.D. and Bowen, V.T. 1979 Pu and ^{137}Cs in Coastal Sediments. *Earth and Planetary Science Letters* **43**: 29-45
- Livingston, H.D. and Anderson, R.F. 1983 Large particle transport of plutonium and other fallout radionuclides to the deep ocean. *Nature* **303**: 228-231
- McAninch, J.E., Hamilton, T.F., Brown, T.A., Jokela, T.A., Knezovich, J.P., Ognibene, T.J., Proctor, I.D., Roberts, M.L., Sideras,-Haddad, E., Southon, J.R., Vogel, J.S. 2000 Plutonium measurements by accelerator mass spectrometry at LLNL. *Nuclear Instruments and Methods in Physics Research B* **172**: 711-716
- McCave I.N. 1988 Biological pumping upwards of the coarse fraction of deep-sea sediments *Sedimentary Petrology* **58**: 148-158.
- McCave, I.N., Manighetti, B., Beveridge, N.A.S. 1995 Circulation in the glacial North Atlantic inferred from grain-size measurements. *Nature* **374**: 149-151
- McCave, I.N. 1995 Sedimentary processes and the stratigraphic record in the Late Quaternary North East Atlantic. *Philosophical Transactions of the Royal Society of London B* **348**: 229-241
- McCormac, F.G., Hogg, A.G., Higham, T.F.G., Baillie, M.G.L., Palmer, J.G., Xiong, L.M., Pilcher, J.R., Brown, D., Hoper, S.T. 1998 Variations of radiocarbon in tree rings: Southern hemisphere offset preliminary results. *Radiocarbon* **40**: 1153-1159
- MacKenzie, A.B., Cook, G.T., McDonald, P., Jones, S.R. 1998 The influence of mixing timescales and Re-dissolution processes on the distribution of radionuclides in Northeast Irish Sea sediments. *Journal of Environmental Radioactivity* **39**: 35-53
- MacKenzie, A.B. and Scott, R.D. 1993 Sellafield waste radionuclides in Irish Sea intertidal and salt marsh sediments. *Environmental Geochemistry and Health* **15**: 173-184

- McKinley, I.G., Baxter, M.S., Ellett, D.J., Jack, W. 1981 Tracer applications of radiocaesium in the Sea of the Hebrides. *Estuarine, Coastal and Shelf Science* **13**: 69-82
- Malcolm, S.J., Kershaw, P.J., Lovell, M.B., Harvey, B.R. 1990 The interstitial water chemistry of $^{239,240}\text{Pu}$ and ^{241}Am in the sediments of the north-east Irish Sea. *Geochimica et Cosmochimica Acta* **54**: 29-35
- Mangerud, J. and Gulliksen, S. 1976 Apparent radiocarbon ages of recent marine shells from Norway, Spitsbergen and Arctic Canada. *Quaternary Research* **5**: 263-273
- Manighetti, B., McCave, I.N., Maslin, M., Shackleton, N.J. 1995 Chronology for climate change: Developing age models for Biogeochemical Ocean Flux Study cores. *Palaeoceanography* **10**: 513-525
- Mayer, L.M. 1994 Surface area control of organic carbon accumulation in continental shelf sediments. *Geochimica Cosmochimica Acta* **58**: 1271-1284
- Mazaud, A., Laj, C., Bard, E., Arnold, M., Tric, E. 1991 Geomagnetic field control of ^{14}C production over the last 80 ky - implications for the radiocarbon timescale. *Geophysical Research Letters* **18**: 1885-1888
- Middelburg, J.J., Soetaert, K., Herman, P.M.J. 1997 Empirical relationships for use in global diagenetic models. *Deep Sea Research I* **44**: 327-344
- Mook, W.G. and Van der Plicht, J. 1999 Reporting ^{14}C activities and concentrations. *Radiocarbon* **41**:227-239
- Moore, W.S. and Dymond, J. 1988 Correlation of ^{210}Pb removal with organic carbon fluxes in the Pacific Ocean. *Nature* **331**: 339-341
- Nelson, D.E., Korteling, R.G., Scott, W.R. 1977 *Science* **198**:507
- Nies, H., Harms, I.H., Karchr, M.J., Dethleff, D., Bahe, C. 1999 Anthropogenic radioactivity in the Arctic Ocean - review of the results from the joint German project. *Science of the Total Environment* **237/238**: 181-191
- Nowell, A.R.M., Jumars, P.A., Fauchald, K. 1984 The foraging strategy of a subtidal and deep-sea deposit feeder. *Limnology and Oceanography* **29**: 645-649
- Nozaki, Y., Cochran, J.K. and Turekian, K.K. 1977 Radiocarbon and ^{210}Pb distributions in submersible-taken deep-sea cores from project FAMOUS. *Earth and Planetary Science Letters* **34**: 167-173
- Nydal, R., Gulliksen, S., Lovseth, K., Skogseth, F.H. 1984 Bomb ^{14}C in the ocean surface 1966-1981. *Radiocarbon* **26**, 7-45

- Oehmig, R. 1993 Entrainment of planktonic foraminifera: effects of bulk density. *Sedimentology* **40**: 869-877
- Officer, C.B. 1982 Mixing, sedimentation rates and age dating for sediment cores. *Marine Geology* **46**: 261-278
- Paul C.K., Hills S.J., Thiersten H.R., Bonani G., Wolfli W. 1991. ^{14}C offsets and apparently non-synchronous $\delta^{18}\text{O}$ stratigraphies between nannofossil and foraminiferal calcites. *Quaternary Research* **35**: 274-290.
- Peng, T-H. and Broecker, W.S. 1979 Rates of benthic mixing in deep-sea sediments as determined by radioactive tracers. *Quaternary Research* **11**:141-149
- Peng, T-H. and Broecker, W.S. 1984 The impacts of bioturbation on the age difference between benthic and planktonic foraminifera in deep sea sediments. *Nuclear Instruments and Methods in Physics Research* **B5**: 346-352
- Pentreath, R.J. Sources of artificial radionuclides in the marine environment. In "Radionuclides: A Tool for Oceanography" Guary, J.C., Guegueniat, P. and Pentreath, R.J., eds, Elsevier Science Publishers, 1988
- Perkins, R.W., and Thomas, C.W. Worldwide Fallout. In "Transuranic Elements in the Environments" Hanson, W.C., ed., Department of Energy Publishers, 1980
- Polach, H., Gower, J., Kojola, H., Heinonen, A. An ideal vial and cocktail for low level liquid scintillation counting. In "Advances in Scintillation Counting" McQuarrie, S.A., Ediss, C., Wiebe, L.I., eds., University of Alberta Press, 1983
- Polach, H.A. 1987 Evaluation and status of liquid scintillation counting for radiocarbon dating. *Radiocarbon* **29**: 1-11
- Ramanujam, A., Nadkarni, M.N., Ramakrishna, V.V., Patil, S.K. 1978 Studies on the HTTA extraction of tetravalent actinides. *Journal of Radioanalytical Chemistry* **42**: 349-357
- Ransom, B., Shea, K.F., Burkett, P.J., Bennet, R.H., Baerwald, R. 1998 Comparison of pelagic and nepheloid layer marine snow: implications for carbon cycling. *Marine Geology* **150**: 39-50
- Redfield A.C. 1958 The biological control of chemical factors in the environment. *American Science* **46**: 206-226
- Rice, A.L., Thurston, M.H., Bett, B.J. 1994 The IOSDL DEEPSEAS programme - introduction and photographic evidence for the presence and absence of a seasonal input of phytodetritus at contrasting abyssal sites in the Northeastern Atlantic.

- Richards, K.J. 1990 Physical processes in the benthic boundary layer. *Philosophical Transactions of the Royal Society of London A* **331**: 3-13
- Rozanski, K., Stichler, W., Gonfanti, R., Scott, E.M., Beukens, R.P., van der Plicht, J. 1992 The ^{14}C intercomparison exercise 1990. *Radiocarbon* **34**:506-519
- Rutgers van der Loeff, M.M. and Boudreau, B.P. 1997 The effect of resuspension on chemical exchanges at the sediment-water interface in the deep sea - a modelling and natural radiotracer approach. *Journal of Marine Systems* **11**: 305-342
- Saito, N. 1984 Selected data on ion exchange separations in radioanalytical chemistry. *Pure and Applied Chemistry* **56**:523-539
- Santschi, P.H., Li, Y-H., Bell, J.J., Trier, R.M., Kawtaluk, K. 1980 Pu in coastal marine environments. *Earth and Planetary Science Letters* **51**: 248-265
- Santschi P.H. Adler, D., Amdurer, M., Li, Y-H., Bell, J.J. 1980 Thorium isotopes as analogues for 'Particle Reactive' pollutants in coastal marine environments. *Earth and Planetary Science Letters* **47**: 327-335
- Santschi, P.H., Li, Y-H., Adler, D.M., Amdurer, M., Bell, J., Nyffeler, U.P. 1983 The relative mobility of natural (Th, Pb and Po) and fallout (Pu, Am, Cs) radionuclides in the coastal marine environment: results from model ecosystems (MERL) and Narragansett bay. *Geochimica et Cosmochimica Acta* **47**, 201-210
- Sanyal A, Hemming NG, Hanson GH, Broecker WS. 1995 Evidence for a higher pH in the glacial ocean from boron isotopes in foraminifera. *Nature* **373**: 234-236.
- Sarnthein, M., Pflaumann, U., Ross, R., Tiedemann, R., Winn, K. 1992 Transfer functions to reconstruct ocean palaeoproductivity: A comparison. *Geological Society of London Special Publication* **63**: 411-437
- Sayles, F.S. and Livingston, H.D. 1987 The distribution of $^{239,240}\text{Pu}$, ^{137}Cs and ^{55}Fe in continental margin sediments: relation to sedimentary redox environment. *Proceedings of the 4th International Ocean Disposal Symposium*
- Schiffelbein P 1984 Effect of benthic mixing on the information content of deep sea stratigraphic signals. *Nature* **311**: 651-653
- Schleicher, M., Grootes, P.M., Nadeau, M-J., Schoon, A. 1998 The carbonate ^{14}C background and its components at the Leibniz AMS facility. *Radiocarbon* **40**: 85-93

- Self, R.F.L. and Jumars, P.A. 1988 Cross-phyletic patterns of particle selection by deposit feeders. *Journal of Marine Research* **46**: 119-143
- Sholkovitz, E.R. 1983 The geochemistry of plutonium in fresh and marine water environments. *Earth Science Reviews* **19**: 95-161
- Sholkovitz, E.R., Cochran, J.K., Carey, A.E. 1983 Laboratory studies of the diagenesis and mobility of $^{239,240}\text{Pu}$ and ^{137}Cs in nearshore sediments. *Geochimica et Cosmochimica Acta* **47**: 1369-1379
- Silverberg, N., Nguyen, H.V., Delibrias, G., Koide, M., Sunby, B., Yokoyama, Y., Chesslet, R. 1986 Radionuclide profiles, sedimentation rates and bioturbation in modern sediments of the Laurentian Trough. *Oceanologica Acta* **9**: 285-290
- Slota PJ Jr, Jull AJT, Linick TW, Toolin LJ. 1987 Preparation of small samples for ^{14}C accelerator targets by catalytic reduction of CO. *Radiocarbon* **29**: 303-306.
- Smith, J.D. and Hamilton, T.F. 1984 Improved technique for recovery and measurement of polonium-210 from environmental materials. *Analytica Chimica Acta* **160**:69-77
- Smith, J.N and Schafer, C.T. 1984 Bioturbation processes in continental slope and rise sediments delineated by Pb-210, microfossil and textural indicators. *Journal of Marine Research* **42**: 1117-1145
- Smith, J.N., Boudreau, B.P., Noshkin, V. 1986 Plutonium and ^{210}Pb distributions in northeast Atlantic sediments: subsurface anomalies caused by non-local mixing. *Earth and Planetary Science Letters* **81**: 15-28
- Smith, C.R., Pope, R.H., DeMaster, D.J., Magaard, L. 1993 Age-dependent mixing of deep sea sediments. *Geochimica et Cosmochimica Acta* **57**: 1473-1488
- Soetaert, K., Vanaverbeke, J., Heip, C., Herman, P.M.J., Middelburg, J.J., Sandee, A., Duineveld, G. 1997 Nematode distribution in ocean margin sediments of the Goban Spur (northeast Atlantic) in relation to sediment geochemistry. *Deep Sea Research I* **44**: 1671-1683
- Soetaert, K., Herman, P.M.J., Middelburg, J.J., Heip, C., deStiger, H.S., vanWeering, T.C.E., Epping, E., Helder, W. 1996 Modelling ^{210}Pb -derived mixing activity in ocean margin sediments: diffusive versus non-local mixing. *Journal of Marine Research* **54**: 1207-1227
- Somayajulu, B.L.K., Sharma, P., Berger, W.H. 1983 ^{10}Be , ^{14}C and U-Th series nuclides and $\delta^{18}\text{O}$ in a box core from the central North Atlantic. *Marine Geology* **54**: 169-180

- Spencer, D.W., Bacon, M.P., Brewer, P.G. 1980 Models of the distribution of Pb-210 in a section across the North Equatorial Atlantic Ocean. *Journal of Marine Research* **39**: 119-138
- Stordal, M.C., Johnson, J.W., Guinasso, N.L., Schink, D.R. 1985 Quantitative evaluation of bioturbation rates in deep ocean sediments 2: comparison of rates determined by ^{210}Pb and $^{239,240}\text{Pu}$. *Marine Chemistry* **17**: 99-114
- Stuiver, M. and Polach, H.A. 1977 Discussion: reporting of ^{14}C data. *Radiocarbon* **19**: 355-363
- Stuiver, M. and Quay, P.D. 1981 A 1600-year long record of solar change derived from atmospheric ^{14}C levels. *Solar Physics* **74**: 479-481
- Stuiver, M. and Braziunas, T.F. 1993 Sun, ocean, climate and atmospheric $^{14}\text{CO}_2$: an evaluation of causal and spectral relationships. *The Holocene* **3**: 289-305
- Sugai, S.F., Alperin, M.A., Reeburgh, W.S. 1994 Episodic deposition and ^{137}Cs immobility in Skan Bay sediments: A ten-year ^{210}Pb and ^{137}Cs time series. *Marine Geology* **116**: 351-372
- Talvitie, N.A. 1972 Electrodeposition of actinides for alpha spectrometric determination. *Analytical Chemistry* **43**: 280
- Thomson, J. and Turekian, K.K. 1976 Po-210 and Pb-210 distributions in ocean water profiles from the eastern south Pacific. *Earth and Planetary Science Letters* **32**: 297-303
- Thomson, J., Colley, S., Anderson, R., Cook, G.T., MacKenzie, A.B., Harkness, D.D. 1993 Holocene sediment fluxes in the Northeast Atlantic Ocean from $^{230}\text{Th}_{\text{excess}}$ and radiocarbon measurements. *Palaeoceanography* **8**: 631-650
- Thomson, J., Colley, S., Anderson, R., Cook, G.T., MacKenzie, A.B. 1993 ^{210}Pb in the sediments and water column of the Northeast Atlantic from 47 to 59°N along 20°W. *Earth and Planetary Science Letters* **115**: 75-87
- Thomson, J. and Weaver, P.P.E. 1994 An AMS radiocarbon method to determine the emplacement time of recent deep-sea turbidites. *Sedimentary Geology* **89**: 1-7
- Thomson J., Cook G.T., Anderson R., MacKenzie A.B., Harkness D.D., McCave I.N. 1995 Radiocarbon age offsets in different-sized carbonate components of deep-sea sediments. *Radiocarbon* **37**: 91-101.
- Thomson, J., Brown, L., Nixon, S., Cook, G.T., MacKenzie, A.B. 2000 Bioturbation and Holocene sediment accumulation fluxes in the north-east Atlantic Ocean (Benthic Boundary Layer experiment sites). *Marine Geology* **169**: 21-39

- Trauth, M.H., Sarnthein, M., Arnold, M. 1997 Bioturbational mixing depth and carbon flux at the sea floor. *Palaeoceanography* **12**, 517-526
- UNSCEAR "Sources and Effects of Ionizing Radiation." United Nations Scientific Committee on the Effects of Atomic Radiation, United Nations, New York 1993
- Van Dalen, A. and Wijkstra, J. 1986 Neptunium and Americium distribution and diffusion measurements in deep ocean sediment samples. *Journal of the Less Common Metals* **122**: 563-567
- Wang, H. and McCave, I.N. 1990 Distinguishing climatic and current effects in mid-Pleistocene sediments of Hatton and Gardar Drifts, NE Atlantic. *Journal of the Geological Society, London* **147**: 373-383
- Weast, R.C. (ed.) CRC Handbook of Chemistry and Physics - 61st Edition. 1981 CRC Press
- Wheatcroft, R.A. and Jumars, P.A. 1987 Statistical re-analysis for size-dependency in deep sea mixing. *Marine Geology* **77**: 157-163
- Wheatcroft, R.A. 1992 Experimental tests for particle size-dependent bioturbation in the deep ocean. *Limnology and Oceanography* **37**: 90-104
- Wohlfarth, B., Björck, S., Possnert, G. 1995 The Swedish time scale: A potential calibration tool for the radiocarbon timescale during the Late Weichselian. *Radiocarbon* **37**: 347-360
- Wold, C.N. 1994 Cenozoic sediment accumulation on drifts in the northern North Atlantic. *Palaeoceanography* **9**: 917-941
- Wong, K.M. 1971 Radiochemical determination of plutonium in seawater, sediments and marine organisms. *Analytica Chimica Acta* **56**: 355-364
- Woodhead, D.S. Mixing processes in inshore marine sediments as inferred from the distribution of radionuclides discharges into the northeast Irish Sea from BNFL Sellafield. In "Radionuclides: A Tool for Oceanography" Guary, J.C., Guegueniat, P. and Pentreath, R.J., eds., Elsevier Science Publishers, 1988
- Yingst, J.Y. and Aller, R.C. 1982 Biological activity and associated sedimentary structures in HEBBLE area deposits, western North Atlantic. *Marine Geology* **48**: M7-M15

